DOCTORAL DISSERTATION

Dynamics of Complex Capillary Flows: Stability, Rupture, and Influence of Surfactants

A dissertation submitted in partial fulfillment of the requirements for the degree of Doctor of Philosophy in Fluid Mechanics

Universidad Carlos III de Madrid

AUTHOR

Alejandro Martínez Calvo

ADVISOR

Alejandro Sevilla Santiago

Alejandro Martínez Calvo
Grupo de Mecánica de Fluidos
Escuela Politécnica Superior
Universidad Carlos III de Madrid
Leganés, 28911, Madrid, España

Dynamics of Complex Capillary Flows:
Stability, Rupture, and Influence of Surfactants
Doctoral Dissertation
Programa de Doctorado Interuniversitario en Mecánica de Fluidos
Tesis depositada en cumplimiento parcial de los requisitos para el grado de Doctor
Leganés, noviembre 2020

This doctoral dissertation was supported by Ministerio de Educación, Cultura, y Deporte through the fellowship FPU16/02562, and its associated program Ayudas a la Movilidad 2017 and 2018 during my stays with the group of Prof. Benoit Scheid (TIPs) at the University of Brussels, and with the group of Prof. Howard A. Stone at Princeton University.

This work also had financial support by Ministerio de Economía y Competitividad, Subdirección General de Gestión de Ayudas a la Investigación, under the projects DPI2014-59292-C3-1-P, DPI2014-59292-C3-3-P, DPI2015-71901-REDT, and by Ministerio de Ciencia, Innovación y Universidades-Agencia Estatal de Investigación through the project DPI2017-88201-C3-3-R, partly financed through FEDER European funds. Support from the Red Nacional para el Desarrollo de la Microfluídica, RED2018-102829-T, is also acknowledged.

A MI FAMILIA

Acknowledgements

This thesis would not have been possible without the help and support of many people during this period as a Ph.D student. Although these brief lines cannot express how grateful I am, I would like to take the opportunity to thank all the people that have contributed, directly or indirectly, to this thesis.

Seguramente no haya palabras que expresen la gratitud que siento hacia mi director de tesis. Gracias, Alejandro, por guiarme de la mejor manera y con el mayor rigor científico posible que siempre me has inculcado, por enseñarme tanto, y por abrirme las puertas a otras tantas fuentes de aprendizaje, las cuales me has dejado explorar siempre con total libertad. En definitiva, gracias por iniciarme en el mundo de la investigación, en el cual he encontrado una verdadera vocación, por haber confiado siempre en mí, y por haberme dado la oportunidad de recorrer esta emocionante etapa, que con tu amistad en el día a día no ha podido ser mejor.

I want to especially thank Benoit Scheid for giving me the opportunity to spend three exciting months in his amazing group at Brussels University, which brings so many good memories. You always had time for discussing science with a smile on your face, even if it was late in the evening! Thank you for your guidance and patience, for your teachings, which opened me the door to the fascinating world of interfacial rheology, and for your support during all these years. De mi etapa en Bruselas quiero agradecer especialmente a Javier Rivero, ya que gran parte de esta tesis no habría sido posible sin su ayuda. Gracias, Javi, por tu amistad y por acompañarme casi diariamente en mi estancia en Bruselas, de la cual no puedo guardar mejor recuerdo. Esas caminatas por el centro con interminables charlas sobre ciencia hasta acabar en Flagey no se olvidan fácilmente.

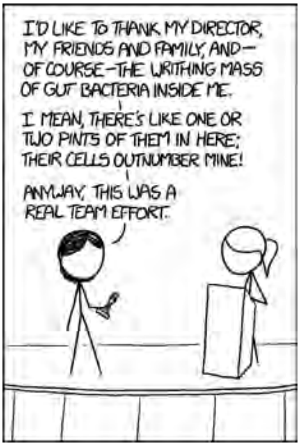

I also want to express my deep gratitude to Howard A. Stone and his magnificent group in Princeton, where I spent three wonderful months. Thank you, Howard, for being an inspiration, for your help and support, and for always caring about me during these years – my stay in Princeton has been probably one of the most enriching experiences.

I would also like to warmly thank Sujit S. Datta, for all the help and support during these last months. I hope to meet you in person soon!

También me gustaría dar las gracias a José Manuel Gordillo, por preocuparse siempre por mí y darme todo su apoyo.

Quiero también agradecer especialmente a Daniel Moreno, por toda la ayuda y enseñanzas

que me ha brindado durante estos años. Gracias por tu amistad y por todos los buenos momentos vividos, así como por las interminables y fructíferas charlas sobre ciencia.

También quiero agradecer a toda la gente del departamento que durante esta etapa, de un modo u otro, han contribuido a esta tesis, y sobre todo a que el día a día fuese lo más agradable posible. A Rafa, Marta, y Dani por ser una fuente de ánimo y risas inagotable – los buenos momentos por Leganés no han podido ser mejores. A Fernando, por su amistad y por ser el mejor compañero posible de despacho. A Mariano, por su apoyo y por estar siempre disponible para cualquier cosa. A Jorge Arrieta, por haberme ayudado tanto en esta última etapa. Y quiero agradecer también especialmente al resto de gente del departamento, o que han pasado por él, y que han hecho que estos años hayan sido muy divertidos y agradables: Alberto Cuadra, Alberto Quintero, Alen Horvat, César Huete, Daniel Gómez, Daniel Martínez, Eduardo Tarrazo, Enrique Ibáñez, Immaculada Iglesias, Javier Rodríguez, Jesús Gómez, Lorène Champougny, Miguel Parrales, Marcos Vera, María Fernández, Mario Sánchez, Patricia Vega, Vanesa Muñoz y Wilfried Coenen. También me gustaría agredecer muy especialmente a Antonio L. Sánchez, por apoyarme siempre que nos hemos encontrado, y por haberme ayudado en esta última etapa.

Quiero agradecer también a Miguel Ruiz García, por toda la ayuda que me ha proporcionado y por las buenas charlas a lo largo de estos años. Gracias a ti y a Carmen también por acogernos en nuestro breve paso por Filadelfia.

También me gustaría dar las gracias a Luis Bonilla y a Manuel Carretero, quienes fueron mis profesores durante el Máster, por todas sus enseñanzas y ayuda que me proporcionaron durante aquella etapa, donde toda esta andadura comenzó. De esta etapa tengo que agradecer por todos los buenos momentos a Filippo, Miguel (de nuevo), Juan, Rocío, y Sergei.

A Miguel Benéitez, por ser tan buen amigo desde hace ya tantos años. ¡Mucho ánimo con la tesis que ya queda poco! Al resto de mis amigos de la carrera, Carlos, Luis, Marcos, Miguel, Silvia, y muchos más con quien tan buenos momentos he vivido.

A mis amigos de Gumiel de Mercado, que aunque no les haya podido ver tan a menudo como me gustaría durante estos años, siempre han estado ahí.

A José Antonio y Carmen, por su cariño, ayuda, y apoyo durante estos años.

A mi familia. A mis tíos y primos: Alejandro, Belén, Aure, Consu, Gadea, Mario, Marta, Miguel Ángel, Sergio, Tere, y Vega, quienes siempre han estado ahí para animarme y apoyarme. A mis abuelos: Aurelio, María, Teófilo y Virgilia – desearía con todas mis fuerzas que pudiéseis leer estas líneas y poder vivir con vosotros este momento. Y especialmente a mis padres, Teófilo y Milagros, por cuidar de mí siempre, por vuestros consejos y ayuda constante. Esto es vuestro también. Os lo debo todo.

A Carolina, por su cariño y amor durante todos estos años. Tu ayuda y la ilusión que me transmites día a día han sido fundamentales, gracias por apoyarme y animarme en todo lo que hago, y por hacer que todo sea mas fácil a tu lado. Esta andadura no hubiera sido lo mismo sin ti.

Abstract

Fluid-fluid interfaces are ubiquitous in nature and everyday life, where they are found across scales and material properties, as for instance in many engineering, biological, and physiological applications and processes. In particular, cylindrical interfaces and, in general, the spontaneous tendency of surface-tension-driven flows to break up into drops, have fascinated naturalists and scientists throughout history; a fascination that lasts to date due to its crucial relevance in many phenomena of fundamental and applied interest. This is the reason for the huge research effort devoted to understand the behavior and dynamics of these filaments, namely elongated vesicles and membranes which are frequent in biological environments, or liquid jets that are routinely used for additive manufacturing applications. In most of these scenarios, the interface is usually populated with surface-active molecules, macromolecules, proteins, or contaminated with particles, which eventually form a complex microstructure that endows the interface with a rheologically complex behavior. The interaction between this structure and the hydrodynamic forces is traduced macroscopically into nonlinear interfacial rheological properties and nontrivial constitutive equations relating the surface stress with the deformation of the surface. An interface that possesses these kinds of properties is usually referred to as a *complex interface*, and the particular field of study is typically denoted by *interfacial rheology*. Nonetheless, despite of this complexity, these material cylinders share the same intrinsic instability induced by the interfacial tension known as the Plateau-Rayleigh instability, where disturbances of sufficiently long wavelength trigger the instability by decreasing the surface energy at constant volume.

The complex interactions between the bulk fluids and the surface layer complicate the theoretical modelling and the experimental protocols and measurements of the material properties associated with the interface. A vast number of issues regarding the behavior and dynamics of such complex fluid threads are yet not understood. In particular, this thesis aims to unravel fundamental aspects of the linear and nonlinear dynamics of liquid filaments whose interface is endowed with complex surface rheology, which can be elastic and/or viscous. We first deduce the components of the surface stress balance modified by interfacial elastic and viscous forces, which is necessary for the derivation of leading-order and second-order one-dimensional models. The performance of these approximations is then evaluated in the linear regime by comparing their associated growth rate of small perturbations with the one obtained from the complete conservation equations. To this end, we use Rayleigh's temporal linear stability analysis to deduce the corresponding dispersion relation of a liquid filament with interfacial rheology. Additionally, by performing simulations of the full conservation equations, we then investigate the nonlinear dynamics of these complex filaments. In particular we study the effect of Marangoni and surface viscous stresses on the natural breakup and thinning of threads, and the subsequent formation of satellite droplets. Finally, we study the linear and nonlinear dynamics of a capillary jet injected in the direction of gravity and confined between the nozzle and a bath of the same fluid.

List of Publications

Some parts of this thesis have been extracted from the refereed research journal articles listed below. I hereby declare that the results included within this document are my own work and that of my adviser and collaborators.

Refereed Journal Articles

Included in the document

1. Martínez-Calvo, A., Rubio-Rubio, M. & Sevilla, A. 2018 The nonlinear states of viscous capillary jets confined in the axial direction. *J. Fluid Mech.* **834**, 335-358. Ch. 5
2. Martínez-Calvo, A. & Sevilla, A. 2018 Temporal stability of free liquid threads with surface viscoelasticity. *J. Fluid Mech.* **846**, 877-901. Chs. 1, 2, and 3.
3. Martínez-Calvo, A., Rivero-Rodríguez, J., Scheid, B. & Sevilla, A. 2020 Natural break-up and satellite formation regimes of surfactant-laden liquid threads. *J. Fluid Mech.* **883**, A35. Chs. 1, 3, and 4.
4. Martínez-Calvo, A. & Sevilla, A. 2020 Universal thinning of liquid filaments under dominant surface forces. *Phys. Rev. Lett.* **125** (11), 114502. Ch. 1 and 4.

Not included in the document

5. Martínez-Calvo, A., Sevilla, A., Peng, G. G. & Stone, H. A. 2020 Start-up flow in shallow deformable microchannels. *J. Fluid Mech.* **885**, A25.
6. Moreno-Boza, D., Martínez-Calvo, A. & Sevilla, A. 2020 Stokes theory of thin-film rupture. *Phys. Rev. Fluids* **5**, 014002.
7. Martínez-Calvo, A. Moreno-Boza, D., & Sevilla, A. 2020 The effect of wall slip on the dewetting of ultrathin films on solid substrates: Linear instability and second-order lubrication theory. *Phys. Fluids* **32**, 102107.
8. Moreno-Boza, D., Martínez-Calvo, A. & Sevilla, A. 2020 The role of inertia in the rupture of ultrathin liquid films. *accepted in Phys. Fluids*.
9. Martínez-Calvo, A., Moreno-Boza, D., & Sevilla, A. 2020 Stability and rupture of viscoelastic liquid coatings. *under review in Soft Matter*.
10. Martínez-Calvo, A., Moreno-Boza, D., Guil-Pedrosa, J.F., & Sevilla, A. 2020 Dewetting of liquid films embedded in an unbounded viscous bath. *In preparation*.

List of Notations

We have tried to keep the notation of this thesis as simple and consistent as possible. Light italic fonts are used for scalar quantities, vectors are denoted by boldface italic letters, and tensors and matrices by bold sloping sans serif fonts.

Symbols (Latin and Greek letters)

k_a	Adsorption constant
A	Amplitude
z	Axial coordinate
w	Axial velocity
k	Axial wavenumber
θ	Azimuthal coordinate
C	Bulk concentration of a quantity
μ	Bulk viscosity
L	Capillary jet length
ρ	Density
k_d	Desorption constant
K	Dilatational elastic moduli
a	Filament radius
Q	Flow rate
$\mathcal{V}$	Fluid domain
E	Gibbs elasticity
G_f	Gibbs free energy
ω	Growth rate of perturbations
$\mathcal{C}$	Interfacial curvature
$\partial\mathcal{V}$	Interfacial domain
Γ_∞	Maximum packaging concentration
Δt_{NL}	Nonlinear correction of the breakup time
ϵ	Perturbation amplitude
p	Pressure field
r	Radial coordinate
u	Radial velocity
G	Shear elastic moduli
$\mathcal{S}$	Sphericity
Σ	Superficial area
Γ	Surface concentration of a quantity
κ_s	Surface dilational viscosity coefficient
Π	Surface pressure

μ_s	Surface shear viscosity coefficient
σ	Surface-tension coefficient
T	Temperature
R_o	Unperturbed radius
V	Volume
λ	Wavelength

Dimensionless numbers

Bo	Bond number
Bq_κ	Boussinesq number (dilational)
Bq	Boussinesq number (shear)
Ca	Capillary number
Da	Damköhler number
N_ρ	Density ratio
$\mathcal{L}$	Dimensionless depletion depth
β	Elasticity parameter
$\mathcal{G}$	Elastic shear parameter
Ξ	Elastic moduli ratio
Ka	Kapitza number
La	Laplace number
Oh	Ohnesorge number
Pe	Peclet number
K_d	Ratio between the desorption time and the viscocapillary time
Λ	Ratio between the maximum concentration and the initial one
Re	Reynolds number
Θ	Surface viscosity ratio
N_μ	Viscosity ratio
We	Weber number

Vectors and tensors

$\boldsymbol{d}$	Displacement field
$\boldsymbol{g}$	Gravitational acceleration vector
$\boldsymbol{F}_s$	Interfacial deformation gradient tensor
$\boldsymbol{B}_s$	Interfacial left-Cauchy-Green strain tensor
$\boldsymbol{x}$	Position vector
$\boldsymbol{X}$	Position vector in the reference configuration
$\boldsymbol{T}$	Stress tensor
$\boldsymbol{n}$	Unit normal vector to the interface
$\boldsymbol{t}$	Unit tangential vector to the interface
$\boldsymbol{u}$	Velocity field

Contents

CHAPTER 1

Introduction

Filamentary structures and cylindrical interfaces are ubiquitous in nature and occur in countless everyday phenomena and engineering contexts, where they are encountered across scales and material properties (Stone, 1994; Eggers, 1997; Stone *et al.*, 2004; Eggers & Villermaux, 2008; Rodríguez-Rodríguez *et al.*, 2015; Anna, 2016). Figure 1.1 shows a panoramic assortment of the different contexts where cylindrical interfaces can be found. For instance, elongated vesicles and membranes can be found in biological environments, liquid jets are routinely used for inkjet printing and additive manufacturing applications, and we can even find them associated to very large scales, for example in filamentary galaxies and in jets associated with astrophysical accretion processes. In particular, in the present document we will focus on the stability and dynamics of cylindrical filaments at scales where the intrinsic interfacial tension associated with the surface separating two immiscible fluids, plays a relevant role. These flows, usually termed *surface-tension-driven flows*, and their spontaneous tendency to break up into drops, have fascinated scientists for many years, not only for their beauty from the fundamental point of view, but also for their central importance in many applications like the ones mentioned above. From the thermodynamic point of view, this interfacial tension can be seen as the energy per unit area associated to the interface of two immiscible media. Creating the boundary between the two media requires an extra energy, thus the surface tension coefficient can be defined as $\sigma = (\partial G_f / \partial A)_{T,V,N}$, where G_f is the free energy and A is the interfacial area, for a system of volume V containing N molecules at temperature T. Due to the asymmetric force felt by the molecules placed at the interface, they have a larger associated free energy, and thus at equilibrium the system tends to minimize such energy, whereby the configuration that results is the one that minimizes the interfacial area in the absence of additional forces acting on the system.

The first documented insightful observations on the breakup of drops and liquid threads are due to Leonardo Da Vinci in Codex Leicester (da Vinci, 1508), who argued that what he called *cohesive forces* had to be overcome by the gravitational force, whereby gravity would be the force responsible for the breakup of a drop detaching from an orifice. Following this line of reasoning, Edme Mariotte conjectured in 1686 that the spontaneous breakup was due to the gravitational force, and that a jet injected upwards did not break (Mariotte, 1686). However, constant forces cannot lead to rupture, as shown almost two centuries later by Savart (1833), who reported the first qualitative experimental results of the instability of liquid threads, evidencing that the breakup into drops was spontaneous and independent of any external force or the direction in which the jet is projected (see figure 1.2). Hence, he revealed that the instability process must be an intrinsic characteristic of the jet dynamics, and that it occurs due to the presence of small perturbations at the injection nozzle which eventually grow downstream leading to the rupture of the jet. Nonetheless, despite his correct and fundamental insights, Savart did not realize that the mechanism driving the instability is the surface tension force, which had been discovered and mathematically described several years earlier by Young (1805) and Laplace (1805).

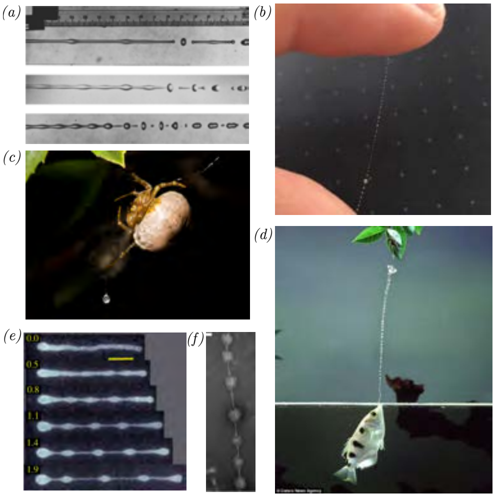

Figure 1.1: (*a*) Snapshots of a liquid jet breaking up intro droplets for three different excitation frequencies (taken from Rutland & Jameson, 1970). (*b*) My two fingers sustaining a filament of saliva displaying the *beads-on-a-string* structure. (*c*) *Bolas* spider after forming its hunting weapon: a filament connected to a droplet made of silk fibers embedded in a viscous liquid. (*d*) Archer fish throwing a high-speed liquid jet to hunt insects outside water. (*e*) Pearling instability in a vesicle (taken from Kantsler, 2007; Kantsler *et al.*, 2008; Narsimhan *et al.*, 2015). (*f*) Rayleigh-Plateau instability inducing the formation of protein droplets on a microtubule (taken from Setru *et al.*, 2020).

It was finally Joseph Plateau in 1849 who unambiguously identified the surface tension as the mechanism driving the instability of a liquid jet and its subsequent breakup into drops (Plateau, 1849). Plateau's crucial insight is that a liquid column is unstable to any perturbation which reduces the surface area at constant volume or, in other words, to disturbances of sufficiently long wavelength which generically decrease the surface energy at constant volume. Specifically, he deduced that the latter scenario applies to disturbances with a wavelength larger than the circumference of the unperturbed thread cross section. To better understand the concept of surface area reduction, let us first present an elementary argument, which consists in computing the ratio between the surface of the initial undisturbed cylinder and the n drops formed after breakup, with the additional constraint of mass conservation (De Gennes *et al.*, 2013). Mass conservation dictates that $\pi R_o^2 L = 4\pi R_d^3 n/3$, where L and R_o are the length of the cylinder and its undisturbed radius, respectively, and R_d is the radius of the spherical drops after breakup. Hence the ratio of surface areas, after eliminating n, reads $A_d/A_o = 3R_o/(2R_d)$, which means that the final surface area is lower than that of the original cylinder if $R_d > 3R_o/2$, indicating that the radii of the drops formed after breakup are on the order of R_o. Plateau's original argument is stronger, in that it provides the cut-off wavelength above which the liquid cylinder is unstable to small perturbations. To explain Plateau's deduction, we introduce a harmonic perturbation of the thread shape,

$a(z,\theta) = \tilde{R} + \epsilon \cos(m\theta)\cos(kz)$, where k is the real axial wavenumber, m the integer azimuthal number, and ϵ the amplitude of the harmonic disturbance. Here, $\tilde{R}$ is the radius that enforces a constant volume V independently of the value of ϵ,

$$V = \int_0^{\pi} \int_0^{\pi/k} a^2 \,\mathrm{d}z\mathrm{d}\theta = \frac{\pi^2(4\tilde{R}^2 + \epsilon^2)}{4k}, \tag{1.1}$$

which yields $\tilde{R} = (Vk/\pi^2 - \epsilon^2/4)^{1/2}$. For simplicity we assume that the volume is the same as that of a straight cylinder of unit radius and whose length is π/k, thus $V = \pi^2/k$. The surface area of the perturbed cylinder is

$$\Sigma = \int_0^{2\pi} \int_0^{\pi/k} a\sqrt{1 + (\partial_z a)^2 + (\partial_\theta a/a)^2}\,\mathrm{d}z\mathrm{d}\theta = \frac{2\pi^2}{k} + \epsilon^2\pi^2\frac{k^2 - 1 + m^2}{8k} + O(\epsilon^4). \tag{1.2}$$

Therefore, Σ only decreases if the perturbation is axisymmetric, $m = 0$, and if the dimensionless wavenumber $k < 1$ or, equivalently, if the wavelength $\lambda > 2\pi$, where the length scales have been non-dimensionalized with the unperturbed thread radius R_o. It is therefore deduced that axisymmetric disturbances with a wavelength larger than the circumference of the unperturbed cross section are unstable.

However, the quasi-static argument of Plateau leaves out the dynamics of the thread, a task that was pioneered by Rayleigh (Rayleigh, 1878, 1892), by means of a temporal linear stability analysis. This analysis consists of linearising the flow variables around a static liquid cylinder, and taking advantage of the invariance of the linearized equations of motion with respect to time, the axial coordinate, and the azimuthal angle, what allows decomposing the perturbations into independent wave-like Fourier modes, defined by a complex frequency ω, a real axial wavenumber k, and an integer azimuthal number m. The outcome of such analysis is a dispersion relation, $D(\omega, k, m) = 0$ which, for a given value of m, is only satisfied by certain pairs of frequency and wavenumber. An elementary analysis of the dispersion relation explains the onset of the instability and predicts the most amplified wavelength. In the limiting case of dominant inertia, this optimal wavelength is approximately nine times the unperturbed thread radius R_o. The latter wavelength, usually referred to as the natural wavelength, thus dictates the drop size after the breakup of the liquid column. A detailed derivation of Rayleigh's dispersion relation is presented in §3.2.

Although the effect of viscosity on the stability of liquid threads was first mentioned by Plateau (1873), the linear temporal stability analysis considering the full Navier-Stokes equations was first solved by Rayleigh (1892) (see also Chandrasekhar, 1961), who revealed that the optimal wavelength becomes much larger than the thread radius when viscous forces are dominant.

About eighty years later, the local spatial and spatiotemporal problems, in which the liquid jet moves with uniform velocity U with respect to the injector, were solved (Keller *et al.*, 1973; Leib & Goldstein, 1986*a*,*b*). In particular, it was demonstrated by Keller *et al.* (1973) that the spatial and temporal stability analyses are equivalent if U is sufficiently larger

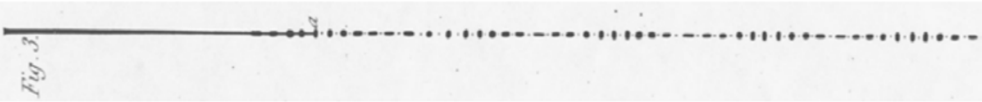

Figure 1.2: Breakup of a liquid jet of 6 mm diameter, showing the succession of main and satellite drops as well as drop shape oscillations. The picture is taken from Savart's original work (Savart, 1833).

than the speed of small-amplitude capillary instability waves, U_σ. In the spatial setting, the latter condition means that the relative growth of the wave amplitude along one wavelength is small. Thus, in a frame of reference moving with the jet, the amplitude growth is spatially uniform in a first approximation, what explains the equivalence of the temporal and spatial approaches if $U \gg U_\sigma$. Since the wavelength of the unstable capillary waves is much larger than the unperturbed cylinder radius, the scaling of U_σ depends on the value of the associated Reynolds number, $Re_\sigma = \rho U_\sigma \bar{R}/\mu$, where ρ and μ are the liquid density and viscosity, respectively. In the limit of Euler flow, $Re_\sigma \gg 1$, the value of U_σ is given by the balance $\sigma_0/R_o \sim \rho U_\sigma^2$, where σ_0 is the surface tension, yielding $U_\sigma \sim \sqrt{\sigma_0/(\rho R_o)}$, usually referred to as the *capillary velocity*, and $U/U_\sigma \sim \sqrt{We}$, where $We = \rho U^2 R_o/\sigma_0$ is the Weber number. Note that, in this case, $Re_\sigma = \sqrt{La} \gg 1$, where $La = \rho\bar{R}\sigma_0/\mu^2$ is the Laplace number, which may also be written as $La = Oh^{-2}$ in terms of the usual Ohnesorge number, $Oh = \mu/\sqrt{\rho\bar{R}\sigma_0}$. In the opposite limit of Stokes flow, $Re_\sigma \ll 1$, the proper balance is $\sigma_0/\bar{R} \sim \mu U_\sigma/\bar{R}$, whence $U_\sigma \sim \sigma_0/\mu$, usually referred to as the *visco–capillary velocity*. In this limit, $U/U_\sigma \sim Ca$, where $Ca = \mu U/\sigma_0$ is the capillary number, and $Re_\sigma = La \ll 1$. Therefore, the condition that must be satisfied for the temporal and spatial approaches to be equivalent is that $\sqrt{We} \gg 1$ when $\sqrt{La} \gg 1$, or that $Ca \gg 1$ when $La \ll 1$, this resulting in periodic disturbances practically uniform in space. It is also important to point out that the formation of a slender jet from a nozzle requires that $We > We_c \sim O(1)$ when $\sqrt{La} \gg 1$, or that $Ca > Ca_c \sim O(1)$ when $La \ll 1$, where We_c and Ca_c are the critical Weber and capillary numbers for the transition from convective to absolute instability (Leib & Goldstein, 1986*a*,*b*). After these pioneering works, the spatiotemporal stability of the liquid jet was refined in several studies that accounted for the non-parallelism of the thread due to the effects of gravity and of the viscous relaxation of the initially non-uniform velocity profile at the injector exit (see e.g. Le Dizès, 1997; Sevilla, 2011; Rubio-Rubio *et al.*, 2013; Le Dizès & Villermaux, 2017; Martínez-Calvo *et al.*, 2018; Shukla & Gallaire, 2020).

Concerning the experimental studies on the linear stage of the instability, the first quantitative measurements of the linear growth of perturbations in a liquid thread were due to Haenlein (1931), Donnelly & Glaberson (1966), and Goedde & Yuen (1970), whose main goal was to test the linear theory of Rayleigh and Chandrasekhar for different liquid viscosities. In particular, the latest and most precise experiments measuring the temporal amplification curve are due to González & García (2009), who found an excellent agreement with the predictions of the linear stability theory.

Although linear theory is able to accurately predict the growth rate of harmonic disturbances and the jet break-up length (Kalaaji *et al.*, 2003), it fails at providing accurate predictions for the size of the drops formed after break-up. Indeed, the linear stage of the instability is followed by a nonlinear self-accelerated stage during which the interface shape is considerably distorted. Consequently, a nonlinear theory is required to describe the thread breakup into main drops and satellite droplets, as detailed in chapter 4. The first efforts to include nonlinear effects in the description were based on perturbation theory, pioneered by the weakly-nonlinear analyses of Yuen (1968) and Nayfeh (1970). These theories provided predictions for the size of the main and satellite droplets. The first experimental tests were performed by Goedde & Yuen (1970), who were the first authors to systematically investigate such nonlinear effects in detail, comparing their experimental results with the theory of Yuen (1968). The satellite drop formation process was first quantified by Rutland & Jameson (1970) and Lafrance (1975), while Chaudhary & Maxworthy (1980) studied how the satellite drop formation is affected by forcing the liquid jet with different harmonics, revealing the conditions needed to inhibit their formation.

The high numerical cost associated to solving the full Navier-Stokes equations with a free boundary, together with the development of the inkjet printing technology in the early 1970s, motivated the development of one-dimensional approximations of the mass and momentum equations, which were pioneered by Lee (1974), and refined later on by a number of authors (see Eggers, 1997, and references therein). The correct form of the leading-order one-dimensional equations was independently obtained by Eggers & Dupont (1994) and García & Castellanos (1994), and has been extensively and successfully used in many different configurations (see e.g. Ambravaneswaran *et al.*, 2004; Rubio-Rubio *et al.*, 2013; Martínez-Calvo *et al.*, 2018).

The increase in computational power finally allowed a fully nonlinear approach by means of direct numerical simulations of the axisymmetric Navier-Stokes equations. In particular Mansour & Lundgren (1990) and Ashgriz & Mashayek (1995) computed the satellite droplet radii just prior to pinch-off, finding an excellent agreement with the experiments of Rutland & Jameson (1970) and Lafrance (1975).

Of particular importance is the fact that the last stages prior to the pinch-off singularity are self-similar. Indeed, it was revealed by Eggers (1993) that the local flow near the minimum thread radius loses memory of the initial and boundary conditions, and is governed by a local balance of the driving surface tension force with viscous and inertial forces, leading to a universal solution that describes the final approach to the singularity. Interestingly, self-similar solutions different from Eggers' one were also discovered in the limiting cases of an inviscid liquid thread, where the local balance is established between inertia and surface tension forces (Keller & Miksis, 1983; Day *et al.*, 1998), and of a very viscous thread (Papageorgiou, 1995), for which the local balance takes place between viscous and surface tension forces. In a recent investigation, Castrejón-Pita *et al.* (2015) revealed the different transitions that take place between these three self-similar solutions during the thinning of an axisymmetric liquid thread, depending on the liquid viscosity, prior to the establishment of Eggers' universal solution.

The main goal of this thesis is to unravel a number of key aspects of the linear and nonlinear dynamics of liquid filaments whose interface is endowed with rheological properties. Such *complex interfaces*, whose mechanical, thermodynamic and chemical properties are studied in the field of *interfacial rheology*, are the surface counterpart of *complex fluids*, a term that encompasses fluids with unusual mechanical properties, namely polymer solutions, colloidal suspensions, active fluids, or surfactant-laden liquids, which are part of our everyday life. A few examples include the milk we drink, our saliva, the tear films, or the pulmonary surfactant present in mammalian alveoli. These properties manifest, for instance, in nonlinear relationships between the stress and the rate of strain, or rheological and active behaviors in the bulk fluids or at the interface between two immiscible fluids. Despite this complex behavior, all material cylinders share the same instability mechanism induced by the interfacial tension, which is the Plateau-Rayleigh instability discussed above, and where disturbances of sufficiently long wavelength generically decrease the surface energy at constant volume.

1.1 Complex interfaces

Fluid-fluid interfaces of cylindrical shape occur everywhere, as outlined previously, be it in nature and living systems, or in technological and industrial applications, as food processing or cosmetics, which is the main reason for the huge research effort devoted to understand their dynamics. Nonetheless, the interfaces involved in these realistic configurations are usually far from being accurately described by the idealized scenario considered so far in this thesis, which is an interface characterized by a single value of the surface tension coefficient. In particular, when surface-active molecules, macromolecules, proteins or particles populate the interface, this ideal description is not valid due to the complex microstructure formed by these molecules or particles. Such structures are intrinsically coupled with bulk and interfacial hydrodynamic forces, which manifests macroscopically in linear or nonlinear rheological properties and complex constitutive equations relating the surface stress with the interfacial rate of deformation. These interfaces are usually referred to as *complex interfaces*, comprising material surfaces whose mechanical properties are nontrivial, usually rationalized in terms of an *interfacial rheology*, thereby modifying its material properties and thus its dynamics. Apart from this complexity, an additional difficulty is associated with the interfacial transport phenomena of these molecules and particles, both across and within the interface, which must be taken into for a correct description of complex interfacial processes. All these exciting ingredients are the reason for the great attraction that this field has raised, from the early observations of Pliny the Elder (Fuller & Vermant, 2012), and later investigations of scientists and naturalists as Benjamin Franklin (Franklin, 1774), Plateau (Plateau, 1849), Marangoni (Marangoni, 1871), Rayleigh (Rayleigh, 1889) and Agnes Pockels (Pockels, 1892, 1893, 1894), to our days, ranging from physicists and chemists to engineers and biologists.

As pointed out above, notwithstanding the complexity of the interface, all material cylinders share the same instability mechanism induced by the interfacial tension. Indeed, the

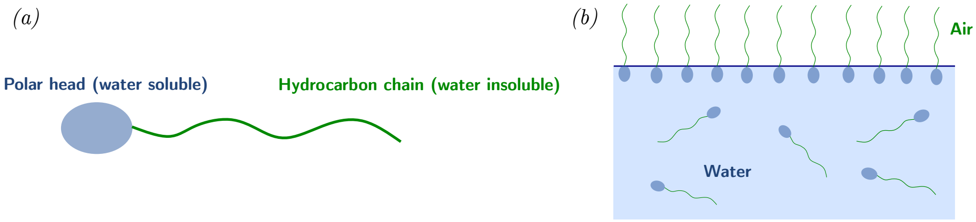

Figure 1.3: (*a*) Scheme of a surfactant molecule, and (*b*) of a surfactant monolayer covering an air-water interface.

generality and power of Rayleigh's ideas is demonstrated by the fact that his analysis is still routinely used to explain the instability process of material cylinders in contexts completely different from liquid threads, including phenomena like pearling of vesicles (Bar-Ziv & Moses, 1994; Powers, 2010; Narsimhan *et al.*, 2015) where the isotropic membrane tension can trigger the instability in competition with the bending and shear resistance, nucleation of protein droplets on microtubules (Setru *et al.*, 2020), microtubule-growth-driven lipidic membranes (Fygenson *et al.*, 1997), or cytokinesis of active and passive cells (Prost *et al.*, 2015) (see figure 1.1).

The present thesis is devoted to study the linear and nonlinear dynamics of cylindrical filaments whose interface is endowed with surfactant-induced elasticity, viscous resistance to flow, or bending and shear resistance. These effects translate into changes in the surface stress balance at the interface between the two immiscible fluids, as will be detailed in §1.2. In particular, concerning the theoretical approach, throughout the present document we utilize continuum approximations, both for the description of the bulk and the interface. Indeed, these interfacial effects can be collected into a surface stress tensor that includes the new material parameters that quantify these rheologically complex behaviors. In §1.2 we detail the full conservation equations from which we start all the derivations and computations in the subsequent chapters, as well as the characteristic scales used in most of the sections. However, prior to the mathematical formulation, we will now provide a brief historical review of the different interfacial properties of interest for the present thesis, as well as an account of the most recent studies dealing with these effects in the context of liquid filaments.

Surfactant-induced elasticity

The core of this thesis is devoted to the study of the stability and nonlinear dynamics of liquid threads in the presence of surface-active agents, usually referred to as surfactants. Surfactants are amphiphilic molecules, which means that they are composed of a polar head and a hydrophobic tail, as sketched in figure 1.3. Therefore, their solubility in water and organic liquids as oils is limited, and in many cases they are easily adsorbed at fluid-fluid interfaces forming monolayers. In particular, as previously outlined, it has been known for a long time that the presence of surface-active molecules modifies the dynamics of fluid interfaces (for a historical account the reader is referred to Scriven & Sternling, 1960; Fuller & Vermant, 2012), as evidenced by the early studies of Plateau, Marangoni, Pockels, and Rayleigh on the effect of contamination and impurities on the surface tension of an interface (Plateau, 1849; Marangoni, 1871; Pockels, 1892, 1893; Rayleigh, 1889, 1890). The crucial importance of surfactants in the respiratory system (Van Golde *et al.*, 1988), as well as in many applications like the generation and stabilisation of emulsions, foams and contrast agents for medical imaging (Rodríguez-Rodríguez *et al.*, 2015), justifies the intense research effort oriented towards a quantitative understanding of their effects on the dynamics of interfaces. The role of the surfactant is twofold. First, it reduces the surface tension coefficient, σ, by an amount that depends on the interfacial concentration of surfactant, Γ. Second, it induces an effective surface rheology through elastic and viscous stresses. The former are the Marangoni stresses, termed in honour of the Italian physicist, generated by the imbalances of σ produced by the variations of Γ along the interface, which leads to the central concept of *surfactant-induced surface elasticity*.

The effects of surface elasticity induced by the presence of surfactants have been studied theoretically and experimentally in the linear and nonlinear regimes of several configurations of practical relevance, e.g. liquid threads (Whitaker, 1976; Craster *et al.*, 2002; Timmermans & Lister, 2002; Kamat *et al.*, 2018; Martínez-Calvo & Sevilla, 2018; Martínez-Calvo *et al.*, 2020), dip coating (Campana *et al.*, 2011; Seiwert *et al.*, 2014; Champougny *et al.*, 2015), bubbles immersed in a viscous medium (Hameed *et al.*, 2008) or drop deformation and breakup (Stone & Leal, 1990; Milliken *et al.*, 1993), to cite a few. Within the context of liquid filaments embedded in a passive ambient fluid, the effect of surface elasticity has been explored by means of experiments (Liao *et al.*, 2004, 2006; Ponce-Torres *et al.*, 2016*b*), theory (Whitaker, 1976; Timmermans & Lister, 2002) and numerical simulations (Campana & Saita, 2006; Dravid *et al.*, 2006; McGough & Basaran, 2006; Ponce-Torres *et al.*, 2016*a*; Kamat *et al.*, 2018; Martínez-Calvo *et al.*, 2020). In particular, the linear stability of a surfactant-laden thread was first explored by Whitaker (1976), who also considered the effect of solubility and sorption kinetics, and it was later on corrected by Timmermans & Lister (2002) in the insoluble case. In chapter 3 we will briefly revisit the stabilizing effect of Marangoni stresses on a surfactant-laden thread in the linear regime.

Additionally, previous related studies have extended the seminal work of Tomotika (1935) on the stability of liquid threads embedded in an immiscible unbounded liquid by including the effects of surfactants. In particular, the work of Hansen *et al.* (1999) deals with soluble surfactants and studies the role of surface diffusion and Marangoni stresses on the linear growth of small perturbations. Kwak & Pozrikidis (2001) extended the problem for an insoluble surfactant by including internal and external coaxial solid boundaries, and also retaining the effect of surface diffusion. Previously, Carroll & Lucassen (1974) analyzed both, experimentally and theoretically, the effect of solid oleophilic filaments coated by a cylindrical oil film, observing that the presence of an insoluble surfactant at the outer oil-air interface substantially decreases the growth rate of the instability.

Regarding the subsequent nonlinear dynamics, the works of McGough & Basaran (2006) and Kamat *et al.* (2018) focused on the micro-thread cascade that appears close to break-up due to the presence of surfactants. These works also analyze the different scalings close to pinch-off and the evolution of the minimum radius of the thread and its axial position during the unfolding of the micro-cascade. Moreover, Kamat *et al.* (2018) revealed that the mechanism responsible for the dynamical surface tension effects induced by surfactants in filament break-up is the action of Marangoni stresses rather than surface tension lowering. Dravid *et al.* (2006) and Martínez-Calvo *et al.* (2018) extensively studied the effect of surface elasticity on the satellite formation of a surfactant-laden filament embedded in a passive ambient fluid and under negligible gravitational effects, which will be detailed in chapter 4.

Surface viscous effects

The conjecture about the existence of a viscous resistance of an interface separating two immiscible media can be found in the writings of Descartes and Rumford, as outlined by Rayleigh (1890) (see also Fuller & Vermant, 2012). However, it was to Plateau's observations that its acceptance was due. In particular, Plateau designed an experiment where he was able to compare the damping of a magnetic needle between a clean and a surfactant-laden interface. However, Marangoni correctly pointed out that the needle sweeps the surfactant and thus generates concentration gradients, claiming that the differences observed by Plateau could be a consequence of the interfacial forces arising due to surface tension gradients (Marangoni, 1871), later on called *surface elasticity* or Marangoni stresses in his honor. To prove this, he conducted an experiment with a modified setup consisting of a solid brass disk placed at the interface, which yielded no surface viscous forces. It was finally Rayleigh who unambiguously and separately identified the existence of Marangoni stresses and surface viscous stresses (Rayleigh, 1890), by using a ring, thus avoiding concentration gradients and showing the importance of reducing the contact area between the measurement device and the interface. Several years later, Boussinesq (1913) introduced the rheological material parameters associated with the interface, and posed the theoretical formalism to explain the observations of Lebedev (1916) and Silvey (1916), who showed that contaminated small bubbles moved through an outer liquid with a velocity similar to that of a rigid sphere (Stokes, 1851). It was eventually Scriven (1960) who correctly deduced the linear constitutive equation relating the surface stress with the rate of strain of a complex interface with viscous resistance to flow, and which is usually referred to as the *Boussinesq–Scriven law* in their honor.

In particular, surface viscous stresses arising due to the resistance to surface deformation are usually described through two surface viscosity coefficients, namely the surface shear and dilatational viscosities, $\mu_s(\Gamma, T)$ and $\kappa_s(\Gamma, T)$ (Scriven, 1960; Langevin, 2014; Fuller & Vermant, 2012; Jaensson & Vermant, 2018). Note that, as happens with the surface-tension coefficient, the two surface viscosity coefficients generally depend on the concentration of surface-active molecules Γ and on the temperature T. It is important to emphasize that in this thesis we will restrict the study to isothermal configurations. Experiments and theory have clearly demonstrated that surface viscous effects play a central role in many interfacial flows like foams (Joye *et al.*, 1994), liquid films (Scheid *et al.*, 2010), liquid bridges (Ponce-Torres *et al.*, 2016*a*,*b*) and drop break-up (Ponce-Torres *et al.*, 2017), to cite a few. As mentioned in the previous paragraph, the simplest constitutive equation relating the surface stress with the surface rate of strain is the Boussinesq-Scriven (BS) law (Boussinesq, 1913; Scriven, 1960), which may be seen as the surface analog of the Navier-Poisson law. Indeed, the BS law assumes that the surface state of stress is isotropic, instantaneous, and linear in the surface rate of strain, and disregards complex surface rheology (Edwards *et al.*, 1991; Fuller & Vermant, 2012; Langevin, 2014; Jaensson & Vermant, 2018), leading to the concept of a *Newtonian surface* (Scriven, 1960). Although in this thesis we will make extensive use of the concept of a Newtonian interface modeled with the BS law, which will be derived in detail in section §1.7, it is important to emphasize that non-Newtonian surface rheology can arise in certain surfactant monolayers (Scheid *et al.*, 2012). For a complete and exhaustive review of the state of the field, the reader is referred to Edwards *et al.* (1991), Fuller & Vermant (2012), Langevin (2014), Raghunandan *et al.* (2018), Jaensson & Vermant (2018), and references therein, where more complex interfacial constitutive equations can be found.

Surface viscous resistance does not arise only in surfactant-laden interfaces, but also, for instance, in vesicles, biological membranes, or active interfaces, where they coexist with the intrinsic elastic forces, and they may have a dominant role in their dynamics (see for instance Powers, 2010; Narsimhan *et al.*, 2015; Mietke *et al.*, 2019*b*,*a*; Farutin *et al.*, 2019, and references therein), polymersomes being the prominent example.

Interfaces with solid-like mechanics

There is a vast number of technological and biological scenarios where interfaces present a solid-like behavior. In these cases, the interface is usually treated as a thin elastic membrane separating two media (Helfrich, 1973; Seifert, 1997; Hegemann *et al.*, 2018; Jaensson & Vermant, 2018). This elastic interface can be produced artificially by different chemical processes as cross-linking and polymerization at the interface, and they can also be formed by the adsorption and self-assembly of particles, surface-active molecules, proteins, lipids or colloids, for instance in red blood cells (Skalak & Branemark, 1969; Skalak *et al.*, 1973; Barthes-Biesel, 2016; Secomb, 2017) or colloidosomes (Dinsmore *et al.*, 2002). The most common configuration is an elastic shell encapsulating and transporting a fluid, which routinely occurs in the pharmaceutical and chemical industry to transport and delivery different compounds, and also in the biological realm, namely in red blood cells, whose membrane, composed of proteins and phospholipids, presents specific elastic properties to resist external shear flows and collisions/adhesions with other cells.

Within the context of vesicles and biological membranes, namely lipidic bilayers, a common choice to model the elastic membrane is the usually referred to as Helfrich potential (Helfrich, 1973; Zhong-Can & Helfrich, 1987, 1989; Seifert, 1997), which accounts for the bending resistance of the membrane, leading to a net force in the direction normal to the interface which is proportional to the bending modulus κ_B, and to higher-order terms in the interfacial curvature. When the interface also exhibits elastic shear resistance, a popular choice is the semi-empirical model derived by Skalak *et al.* (1973), which has been widely used to study the dynamics of red blood cells and vesicles both theoretically and numerically (Barthes-Biesel & Rallison, 1981; Barthes-Biesel, 2016; Secomb, 2017). Very recently, within the context of surface-active molecules assembled at the interface, an interfacial neo-Hookean constitutive equation has been derived (Pepicelli *et al.*, 2017; Jaensson & Vermant, 2018), and used to describe new and fascinating phenomena that take place in pendant drops covered by octadecyltrichlorosilan (OTS), and bubbles coated with hydrophobinm (HFBI) (Knoche *et al.*, 2013; Hegemann *et al.*, 2018).

Finally, as outlined previously, at sufficiently small scales these intrinsic elastic forces coexist with surface viscous forces (see Powers, 2010, and references therein), as it is the case of liposomes (Dimova *et al.*, 1999, 2000, 2006), and polymersomes (Dimova *et al.*, 2002), where surface viscous forces may even be dominant over elastic forces.

1.2 Governing equations

Throughout the present document we consider the axisymmetric motion of an incompressible liquid thread of density ρ, viscosity μ, and interfacial tension $\bar{\sigma}$, embedded in a surrounding fluid of density $\hat{\rho}$ and viscosity $\hat{\mu}$. Hatted variables and upper bars will hereafter denote properties of the outer fluid and dimensional variables, respectively, unless specified otherwise. The liquid filament, whose interface $\partial\mathcal{V}(\bar{t})$ is placed at a radial position $\bar{r} = \bar{a}(\bar{z}, \bar{t})$, occupies a volume $\mathcal{V}(\bar{t})$ (see figure 1.4).

To describe the flow we make use of the incompressible Navier-Stokes equations, which are non-dimensionalized with the unperturbed thread radius, the visco-capillary time and velocity, and the capillary pressure, as characteristic length, time, velocity, and pressure scales

$$\ell_c = R_o, \quad v_c = \frac{\sigma_o}{\mu}, \quad t_c = \frac{\mu R_o}{\sigma_o}, \quad p_c = \frac{\sigma_o}{R_o}, \quad \sigma_c = \sigma_o, \tag{1.3}$$

where σ_o denotes surface tension coefficient associated to an initial concentration of surfactant molecules, lipids, or particles at the interface, Γ_o, yielding the dimensionless Navier-Stokes equations,

$$\nabla \cdot \boldsymbol{u} = 0, \quad \text{and} \quad La\left(\frac{\partial \boldsymbol{u}}{\partial t} + \boldsymbol{u}\cdot\nabla\boldsymbol{u}\right) = \nabla\cdot\boldsymbol{T} \quad \boldsymbol{x} \in \mathcal{V}, \tag{1.4}$$

where $\boldsymbol{x}$ is the position vector, $\boldsymbol{u}(\boldsymbol{x}, t) = u\,\boldsymbol{e}_r + w\,\boldsymbol{e}_z$ is the velocity field, and u, w, and $\boldsymbol{e}_r$, $\boldsymbol{e}_z$ are the radial and axial velocity components and the corresponding unit vectors, respectively. Note that, r, z and t stand for the radial and axial coordinates and time, respectively. In equation (1.4), $\boldsymbol{T} = -p\boldsymbol{I} + [\nabla\boldsymbol{u} + (\nabla\boldsymbol{u})^{\mathrm{T}}]$ is the stress tensor for an incompressible Newtonian liquid, where $\boldsymbol{I}$ is the identity tensor and $p(\boldsymbol{x}, t)$ is the pressure field. Additionally, $La =$

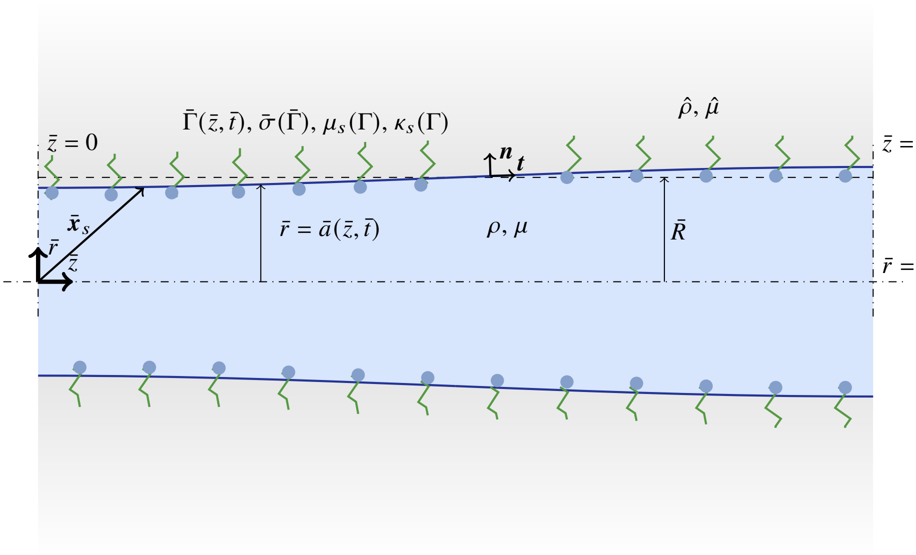

Figure 1.4: Dimensional sketch of the flow configuration considered in most parts of the present document.

$\rho\sigma_o R_o/\mu^2$ denotes the Laplace number, which is built by taking the visco-capillary velocity, σ_o/μ, as the characteristic velocity in the standard Reynolds number.

When an outer bath is considered, we also assume that the flow is incompressible and thus the dimensionless mass and momentum conservation equation read,

$$\nabla \cdot \hat{\boldsymbol{u}} = 0, \quad \text{and} \quad La\, N_\rho \left(\frac{\partial \hat{\boldsymbol{u}}}{\partial t} + \hat{\boldsymbol{u}} \cdot \nabla \hat{\boldsymbol{u}} \right) = \nabla \cdot \hat{\boldsymbol{T}} \quad \boldsymbol{x} \in \hat{\mathcal{V}}, \tag{1.5}$$

where $\hat{\mathcal{V}}$ denotes the outer fluid domain, $N_\rho = \hat{\rho}/\rho$ is the outer-to-inner density ratio, and $\hat{\boldsymbol{T}} = -\hat{p}\boldsymbol{I} + N_\mu \left[\nabla\hat{\boldsymbol{u}} + (\nabla\hat{\boldsymbol{u}})^{\mathrm{T}}\right]$ is the outer stress tensor, $N_\mu = \hat{\mu}/\mu$ being the outer-to-inner viscosity ratio.

At the free surface $\partial\mathcal{V}$ we impose the continuity of velocities, the kinematic condition, and the stress balance boundary conditions, which read

$$\boldsymbol{u} = \hat{\boldsymbol{u}}, \quad \boldsymbol{x} \in \partial\mathcal{V} \tag{1.6a}$$

$$\boldsymbol{n} \cdot (\partial_t \boldsymbol{x}_s - \boldsymbol{u}_s) = 0, \quad \boldsymbol{x} \in \partial\mathcal{V} \tag{1.6b}$$

$$(\hat{\boldsymbol{T}} - \boldsymbol{T}) \cdot \boldsymbol{n} + \nabla_s \cdot \boldsymbol{T}_s = \boldsymbol{0}, \quad \boldsymbol{x} \in \partial\mathcal{V} \tag{1.6c}$$

respectively, where $\boldsymbol{u}_s = \boldsymbol{u}(\boldsymbol{x}_s)$ is the liquid velocity at the interface, $\boldsymbol{x}_s$ is the parametrization of the interface, located at $r = a(z,t)$, $\boldsymbol{n}$ is the unit normal vector to the interface and $\nabla_s = \boldsymbol{I}_s \cdot \nabla$ is the surface gradient operator, where $\boldsymbol{I}_s = \boldsymbol{I} - \boldsymbol{nn}$ is the surface projection tensor.

This operator will be appropriately defined in cylindrical coordinates in the subsection §§1.7.1. Here $\boldsymbol{T}_s$ is the surface stress tensor, which takes different functional forms depending on the nature and intrinsic behavior of the interface, as will be extensively discussed and detailed in §1.7. The set of equations (1.4)–(1.6) forms a closed system to determine $\boldsymbol{u}$, p, and $\boldsymbol{x}_s$. Hereinafter, every surface quantity will be denoted by the subscript $()_s$, whereas the tangential and normal projections will be referred to with the subscripts $()_t$ and $()_n$, respectively. The remaining boundary and initial conditions will depend on the configuration under study, which will be detailed in the corresponding chapters and sections.

1.3 Transport equation of a scalar quantity at a moving interface

When the interface is laden with a surface concentration Γ of surfactant molecules, particles or polymers, a transport equation for Γ at the moving interface is generally needed to close the mathematical model. To that end, let us consider the interfacial surface element $\delta\boldsymbol{S} = \mathrm{d}S\,\boldsymbol{n}$ that moves with the local fluid velocity, $\boldsymbol{u}_s$. The material derivative of the surface element is

$$\frac{\mathrm{D}(\mathrm{d}S)}{\mathrm{D}t} = \mathrm{d}S(\boldsymbol{\nabla}_s \cdot \boldsymbol{u}_s), \tag{1.7}$$

which is identical to equation (4) of Stone (1990). Dividing by $\mathrm{d}S$ and taking the limit $\mathrm{d}S \longrightarrow 0$, it is readily deduced that $\boldsymbol{\nabla}_s \cdot \boldsymbol{u}_s$ is the rate of change of area per unit area of the material interface. In the absence of sources and sinks, and neglecting molecular diffusion, the conservation of Γ requires that

$$\frac{\mathrm{D}}{\mathrm{D}t}\int_S \Gamma \mathrm{d}S = \int_S \left(\frac{\mathrm{D}\Gamma}{\mathrm{D}t} + \Gamma\,\boldsymbol{\nabla}_s \cdot \boldsymbol{u}_s\right)\mathrm{d}S = 0, \tag{1.8}$$

whereby the following equation must hold at every point of the surface,

$$\frac{\mathrm{D}\Gamma}{\mathrm{D}t} + \Gamma\,\boldsymbol{\nabla}_s \cdot \boldsymbol{u}_s = 0. \tag{1.9}$$

A key point here is to properly define the material derivative, $\mathrm{D}/\mathrm{D}t$, in a way that is consistent with the chosen reference frame. For instance, in the laboratory frame it has the usual meaning, $\mathrm{D}/\mathrm{D}t = (\partial_t\Gamma)_M + \boldsymbol{u}_s \cdot \boldsymbol{\nabla}\Gamma$, where, following the same notation as in Pereira & Kalliadasis (2008), M denotes a fixed point in the laboratory frame. Hence, the surfactant transport equation in the laboratory frame reads

$$\left(\frac{\partial\Gamma}{\partial t}\right)_M + \boldsymbol{u}_s \cdot \boldsymbol{\nabla}_{||}\Gamma + \Gamma\,\boldsymbol{\nabla}_s \cdot \boldsymbol{u}_s = 0. \tag{1.10}$$

As pointed out by Pereira & Kalliadasis (2008), since Γ is only a function of z, θ and t, $\boldsymbol{\nabla}_{||}$ is in fact the in-plane nabla operator. In the particular case of cylindrical coordinates,

$\boldsymbol{\nabla}_{||} = \boldsymbol{e}_z\, \partial_z + \boldsymbol{e}_\theta\, r^{-1} \partial_\theta$ and, since we assume axisymmetry, $\boldsymbol{\nabla}_{||} = \boldsymbol{e}_z\, \partial / \partial z$.

In contrast, Stone (1990) defines the material derivative as $\mathrm{D}/\mathrm{D}t = (\partial_t \Gamma)_{\boldsymbol{n}} + \boldsymbol{u}_t \cdot \boldsymbol{\nabla}_s \Gamma$, which leads to a version of the surfactant transport equation analogous to the three-dimensional Reynolds transport equation,

$$\left(\frac{\partial \Gamma}{\partial t}\right)_{\boldsymbol{n}} + \boldsymbol{u}_t \cdot \boldsymbol{\nabla}_s \Gamma + \Gamma\, \boldsymbol{\nabla}_s \cdot \boldsymbol{u}_s = \left(\frac{\partial \Gamma}{\partial t}\right)_{\boldsymbol{n}} + \boldsymbol{\nabla}_s \cdot (\boldsymbol{u}_s \Gamma) = 0. \tag{1.11}$$

Although Stone (1990) does not specify the nature of the partial time derivative used in his paper, it is in fact referred to a coordinate system that moves with the normal velocity of the interface, as pointed out by Wong *et al.* (1996) and by Pereira & Kalliadasis (2008). Indeed, since the third term of the left-hand side of equation (1.11) only accounts for the distortion of the interface, the only advection term in equation (1.11) is $\boldsymbol{u}_t \cdot \boldsymbol{\nabla}_s \Gamma$, which is tangential to the interface, and it is indeed the only advection that is present if the partial time derivative is interpreted in a reference frame that follows the interface in the normal direction. The latter point can be seen more clearly by transforming the reference frame from the *Stone axes* to the laboratory frame using the relation

$$\left(\frac{\partial \Gamma}{\partial t}\right)_{\boldsymbol{n}} = \left(\frac{\partial \Gamma}{\partial t}\right)_M + \boldsymbol{u}_n \cdot \boldsymbol{\nabla} \Gamma. \tag{1.12}$$

Equation (1.12) indicates that if we take the laboratory frame, we also need to account for the advection along the normal direction of the moving interface. Substituting equation (1.12) into equation (1.11),

$$\begin{aligned}
&\left(\frac{\partial \Gamma}{\partial t}\right)_M + \boldsymbol{u}_n \cdot \boldsymbol{\nabla} \Gamma + \boldsymbol{u}_t \cdot \boldsymbol{\nabla}_s \Gamma + \Gamma \boldsymbol{\nabla}_s \cdot \boldsymbol{u}_s = \\
&\left(\frac{\partial \Gamma}{\partial t}\right)_M + \boldsymbol{u}_n \cdot \boldsymbol{\nabla} \Gamma + \boldsymbol{u}_t \cdot (\boldsymbol{I}_s \cdot \boldsymbol{\nabla})\, \Gamma + \Gamma \boldsymbol{\nabla}_s \cdot \boldsymbol{u}_s = \\
&\left(\frac{\partial \Gamma}{\partial t}\right)_M + \boldsymbol{u}_n \cdot \boldsymbol{\nabla} \Gamma + \boldsymbol{u}_t \cdot \boldsymbol{\nabla} \Gamma + \Gamma \boldsymbol{\nabla}_s \cdot \boldsymbol{u}_s = \left(\frac{\partial \Gamma}{\partial t}\right)_M + \boldsymbol{u}_s \cdot \boldsymbol{\nabla} \Gamma + \Gamma \boldsymbol{\nabla}_s \cdot \boldsymbol{u}_s = 0,
\end{aligned} \tag{1.13}$$

which demonstrates that equation (1.10) is indeed recovered if the transformation (1.12) is applied to the surfactant transport equation (1.11) deduced by Stone (1990).

There is also another common way of defining the temporal derivative, deduced by Wong *et al.* (1996), in which the coordinate system moves with the interface at a velocity $\dot{\boldsymbol{x}}_s = \partial_t \boldsymbol{x}_s$, where $\boldsymbol{x}_s$ denotes a given parametrization of the position of the interface with respect to a fixed frame. Using the notation $(\partial / \partial t)_{\boldsymbol{n},\boldsymbol{t}}$ for this particular time derivative, its relationship with $(\partial / \partial t)_M$ is given by

$$\left(\frac{\partial \Gamma}{\partial t}\right)_{\boldsymbol{n},\boldsymbol{t}} = \left(\frac{\partial \Gamma}{\partial t}\right)_M + \dot{\boldsymbol{x}}_s \cdot \boldsymbol{\nabla} \Gamma. \tag{1.14}$$

Note that

$$\dot{\boldsymbol{x}}_s \cdot \boldsymbol{\nabla}_s\Gamma = \dot{\boldsymbol{x}}_s \cdot (\boldsymbol{I}_s \cdot \boldsymbol{\nabla})\Gamma = [\dot{\boldsymbol{x}}_s - (\dot{\boldsymbol{x}}_s \cdot \boldsymbol{n})\boldsymbol{n}] \cdot \boldsymbol{\nabla}\Gamma = (\dot{\boldsymbol{x}}_s - \boldsymbol{u}_n) \cdot \boldsymbol{\nabla}\Gamma, \tag{1.15}$$

where the kinematic condition, $u_n = \dot{\boldsymbol{x}}_s \cdot \boldsymbol{n}$, has been used. Substituting equation (1.15) into equation (1.14),

$$\left(\frac{\partial\Gamma}{\partial t}\right)_{\boldsymbol{n},t} = \left(\frac{\partial\Gamma}{\partial t}\right)_M + \dot{\boldsymbol{x}}_s \cdot \boldsymbol{\nabla}_s\Gamma + \boldsymbol{u}_n \cdot \boldsymbol{\nabla}\Gamma, \tag{1.16}$$

and substituting equation (1.16) into equation (1.10),

$$\begin{aligned}
&\left(\frac{\partial\Gamma}{\partial t}\right)_{\boldsymbol{n},t} - \dot{\boldsymbol{x}}_s \cdot \boldsymbol{\nabla}_s\Gamma - \boldsymbol{u}_n \cdot \boldsymbol{\nabla}\Gamma + \boldsymbol{u}_s \cdot \boldsymbol{\nabla}\Gamma + \Gamma\boldsymbol{\nabla}_s \cdot \boldsymbol{u}_s = \\
&\left(\frac{\partial\Gamma}{\partial t}\right)_{\boldsymbol{n},t} - \dot{\boldsymbol{x}}_s \cdot \boldsymbol{\nabla}_s\Gamma + \boldsymbol{u}_s \cdot (\boldsymbol{I}_s \cdot \boldsymbol{\nabla})\Gamma + \Gamma\boldsymbol{\nabla}_s \cdot \boldsymbol{u}_s = \\
&\left(\frac{\partial\Gamma}{\partial t}\right)_{\boldsymbol{n},t} - \dot{\boldsymbol{x}}_s \cdot \boldsymbol{\nabla}_s\Gamma + \boldsymbol{u}_s \cdot \boldsymbol{\nabla}_s\Gamma + \Gamma\boldsymbol{\nabla}_s \cdot \boldsymbol{u}_s = \left(\frac{\partial\Gamma}{\partial t}\right)_{\boldsymbol{n},t} - \dot{\boldsymbol{x}}_s \cdot \boldsymbol{\nabla}_s\Gamma + \boldsymbol{\nabla}_s \cdot (\boldsymbol{u}_s\Gamma) = 0,
\end{aligned} \tag{1.17}$$

which is equivalent to equation (8) of Wong *et al.* (1996).

In all the numerical simulations performed in this thesis we make use of the above transport equation of Γ. The details of the numerical technique are explained in chapter 4, section §4.2.

1.4 Difussion of a scalar quantity at a moving interface

In the previous section, the surface diffusion of the scalar quantity Γ has been neglected in all the versions of the transport equation. The relative importance of surface diffusion compared with surface advection of Γ is measured by the surface Péclet number, which is defined as $Pe_s = U_{sc}R_o/D_s$, where D_s is the surface diffusion coefficient and U_{sc} is the characteristic liquid velocity at the interface. The correct scaling for U_{sc} depends on the value of La. In the limit of dominant inertia, $La \gg 1$, the appropriate velocity scale is the capillary velocity, $[\sigma_0/(\rho R_o^3)]^{1/2}$, so that $Pe_s = [\sigma_0 R_o/(\rho D_s^2)]^{1/2}$. For instance, if we consider a water thread of radius within the range 1-100 μm, the corresponding Laplace numbers lie in the range $10^2 \lesssim La \lesssim 10^4$. Typical values of D_s for SDS, SB12 and other monomers in aqueous solution are within the range $10^{-9} \lesssim D_s \lesssim 10^{-8}$ m^2 s^{-1} when Γ is below the critical micelle concentration (CMC) (Siderius *et al.*, 2002), providing values of the surface Péclet number in the range $10^4 \lesssim Pe_s \lesssim 10^5$. Therefore, in configurations where $La \gg 1$, it is expected that surface diffusion has a very small effect. In the opposite limit of dominant viscous forces, $La \lesssim 1$, the appropriate velocity scale is the visco-capillary velocity, σ_0/μ, leading to $Pe_s = \sigma_0 R_o/(\mu D_s)$. Considering, for instance, a polydimethylsiloxane silicon oil of dynamic viscosity in the range 0.1-10 Pa s, density $\rho \approx 970$ kg m^{-3} and surface tension $\sigma_0 \approx 21.1$ mN m^{-1}, the Laplace number takes values in the range $10^{-4} \lesssim La \lesssim 1$. Although we are not aware of experimental studies reporting the typical values of D_s in highly viscous solutions, if we assume that they are of the same order as those in aqueous solutions, the Péclet number lies in the range $1 \lesssim Pe_s \lesssim 10^6$. It is thereby deduced that when $La \lesssim 1$ there may be cases where surface diffusion cannot be neglected in the analysis. In these cases, the appropriate transport equation referred to the laboratory frame reads

$$\left(\frac{\partial \Gamma}{\partial t}\right)_M + \boldsymbol{u}_s \cdot \boldsymbol{\nabla}_{||}\Gamma + \Gamma\, \boldsymbol{\nabla}_s \cdot \boldsymbol{u}_s = Pe_s^{-1} \boldsymbol{\nabla}_s^2 \Gamma, \tag{1.18}$$

where $\boldsymbol{\nabla}_s^2$ is the surface Laplacian, and we have assumed that the surface difussion coefficient is constant.

1.5 Adsorption/desorption kinetics between the bulk fluids and the interface

Until now we have only considered the transport of species within the interface, where the particles or molecules are restricted to move and cannot be transported to or from the bulk fluids. This so-called *insoluble limit* is a good approximation, for instance, in the case of highly insoluble surfactants which are quickly absorbed to the surface forming a monolayer, and do not experience desorption. Nonetheless, in many relevant configurations of practical interest, the compounds are soluble in the bulk fluids, in which case it is essential to consider the transport of surfactant molecules inside the bulk and their corresponding interfacial sorption kinetics.

Additionally, it is important to emphasize here that the surface concentration of surfactants, $\bar{\Gamma}$, is extremely difficult to measure directly in practice, and their bulk concentration $\bar{C}$ is normally used instead as the experimental control parameter. However, the relationship between $\bar{\Gamma}$ and $\bar{C}$ is not universal, but depends on the particular system under study in a non-trivial way that is usually rationalized in terms of appropriate adsorption isotherms (Prosser & Franses, 2001; Leal, 2007; Manikantan & Squires, 2020). The distinction between soluble and insoluble amphiphiles at interfaces is usually expressed as *Gibbs monolayers* in the former case, and *Langmuir films* in the latter one (Fuller & Vermant, 2012). In particular when monolayers are formed from soluble molecules, Josiah W. Gibbs arrived at the following relationship between $\bar{\Gamma}$ and $\bar{C}$ (Gibbs, 1879)

$$\bar{\Gamma} = -\frac{1}{RT}\left(\frac{\partial \bar{\sigma}}{\partial \ln \bar{C}}\right)_{T,p}, \tag{1.19}$$

usually referred to as *Gibbs adsorption isotherm*, which is valid at small enough concentrations under the assumption of thermodynamic equilibrium. Here, R is the universal gas constant, T is the temperature and $\bar{\sigma}$ is the surface tension coefficient. In this thesis we will restrict all the analyses to insoluble surfactants, or to limiting cases like that of a saturated interface, where bulk and interfacial transport of molecules are irrelevant, as detailed in the following section. Hence, for a detailed description of these isotherms the reader is referred to Gibbs (1879), Leal (2007), or Manikantan & Squires (2020), and references therein.

Nonetheless, let us briefly explain the procedure to account for surfactant solubility in the mathematical model. First, the transport equation has to be modified by adding a flux term which, depending on its sign, indicates that the surfactant transport takes place from the interface to the bulk (surfactant desorption) or vice versa (surfactant adsorption). For simplicity, here we will assume that there is only one bulk phase conveying surfactant molecules, although in the case of having two media carrying molecules, it would be necessary to include two flux terms. Hence, the dimensionless surfactant transport equation referred to the laboratory frame now reads

$$\left(\frac{\partial \Gamma}{\partial t}\right)_M + \boldsymbol{u}_s \cdot \boldsymbol{\nabla}_{||}\Gamma + \Gamma\, \boldsymbol{\nabla}_s \cdot \boldsymbol{u}_s = Pe_s^{-1}\boldsymbol{\nabla}_s^2\Gamma + (K_d\mathcal{L})^{-1}J_{bs}, \tag{1.20}$$

where $K_d = \sigma_o/(\mu R_o k_d)$ is the ratio between the desorption time k_d^{-1} and the viscocapillary time, $\mathcal{L} = \Gamma_o k_d/(C_o k_a)$ is the dimensionless depletion depth (Manikantan & Squires, 2020), where k_a is the adsorption velocity, and $J_{bs}(C,\Gamma)$ is the net kinetic flux of adsorption/desorption to the interface, i.e. the flux of surfactant molecules entering or leaving the interface. Assuming linear dependencies for the desorption rate as a function of the surface concentration, and for the adsorption rate as a function of the bulk concentration and the space available at the interface, the net flux reads

$$J_{bs} = \left[C\left(1-\frac{\Gamma}{\Lambda}\right) - \mathcal{L}\Gamma\right] \quad \boldsymbol{x} \in \partial\mathcal{V}, \tag{1.21}$$

which is usually referred to as the *Langmuir isotherm* (Leal, 2007; Manikantan & Squires, 2020) [†]. Here, the bulk concentration has been non-dimensionalized with its initial value, C_o, and $\Lambda = \Gamma_\infty/\Gamma_o$ is the ratio between the maximum concentration of surfactant at the interface and the initial one. The transport of surfactant molecules in the bulk is governed by the following convection-diffusion equation,

$$\frac{\partial C}{\partial t} + \boldsymbol{u}\cdot\boldsymbol{\nabla}C = Pe^{-1}\boldsymbol{\nabla}^2 C \quad \boldsymbol{x} \in \mathcal{V} \tag{1.22}$$

where $Pe = \sigma_o R_o/(\mu D_b)$ is the Péclet number comparing the relative importance of advection and diffusion of surfactants and D_b is the bulk diffusivity coefficient of surfactant molecules. Moreover, if there are gradients of bulk concentration at the interface, so that $\boldsymbol{n}\cdot\boldsymbol{\nabla}C \neq 0$, a diffusive flux onto or off the interface is established. Hence, the conservation of surfactant molecules requires imposing an additional boundary condition at the interface, which reads

$$J_{bs} = -Da^{-1}(\boldsymbol{n}\cdot\boldsymbol{\nabla}C) \quad \boldsymbol{x} \in \partial\mathcal{V}, \tag{1.23}$$

[†] An example of a simpler sorption isotherm is the *Henry isotherm*, which is linear in C and Γ, while a more complex one is the *Frumkin isotherm*, which considers that the energy barriers for a molecule to be absorbed/desorbed to the interface depends on the local surface concentration.

where $Da = k_a R_o / D_b$ is the Damköhler number, which compares the diffusion time R_o^2/D_b over the adsorption time R_o/k_a.

In the light of the previous formulation, it is now possible to establish the validity conditions for the insoluble limit considered in this thesis. Note that, in terms of the Damköhler number, the insoluble case corresponds to the limit $Da \gg 1$, in which case the process is said to be *diffusion-limited*. In this limit, the sorption kinetics are fast enough for Γ to be approximately equal to the concentration in the sub-surface layer. In the opposite limit, $Da \ll 1$, the process is *kinetically-limited*, in which case bulk diffusion can be considered instantaneous in a first approximation, since the characteristic sorption time of a molecule traveling through the sub-surface layer is much smaller than the characteristic diffusion time.

1.6 Saturated interface

A particularly interesting limit is that of a *saturated interface*, in which the adsorbed surfactant molecules reach their maximum packing limit, and the corresponding surface concentration achieves its maximum value, $\bar{\Gamma} = \bar{\Gamma}_\infty$. The maximum surface concentration $\bar{\Gamma}_\infty$ is typically associated with bulk concentrations $\bar{C}$ of several times the so-called *critical micelle concentration* (CMC), which is the bulk concentration for which the surfactant molecules begin to assemble into micelles. The absence of gradients of surface concentration in saturated interfaces implies the absence of Marangoni stresses and a negligible effect of surfactant solubility. Consequently, the surface tension coefficient, as well as the shear and dilatational surface viscosity coefficients, are uniform along the interface, having values $\sigma^{\text{sat}} = \sigma(\bar{\Gamma}_\infty)$, $\mu_s^{\text{sat}} = \mu_s(\bar{\Gamma}_\infty)$ and $\kappa_s^{\text{sat}} = \kappa_s(\bar{\Gamma}_\infty)$, respectively. Note also that, in this limit, there is no need to solve the surfactant transport equation, and no equations of state are required to relate σ, μ_s and κ_s with $\bar{\Gamma}$. In addition, the absence of Marangoni stresses in saturated interfaces opens promising avenues in the development of measurement techniques for the surface viscosity coefficients, which are notoriously difficult to measure using the existing methods. In this thesis, the saturated limit is used in chapter §4, section §§4.4 to analyze the capillary thinning of liquid filaments, leading us to propose a novel technique for the high precision measurement of the surface viscosity coefficients.

1.7 Constitutive equations of complex interfaces

In this section we derive the different constitutive equations used in the thesis for the surface stress tensor $\boldsymbol{T}_s$ depending on the material properties of the interface. In particular, in §§1.7.1, we derive the most common law for an interface with surface viscous resistance to flow, which is usually referred to as the Boussinesq–Scriven law. Then, in §§1.7.2, we derive the Hookean and neo–Hookean constitutive equations, which are appropriate for cases where the interface presents a solid-like behavior.

1.7.1 Boussinesq–Scriven law

To deduce the surface stress balance taking into account surface viscous resistance, the axisymmetric interface, of radius $r = a(z,t)$, is described as a compressible two-dimensional Newtonian surface without inertia and obeying the BS constitutive equation (Boussinesq, 1913; Scriven, 1960). To derive the latter equation in cylindrical coordinates, which will be needed to perform all the linear and nonlinear analyses reported in the forthcoming chapters, the free surface is parametrized in terms of the axial coordinate z and the azimuthal angle θ as

$$\boldsymbol{x}_s = \boldsymbol{x}_s(z,\theta,t) = a(z,t)\,\boldsymbol{e}_r + z\,\boldsymbol{e}_z. \tag{1.24}$$

For the following development surface operators need to be defined. To that end we build an orthonormal curvilinear basis $\{\boldsymbol{t}, \boldsymbol{e}_\theta, \boldsymbol{n}\}$ intrinsic to the surface, where

$$\boldsymbol{n} = \frac{1}{\sqrt{1+a'^2}}(\boldsymbol{e}_r - a'\,\boldsymbol{e}_z), \quad \boldsymbol{t} = \frac{1}{\sqrt{1+a'^2}}(a'\,\boldsymbol{e}_r + \boldsymbol{e}_z), \tag{1.25}$$

with $\boldsymbol{t}$, $\boldsymbol{e}_\theta$ denoting the unit meridional and azimuthal tangent vectors. Throughout this section, for simplicity we use primed variables to denote the partial derivatives with respect to z. The latter basis introduces a covariant metric tensor of components $g_{11} = 1 + (a')^2$, $g_{22} = a^2$, $g_{12} = g_{21} = 0$, whose determinant is given by $g = a^2[1 + (a')^2]$. Hence, the surface gradient operator, $\boldsymbol{\nabla}_s$, is defined as

$$\boldsymbol{\nabla}_s = \frac{1}{\sqrt{1+a'^2}}\boldsymbol{t}\frac{\partial}{\partial z} + \frac{1}{a}\boldsymbol{e}_\theta\frac{\partial}{\partial\theta}. \tag{1.26}$$

The velocity field of the fluid at the surface, $\boldsymbol{u}_s$, can be decomposed into a tangential velocity $\boldsymbol{u}_t$, and a normal velocity $\boldsymbol{u}_n$,

$$\boldsymbol{u}_s = \boldsymbol{u}(\boldsymbol{x}_s,t) = \boldsymbol{u}_t(\boldsymbol{x}_s,t) + \boldsymbol{u}_n(\boldsymbol{x}_s,t) = \boldsymbol{u}_t(\boldsymbol{x}_s,t) + u_n(\boldsymbol{x}_s,t)\,\boldsymbol{n}, \tag{1.27}$$

where $\boldsymbol{u}_t = \boldsymbol{I}_s \cdot \boldsymbol{u}_s$, $\boldsymbol{u}_n = \boldsymbol{nn} \cdot \boldsymbol{u}_s$. Notice that the surface gradient operator given by equation (1.26) can also be written as $\boldsymbol{\nabla}_s = \boldsymbol{I}_s \cdot \boldsymbol{\nabla}$ in terms of the standard gradient and the surface projection operator, as defined in §2.1. Since the interface is axisymmetric, $\boldsymbol{u}_t(\boldsymbol{x}_s,t) = u_t(\boldsymbol{x}_s,t)\,\boldsymbol{t}$, and thus the normal and the meridional tangent velocity components read, respectively,

$$u_n = \frac{u - a'w}{\sqrt{1+a'^2}}, \quad u_t = \frac{w + a'u}{\sqrt{1+a'^2}}, \tag{1.28}$$

For simplicity, in equation (1.28) we have omitted the evaluation of u and w at $r = a(z,t)$.

To derive the stress balance (1.6c) for the fluid interface we apply the integral momentum conservation equation to a surface element S, $\int\int_S (\hat{\boldsymbol{T}} - \boldsymbol{T}) \cdot \boldsymbol{n}\,\mathrm{d}A + \int_C \boldsymbol{T}_s \cdot \boldsymbol{n}_s\,\mathrm{d}l = \boldsymbol{0}$, where $\boldsymbol{T}_s$ is proportional to the line element enclosing the surface, C, whose unitary normal vector embedded in S is $\boldsymbol{n}_s$, and thus $\boldsymbol{n} \cdot \boldsymbol{n}_s = 0$. The generalized Stokes theorem is applied to the line integral to give, $(\hat{\boldsymbol{T}} - \boldsymbol{T}) \cdot \boldsymbol{n} + \boldsymbol{\nabla}_s \cdot \boldsymbol{T}_s - (\boldsymbol{\nabla}_s \cdot \boldsymbol{n})\boldsymbol{n} \cdot \boldsymbol{T}_s = \boldsymbol{0}$ (see appendix A of Rivero-Rodríguez

& Scheid, 2018). In the present subsection, the surface stress tensor $\boldsymbol{T}_s$ is modeled with the BS approximation (Boussinesq, 1913; Scriven, 1960) in the limit of negligible surface density, which disregards complex interfacial rheology and assumes that the deviatoric component of $\boldsymbol{T}_s$ is isotropic, linear and instantaneous in the surface rate of strain tensor,

$$\boldsymbol{T}_s = \left[\sigma + Bq(\Theta - 1)(\boldsymbol{\nabla}_s \cdot \boldsymbol{u}_s)\right] \boldsymbol{I}_s + Bq\left[(\boldsymbol{\nabla}_s \boldsymbol{u}_s) \cdot \boldsymbol{I}_s + \boldsymbol{I}_s \cdot (\boldsymbol{\nabla}_s \boldsymbol{u}_s)^T\right]. \tag{1.29}$$

According to equation (1.29), $\boldsymbol{T}_s$ is restricted to be tangent to the interface, i.e. $\boldsymbol{n} \cdot \boldsymbol{T}_s = \boldsymbol{0}$, and thus the third term of the interfacial stress balance in differential form cancels out, yielding the same expression as in equation (1.6c), that is $(\hat{\boldsymbol{T}} - \boldsymbol{T}) \cdot \boldsymbol{n} + \boldsymbol{\nabla}_s \cdot \boldsymbol{T}_s = \boldsymbol{0}$. Finally, introducing equation (1.29) for $\boldsymbol{T}_s$ in the previous equation, the surface equation of motion reads

$$\begin{aligned}
&(\hat{\boldsymbol{T}} - \boldsymbol{T}) \cdot \boldsymbol{n} + \boldsymbol{\nabla}_s \sigma - \boldsymbol{n}(\boldsymbol{\nabla}_s \cdot \boldsymbol{n})\sigma + \boldsymbol{\nabla}_s\left[Bq(\Theta - 1)(\boldsymbol{\nabla}_s \cdot \boldsymbol{u}_s)\right] \\
&- \boldsymbol{n}(\boldsymbol{\nabla}_s \cdot \boldsymbol{n})Bq(\Theta - 1)(\boldsymbol{\nabla}_s \cdot \boldsymbol{u}_s) + \boldsymbol{\nabla}_s \cdot \left\{Bq\left[(\boldsymbol{\nabla}_s \boldsymbol{u}_s) \cdot \boldsymbol{I}_s + \boldsymbol{I}_s \cdot (\boldsymbol{\nabla}_s \boldsymbol{u}_s)^{\mathrm{T}}\right]\right\} = \boldsymbol{0},
\end{aligned} \tag{1.30}$$

which is Newton's second law for a fluid surface with negligible inertia and viscous resistance to flow. Since the flow is considered axisymmetric, equation (1.30) yields two independent scalar boundary conditions at the interface. Hence, taking the inner product of (1.30) with $\boldsymbol{n}$ and $\boldsymbol{t}$, and considering that the outer fluid remains at constant pressure, thus setting $\hat{\boldsymbol{T}} = -\boldsymbol{I}$ without loss of generality, the normal and tangential stress balances in cylindrical coordinates read, respectively,

$$\begin{aligned}
&p\big|_{r=a(z,t)} - \frac{2}{1+a'^2}\left[\frac{\partial u}{\partial r} + a'^2\frac{\partial w}{\partial z} - a'\left(\frac{\partial w}{\partial r} + \frac{\partial u}{\partial z}\right)\right]\Bigg|_{r=a(z,t)} \\
&= C\left[\sigma + Bq(\Theta - 1)\left(\frac{(au_t)'}{a\sqrt{1+a'^2}} + Cu_n\right)\right] \\
&+ \frac{2Bq}{1+a'^2}\left[\frac{a'u_t + u_n}{a^2} - \frac{a''}{1+a'^2}\left(u_t' - \frac{a''u_n}{1+a'^2}\right)\right],
\end{aligned} \tag{1.31}$$

and

$$\begin{aligned}
&\frac{1}{\sqrt{1+a'^2}}\left[\left(\frac{\partial w}{\partial r} + \frac{\partial u}{\partial z}\right)(1 - a'^2) + 2a'\left(\frac{\partial u}{\partial r} - \frac{\partial w}{\partial z}\right)\right]\Bigg|_{r=a(z,t)} = \frac{\partial \sigma}{\partial z} \\
&+ \frac{\partial}{\partial z}\left[Bq(\Theta - 1)\left(\frac{(au_t)'}{a\sqrt{1+a'^2}} + Cu_n\right)\right] + \frac{\sqrt{1+a'^2}}{a}\frac{\partial}{\partial z}\left[\frac{2Bqa}{1+a'^2}\left(u_t' - \frac{a''u_n}{1+a'^2}\right)\right] \\
&- \frac{2Bqa'}{\sqrt{1+a'^2}}\left[\frac{a'u_t + u_n}{a^2} - \frac{a''}{1+a'^2}\left(u_t' - \frac{a''u_n}{1+a'^2}\right)\right],
\end{aligned} \tag{1.32}$$

where $C = \boldsymbol{\nabla} \cdot \boldsymbol{n} = \boldsymbol{\nabla}_s \cdot \boldsymbol{n} = a^{-1}(1 + a'^2)^{-1/2} - a''(1 + a'^2)^{-3/2}$ is twice the mean curvature of the interface and the identity $\boldsymbol{\nabla}_s \cdot \boldsymbol{u}_s = \boldsymbol{\nabla}_s \cdot \boldsymbol{u}_t + Cu_n$ has been used. Note that the left-hand side of equations (1.31) and (1.32) are terms arising from the bulk evaluated at $r = a(z, t)$, whereas the terms on their right-hand side are interface quantities and thus they are previously evaluated at the interface, a fact that must be considered when taking the derivatives of the quantities u_t and u_n defined in (1.28). For instance, the z-derivative of the axial velocity at the interface reads, $\partial w(r = a(z,t), z, t)/\partial z = \partial w/\partial z|_{r=a(z,t)} + a' \partial w/\partial r|_{r=a(z,t)}$.

Equation (1.30) and its normal and tangential projections in tensor notation are in agreement with those derived by Aris (1962) and Slattery *et al.* (2007), which correct the typographical errors in Scriven (1960). However, inasmuch as the boundary conditions (1.31) and (1.32) are necessary in the remainder of the thesis, we present them here in terms of u, w, p and a, and their spatial derivatives. Indeed, to the best of our knowledge, equations (1.31) and (1.32) had not been reported in the literature in their complete and correct form. Thus, Whitaker (1976) only presents the equations in tensor notation and their linearisation, Aris (1962) and Slattery *et al.* (2007) considered the particular case of a cylinder, $r = R$ and $r = R(t)$, and Slattery *et al.* (2007) on page 732 presents the projections of the surface equation of motion onto the radial, axial and azimuthal directions in cylindrical coordinates, but not the normal and tangential stress balances.

Furthermore, recent studies in similar axisymmetric configurations have considered surface viscosities in the formulation, e.g. Ponce-Torres *et al.* (2016*b*,*a*) to study liquid bridges, and Ponce-Torres *et al.* (2017) on the breakup of liquid drops. However, in all these cases there are missing terms both in the normal and tangential stress balances. The latter mistakes explain why the particular case of a cylinder, $r = R(t)$ (Aris, 1962; Slattery *et al.*, 2007) is not recovered, whereas equations (1.31) and (1.32) correctly reproduce this limit.

1.7.2 Elastic interface: Hookean and neo-Hookean constitutive equations

As explained in section §1.1, there are molecules, as certain polymer chains and proteins, or fatty acids, that can provide the interface with an elastic resistance to deformation, which is completely different from the surfactant-induced elasticity. In this scenario, the interface behaves as a thin elastic membrane, and it is usually referred to as a *solid-like interface*. In section §1.1 we have given a brief panoramic view of the constitutive equations used in different contexts. In particular, in this thesis we will restrict to the Hookean and neo-Hookean models derived in Barthes-Biesel (2016) and Pepicelli *et al.* (2017), respectively.

The simplest constitutive equation relating the surface stress with the strain is deduced by assuming a linear Hookean response, which is valid under the small-strain and small-displacement approximations. Hence, in this case the surface stress tensor of a two-dimensional solid-like moving interface reads (Barthes-Biesel & Rallison, 1981; Pepicelli *et al.*, 2017; Jaensson & Vermant, 2018)

$$\boldsymbol{T}_s = \sigma \boldsymbol{I}_s + \mathcal{G}(\Xi - 1)(\boldsymbol{\nabla}_s \cdot \boldsymbol{d}_s)\boldsymbol{I}_s + \mathcal{G}\left[(\boldsymbol{\nabla}_s \boldsymbol{d}_s) \cdot \boldsymbol{I}_s + \boldsymbol{I}_s \cdot (\boldsymbol{\nabla}_s \boldsymbol{d}_s)^{\mathrm{T}}\right], \qquad (1.33)$$

which is the surface equivalent to the bulk stress tensor used in continuum solid mechanics for small strains and small displacements. Note that under this approximations we do not need to distinguish between the Eulerian and Lagrangian frame of references, since both coincide at leading order in the displacement field (Landau & Lifshitz, 1959). Here, $\boldsymbol{d}_s$ is the displacement field evaluated at the interface, which must satisfy the kinematic condition $\partial_t \boldsymbol{d}_s = \boldsymbol{u}_s$, and $\mathcal{G} = G/\sigma_o$ and $\Xi = K/G$ are dimensionless parameters comparing the surface shear elastic forces with the surface tension force, and the surface dilatational-to-shear elastic moduli ratio, respectively.

An interfacial neo-Hookean constitutive equation, which goes beyond the small-strain and small-displacement approximations, has been recently derived by Pepicelli *et al.* (2017) in the form

$$\boldsymbol{T}_s = \left[\sigma + \frac{\Xi}{J}\ln(J)\right]\boldsymbol{I}_s + \frac{\mathcal{G}}{J}\left[\frac{\boldsymbol{B}_s}{J} - \frac{1}{2}\mathrm{tr}\left(\frac{\boldsymbol{B}_s}{J}\right)\boldsymbol{I}_s\right], \tag{1.34}$$

where $\boldsymbol{B}_s = \boldsymbol{F}_s \cdot \boldsymbol{F}_s^{\mathrm{T}}$ is the surface left-Cauchy-Green strain tensor, and $\boldsymbol{F}_s = \boldsymbol{I}_s \cdot (\partial \boldsymbol{x}_s / \partial \boldsymbol{X}_s) \cdot (\boldsymbol{I} - \boldsymbol{N}\boldsymbol{N})$ is the interfacial deformation gradient tensor. Here $\boldsymbol{N}$ is the unit normal vector to the interface in the undeformed or reference configuration, denoted by $\boldsymbol{X}_s$, and $J = \det(\boldsymbol{F}_s)$ is the relative change of interfacial area.

1.8 Surface equations of state

As has been previously explained, a single value of the surface tension coefficient does not suffice to characterize a complex fluid-fluid interface. Moreover, the coupling between hydrodynamic forces and the presence of proteins, surfactants, or macromolecules gives rise to complex constitutive equations relating the deformation of the interface with the surface stress. Thus, to close the mathematical description of such complex interfaces, we need to account for the dependence of the associated material parameters on the surface concentration of molecules or particles populating the interface, which are typically provided as *surface equations of state*.

Surface-tension coefficient

When the interface is covered with a surfactant monolayer, the surface tension coefficient σ decreases by an amount that depends on the concentration of surfactant molecules Γ. Hence, an equation of state that relates σ with Γ is needed. Surface-active molecules at the interface induce a surface pressure $\bar{\Pi}$ which depends on the surfactant concentration, $\bar{\Pi} = \bar{\Pi}(\bar{\Gamma})$. The surface pressure is defined as the difference in the surface tension due to the presence of surfactant, $\bar{\Pi}(\bar{\Gamma}) = \sigma_{\mathrm{clean}} - \bar{\sigma}(\bar{\Gamma})$, and thus $\boldsymbol{\nabla}_s \bar{\Pi} = -\boldsymbol{\nabla}_s \bar{\sigma}$. In addition, the Gibbs elasticity E relates the changes of interface area, $\bar{A}$, with the surface pressure through the surface compressibility $1/E = -(1/\bar{A})(\partial \bar{A}/\partial \bar{\Pi})_T$, where T is the temperature evaluated at the interface, which is assumed to remain constant. Hence,

$$E = -\bar{A}\frac{\partial \bar{\Pi}}{\partial \bar{A}} = \bar{A}\frac{\partial \bar{\sigma}}{\partial \bar{A}} = -\bar{\Gamma}\frac{\partial \bar{\sigma}}{\partial \bar{\Gamma}}, \tag{1.35}$$

where in the last equation it has been taken into account that, in the insoluble case considered in this thesis, the number of surfactant molecules is conserved at the interface. Equation (1.35) can be used to relate $\bar{\sigma}$ and $\bar{\Gamma}$,

$$\nabla_s \bar{\sigma} = \frac{\partial \bar{\sigma}}{\partial \bar{\Gamma}} \nabla_s \bar{\Gamma} = -\frac{E}{\bar{\Gamma}} \nabla_s \bar{\Gamma}. \tag{1.36}$$

Making $\bar{\sigma}$ and $\bar{\Gamma}$ dimensionless with σ_0 and Γ_0, respectively, equation (1.36) finally yields the dimensionless equation of state

$$\sigma = 1 - \beta \ln \Gamma, \tag{1.37}$$

where $\beta = E/\sigma_0$ is the so-called *elasticity parameter*, also referred to as the Marangoni number (Champougny *et al.*, 2015). Note that similar equations of state can be obtained by combining the flux isotherm (1.21) with the Gibbs equilibrium isotherm (1.19).

As explained in section §1.1, the presence of surfactant at an interface induces substantial modifications in its dynamics and mechanical properties. In the simplest scenario, in which we neglect surface viscosity and all the other interfacial rheological effects, the surface stress tensor is given by $\boldsymbol{T}_s = \sigma \boldsymbol{I}_s$, and the stress balance at the interface takes the following form,

$$(\boldsymbol{T} - \hat{\boldsymbol{T}}) \cdot \boldsymbol{n} = \nabla_s \sigma - \boldsymbol{n}(\nabla_s \cdot \boldsymbol{n})\sigma \quad \boldsymbol{x} \in \partial\mathcal{V}, \tag{1.38}$$

which is a limiting form of the surface stress balance (1.30) when surface viscous stresses are negligible. The two terms on the right-hand side of equation (1.38) illustrate that the effect of the Marangoni stress is twofold: first it induces changes in the normal stress balance by locally modifying the surface tension coefficient in an amount that depends on Γ, and second, by exerting a tangential stress to the interface when there is an imbalance in σ. Finally, the surface stress balance can be rewritten in terms of Γ as

$$(\boldsymbol{T} - \hat{\boldsymbol{T}}) \cdot \boldsymbol{n} = -\frac{\beta}{\Gamma} \nabla_s \Gamma - \boldsymbol{n}\,(\nabla_s \cdot \boldsymbol{n})\,(1 - \beta \ln \Gamma) \quad \boldsymbol{x} \in \partial\mathcal{V}. \tag{1.39}$$

Surface viscosity coefficients

The dependence of surface viscous coefficients on the bulk and surface concentrations of surfactants is still under intense debate (Edwards *et al.*, 1991; Fuller & Vermant, 2012; Langevin, 2014; Jaensson & Vermant, 2018; Manikantan & Squires, 2020). The controversy, which started in the mid and late 19th century with Plateau, Marangoni, and Rayleigh as explained in section §1.1, is that even the interaction between monolayers with simple flows produces intricate mixed surface deformations and surfactant transport processes which hinder enormously both, the characterization of the material properties, and the derivation of interfacial constitutive laws and equations of state able to accurately reproduce the observed behaviors.

Recent works within the context of surfactant-laden threads have arbitrarily considered linear relationships between μ_s and κ_s and Γ (Ponce-Torres *et al.*, 2016*a*, 2017; Wee *et al.*, 2020; Ponce-Torres *et al.*, 2020). Additionally, some studies on Langmuir monolayers (insoluble surfactants) have reported an exponential dependence of the surface viscosity coefficients on the surface pressure $\bar{\Pi}(\bar{\Gamma})$ (Fuller & Vermant, 2012; Manikantan & Squires, 2017, 2020). For instance, monolayers of dipalmitoylphosphatidylcholine (DPPC), one of the major constituents of lung surfactant in mammalian alveoli, exhibit a Π-thickening behavior (Kim *et al.*, 2011; Fuller & Vermant, 2012; Kim *et al.*, 2013; Hermans & Vermant, 2014). Another example is that of eicosanol, which has a Π-thinning behavior (Kurtz *et al.*, 2006; Zell *et al.*, 2014).

In this thesis, for simplicity and to avoid the arbitrariness associated with more complex equations of state, we will consider that the surface viscosity coefficients remain constant. In particular, this is irrelevant in the linear regime, which is independent of the chosen equation of state, and thus considering constant surface viscosities does not introduce any approximation, as will be shown in chapter 3. Regarding the nonlinear dynamics, part of the forthcoming results are restricted to the limit of a saturated interface, where the surface viscosity coefficients can also be considered to remain constant along the interface. The applicability conditions of this saturated limit has been discussed in §1.6, and will be recalled in chapter 4, section §4.4.

1.9 Outline of the thesis

The remainder of the document is organized as follows. In chapter 2 we derive the leading-order and second-order one-dimensional models accounting for interfacial viscoelasticity. Chapter 3 is devoted to study the linear stability of a liquid filament under negligible gravitational effects, when the interface is endowed with a complex surface rheology, which may be elastic and/or viscous. We then evaluate the performance of the one-dimensional approximations in the linear regime by comparing their associated growth rate of small perturbations with the one obtained from the complete conservation equations. In chapter 4, we extend the results of chapter 3 by assessing the nonlinear dynamics of these complex filaments. In particular we study the effect of Marangoni stresses, surface viscous forces and surface diffusion on the natural breakup and thinning of threads, and the subsequent satellite droplet formation. Finally, chapter 5 deals with the linear and nonlinear dynamics of a capillary jet injected in the direction of gravity and confined between the nozzle and a bath of the same fluid.

References

AMBRAVANESWARAN, B., SUBRAMANI, H.J., PHILLIPS, S.D. & BASARAN, O.A. 2004 Dripping-jetting transitions in a dripping faucet. *Phys. Rev. Lett.* **93**, 034501.

ANNA, S.L. 2016 Droplets and bubbles in microfluidic devices. *Annu. Rev. Fluid Mech.* **48**, 285–309.

ARIS, R. 1962 *Vectors, Tensors and the Basic Equations of Fluid Mechanics*. Prentice-Hall Editor.

ASHGRIZ, N. & MASHAYEK, F. 1995 Temporal analysis of capillary jet breakup. *J. Fluid Mech.* **291**, 163–190.

BAR-ZIV, R. & MOSES, E. 1994 Instability and "pearling" states produced in tubular membranes by competition of curvature and tension. *Phys. Rev. Lett.* **73** (10), 1392.

BARTHES-BIESEL, D. 2016 Motion and deformation of elastic capsules and vesicles in flow. *Annu. Rev. Fluid Mech.* **48**, 25–52.

BARTHES-BIESEL, D. & RALLISON, J. M. 1981 The time-dependent deformation of a capsule freely suspended in a linear shear flow. *J. Fluid Mech.* **113**, 251–267.

BOUSSINESQ, J. V. 1913 *J. Ann. Chim. Phys.* **29**, 349.

CAMPANA, D. M. & SAITA, F. A. 2006 Numerical analysis of the rayleigh instability in capillary tubes: The influence of surfactant solubility. *Phys. Fluids* **18**, 022104.

CAMPANA, D. M., UBAL, S., GIAVEDONI, M. D. & SAITA, F. A. 2011 A deeper insight into the dip coating process in the presence of insoluble surfactants: A numerical analysis. *Phys. Fluids* **23** (5), 052102.

CARROLL, B. J. & LUCASSEN, J. 1974 Effect of surface dynamics on the process of droplet formation from supported and free liquid cylinders. *J. Chem. Soc. Faraday Trans.* **70**, 1228–1239.

CASTREJÓN-PITA, J. R., CASTREJÓN-PITA, A. A., THETE, S. S., SAMBATH, K., HUTCHINGS, I. M., HINCH, J., LISTER, J. R. & BASARAN, O. A. 2015 Plethora of transitions during breakup of liquid filaments. *Proc. Natl. Acad. Sci. U.S.A.* **112** (15), 4582–4587.

CHAMPOUGNY, L., SCHEID, B., RESTAGNO, F., VERMANT, J. & RIO, E. 2015 Surfactant-induced rigidity of interfaces: a unified approach to free and dip-coated films. *Soft Matter* **11** (14), 2758–2770.

CHANDRASEKHAR, S. 1961 *Hydrodynamic and Hydromagnetic Stability*. ed and Transl. E MacCurdy (New York: George Brazillier).

CHAUDHARY, K.C. & MAXWORTHY, T. 1980 The nonlinear capillary instability of a liquid jet. part 3. experiments on satellite drop formation and control. *J. Fluid. Mech.* **96** (2), 287–297.

CRASTER, R. V., MATAR, O. K. & PAPAGEORGIOU, D. T. 2002 Pinchoff and satellite formation in surfactant covered viscous threads. *Phys. Fluids* **14** (4), 1364–1376.

DAY, R. F., HINCH, E. J. & LISTER, J. R. 1998 Self-similar capillary pinchoff of an inviscid fluid. *Phys. Rev. Lett.* **80** (4), 704.

DE GENNES, P.-G., BROCHARD-WYART, F. & QUÉRÉ, D. 2013 *Capillarity and wetting phenomena: drops, bubbles, pearls, waves*. Springer Science & Business Media.

DIMOVA, R., ARANDA, S., BEZLYEPKINA, N., NIKOLOV, V., RISKE, K. A. & LIPOWSKY, R. 2006 A practical guide to giant vesicles. probing the membrane nanoregime via optical microscopy. *J. Phys.: Condens. Matter* **18** (28), S1151.

DIMOVA, R., DIETRICH, C., HADJIISKY, A., DANOV, K. & POULIGNY, B. 1999 Falling ball viscosimetry of giant vesicle membranes: finite-size effects. *Eur. Phys. J. B* **12** (4), 589–598.

DIMOVA, R., POULIGNY, B. & DIETRICH, C. 2000 Pretransitional effects in dimyristoylphosphatidylcholine vesicle membranes: optical dynamometry study. *Biophys. J.* **79** (1), 340–356.

DIMOVA, R., SEIFERT, U., POULIGNY, B., FÖRSTER, S. & DÖBEREINER, H.-G. 2002 Hyperviscous diblock copolymer vesicles. *Eur. Phys. J. E* **7** (3), 241–250.

DINSMORE, A. D., HSU, M. F., NIKOLAIDES, M. G., MARQUEZ, M., BAUSCH, A. R. & WEITZ, D. A. 2002 Colloidosomes: selectively permeable capsules composed of colloidal particles. *Science* **298** (5595), 1006–1009.

DONNELLY, R. J. & GLABERSON, W. I. 1966 Experiments on the capillary instability of a liquid jet. *Proc. Roy. Soc.* **A290**, 547–566.

DRAVID, V., SONGSERMPONG, S., XUE, Z., CORVALAN, C. M. & SOJKA, P. E. 2006 Two-dimensional modeling of the effects of insoluble surfactant on the breakup of a liquid filament. *Chem. Eng. Sci.* **61**, 3577–3585.

EDWARDS, D. A., BRENNER, H. & WASAN, D. T. 1991 *Interfacial transport processes and rheology*. Butterworth-Heinemann.

EGGERS, J. 1993 Universal pinching of 3d axisymmetric free-surface flow. *Phys. Rev. Lett.* **71**, 3458.

EGGERS, J 1997 Nonlinear dynamics and breakup of free surface flows. *Rev. Mod. Phys.* **69**, 865–929.

EGGERS, J. & DUPONT, T. F. 1994 Drop formation in a one-dimensional approximation of the Navier-Stokes equation. *J. Fluid Mech.* **262**, 205–222.

EGGERS, J. & VILLERMAUX, E. 2008 Physics of liquid jets. *Rep. Prog. Phys.* **71**, 036601.

FARUTIN, A., ÉTIENNE, J., MISBAH, C. & RECHO, P. 2019 Crawling in a fluid. *Phys. Rev. Lett.* **123** (11), 118101.

FRANKLIN, B. 1774 Of the stilling of waves by means of oil. *Philos. Trans.* (64), 445–460.

FULLER, G.G. & VERMANT, J. 2012 Complex fluid-fluid interfaces: rheology and structure. *Annu. Rev. Chem. Biomol. Eng.* **3**, 519–543.

FYGENSON, D. K., MARKO, J. F. & LIBCHABER, A. 1997 Mechanics of microtubule-based membrane extension. *Phys. Rev. Lett.* **79** (22), 4497.

GARCÍA, F. J. & CASTELLANOS, A. 1994 One-dimensional models for slender axisymmetric viscous liquid jets. *Phys. Fluids* **6** (8), 2676–2689.

GIBBS, J. W. 1879 On the equilibrium of heterogeneous substances. *Trans. Conn. Acad.* **III**, 108–248, 343–524.

GOEDDE, E. F. & YUEN, M. C. 1970 Experiments on liquid jet instability. *J. Fluid Mech.* **40** (3), 495–511.

GONZÁLEZ, H. & GARCÍA, F. J. 2009 The measurement of growth rates in capillary jets. *J. Fluid Mech.* **619**, 179–212.

HAENLEIN, A. 1931 On the breaking up of a jet of liquid. *Forschung. Geb. Ing.* **2**, 139.

HAMEED, M., SIEGEL, M., YOUNG, Y.-N., LI, J., BOOTY, M.R. & PAPAGEORGIOU, D.T. 2008 Influence of insoluble surfactant on the deformation and breakup of a bubble or thread in a viscous fluid. *J. Fluid Mech.* **594**, 307–340.

HANSEN, S., PETERS, G.W.M. & MEIJER, H.E.H. 1999 The effect of surfactant on the stability of a fluid filament embedded in a viscous fluid. *J. Fluid Mech.* **382**, 331–349.

HEGEMANN, J., KNOCHE, S., EGGER, S., KOTT, M., DEMAND, S., UNVERFEHRT, A., REHAGE, H. & KIERFELD, J. 2018 Pendant capsule elastometry. *J. Colloid Interface Sci.* **513**, 549–565.

HELFRICH, W. 1973 Elastic properties of lipid bilayers: theory and possible experiments. *Z. Naturforsch. C.* **28** (11-12), 693–703.

HERMANS, E. & VERMANT, J. 2014 Interfacial shear rheology of dppc under physiologically relevant conditions. *Soft matter* **10** (1), 175–186.

JAENSSON, N. & VERMANT, J. 2018 Tensiometry and rheology of complex interfaces. *Curr. Opin. Colloid Interface Sci* **37**, 136–150.

JOYE, J.-L., HIRASAKI, G. J. & MILLER, C. A. 1994 Asymmetric drainage in foam films. *Langmuir* **10**, 3174–3179.

KALAAJI, A., LOPEZ, B., ATTANE, P. & SOUCEMARIANADIN, A. 2003 Breakup length of forced liquid jets. *Phys. Fluids* **15**, 2469–2479.

KAMAT, P. M., WAGONER, B. W., THETE, S. S. & BASARAN, O. A. 2018 Role of marangoni stress during breakup of surfactant-covered liquid threads: Reduced rates of thinning and microthread cascades. *Phys. Rev. Fluids* **3** (4), 043602.

KANTSLER, VASILIY 2007 Hydrodynamics of fluid vesicles. PhD thesis, Weizmann Institute of Science.

KANTSLER, V., SEGRE, E. & STEINBERG, V. 2008 Critical dynamics of vesicle stretching transition in elongational flow. *Phys. Rev. Lett.* **101** (4), 048101.

KELLER, J. B. & MIKSIS, M. J. 1983 Surface tension driven flows. *SIAM J. App. Math.* **43** (2), 268–277.

KELLER, J. B., RUBINOW, S. I. & TU, Y. O. 1973 Spatial instability of a jet. *Phys. Fluids* **16**, 2052–2055.

KIM, K., CHOI, S. Q., ZASADZINSKI, J. A. & SQUIRES, T. M. 2011 Interfacial microrheology of dppc monolayers at the air–water interface. *Soft Matter* **7** (17), 7782–7789.

KIM, K., CHOI, S. Q., ZELL, Z. A., SQUIRES, T. M. & ZASADZINSKI, J. A. 2013 Effect of cholesterol nanodomains on monolayer morphology and dynamics. *Proc. Natl. Acad. Sci. U.S.A.* **110** (33), E3054–E3060.

KNOCHE, S., VELLA, D., AUMAITRE, E., DEGEN, P., REHAGE, H., CICUTA, P. & KIERFELD, J. 2013 Elastometry of deflated capsules: Elastic moduli from shape and wrinkle analysis. *Langmuir* **29** (40), 12463–12471.

KURTZ, R. E., LANGE, A. & FULLER, G. G. 2006 Interfacial rheology and structure of straight-chain and branched fatty alcohol mixtures. *Langmuir* **22** (12), 5321–5327.

KWAK, S. & POZRIKIDIS, C. 2001 Effect of surfactants on the stability of instability of a liquid thread or annular layer. Part 1: Quiescent fluids. *Int. J. Multiphase Flow* **27**, 1–37.

LAFRANCE, P. 1975 Nonlinear breakup of a laminar liquid jet. *Phys. Fluids* **18** (4), 428–432.

LANDAU, L. D. & LIFSHITZ, E. M. 1959 *Course of Theoretical Physics Vol. 7: Theory and Elasticity*. Pergamon press.

LANGEVIN, D. 2014 Rheology of adsorbed surfactant monolayers at fluid surfaces. *Annu. Rev. Fluid Mech.* **46**, 47–65.

LAPLACE, P. S. 1805 Mechanique celeste supplement au x libre .

LE DIZÈS, S. 1997 Global modes in falling capillary jets. *Eur. J. Mech. B/Fluids* **16**, 761–778.

LE DIZÈS, S. & VILLERMAUX, E. 2017 Capillary jet breakup by noise amplification. *J. Fluid Mech.* **810**, 281–306.

LEAL, L. G. 2007 *Advanced transport phenomena: fluid mechanics and convective transport processes*, , vol. 7. Cambridge University Press.

LEBEDEV, A. A. 1916 Stokes' law as applied to liquid balls. *J. Russ. Phys. Chem. Soc. Part. Phys.* **48**, 97–131.

LEE, H. C. 1974 Drop formation in a liquid jet. *IBM Journal of Research and Development* **18** (4), 364–369.

LEIB, S. J. & GOLDSTEIN, M. E. 1986*a* Convective and absolute instability of a viscous liquid jet. *Phys. Fluids* **29** (4), 952–954.

LEIB, S. J. & GOLDSTEIN, M. E. 1986*b* The generation of capillary instabilities on a liquid jet. *J. Fluid Mech.* **168**, 479–500.

LIAO, Y. C., FRANSES, E. I. & BASARAN, O. A. 2006 Deformation and breakup of a stretching liquid bridge covered with an insoluble surfactant monolayer. *Phys. Fluids* **18** (2), 022101.

LIAO, Y. C., SUBRAMANI, H. J., FRANSES, E. I. & BASARAN, O. A. 2004 Effects of soluble surfactants on the deformation and breakup of stretching liquid bridges. *Langmuir* **20** (23), 9926–9930.

MANIKANTAN, H. & SQUIRES, T. M. 2017 Pressure-dependent surface viscosity and its surprising consequences in interfacial lubrication flows. *Phys. Rev. Fluids* **2** (2), 023301.

MANIKANTAN, H. & SQUIRES, T. M. 2020 Surfactant dynamics: hidden variables controlling fluid flows. *Journal of Fluid Mechanics* **892**.

MANSOUR, NAGI N & LUNDGREN, THOMAS S 1990 Satellite formation in capillary jet breakup. *Phys. Fluids A: Fluid Dyn.* **2** (7), 1141–1144.

MARANGONI, C. 1871 Sul principio della viscosita'superficiale dei liquidi stabilito dalsig. j. plateau. *Il Nuovo Cimento (1869-1876)* **5** (1), 239–273.

MARIOTTE, E. 1686 Traité du mouvement des eaux et des autres corps fluides .

MARTÍNEZ-CALVO, A., RIVERO-RODRÍGUEZ, J., SCHEID, B. & SEVILLA, A. 2020 Natural break-up and satellite formation regimes of surfactant-laden liquid threads. *J. Fluid Mech.* **883**, A35.

MARTÍNEZ-CALVO, A., RUBIO-RUBIO, M. & SEVILLA, A. 2018 The nonlinear states of viscous capillary jets confined in the axial direction. *J. Fluid Mech.* **834**, 335–358.

MARTÍNEZ-CALVO, A. & SEVILLA, A. 2018 Temporal stability of free liquid threads with surface viscoelasticity. *J. Fluid Mech.* **846**, 877–901.

MCGOUGH, P. T. & BASARAN, O. A. 2006 Repeated formation of fluid threads in breakup of a surfactant-covered jet. *Phys. Rev. Lett.* **96** (5), 054502.

MIETKE, A., JEMSEENA, V., KUMAR, K. V., SBALZARINI, I. F. & JÜLICHER, F. 2019*a* Minimal model of cellular symmetry breaking. *Phys. Rev. Lett.* **123** (18), 188101.

MIETKE, A., JÜLICHER, F. & SBALZARINI, I. F. 2019*b* Self-organized shape dynamics of active surfaces. *Proc. Natl. Acad. Sci. U.S.A.* **116** (1), 29–34.

MILLIKEN, W. J., STONE, H. A. & LEAL, L. G. 1993 The effect of surfactant on the transient motion of Newtonian drops. *Phys. Fluids A: Fluid Dynamics* **5** (1), 69–79.

NARSIMHAN, V., SPANN, A. P. & SHAQFEH, E. S. G. 2015 Pearling, wrinkling, and buckling of vesicles in elongational flows. *J. Fluid Mech.* **777**, 1–26.

NAYFEH, A.H. 1970 Nonlinear stability of a liquid jet. *Phys. Fluids* **13** (4), 841–847.

PAPAGEORGIOU, D.T. 1995 On the breakup of viscous liquid threads. *Phys. Fluids* **7** (7), 1529–1544.

PEPICELLI, M., VERWIJLEN, T., TERVOORT, T. A. & VERMANT, J. 2017 Characterization and modelling of langmuir interfaces with finite elasticity. *Soft Matter* **13** (35), 5977–5990.

PEREIRA, A. & KALLIADASIS, S. 2008 On the transport equation for an interfacial quantity. *Eur. Phys. J. Appl. Phys.* **44** (2), 211–214.

PLATEAU, J. 1849 Statique expérimentale et théorique des liquides soumis aux seules forces moléculaires acad. *Sci. Bruxelles Mém* **23** (5).

PLATEAU, J. 1873 *Statique expérimentale et théorique des liquides*. Gauthier-Villars et C^{ie}, Paris.

POCKELS, A. 1892 On the relative contamination of the water-surface by equal quantities of different substances. *Nature* **46** (1192), 418–419.

POCKELS, A. 1893 Relations between the surface-tension and relative contamination of water surfaces. *Nature* **48**, 152—-154.

POCKELS, A. 1894 On the spreading of oil upon water. *Nature* **50** (1288), 223–224.

PONCE-TORRES, A., HERRADA, M. A., MONTANERO, J. M. & VEGA, J. M. 2016*a* Linear and nonlinear dynamics of an insoluble surfactant-laden liquid bridge. *Phys. Fluids* **28**, 112103.

PONCE-TORRES, A., MONTANERO, J. M., HERRADA, M. A., VEGA, E. J. & VEGA, J. M. 2017 Influence of the surface viscosity on the breakup of a surfactant-laden drop. *Phys. Rev. Lett.* **118**, 024501.

PONCE-TORRES, A., RUBIO, M., HERRADA, M. A., EGGERS, J. & MONTANERO, J. M. 2020 Influence of the surface viscous stress on the pinch-off of free surfaces loaded with nearly-inviscid surfactants. *Sci. Rep.* **10**, 16065.

PONCE-TORRES, A., VEGA, E. J. & MONTANERO, J. M. 2016*b* Effect of surface-active impurities on the liquid bridge dynamics. *Exp. Fluids* **57**, 67.

POWERS, THOMAS R. 2010 Dynamics of filaments and membranes in a viscous fluid. *Rev. Mod. Phys.* **82**, 1607–1631.

PROSSER, A. J. & FRANSES, E. I. 2001 Adsorption and surface tension of ionic surfactants at the air-water interface: Review and evaluation of equilibrium models. *Colloid Surface A* **178** (1-3), 1–40.

PROST, J., JÜLICHER, F. & JOANNY, J.-F. 2015 Active gel physics. *Nat. Phys.* **11** (2), 111–117.

RAGHUNANDAN, A., HIRSA, A. H., UNDERHILL, P. T. & LOPEZ, J. M. 2018 Predicting steady shear rheology of condensed-phase monomolecular films at the air-water interface. *Phys. Rev. Lett.* **121** (16), 164502.

RAYLEIGH, L. 1889 Measurements of the amount of oil necessary in order to check the motions of camphor upon water. *Proc. R. Soc. Lond.* **47**, 364–367.

RAYLEIGH, W. S. 1878 On the instability of jets. *Proc. R. Soc. Lond.* **10**, 4–13.

RAYLEIGH, W. S. 1890 On the superficial viscosity of water. *Proc. R. Soc. Lond.* **48**, 127–140.

RAYLEIGH, W. S. 1892 On the instability of a cylinder of viscous liquid under capillary force. *Phil. Mag. and J. Science* **34** (207), 145–154.

RIVERO-RODRÍGUEZ, J. & SCHEID, B. 2018 Bubble dynamics in microchannels: inertial and capillary migration forces. *J. Fluid Mech.* **842**, 215–247.

RODRÍGUEZ-RODRÍGUEZ, J., SEVILLA, A., MARTÍNEZ-BAZÁN, C. & GORDILLO, J. M. 2015 Generation of microbubbles with applications to industry and medicine. *Annu. Rev. Fluid Mech.* **47**, 405–429.

RUBIO-RUBIO, M., SEVILLA, A. & GORDILLO, J. M. 2013 On the thinnest steady threads obtained by gravitational stretching of capillary jets. *J. Fluid Mech.* **729**, 471–483.

RUTLAND, D.F. & JAMESON, G.J. 1970 Theoretical prediction of the sizes of drops formed in the breakup of capillary jets. *Chem. Eng. Sci.* **25** (11), 1689–1698.

SAVART, F. 1833 Mémoire sur la constitution des veines liquides lancées par des orifices circulaires en mince paroi. *Ann. Chim.* **53**, 337–386.

SCHEID, B., DELACOTTE, J., DOLLET, B., RIO, E., RESTAGNO, F., VAN NIEROP, E. A., CANTAT, I., LANGEVIN, D. & STONE, H. A. 2010 The role of surface rheology on liquid film formation. *EPL* **90**, 24002.

SCHEID, B., DORBOLO, S., ARRIAGA, L. R. & RIO, E. 2012 Antibubble dynamics: the drainage of an air film with viscous interfaces. *Phys. Rev. Lett.* **109** (26), 264502.

SCRIVEN, L. E. 1960 Dynamics of a fluid interface. Equation of motion for Newtonian surface fluids. *Chem. Eng. Sci.* **12** (2), 98–108.

SCRIVEN, L. E. & STERNLING, C. V. 1960 The Marangoni effects. *Nature* **187**, 186–188.

SECOMB, TIMOTHY W 2017 Blood flow in the microcirculation. *Annu. Rev. Fluid Mech.* **49**, 443–461.

SEIFERT, U. 1997 Configurations of fluid membranes and vesicles. *Adv. Phys.* **46** (1), 13–137.

SEIWERT, J., DOLLET, B. & CANTAT, I. 2014 Theoretical study of the generation of soap films: Role of interfacial visco-elasticity. *J. Fluid Mech.* **739**, 124–142.

SETRU, S. U., GOUVEIA, B., ALFARO-ACO, R., SHAEVITZ, J. W., STONE, H. A. & PETRY, S. 2020 A hydrodynamic instability drives protein droplet formation on microtubules to nucleate branches. *arXiv preprint arXiv:2001.06389* .

SEVILLA, A 2011 The effect of viscous relaxation on the spatiotemporal stability of capillary jets. *J. Fluid Mech.* **684**, 204–226.

SHUKLA, I. & GALLAIRE, F. 2020 Frequency selection in a gravitationally stretched capillary jet in the jetting regime. *J. Fluid Mech.* **894**.

SIDERIUS, A., KEHL, S. K. & LEAIST, D. G. 2002 Surfactant diffusion near critical micelle concentrations. *J. Solution Chem.* **31** (8), 607–625.

SILVEY, O. W. 1916 The fall of mercury droplets in a viscous medium. *Phys. Rev.* **7** (1), 106.

SKALAK, R. & BRANEMARK, P. I. 1969 Deformation of red blood cells in capillaries. *Science* **164** (3880), 717–719.

SKALAK, R., TOZEREN, A., ZARDA, R. P. & CHIEN, S. 1973 Strain energy function of red blood cell membranes. *Biophys. J.* **13** (3), 245.

SLATTERY, J. C., SAGIS, L. & OH, E. S. 2007 *Interfacial Transport Phenomena*. Springer US.

STOKES, G. G. 1851 On the effect of the internal friction of fluids on the motion of pendulums. *Trans. Cambridge Philos. Soc.* **9**, 8–106.

STONE, H. A. 1990 A simple derivation of the time-dependent convective-diffusion equation for surfactant transport along a deforming interface. *Phys. Fluids A* **2** (1), 111–112.

STONE, H. A. 1994 Dynamics of drop deformation and breakup in viscous fluids. *Annu. Rev. Fluid Mech.* **26** (1), 65–102.

STONE, H. A. & LEAL, L. G. 1990 The effects of surfactants on drop deformation and breakup. *J. Fluid Mech.* **220**, 161–186.

STONE, H. A., STROOCK, A. D. & AJDARI, A. 2004 Engineering flows in small devices: microfluidics toward a lab-on-a-chip. *Annu. Rev. Fluid Mech.* **36**, 381–411.

TIMMERMANS, M.-L. & LISTER, J. R. 2002 The effect of surfactant on the stability of a liquid thread. *J. Fluid Mech.* **459**, 289–306.

TOMOTIKA, S. 1935 On the instability of a cylindrical thread of a viscous liquid surrounded by another viscous fluid. *Proc. Roy. Soc.* **150**, 322–337.

VAN GOLDE, L. M., BATENBURG, J. J. & ROBERTSON, B. 1988 The pulmonary surfactant system: biochemical aspects and functional significance. *Physiological Reviews* **68** (2), 374–455.

DA VINCI, L. 1508 *The Notebooks of Leonardo da Vinci*. ed and Transl. E MacCurdy (New York: George Brazillier).

WEE, H., WAGONER, B. W., KAMAT, P. M. & BASARAN, O. A. 2020 Effects of surface viscosity on breakup of viscous threads. *Phys. Rev. Lett.* **124** (20), 204501.

WHITAKER, S. 1976 Studies of the drop-weight method for surfactant solutions III. Drop stability, the effect of surfactants on the stability of a column of liquid. *J. Colloid Interf. Sci.* **54** (2), 231–248.

WONG, H., RUMSCHITZKI, D. & MALDARELLI, C. 1996 On the surfactant mass balance at a deforming fluid interface. *Phys. Fluids* **8** (11), 3203–3204.

YOUNG, T. 1805 An essay on the cohesion of fluids. *Phil. Trans. R. Soc. Lond.* **95**, 65–87.

YUEN, M.-C. 1968 Non-linear capillary instability of a liquid jet. *J. Fluid Mech.* **33** (1), 151–163.

ZELL, Z. A., NOWBAHAR, A., MANSARD, V., LEAL, L. G., DESHMUKH, S. S., MECCA, J. M., TUCKER, C. J. & SQUIRES, T. M. 2014 Surface shear inviscidity of soluble surfactants. *Proc. Natl. Acad. Sci. U.S.A.* **111** (10), 3677–3682.

ZHONG-CAN, O. Y. & HELFRICH, W. 1987 Instability and deformation of a spherical vesicle by pressure. *Phys. Rev. Lett.* **59** (21), 2486.

ZHONG-CAN, O. Y. & HELFRICH, W. 1989 Bending energy of vesicle membranes: General expressions for the first, second, and third variation of the shape energy and applications to spheres and cylinders. *Phys. Rev. A* **39** (10), 5280.

CHAPTER 2

One-dimensional modeling of axisymmetric cylinders with complex interfaces†

2.1 Introduction

The system of equations (1.4)-(1.6) represents a nonlinear free-boundary problem that is notoriously difficult to solve, not only analytically, but also using numerical techniques. Therefore, different approximations have been developed over the years to simplify the mathematical description of the kind of free-surface flows like those studied in the present thesis. Among these simplified models, the most successful and widely used ones are the so-called one-dimensional (1D) approximations (see the review by Eggers, 1997, and references therein), which share many methodological similarities with the classical lubrication theory. In particular, all these 1D models take advantage of the assumption of slender flow, and lead to a system of partial differential equations in which the interface position is one of the dependent variables, thus avoiding the need to solve the full equations of motion as a free-boundary problem. The corresponding slenderness parameter, which typically compares the characteristic radial and axial length scales, then constitutes the natural small parameter to develop perturbative expansions of the system (1.4)-(1.6).

The simplest 1D models are the leading-order approximations which, as shown below, are obtained at first order in the slenderness parameter. The leading-order 1D models have been extensively used in previous studies of free-surface flows, and have demonstrated a very good performance in capturing the linear and nonlinear dynamics of clean interfaces in a wide variety of flow configurations and values of the Laplace number (Eggers, 1993, 1997; Eggers & Dupont, 1994; Ambravaneswaran *et al.*, 2002; Notz & Basaran, 2004; Subramani *et al.*, 2006; Yildirim *et al.*, 2005; Eggers & Villermaux, 2008; Rubio-Rubio *et al.*, 2013). Similar leading-order models have also been derived to account for the presence of adsorbed surfactants, and have been applied in a number of settings of practical relevance (Ambravaneswaran & Basaran, 1999; Craster *et al.*, 2002, 2009; Xu *et al.*, 2007). However, as pointed out by Timmermans & Lister (2002) and Martínez-Calvo & Sevilla

---

† This work was reported in a section of Martínez-Calvo & Sevilla (*J. Fluid Mech.*, vol. 846, 2018, pp. 877–901).

(2018), a higher-order approximation is needed when the surface viscoelastic stresses are large enough. The failure of the leading-order 1D models to describe the flow when elastic and surface viscous stresses are important, even in the linear stage of the Plateau-Rayleigh instability, is due to the fact that the leading-order velocity profile cannot accommodate the shear induced by tangential interfacial stresses. In addition to this limitation, all the 1D models previously derived in the literature disregarded the effect of surface viscous stresses.

Hence, as we did in Martínez-Calvo & Sevilla (2018), the present chapter is devoted to derive two different one-dimensional (1D) approximations that take into account the effects of Marangoni stresses and surface viscosities when the liquid column is covered with insoluble surfactant and embedded in a passive ambient fluid. Here, following the same spirit as García & Castellanos (1994), we consider the dimensionless parameter $\varepsilon = R/L$, where L is the characteristic axial length of the liquid thread. Assuming that $L \gg R$, $\varepsilon \ll 1$ is the appropriate small parameter to derive the 1D models. To this end, it proves convenient to make the flow variables dimensionless using the following characteristic scales,

$$r_c = z_c = \frac{R}{\varepsilon}, \; t_c = \frac{\mu R}{\varepsilon\, \sigma_0}, \; u_c = w_c = \frac{\sigma_0}{\mu}, \; a_c = R, \tag{2.1a}$$

$$p_c = \frac{\sigma_0}{R}, \; \sigma_c = \sigma_0, \; \Gamma_c = \Gamma_0, \; \mu_{s,c} = \mu_{s0}, \; \kappa_{s,c} = \kappa_{s0}. \tag{2.1b}$$

The regularity of the solution at $r = 0$ together with the axisymmetry condition require that the pressure and the axial velocity fields have to be even functions of r, whilst the radial velocity field has to be an odd function of r, suggesting the following expansion in the radial coordinate $r \sim \varepsilon$ (García & Castellanos, 1994; Eggers & Dupont, 1994),

$$w(r,z,t) = w_0(z,t) + \frac{1}{2}r^2 w_2(z,t) + ... + \frac{1}{(2j)!}r^{2j} w_{2j}, \tag{2.2}$$

$$p(r,z,t) = p_0(z,t) + \frac{1}{2}r^2 p_2(z,t) + ... + \frac{1}{(2j)!}r^{2j} p_{2j}, \tag{2.3}$$

$$u(r,z,t) = -\frac{1}{2}r w_0'(z,t) - \frac{1}{8}r^3 w_2'(z,t) - ... - \frac{2j+1}{(2j+2)!}r^{2j+1} w_{2j}', \tag{2.4}$$

for $j \in \mathbb{N}$ and equation (2.4) satisfying the continuity equation (1.4).

2.2 Leading-order models

Introducing equations (2.2)–(2.4) into equations (1.6b) and the axial projection of the momentum equation (1.4), the leading-order kinematic condition and the axial momentum equation read, respectively,

$$\frac{\partial a^2}{\partial t} + \frac{\partial (a^2 w_0)}{\partial z} + O(\varepsilon^2) = 0, \tag{2.5}$$

$$La\left(\frac{\partial w_0}{\partial t}+w_0w_0'\right)=-p_0'+\varepsilon(w_0''+2w_2)+O(\varepsilon^2), \tag{2.6}$$

where p_0 and w_2 can be obtained from equations (1.31) and (1.32), respectively, which at leading-order yield the following normal and tangential stress balances at $r=\varepsilon a$,

$$p_0=-\varepsilon w_0'+C\left[\sigma+\varepsilon\frac{Bq(\Theta\kappa_s-\mu_s)}{a}\left((aw_0)'-\frac{C(a^2w_0)'}{2}\right)\right]-\varepsilon\frac{Bq\mu_s w_0'}{a}+O(\varepsilon^2), \tag{2.7}$$

$$\begin{aligned}w_2=&\frac{\sigma'}{\varepsilon a}+\frac{w_0''}{2}+\frac{3a'w_0'}{a}+\frac{1}{a}\frac{\partial}{\partial z}\left[\frac{Bq(\Theta\kappa_s-\mu_s)}{a}\left((aw_0)'-\frac{C(a^2w_0)'}{2}\right)\right]\\&+\frac{2Bq(\mu_s aw_0')'}{a^2}+\frac{Bq\mu_s a'w_0'}{a^2}+O(\varepsilon^2).\end{aligned} \tag{2.8}$$

Additionally, the transport equation for the surfactant concentration, $\Gamma(z,t)$, reads, at leading-order,

$$\frac{\partial\Gamma}{\partial t}+\frac{1}{a}\frac{\partial(aw_0\Gamma)}{\partial z}-\frac{C\Gamma}{2a}\frac{\partial(a^2w_0)}{\partial z}+O(\varepsilon^2)=0. \tag{2.9}$$

It is worth noting that the above leading-order equation for Γ is the same for the three reference frames outlined in chapter 1, section §1.3. Moreover, although it does not affect the linear regime, equation (2.9) retains the full curvature, C, unlike the leading-order expressions for the surfactant concentration derived by Timmermans & Lister (2002); Liao *et al.* (2006); Craster *et al.* (2009), that include the approximation $C\simeq a^{-1}$. Finally, eliminating the small parameter ε from the formulation via the substitutions $z\longrightarrow\varepsilon z$, $t\longrightarrow\varepsilon t$, $w_{2j}\longrightarrow w_{2j}/\varepsilon^{2j}$, the leading-order one dimensional model consists of the following three coupled equations,

$$\frac{\partial a^2}{\partial t}+\frac{\partial(a^2w_0)}{\partial z}=0, \tag{2.10}$$

$$\begin{aligned}La\left(\frac{\partial w_0}{\partial t}+w_0\frac{\partial w_0}{\partial z}\right)=&\frac{3}{a^2}\frac{\partial}{\partial z}\left(a^2\frac{\partial w_0}{\partial z}\right)\\&-\frac{\partial}{\partial z}\left\{C\left[\sigma+\frac{Bq(\Theta\kappa_s-\mu_s)}{a}\left(\frac{\partial(aw_0)}{\partial z}-\frac{C}{2}\frac{\partial(a^2w_0)}{\partial z}\right)\right]\right\}\\&+\frac{2}{a}\frac{\partial}{\partial z}\left[\sigma+\frac{Bq(\Theta\kappa_s-\mu_s)}{a}\left(\frac{\partial(aw_0)}{\partial z}-\frac{C}{2}\frac{\partial(a^2w_0)}{\partial z}\right)\right]+\frac{5Bq}{a^2}\frac{\partial}{\partial z}\left(\mu_s a\frac{\partial w_0}{\partial z}\right),\end{aligned} \tag{2.11}$$

$$\frac{\partial\Gamma}{\partial t}+\frac{1}{a}\frac{\partial(aw_0\Gamma)}{\partial z}-\frac{C\Gamma}{2a}\frac{\partial(a^2w_0)}{\partial z}=0, \tag{2.12}$$

which must be complemented with three equations of state, $\sigma(\Gamma)$, $\mu_s(\Gamma)$ and $\kappa_s(\Gamma)$, relating the surface tension coefficient and the two surface viscosities with the surfactant concentration. However, note that explicit expressions for the equations of state of surface viscosities are not needed in a linearized analysis, like that presented in chapter 3. Equations (2.10)–(2.12) recover the limit when only gradients of σ are considered by setting $Bq \rightarrow 0$ $\Theta Bq \rightarrow 0$ (Timmermans & Lister, 2002; Liao *et al.*, 2006; Craster *et al.*, 2009), and also the limit of a clean liquid thread when $\Gamma \rightarrow 0$, $\sigma \rightarrow 1$, $Bq \rightarrow 0$ $\Theta Bq \rightarrow 0$ (Eggers & Dupont, 1994; García & Castellanos, 1994).

2.3 Second-order parabolic model

The accuracy of the 1D approximation deduced in §2.2 can be improved by retaining terms of order $O(\varepsilon^2)$, leading to the so-called *parabolic model*, whose relative error is of order $O(\varepsilon^4)$ (García & Castellanos, 1994). At order $O(\varepsilon^2)$, the kinematic condition, the surfactant transport equation and the axial momentum equation read, respectively,

$$\frac{\partial a^2}{\partial t}+\frac{\partial(a^2w_0)}{\partial z}+\frac{\varepsilon^2}{4}\frac{\partial(a^4w_2)}{\partial z}+O(\varepsilon^4)=0. \tag{2.13}$$

$$\begin{aligned}
&\frac{\partial\Gamma}{\partial t}+\frac{(aw_0\Gamma)'}{a}-\frac{C(a^2w_0)'\Gamma}{2a}+\frac{\varepsilon^2}{2a}\biggl[(a^3w_2\Gamma)'-a'^2(aw_0)'\Gamma-(aa'(aw_0)')'\Gamma\\
&-\frac{C\Gamma}{2}\left(\frac{(a^4w_2)'}{2}-a'^2(a^2w_0)'\right)\biggr]+O(\varepsilon^4)=0,
\end{aligned} \tag{2.14}$$

$$La\left(\frac{\partial w_2}{\partial t}+w_0w_2'\right)=-p_2'+\varepsilon\left(w_2''+\frac{4w_4}{3}\right)+O(\varepsilon^2), \tag{2.15}$$

where $w_4(z,t)$ can be obtained from the second-order truncation of the tangential stress balance,

$$\begin{aligned}
&a\left(w_2-\frac{w_0''}{2}\right)-3a'w_0'+\varepsilon^2\biggl(\frac{a^3w_4}{6}-\frac{a^3w_2''}{8}-\frac{7a^2a'w_2'}{4}-\frac{3aa'^2w_2}{2}+\frac{3aa'^2w_0''}{4}\\
&+\frac{3a'^3w_0'}{2}\biggr)=\frac{\sigma'}{\varepsilon}+\frac{\partial}{\partial z}\left[\frac{Bq(\Theta\kappa_s-\mu_s)}{a}\left((aw_0)'-\frac{C(a^2w_0)'}{2}\right)\right]+\frac{2Bq(\mu_s aw_0')'}{a}\\
&+\frac{Bq\mu_s a'w_0'}{a}+\varepsilon^2\frac{\partial}{\partial z}\biggl[\frac{Bq(\Theta\kappa_s-\mu_s)}{2a}\biggl((a^3w_2)'-a'^2(aw_0)'-(aa'(aw_0)')'\\
&-\frac{C}{2}\left(\frac{(a^4w_2)'}{2}-a'^2(a^2w_0)'\right)\biggr)\biggr]+\varepsilon^2\frac{Bqa'^2(\mu_s aw_0')'}{a}+\frac{\varepsilon^2Bq}{a}\frac{\partial}{\partial z}\biggl[\mu_s a((a^2w_2)'\\
&-4a'^2w_0'-aa'w_0'')\biggr]+\varepsilon^2Bq\mu_s a'\left(\frac{aw_2'}{4}+2a''w_0'\right)+O(\varepsilon^4),
\end{aligned} \tag{2.16}$$

and $p_2(z,t)$ can be deduced from the first degree approximation in ε of the radial momentum equation (1.4),

$$p_2 = La\left(\frac{1}{2}\frac{\partial w_0'}{\partial t} + \frac{w_0 w_0''}{2} - \frac{w_0'^2}{4}\right) - \frac{\varepsilon}{2}(w_0''' + 2w_2') + O(\varepsilon^3). \tag{2.17}$$

Equation (2.15) is coupled to (2.6), i.e. the first order momentum equation for $w_0(z,t)$, whose unique unknown is $p_0(z,t)$. A higher order approximation of p_0 can be obtained from the second-order normal stress balance,

$$\begin{aligned}
p_0 + \varepsilon^2\frac{a^2 p_2}{2} &= C\sigma + \varepsilon\Bigg[-w_0' + \frac{CBq(\Theta\kappa_s - \mu_s)}{a}\left((aw_0)' - \frac{C(a^2w_0)'}{2}\right) - \frac{Bq\mu_s w_0'}{a} \\
&+\varepsilon^2\left(3a'^2w_0' - \frac{3a^2w_2'}{4} - 2aa'w_2 + aa'w_0''\right) + \varepsilon^2\frac{CBq(\Theta\kappa_s - \mu_s)}{2a}\Bigg((a^3w_2)' - a'^2(aw_0)' \\
&-(aa'(aw_0)')' - \frac{C}{2}\left(\frac{(a^4w_2)'}{2} - a'^2(a^2w_0)'\right)\Bigg) - \varepsilon^2 Bq\mu_s\left(\frac{aw_2'}{4} + 2a''w_0' - \frac{a'^2w_0'}{2a}\right)\Bigg] + O(\varepsilon^4).
\end{aligned} \tag{2.18}$$

Hence, introducing the expressions for p_2, w_4 into (2.15), and p_0, p_2 into (2.6), and eliminating the small parameter ε from the formulation via the substitution $z \longrightarrow \varepsilon z$, $t \longrightarrow \varepsilon t$, $w_{2j} \longrightarrow w_{2j}/\varepsilon^{2j}$, the four equations of the parabolic model read

$$\frac{\partial a^2}{\partial t} + \frac{\partial(a^2w_0)}{\partial z} + \frac{1}{4}\frac{\partial(a^4w_2)}{\partial z} = 0, \tag{2.19}$$

$$\begin{aligned}
&La\left(\frac{\partial w_0}{\partial t} + w_0w_0' - \left[\frac{a^2}{4}\left(\frac{\partial w_0'}{\partial t} + w_0w_0'' - \frac{w_0'^2}{2}\right)\right]'\right) = 2w_0'' + 2w_2 - 6a'a''w_0' \\
&- (4a'^2 + aa'')w_0'' - \frac{3aa'w_0'''}{2} - \frac{a^2w_0''''}{4} + 2(a'^2 + aa'')w_2 + \frac{5aa'w_2'}{2} + \frac{a^2w_2''}{4} \\
&- \frac{\partial}{\partial z}\Bigg[C\sigma + \frac{CBq(\Theta\kappa_s - \mu_s)}{a}\Bigg((aw_0)' + \frac{(a^3w_2)' - a'^2(aw_0)' - (aa'(aw_0)')'}{2} \\
&-\frac{C}{2}\left((a^2w_0)' + \frac{(a^4w_2)'}{4} - \frac{a'^2(a^2w_0)'}{2}\right)\Bigg) - Bq\mu_s\left(\frac{w_0'}{a} + \frac{aw_2'}{4} + 2a''w_0' - \frac{a'^2w_0'}{2a}\right)\Bigg],
\end{aligned} \tag{2.20}$$

$$
\begin{aligned}
&La\left(\frac{\partial w_2}{\partial t}+w_0w_2'+\frac{w_0w_0'''}{2}+\frac{1}{2}\frac{\partial w_0''}{\partial t}\right)=\frac{4w_0''}{a^2}+\frac{24a'w_0'}{a^3}-\frac{8w_2}{a^2}+\frac{w_0''''}{2}-\frac{6a'^2w_0''}{a^2}\\
&-\frac{12a'^3w_0'}{a^3}+3w_2''+\frac{14a'w_2'}{a}+\frac{12a'^2w_2}{a^2}+\frac{8}{a^3}\frac{\partial}{\partial z}\Bigg[\sigma+\frac{Bq(\Theta\kappa_s-\mu_s)}{a}\Bigg((aw_0)'\\
&+\frac{(a^3w_2)'-a'^2(aw_0)'-(aa'(aw_0)')'}{2}-\frac{C}{2}\left((a^2w_0)'+\frac{(a^4w_2)'}{4}-\frac{a'^2(a^2w_0)'}{2}\right)\Bigg)\Bigg)\Bigg]\\
&+\frac{8Bq\mu_sa'}{a^3}\left(\frac{aw_2'}{4}+2a''w_0'\right)+\frac{8Bq}{a^4}\frac{\partial}{\partial z}\Big[\mu_sa(2w_0'+(a^2w_2)'-4a'^2w_0'-aa'w_0'')\Big]\\
&+\frac{8Bq\mu_sa'w_0'}{a^4}+\frac{8Bqa'^2(\mu_saw_0')'}{a^4},
\end{aligned}
\tag{2.21}
$$

$$
\begin{aligned}
&\frac{\partial\Gamma}{\partial t}+\frac{(aw_0\Gamma)'}{a}+\frac{(a^3w_2\Gamma)'-a'^2(aw_0)'\Gamma-(aa'(aw_0)')'\Gamma}{2a}\\
&-\frac{C\Gamma}{2a}\left((a^2w_0)'+\frac{(a^4w_2)'}{4}-\frac{a'^2(a^2w_0)'}{2}\right)=0.
\end{aligned}
\tag{2.22}
$$

Note that equations (2.19)–(2.22), together with the three equations of state $\sigma(\Gamma)$, $\mu_s(\Gamma)$ and $\kappa_s(\Gamma)$, form a closed system which determines the temporal evolution of $a(z,t)$, $w_0(z,t)$, $w_2(z,t)$ and $\Gamma(z,t)$. In this parabolic model, the equation for Γ (2.22) is referred to the laboratory frame, thus the transport equation of Γ differs at second order from the two other versions discussed in chapter 1, section §1.3. The performance of the parabolic model in the linear regime of the Plateau-Rayleigh instability will be assessed in chapter 3, subsection §§3.4.1.

References

AMBRAVANESWARAN, B. & BASARAN, O.A. 1999 Effects of insoluble surfactants on the nonlinear deformation and breakup of stretching liquid bridges. *Phys. Fluids* **11** (5), 997–1015.

AMBRAVANESWARAN, B., WILKES, E. D. & BASARAN, O. A. 2002 Drop formation from a capillary tube: Comparison of one-dimensional and two-dimensional analyses and occurrence of satellite drops. *Phys. Fluids* **14** (8), 2606–2621.

CRASTER, R. V., MATAR, O. K. & PAPAGEORGIOU, D. T. 2002 Pinchoff and satellite formation in surfactant covered viscous threads. *Phys. Fluids* **14** (4), 1364–1376.

CRASTER, R. V., MATAR, O. K. & PAPAGEORGIOU, D. T. 2009 Breakup of surfactant-laden jets above the critical micelle concentration. *J. Fluid Mech.* **629**, 195–219.

EGGERS, J. 1993 Universal pinching of 3d axisymmetric free-surface flow. *Phys. Rev. Lett.* **71**, 3458.

EGGERS, J 1997 Nonlinear dynamics and breakup of free surface flows. *Rev. Mod. Phys.* **69**, 865–929.

EGGERS, J. & DUPONT, T. F. 1994 Drop formation in a one-dimensional approximation of the Navier-Stokes equation. *J. Fluid Mech.* **262**, 205–222.

EGGERS, J. & VILLERMAUX, E. 2008 Physics of liquid jets. *Rep. Prog. Phys.* **71**, 036601.

GARCÍA, F. J. & CASTELLANOS, A. 1994 One-dimensional models for slender axisymmetric viscous liquid jets. *Phys. Fluids* **6** (8), 2676–2689.

LIAO, Y. C., FRANSES, E. I. & BASARAN, O. A. 2006 Deformation and breakup of a stretching liquid bridge covered with an insoluble surfactant monolayer. *Phys. Fluids* **18** (2), 022101.

MARTÍNEZ-CALVO, A. & SEVILLA, A. 2018 Temporal stability of free liquid threads with surface viscoelasticity. *J. Fluid Mech.* **846**, 877–901.

NOTZ, P. K. & BASARAN, O. A. 2004 Dynamics and breakup of a contracting liquid filament. *J. Fluid Mech.* **512**, 223–256.

RUBIO-RUBIO, M., SEVILLA, A. & GORDILLO, J. M. 2013 On the thinnest steady threads obtained by gravitational stretching of capillary jets. *J. Fluid Mech.* **729**, 471–483.

SUBRAMANI, H.J., YEOH, H.K., SURYO, R., XU, Q., AMBRAVANESWARAN, B. & BASARAN, O.A. 2006 Simplicity and complexity in a dripping faucet. *Phys. Fluids* **18** (3), 032106.

TIMMERMANS, M.-L. & LISTER, J. R. 2002 The effect of surfactant on the stability of a liquid thread. *J. Fluid Mech.* **459**, 289–306.

XU, Q., LIAO, Y.-C. & BASARAN, O. A. 2007 Can surfactant be present at pinch-off of a liquid filament? *Phys. Rev. Lett.* **98** (5), 054503.

YILDIRIM, O. E., XU, Q. & BASARAN, O. A. 2005 Analysis of the drop weight method. *Phys. Fluids* **17**, 062107.

Chapter 3

Linear Stability of Complex Liquid Threads[†]

3.1 Introduction

In this chapter, we study the linear stability of liquid threads embedded either in a passive ambient fluid or inside a bath of immiscible liquid, and whose interface is endowed with complex mechanical properties due to the nature of its constituents. In particular, we adopt the same temporal approach pioneered by Rayleigh (Rayleigh, 1878, 1892), introduced in chapter 1. First, to consolidate the main physical ideas, to illustrate the power of Rayleigh's analysis, and to serve as a reference case for the new developments reported in the present document, in §3.2 we briefly revisit the linear stability analysis of a liquid thread with a clean interface. In the following sections, we consider the effect of interfacial rheology on the instability in several relevant instances. We will start with the effect of Marangoni stresses, presented in §3.3, where we deduce the results of Whitaker (1976) and Timmermans & Lister (2002). Then, we will consider interfaces which present a viscous resistance to flow, studied in §3.4. Finally, we will study the case when the interface is purely elastic and behaves as a thin membrane with resistance to bend and shear, which is reported in §3.6.

3.2 Clean interface: Plateau–Rayleigh instability

In chapter 1 we explained the physical basis of the Plateau–Rayleigh instability mechanism by means of Plateau's quasi-static argument (Plateau, 1849), which relies on the idea of surface area reduction at constant volume leading to a final state of minimum energy. Indeed, the number of molecules placed at the interface, which have an extra energy compared with those inside the bulk fluid, is thereby reduced. Here, we first provide a simple force-based dynamical description to illustrate the instability mechanism, and which will help us to understand the results of Rayleigh's temporal stability analysis. In this section, we consider that the thread is immersed in a passive ambient at constant pressure, thus we set $\hat{\boldsymbol{T}} = -\boldsymbol{I}$. Nonetheless, the arguments explaining the instability process are the same if we consider the thread immersed

---

[†] The present chapter includes results that have been published in Martínez-Calvo & Sevilla (*J. Fluid Mech.*, vol. 846, 2018, pp. 877–901), and in Martínez-Calvo *et al.* (*J. Fluid Mech.*, vol. 883, 2020, A35).

in an infinite outer bath of viscosity $\hat{\mu}$ and density $\hat{\rho}$, a problem which was first addressed by Tomotika (1935).

Let us first imagine the situation depicted in figure 3.1(a), in which the cylindrical interface is slightly perturbed by a small-amplitude wave around its unperturbed radius, thus generating a crest with radius R_C, and a trough with a smaller radius $R_T < R_C$. According to the Young-Laplace law (Young, 1805; Laplace, 1805), the surface stress balances in these two regions read, $p_C = \sigma C_C$ and $p_T = \sigma C_T$, where we have neglected viscous forces, and we have assumed that the outer pressure is zero without loss of generality. The curvature of the interface, C, can be decomposed into two contributions

$$C = \boldsymbol{\nabla}_s \cdot \boldsymbol{n} = C^{(z)} + C^{(r)}, \tag{3.1}$$

namely the axial, $C^{(z)}$, and radial curvature, $C^{(r)}$, which read,

$$C^{(z)} = -\frac{\partial_z^2 a}{[1 + (\partial_z a)^2]^{3/2}}, \quad \text{and} \quad C^{(r)} = \frac{1}{a[1 + (\partial_z a)^2]^{1/2}}. \tag{3.2}$$

If the wavelength of the disturbance, λ, is sufficiently large compared with the amplitude of the disturbance, ϵ, the radial curvature is much larger than the axial one. Indeed, according to (3.2), $C^{(z)} \sim \epsilon/\lambda^2$ and $C^{(r)} \sim 1/\epsilon$, and thus $C^{(z)}/C^{(r)} \sim (\epsilon/\lambda)^2 \ll 1$. Consequently, the fluid pressure at the trough is higher than that at the crest due to the fact that $p_T \approx \sigma/R_T$ and $p_C \approx \sigma/R_C$. This imbalance in the pressure field generates an axial pressure gradient that drives the flow out of the trough, leading to the thinning of the trough and the swelling of the crest due to mass conservation. This mechanism induces a self-accelerated unstable process that ultimately leads the thread to breakup, provided that the disturbance wavelength is large enough. In contrast, for small enough perturbation wavelengths, for which $C_r < C_z$, the system is stabilized by driving the fluid towards the trough. Hence, it is the interplay between the radial and axial contributions to the interfacial curvature what determines the stability of the fluid cylinder.

This argument and the ones outlined in chapter 1 reveal the existence of a cut-off wavelength for the interfacial disturbances above which the system is unstable. However, they fail at providing both a wavelength selection mechanism, and a quantitative prediction for the growth rate of these perturbations. To this end, let us now summarize Rayleigh's temporal linear stability analysis (Rayleigh, 1878, 1892), which takes into account the dynamics of the flow, namely inertial and viscous forces, which have to be overcome by the surface tension force to drive the flow out of equilibrium.

The main idea relies on the existence of a reference state, usually referred to as the *base flow*, which satisfies the steady-state equations (1.4)–(1.6c) in §1.2, and that is invariant in at least two directions, say z and θ. In the case of a cylindrical interface, taking the characteristic scales of §1.2, the base flow is simply $p = 1$, $a = 1$, and $\boldsymbol{u} = \boldsymbol{0}$ if the column is at rest, or if we take a co-moving reference frame at the jet injection velocity, provided that the radial velocity profile is uniform. In the present thesis, we will restrict ourselves to the

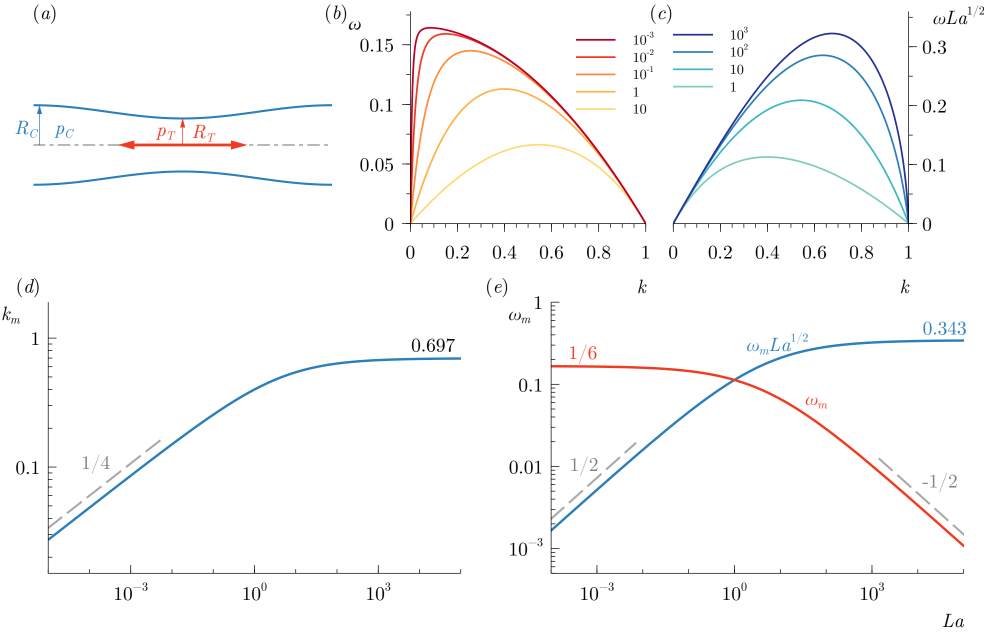

Figure 3.1: (*a*) Schematic representation illustrating the linear dynamics of the liquid thread. (*b*,*c*) Amplification curves for different Laplace numbers indicated in the legend in (*b*) the viscous regime, and (*c*) the inertial regime. Most amplified wavenumber k_m (*d*) and associated growth rate ω_m (*e*) as a function of La. Panel (*e*) also shows $\omega_m La^{1/2}$ which yields the inertial non-dimensionalization.

study of axisymmetric perturbations, since, as explained in chapter 1 by means of Plateau's analysis, non-axisymmetric perturbations are energetically unfavourable and thus stable[†]. The translational invariance of the base flow allows to apply a Fourier transform. Hence, we decompose the perturbation into independent Fourier modes of the form $\exp(\omega t + ikz)$, usually referred to as *normal modes*, defined by their frequency ω and their wavenumber $k = 2\pi/\lambda$, where λ is the wavelength. Within the temporal framework, $k \in \mathbb{R}$ and $\omega \in \mathbb{C}$. Note that a given normal mode is unstable if $\Re(\omega) > 0$, stable if $\Re(\omega) < 0$, and neutral if $\Re(\omega) = 0$.

Therefore, to obtain a dispersion relation $D(\omega, k) = 0$ relating the temporal growth rate ω, and the wavenumber k, we linearize the governing equations around the base flow and decompose the perturbations of all the flow variables as temporal normal modes,

$$(u, w, p, a) = (0, 0, 1, 1) + \epsilon(\hat{u}, \hat{v}, \hat{p}, \hat{a}) \exp(ikz + \omega t). \tag{3.3}$$

where $\epsilon \ll 1$ is a small real number that represents the amplitude of the perturbation.

[†] Note that this argument may fail depending on the forces acting on the interface, for instance in a cylindrical membrane whose isotropic tension is negative, which generates compression effects that can trigger non-axisymmetric buckling instabilities

Introducing (3.3) into the system (1.4)–(1.6c) and keeping terms proportional to ϵ, the following dispersion relation is obtained:

$$La\omega^2 F(k) - k^2(1-k^2) + \frac{4k^4}{La}[F(k) - F(\tilde{k})] + 2\omega k^2[2F(k) - 1] = 0, \tag{3.4}$$

which was first obtained by Rayleigh (1892), where $\tilde{k} = \sqrt{k^2 + La\,\omega}$ and $F(x) = xI_0(x)/I_1(x)$. Here, $I_n(x)$ denotes the nth-order modified Bessel function of the first kind. Figures 3.1(*a*,*b*) show the amplification curves $\omega(k)$ obtained from (3.4) for different values of the Laplace number. The dimensionless cut-off wavenumber $k_c = 1$ is in agreement with Plateau's quasi-static theory that yields $\lambda_c = 2\pi$. As evidenced by figure 3.1(*b*), the most amplified wavenumber, k_m, decreases when the viscous force dominates, that is when *La* decreases, thus generating longer and slender drops after breakup.

When inertia becomes important, the appropriate characteristic time scale is the capillary time, $\sqrt{\rho R_o^3/\sigma}$. To change our non-dimensionalization to the inertial scaling, we introduce the following transformation of the dimensionless growth rate $\omega_I = \omega La^{1/2}$, where ω_I is the inertial dimensionless growth rate, as shown in figure 3.1(*c*). The two distinguished limits are the Stokes limit, or viscous regime, $La \to 0$, and the Euler limit, or inertial regime, $La \to \infty$, which read in their appropriate scales,

$$\omega = \frac{1}{2}\frac{1-k^2}{k^2\left[\frac{I_o(k)^2}{I_1(k)^2} - 1\right] - 1}, \quad \omega_I = \sqrt{\frac{kI_1(k)(1-k^2)}{I_o(k)}}, \tag{3.5}$$

respectively (Rayleigh, 1878, 1892). The amplification curve in the Stokes limit, $La \to 0$, has its maximum at $k_m = 0$, and the associated maximum growth rate is $\omega_m = 1/6$, which is only regularized when considering finite inertia. In the opposite Euler limit, $La \to \infty$, the most amplified wavenumber is $k_m = 0.697$, with associated growth rate, $\omega_{m,I} = 0.343$. These limits are shown in figures 1.1(*d*,*e*), which display most unstable wavenumber, k_m, and associated growth rate ω_m as a function of *La*. Additionally, they show the power-law dependence of k_m for small values of *La* and that of ω_m for large values of *La* (or inversly $\omega_{m,I}$ for $La \ll 1$). These power laws can be deduced from the long-wave approximation of the dispersion relation (3.4) or, equivalently, from the leading-order one-dimensional model for a clean interface deduced by Eggers & Dupont (1994) and García & Castellanos (1994), and which can be found in chapter 2. The leading-order results of the long-wave approximation are $k_m \sim (2 + 3\sqrt{2}La^{-1/2})^{-1/2}$ and $\omega_m \sim (2\sqrt{2} + 6La^{-1/2})^{-1}$ (Eggers & Villermaux, 2008). This approximation provides very accurate results in the whole range of *La*, since $k \in (0, 1)$ accomplishes the slenderness assumption. In the inviscid limit, $La \to \infty$, both ω_m and k_m are slightly overestimated by the 1D model, namely $\omega_m \to 2^{-3/2} \simeq 0.354$ and $k_m \to 2^{-1/2} \simeq 0.707$. However, in the Stokes limit, $La \ll 1$, the values of $\omega_m \to 1/6$ and $k_m = 3^{-1/2}2^{-1/4}La^{1/4}$ are in excellent agreement with the exact linear theory

The first quantitative experiments that obtained accurate measurements of the exponential growth of perturbations were due to Donnelly & Glaberson (1966) and Goedde & Yuen

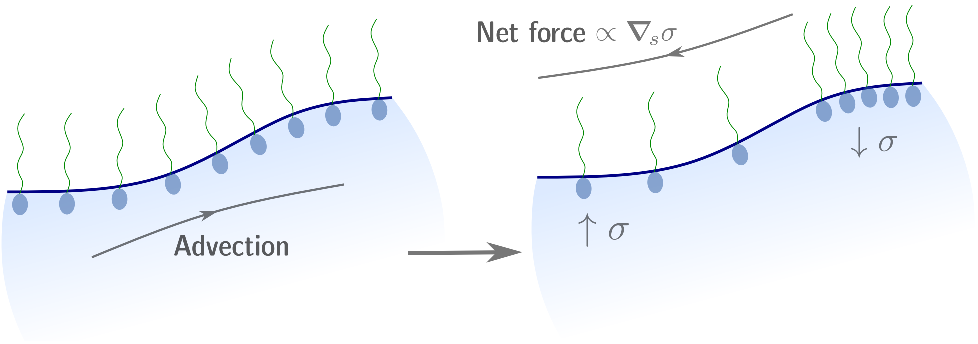

Figure 3.2: Schematic representation of the surface elastic (Marangoni stress) in the linear regime.

(1970), who found good agreement with Rayleigh's theory in the inertial regime, and also when considering viscous effects in the case of Goedde & Yuen (1970). The most precise experiments reported up-to-date are due to González & García (2009), showing an excellent agreement with the theoretical amplification curve.

3.3 Influence of Marangoni stresses: surfactant-induced elastic interface

This section is devoted to study the effects of surface elasticity induced by the presence of insoluble surfactants on the linear stability of a liquid thread, which is embedded in a passive ambient at constant pressure p_a. Under this configuration, the first study who extended the work of Rayleigh to account for Marangoni stresses was due to Whitaker (1976), who also considered the effect of surface viscous stresses. However, this author deduced an incorrect dispersion relation that contained several mistakes in Marangoni and surface viscous terms, as pointed out by Timmermans & Lister (2002), who corrected the analysis considering only Marangoni effects. Moreover, the work of Whitaker (1976) also includes the effect of solubility in the dispersion relation, although it is neither analysed nor discussed. Besides, the results and conclusions of Whitaker (1976) are restricted to the limit of dominant inertia, $La \gg 1$. Hence, this section aims to deliver a compendium of these results and the main physical mechanisms, which will pave the way towards chapter 4 and section §4.3, where we study the subsequent nonlinear dynamics of a surfactant-laden thread.

To describe the transport of insoluble surfactant molecules at the interface $\partial\mathcal{V}$, we use the conservation equation referred to the laboratory frame (Stone & Brenner, 1996; Wong *et al.*, 1996; Pereira & Kalliadasis, 2008) as deduced in §1.3. For the linear stability analysis conducted in the present section, it is convenient to express equation (1.10) in cylindrical

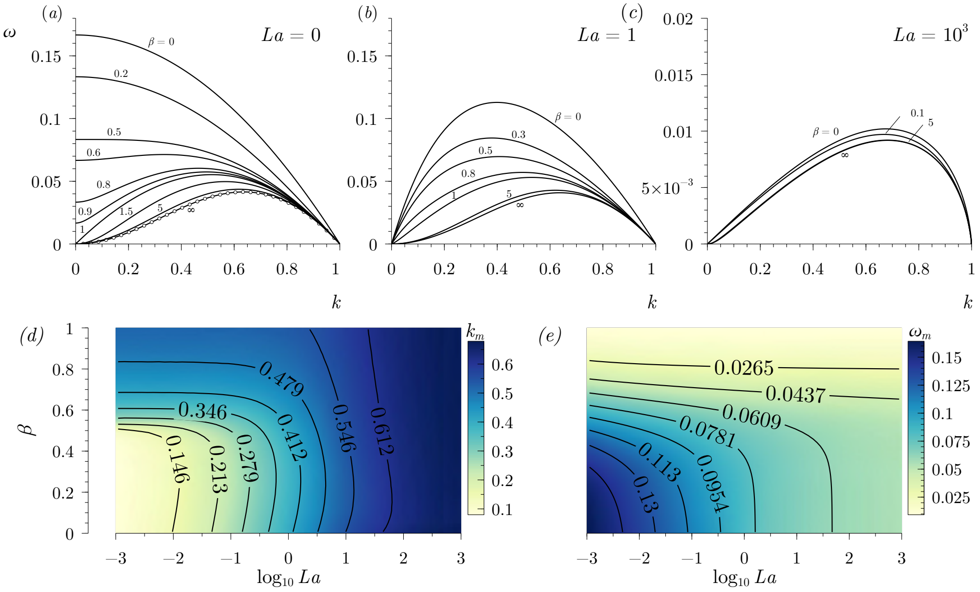

Figure 3.3: Amplification curves for (*a*) $La = 0$, (*b*) 1, and (*c*) 10^3. (*d*) Isocontours of the most amplified wavenumber $k_m(La, \beta)$ and its corresponding growth rate $\omega_m(La, \beta)$ in (*e*).

coordinates, which for an axisymmetric interface reads

$$\frac{\partial \Gamma}{\partial t} + w\frac{\partial \Gamma}{\partial z} + \frac{\Gamma}{a\sqrt{1+a'^2}}\frac{\partial (a u_t)}{\partial z} + C\Gamma u_n = 0, \tag{3.6}$$

where, as a first approximation, we have disregarded the effect of surface diffusion and thus we only consider the limit where the surface Péclet number $Pe_s \to \infty$. See section 1.4 in chapter 1 for a detailed discussion on the relative importance of surface diffusion.

To obtain the desired dispersion relation we follow the same procedure described in §3.2, which yields

$$\begin{aligned} &La\,\omega^2 F(k) - k^2(1-k^2) + \beta k^2[1 + F(k)(F(\tilde{k}) - 2)] \\ &+ \frac{k^4}{La}\left[4 - \frac{\beta}{\omega}\left(2 - \frac{1-k^2}{\omega}\right)\right][F(k) - F(\tilde{k})] + 2\omega k^2(2F(k) - 1) = 0. \end{aligned} \tag{3.7}$$

The dispersion relation (3.7) is exactly the same as the one deduced by Timmermans & Lister (2002), and is also a particular case of the one provided by Martínez-Calvo & Sevilla (2018) in the limit of negligible surface viscosities. The Rayleigh–Chandrasekhar dispersion relation (3.4) is recovered in the limit $\beta \to 0$ (Rayleigh, 1892; Chandrasekhar, 1961).

Surfactant-induced elasticity has a stabilizing effect on the Plateau–Rayleigh instability (Timmermans & Lister, 2002), as illustrated in figure 3.3, which shows that ω

decreases monotonically when β increases, for every value of La. This stabilizing effect can be explained by means of simple physical arguments. When a perturbation with $k < k_c$ is introduced, the flow induced by the Plateau–Rayleigh mechanism advects surfactant molecules from the trough to the valley, which creates an imbalance in Γ, being the concentration larger at the valley. Consequently, the surface tension becomes larger in the trough, where the concentration is smaller, thereby generating a net force at the interface proportional to $\beta\,\boldsymbol{\nabla}_s\sigma$ directed towards the trough (see figure 3.2 for a schematic representation). This Marangoni stress opposes the flow that drains fluid from the region of smaller radius, tends to replenish the original surfactant concentration at the trough, and stabilizes the flow. Additionally, the effect of surface elasticity on the most amplified wavenumber is to increase its value as seen in figure 3.3, thereby less elongated droplets are predicted when β increases, which will be studied in detail in chapter 4, section §4.3.

Concerning the relevant distinguished limits, we first focus on the purely elastic limit, $\beta \gg 1$, where equation (3.7) takes the form (Timmermans & Lister, 2002)

$$La\omega^2[1 + F(k)(F(\tilde{k}) - 2)] - k^2[2\omega - (1 - k^2)][F(k) - F(\tilde{k})] = 0, \qquad (3.8)$$

which only depends on the Laplace number, La. This limit is shown in figures 3.3(*a*–*c*) for different values of La, where if $\beta \gtrsim 10$, it can be considered that the purely elastic limit is reached (Timmermans & Lister, 2002). The most amplified wavenumber k_m and associated growth rate ω_m, and more specifically, the complete amplification curve, only change slightly when La varies, as evidenced by the isocontours of figures 3.3(*d*,*e*). In particular, in the Stokes limit, $La \longrightarrow 0$, the above expression simplifies to the following parameter-free amplification curve

$$\omega = \frac{(1 - k^2)[k^2 - F(k)^2 + 2F(k)]}{2(1 + k^2)}, \qquad (3.9)$$

which is shown in figure 3.3(*a*) with white circles. For arbitrary values of β, in the Stokes limit $La \longrightarrow 0$, the dispersion relation (3.7) simplifies to (Timmermans & Lister, 2002)

$$2\omega[F(k)^2 - 1 - k^2] - (1 - k^2) + \beta(1 + k^2) - \beta\frac{1 - k^2}{2\omega}[k^2 - F(k)^2 + 2F(k)] = 0, \quad (3.10)$$

whose associated amplification curves $\omega(k)$ are shown in figure 3.3(*a*) for different values of β. In particular, this expression takes the limiting form (3.9) when $\beta \longrightarrow \infty$. In this limit of negligible inertia, we observe in figures 3.3(*a*,*d*) that the most amplified wavenumber k_m increases drastically above $\beta = 0.5$ from $k_m \longrightarrow 0$, to $k_m \simeq 0.636$ when $\beta \longrightarrow \infty$. Additionally, the broken Galilean invariance that occurs when $La \longrightarrow 0$ as $k \longrightarrow 0$, disappears drastically when $\beta = 1$.

The other distinguished limit is that of ideal flow, or Euler limit, which is obtained by taking $La \longrightarrow \infty$ and $\omega \longrightarrow \omega/\sqrt{La}$. Nonetheless, as explained by Whitaker (1976) and Timmermans & Lister (2002), this limit yields the exact same result as Rayleigh's original analysis (Rayleigh, 1878), namely equation (3.5) obtained in §3.2. The reason is that the Marangoni stresses cannot be transmitted to the bulk through viscosity, and thus their effect is confined to a thin boundary layer at the interface. Therefore, in the linear regime, the presence of surfactants at the interface only reduces or increases the surface tension coefficient, an effect that can be absorbed into the dimensionless growth rate to yield Rayleigh's dispersion relation. This can be observed in figures 3.3(*c*,*d*,*e*), which show that $\omega(k)$ barely changes as β varies when $La \gg 1$.

3.4 Viscoelastic Interface

As discussed in chapter 1, an interface can have an intrinsic viscous resistance to flow which, in its simplest form, is materialized in two surface viscosity coefficients, namely the shear and dilational ones, μ_s and κ_s, respectively. Here we assume isothermal flow, thus σ, μ_s and κ_s are only functions of the surface concentration of surfactant $\Gamma(z,t)$, which satisfies the transport equation (3.6) at $r = a(z,t)$. For simplicity, in this section we have also disregarded the effect of surface diffusion.

Following the same procedure as in §3.2, we obtain the desired dispersion relation that incorporates the surface viscous stresses,

$$\begin{aligned} &La\omega^2 F(k) - k^2(1-k^2) + \beta k^2[1 + F(k)(F(\tilde{k}) - 2)] + \frac{k^4}{La}\left[4 - \frac{\beta}{\omega}\left(2 - \frac{1-k^2}{\omega} + 4Bq\right)\right. \\ &\left. +6Bq + \frac{1-k^2}{\omega}Bq(1+\Theta) - 2\Theta Bq(1+2Bq)\right][F(k) - F(\tilde{k})] + \omega k^2\left[2Bq(1-\Theta)F(k)\right. \\ &\left. +Bq(1+\Theta)(F(k)F(\tilde{k}) + 1) + 2(2F(k) - 1)\right] = 0. \end{aligned} \tag{3.11}$$

According to equation (3.11), the dispersion relation depends on four dimensionless parameters: the Laplace number, $La = Oh^{-2} = \rho\sigma_0 R/\mu^2$, where Oh is the Ohnesorge number, the elasticity parameter $\beta = E/\sigma_0$, and the shear and dilational Boussinesq numbers, $Bq = \mu_{s0}/(\mu R)$, $\Theta Bq = \kappa_{s0}/(\mu R)$, respectively. Note that the dispersion relation (3.11) reduces to that of Timmermans & Lister (2002) in the limit $Bq \to 0$, and to the Rayleigh–Chandrasekhar dispersion relation when in addition $\beta \to 0$ (Rayleigh, 1892; Chandrasekhar, 1961). However, there are several differences between equation (3.11) and the dispersion relation deduced by Whitaker (1976) in the insoluble limit due to several mistakes made in the latter work (Hansen *et al.*, 1999; Timmermans & Lister, 2002).

To illustrate the effect of surface viscosities on the growth rate of infinitesimal disturbances on the liquid cylinder, figures 3.4 and 3.5 show the amplification function $\omega(k)$ for $La = 0.01$ and $La = 100$, respectively, with the value of Bq indicated near each curve. In both figures, the top and bottom panels correspond with values of the elasticity parameter $\beta = 0$ and $\beta = 1$, while the left and right columns show the results obtained with values of the surface viscosity ratio $\Theta = 10$ and 0.1, respectively. Our results were validated by comparing them with four amplification curves extracted from figure 4 of Timmermans & Lister (2002), represented with symbols, for the particular case $Bq = 0$, finding a perfect agreement.

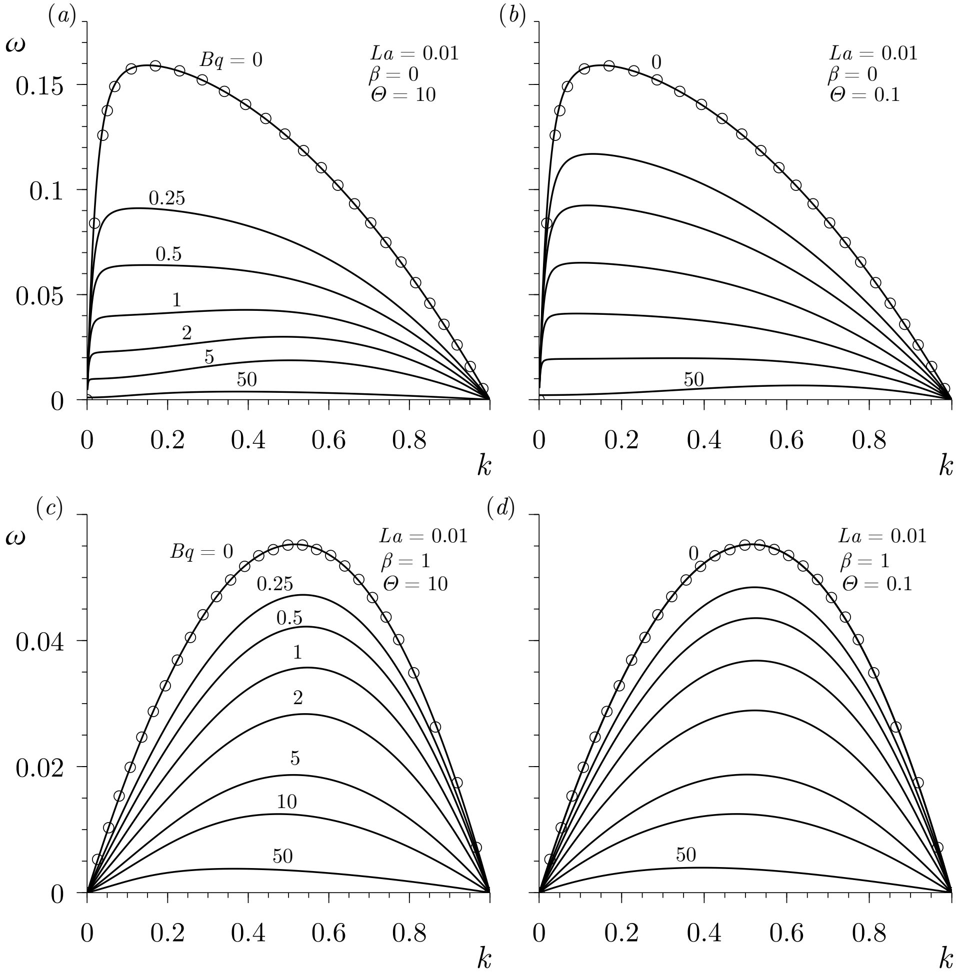

Figure 3.4: Growth rate ω as a function of wavenumber k for La = 0.01 and β = 0 (top row), β = 1 (bottom row), Θ = 10 (left column) and Θ = 0.1 (right column). The values of Bq are indicated near each curve. The symbols are extracted from figure 4 of Timmermans & Lister (2002).

As revealed by figures 3.4 and 3.5, surface viscosity stabilizes the liquid cylinder, since the values of ω decrease monotonically for all values of k as Bq increases. The stabilising effect is more pronounced for small values of La and β. Indeed, in the particular case with La = 0.01 and β = 0, figures 3.4(a,b) show that, for a value of Bq = 1, the maximum growth rate decreases by factors of about 3.8 and 2.4, respectively, compared with the case with Bq = 0. These factors are reduced to approximately 1.5 in figures 3.4(c,d), showing that an increase in the surface elasticity decreases the relative importance of surface viscosity.

As studied in detailed by Timmermans & Lister (2002) and in the previous section, increasing the value of β also has a stabilising effect, which can be seen in figures 3.4 and 3.5 of the present section, and figures 3.3(a–c) of the previous section. However, in contrast with the fact that a finite value of ω is achieved when $\beta \to \infty$, our results reveal that $\omega \to 0$ when $Bq \to \infty$, a behavior similar to that observed for $La \to 0$, and clearly due to the dissipative nature of the surface shear viscosity (see §3.4.3). In particular, the effect of Bq is important both for low and high viscosity threads although, as happens with the effect of β (Timmermans & Lister, 2002), the effect is more pronounced at low capillary Reynolds numbers, as can be deduced by comparing the results of figure 3.4 for $La = 0.01$ with those of figure 3.5 for $La = 100$. Indeed, the reduction factors in the maximum growth rate between the cases $Bq = 0$ and $Bq = 1$ are substantially smaller for $La = 100$ compared with those stated before for $La = 0.01$. In particular, these factors are about 1.3 and 1.2 in figures 3.5(a,b), respectively. The latter limit of dominant inertia, $La \gg 1$, was studied by Whitaker (1976), whose conclusions about the effect of the surface viscosities on ω were correct and coincide with the ones presented herein.

By comparing the left and right columns of figures 3.4 and 3.5 it is deduced that ω is only slightly affected by Θ, with the general trend that an increase in the dilational Boussinesq number, ΘBq, decreases the growth rate, as expected. In particular, for $\beta \lesssim 1$ the maximum growth rate, ω_m, is smaller when Θ is greater than one, as depicted by figures 3.4($a.b$), and 3.5(a,b), this phenomenon being more noticeable for $La \ll 1$. This result is expected, since for a fixed Bq the overall surface viscosity increases when Θ increases, as already noticed by Whitaker (1976) in the limit $La \gg 1$. Figures 3.4 and 3.5 also reveal that the wavenumber of maximum amplification, k_m, depends non-monotonically on Bq for a fixed value of the surface viscosity ratio, most notably at low Laplace numbers and smaller values of Θ.

3.4.1 Performance of the one-dimensional models

Here we study the validity of the leading and second-order 1D approximations accounting for Marangoni and surface viscous stresses derived in chapter 2, in the linear regime. To this end, we compare their temporal stability properties with those provided by the full axisymmetric dispersion relation derived in §3.4. Linearizing equations (2.10)–(2.12) and (2.19)–(2.22), and expanding in normal modes, the dispersion relations associated with the leading-order model and the parabolic model are straightforwardly obtained:

1. **Leading-order model**:

$$\frac{2\omega^2 La}{k^2} - 1 + k^2 + \beta + \omega[6 + Bq(9 + \Theta)] = 0. \tag{3.12}$$

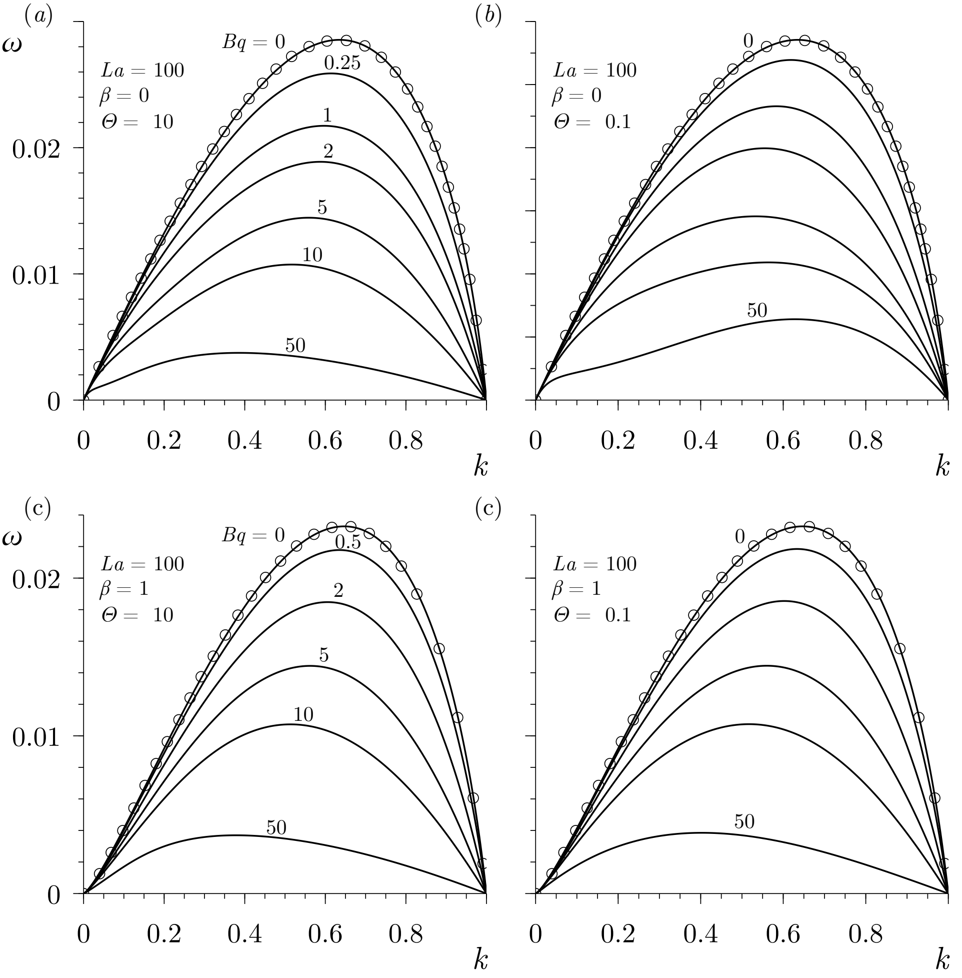

Figure 3.5: Same as figure 3.4 for La = 100.

2. **Parabolic model**:

$$
\begin{aligned}
&La\omega^3(16+4k^2)+\omega^2[128+k^2(96+40\Theta Bq+104Bq)+k^4(18+9\Theta Bq+25Bq)]\\
&+\omega k^2[-8+40\beta+384\,La^{-1}\,(1+3Bq/2+Bq\Theta/6)+k^2(7+9\beta+La^{-1}\,(96+80\Theta Bq\\
&+144Bq+64\Theta Bq^2))+k^4(1+La^{-1}\,(14+9\Theta Bq+25Bq))]+La^{-1}\,k^2[64(\beta-1)\\
&+k^2(48+80\beta-16\Theta Bq-16Bq+64\beta Bq)+k^4(15+9\beta+16\Theta Bq+16Bq)+k^6]\\
&-\frac{16\beta}{La\,\omega}k^4(1-k^2)=0. \qquad (3.13)
\end{aligned}
$$

To illustrate the performance of the two different 1D models deduced in the present

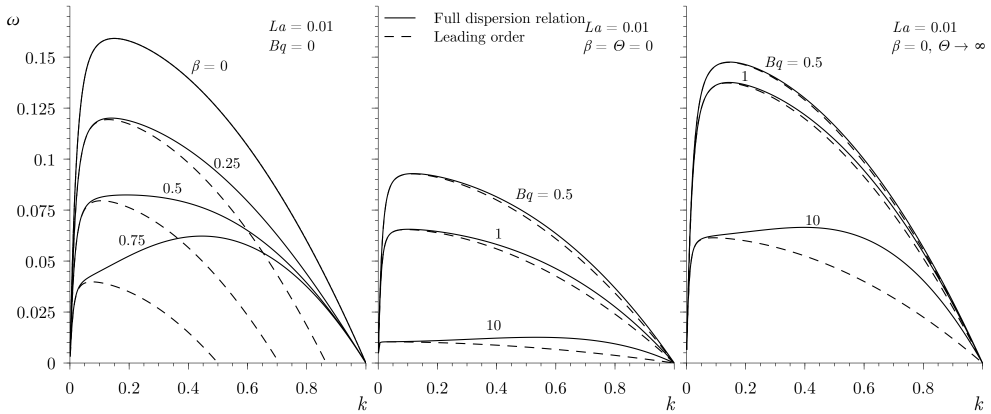

Figure 3.6: Comparison between the full axisymmetric dispersion relation (3.11) (solid lines) and the dispersion relation associated with the leading-order one-dimensional model (3.12) (dashed lines) for $La = 0.01$ and varying the value of β (left column), Bq_μ (middle column) and Bq_κ (right column). The values of the parameters are indicated near each curve.

work, figures 3.6 and 3.7 compare, respectively, the amplification curves obtained with the leading-order model (3.12) and with the parabolic model (3.13), with those given by the full axisymmetric dispersion relation (3.11), for several values of β, Bq and Θ. In the case of the elasticity parameter, β, figure 3.6(*a*) shows that the leading-order 1D model fails at predicting the linear behavior of the liquid column as β increases, as was already pointed out by Timmermans & Lister (2002). In fact, according to this 1D approximation, the liquid column is stable for for every value of k if $\beta \geq 1$. The limit $\beta \longrightarrow \infty$ yields a trivial result, since the only value proportional to β is not balance by any term containing ω, or the curvature term $1 - k^2$. Similarly, with regard to Bq and Θ, figures 3.1(*b*,*c*) show that the leading-order 1D approximation also fails at predicting the growth rate $\omega(k)$, especially when $Bq \gg 1$ and $\Theta Bq \gg 1$.

In contrast, the parabolic model captures the linear regime with high accuracy for every value of β, Bq and Θ, as evidenced by the results of figure 3.7. The agreement between both $\omega(k)$ curves is slightly worse when $\beta \longrightarrow \infty$, whereas it improves when $(Bq, \Theta Bq) \gg 1$ independently of the value of β. In particular, we have checked that in the limit $Bq \longrightarrow \infty$, the dispersion relation (3.13) is identical, at leading order, to equation (3.14) deduced from the exact dispersion relation (3.11).

It is worth mentioning that Timmermans & Lister (2002) also derived a higher-order approximation usually known as the averaged-parabolic model, but only accounting for gradients of σ and not surface viscosities. These authors demonstrated that, for a very viscous thread, i.e. $La \longrightarrow 0$, the averaged-parabolic model shows a very good agreement with the full expression of the dispersion relation (3.11) for $Bq = \Theta Bq = 0$ and different values of β. Indeed, the accuracy of their averaged-parabolic model is slightly better than that of the parabolic model developed herein in the limit $(Bq, \Theta Bq) \longrightarrow 0$, when only surface elasticity is considered. Note that, in the case of a clean interface, a similar conclusion was obtained

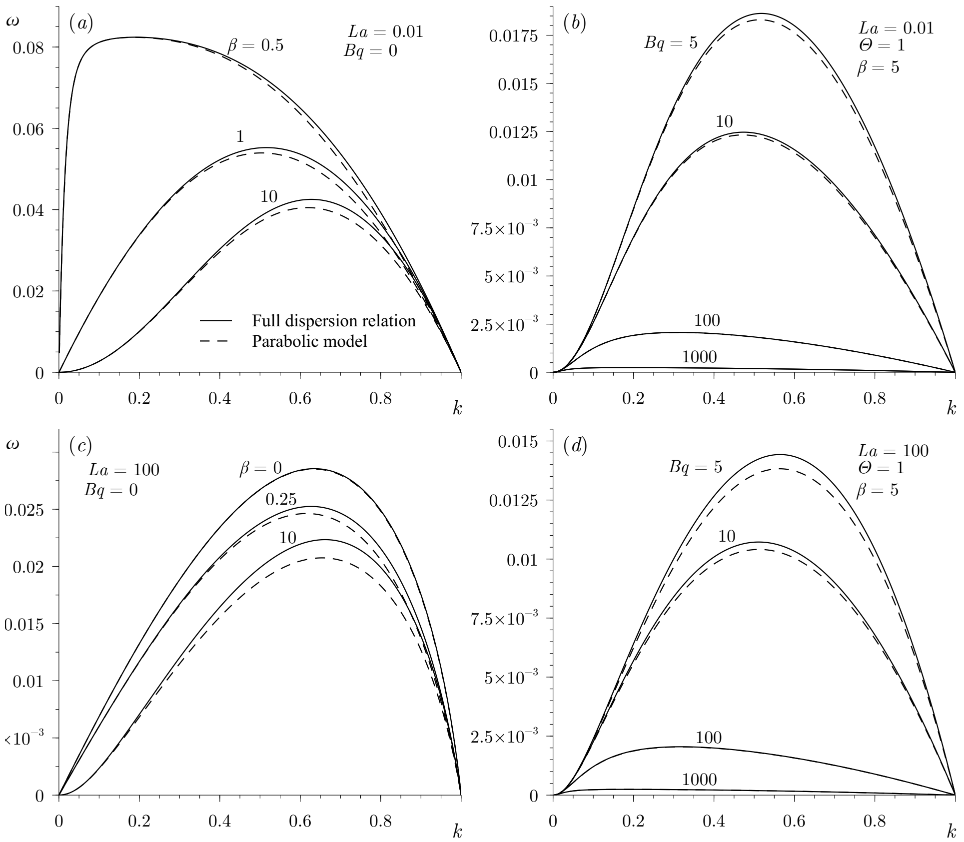

Figure 3.7: Comparison between the full axisymmetric dispersion relation (3.11) (solid lines) and the dispersion relation associated to the parabolic one-dimensional model (3.13) (dashed lines) for $La = 0.01$ in (*a–b*) and $La = 100$ in (*c–d*). The left column shows the amplification curves for $Bq_\mu = Bq_\kappa = 0$ and several values of β, and the right column for $\beta = 5$, $\mu_{s0}/\kappa_{s0} = 1$ and several values of Bq_μ indicated near each curve.

by García & Castellanos (1994), who found that the 1D averaged-parabolic model performs slightly better than the 1D parabolic model in predicting the linear amplification curve.

In summary, the leading-order 1D equations are suitable for small values of β, Bq and ΘBq, including the limit of a clean interface (García & Castellanos, 1994; Eggers & Dupont, 1994). However, when $(\beta, Bq, \Theta Bq) \gtrsim 1$, a higher-order approximation like the parabolic model derived herein, or the averaged-parabolic model due to Timmermans & Lister (2002), are needed to obtain good quantitative results in the linear regime.

3.4.2 Analysis of the maximum growth rate ω_m and its associated wavenumber k_m

To illustrate the parametric dependence of ω_m and k_m we have computed figures 3.8 and 3.9, where the maximum growth rate, ω_m (upper row), and the corresponding wavenumber, k_m (lower row), are plotted as functions of Bq for several values of β indicated in the legends, and three different values of the surface viscosity ratio, namely $\Theta = 10$, 1 and 0.1 in the left, middle and right columns, respectively. The value of $La = 0.01$ in figure 3.8, while $La = 100$ in figure 3.9. The insets show iso-contours of ω_m (upper rows) and of k_m (lower rows), in the (Bq, β) parameter plane. Firstly, as already mentioned, when $Bq \rightarrow \infty$, $\omega_m \rightarrow 0$ due to the dissipative nature of the surface viscosities, in contrast with the finite value of ω_m reached when $\beta \rightarrow \infty$ (Timmermans & Lister, 2002). It can also be observed in figures 3.8(*a*–*c*) and 3.8(*a*–*c*) that, for $\beta \lesssim 1$, ω_m decreases faster when $\Theta \gg 1$. Hence, when both surface viscosities increase and $\kappa_{s0} > \mu_{s0}$, the growth rate of perturbations is smaller, as already deduced from figures 3.4(*a*,*b*), and 3.5(*a*,*b*), and also by Whitaker (1976) in the limit $La \gg 1$.

With regard to k_m, and starting with the influence of β in the limit $Bq \rightarrow 0$, our results reveal that k_m first slightly decreases for $0 \leq \beta \lesssim 0.1$, and that an increase in β upon this limit, i.e. $\beta \gtrsim O(1)$, implies a sudden increase in k_m. As shown by figures 3.8(*d*–*f*) and 3.9(*d*–*f*), the former effect is more pronounced for $La \gg 1$, and the latter effect, which was already highlighted by Timmermans & Lister (2002), is more noticeable for $La \ll 1$.

Concerning the effect of surface viscosities on k_m, figures 3.8(*d*–*f*) for $La = 0.01$ show that, when $\beta \lesssim 0.3$ and Bq increases for a fixed value of Θ, there is a slight decrease of k_m. As Θ decreases, the latter phenomenon is more pronounced and occurs at higher values of Bq. When Bq increases past these limits, there is a sudden growth of k_m, which is more noticeable for smaller values of Θ, also taking place in a larger range of Bq. Hence, for these intervals of Bq surface viscosity provides an alternative mechanism for short-wavelength selection, which can also be seen in figures 3.4(*a*,*b*). Furthermore, when the maximum value of k_m is reached, an increase of Bq decreases k_m monotonically. On the contrary, when $La \gg 1$, this non-monotonic behavior only appears when $\beta \ll 1$ and $\Theta \ll 1$, i.e. when the flow is dominated by the shear viscosity, as depicted by figures 3.9(*d*–*f*). Indeed, for values of $\beta \gtrsim 1$, the dependence of k_m on Bq is monotonically decreasing, independently of La and Θ, as shown in figures 3.8(*d*–*f*) and 3.9(*d*–*f*).

Another interesting feature observed in figures 3.8(*d*–*f*) and 3.9(*d*–*f*) is that there is a certain value of Bq where ω_m and the corresponding k_m are independent of β, since all the curves intersect at this point. For $La = 0.01$ this value is approximately $Bq \sim 8.1$, and for $La = 100$, $Bq \sim 6.8$. Above these values, the dependence of k_m on β changes, since an increase of β reduces the value of k_m. Additionally, past these values of Bq and for $\Theta \gtrsim 1$, every ω_m curve collapses as Bq increases, indicating that ω_m becomes independent of β. On the contrary, for $\Theta \lesssim 1$ and $\beta \lesssim 1$, the maximum growth rate, ω_m, is higher than in the latter case for the same value of Bq, which can also be noticed in figures 3.4(*a*,*b*), and 3.5(*a*,*b*) for $Bq = 50$, with a more pronounced effect for $La \gg 1$.

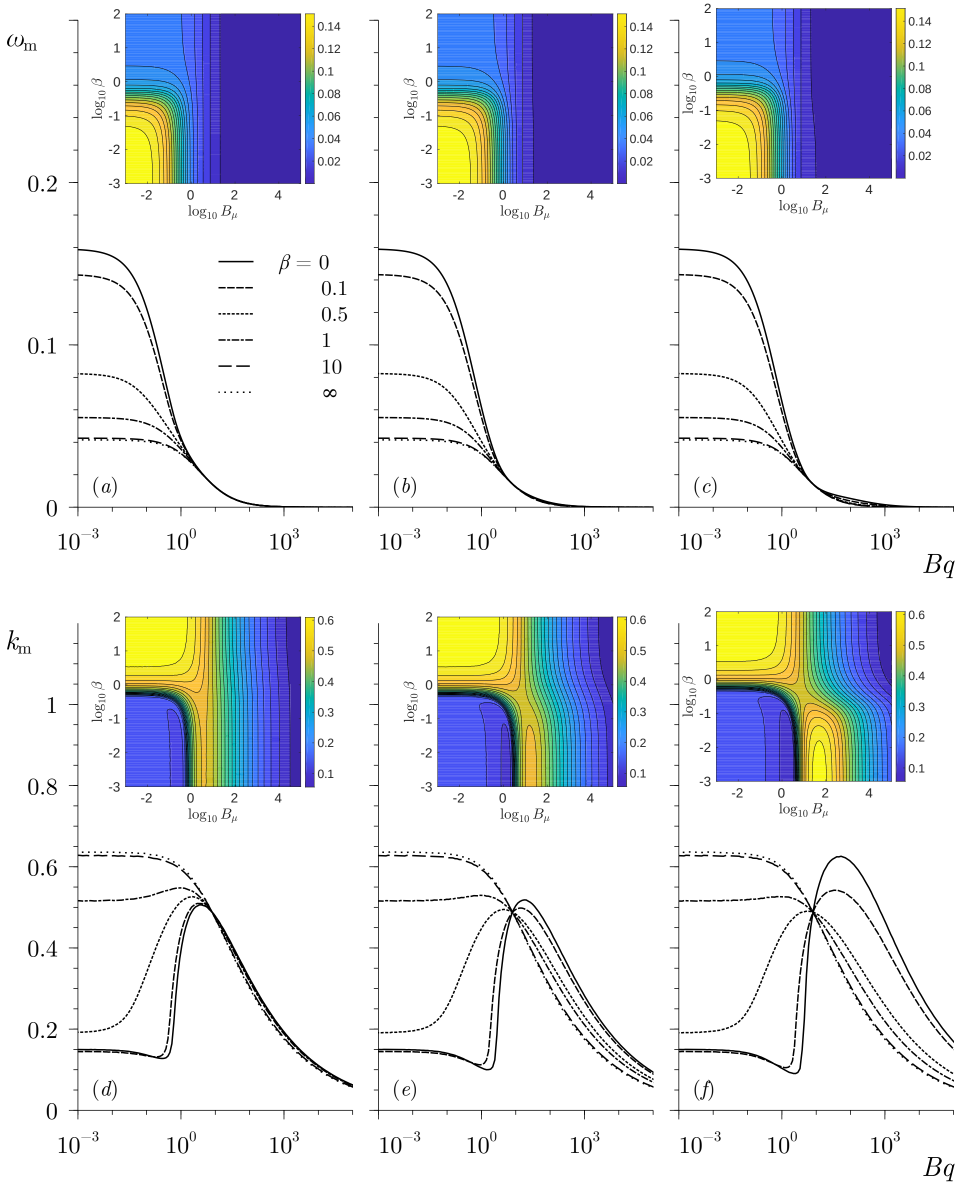

Figure 3.8: (Colour online) (a–c) Maximum growth rate, ω_m, and (d–f) corresponding wavenumber, k_m, as functions of Bq for La = 0.01 and several values of β indicated in the legend, for (a,d) Θ = 10 (b,e) Θ = 1 and (c,f) Θ = 0.1. The insets show the contours of constant ω_m (a–c) and of constant k_m (d–f) in the (Bq, β) parameter plane.

Finally, the values of the surface shear and dilational Boussinesq numbers may seem unrealistically overestimated in figures 3.8 and 3.9. However, if we take as an example a liquid thread of 400 μm radius, and an aqueous octanoic acid solution with a bulk concentration of

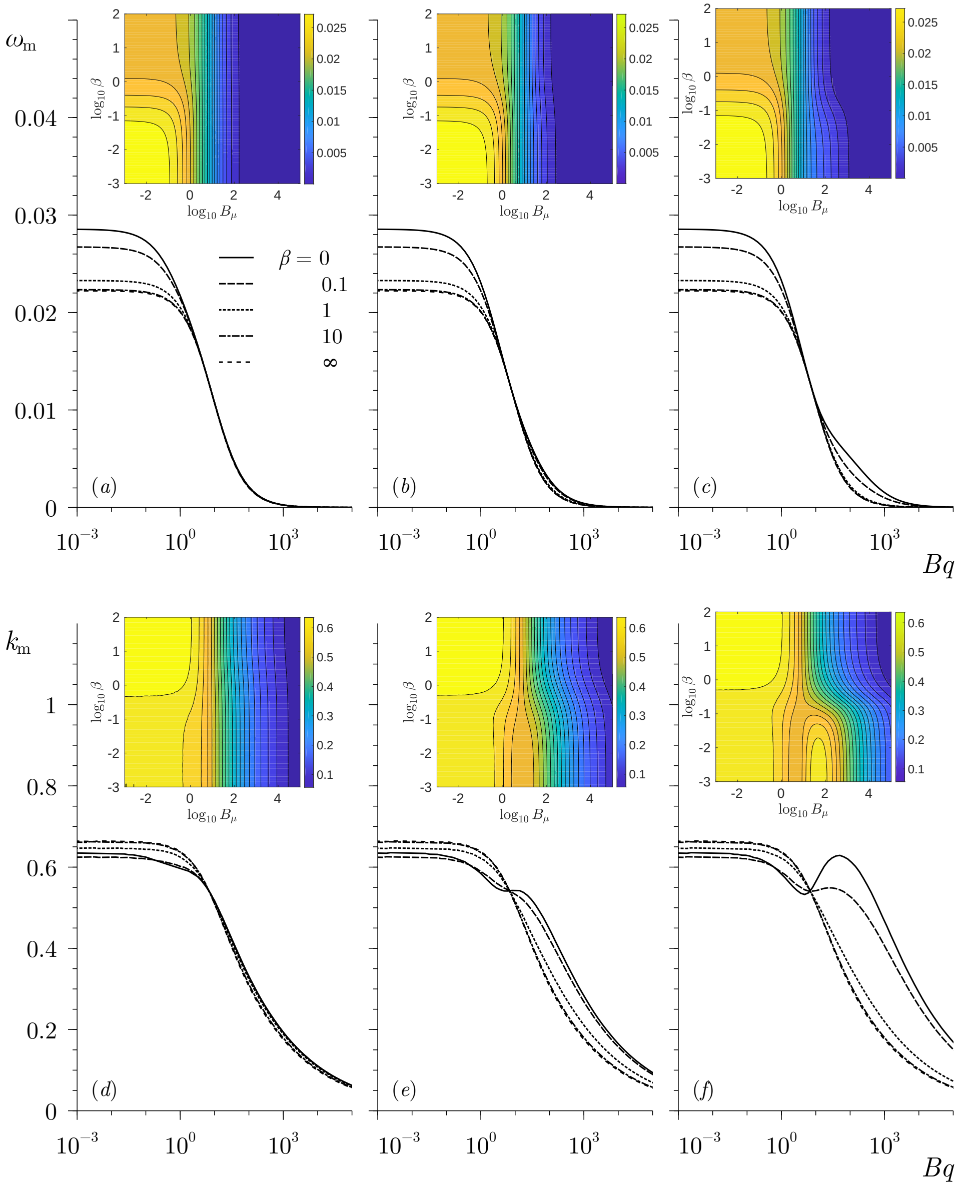

Figure 3.9: (Colour online) Same as figure 3.8 for *La* = 100.

9×10^{-5} mol/ml and the bulk properties of water at 25°C, the surface shear viscosity takes the value of $\mu_s = 4 \times 10^{-5}$ Pa s m, and the dilational viscosity $\kappa_s = 2.7 \times 10^{-4}$ Pa s m (Ting *et al.*, 1984), providing values of the Boussinesq numbers of Bq = 100 and ΘBq = 675, and thus a ratio Θ = 6.76. Since the liquid is water, $La \gg 1$ and thus this example would correspond approximately to figures 3.9(*a*,*d*), with a maximum growth rate of $\omega_m \sim 2 \times 10^{-3}$ and its corresponding wavenumber $k_m \sim 0.33$. Indeed, the surface shear Boussinesq number for this solution can be higher, for example if we consider a concentration of 4.5×10^{-5} mol/ml, $Bq = 150$, $\Theta Bq = 950$, and thus $\Theta = 6.33$, $\omega_m \sim 1.46 \times 10^{-3}$ and $k_m \sim 0.3$. Therefore, these two realistic examples show that the values of Bq and ΘBq may be large enough to produce a substantial decrease in ω_m.

3.4.3 The limit of an interface dominated by viscous stresses

As anticipated in chapter 1, a relevant limit is that of a material interface dominated by surface viscous forces, also referred to as very vicous interface in the present document. We will see now and in chapter 4 that, in this limit, the linear and nonlinear dynamics of the thread is completely dictated by the surface. Physically, this limit can be seen as a thin membrane whose response is purely viscous and which is subject to an isotropic tension σ. This scenario can occur in surfactant-laden interfaces if the molecules can confer a high surface viscous resistance, for instance the phospholipid dipalmitoylphosphatidylcholine (DPPC), which is a major constituent of pulmonary surfactant and lipid bilayer membranes. Indeed, surface viscous forces can also arise in vesicles, biological membranes, or active interfaces, where they coexist with the intrinsic elastic forces, and they may have a dominant role in their dynamics as detailed in Powers (2010), Narsimhan *et al.* (2015), Mietke *et al.* (2019*b*), Mietke *et al.* (2019*a*), and Farutin *et al.* (2019), and references therein, polymersomes being the prominent example. The nonlinear dynamics of cylindrical interfaces in this limit will be studied in detail in chapter 4.

We show in figures 3.3 and 3.4 that in the limit $Bq \longrightarrow \infty$, the temporal growth rate $\omega \longrightarrow 0$ for every value of k within the unstable range, $0 \leq k \leq 1$. This result indicates that the viscocapillary time, $\mu R/\sigma_0$, is not the characteristic time of the Plateau-Rayleigh instability when $Bq \gg 1$. Instead, the appropriate time scale in this limit is the surface viscocapillary time, μ_{s0}/σ_0. If the latter is used to define a new dimensionless growth rate, $\bar{\omega} = \omega Bq$, the dispersion relation (3.11) reduces, in the limit $Bq \gg 1$, to

$$\bar{\omega} = \left(1 + \Theta^{-1}\right) \frac{1 - k^2}{8} - \frac{\beta}{2\Theta} + \sqrt{\frac{\beta}{\Theta}\frac{1 - k^2}{4} + \left[\frac{\beta}{2\Theta} - \left(1 + \Theta^{-1}\right) \frac{1 - k^2}{8}\right]^2} + O(Bq^{-1}), \quad (3.14)$$

where only leading-order terms have been retained. Note that equation (3.14) depends on β and Θ, but it is independent of the Laplace number, La. Consequently, neither the inertia of the liquid nor the bulk viscous stress play any role in the limit $Bq \longrightarrow \infty$, since the flow is dominated by surface viscous stresses. This is markedly different from the limit of dominant surfactant elasticity, $\beta \gg 1$, where the the limiting form of the dispersion relation (3.8) depends on La.

It is also deduced from equation (3.14) that the amplification curve $\bar{\omega}(k)$ reaches its maximum at $k = 0$, similarly to what happens in the Stokes limit $La \longrightarrow 0$. This fact is illustrated in figure 3.10, which shows the amplification curves obtained from the exact dispersion relation provided in equation (3.11) with $La = 0.01$, and for several values of Bq and two different values of Θ and of β. The dashed lines with open circles represent equation (3.14). The insets show that the rescaled maximum growth rates, $\bar{\omega}_m$ (solid lines), tend to a finite value when $Bq \to \infty$, that can be easily computed as a function of β and Θ evaluating equation (3.14) at $k = 0$ (dashed lines).

3.4.4 The limit of a saturated interface

Another interesting limit is when high bulk surfactant concentrations are used, typically several times the critical micelle concentration (CMC), in which case the surface concentration is limited by maximum packing and is said to be *saturated*, $\Gamma = \Gamma_\infty$, and the corresponding values of the surface tension and surface viscosity coefficients reach corresponding asymptotes $\sigma^{\text{sat}} = \sigma(\Gamma_\infty, T)$, $\mu_s^{\text{sat}} = \mu_s(\Gamma_\infty, T)$ and $\kappa_s^{\text{sat}} = \kappa_s(\Gamma_\infty, T)$ (Edwards *et al.*, 1991; Quéré & de Ryck, 1998; Scheid *et al.*, 2010, 2012). In this saturated limit, the effect of the Marangoni stress $\boldsymbol{\nabla}_s \sigma$ becomes negligible (Quéré & de Ryck, 1998; Scheid *et al.*, 2010, 2012), thus a surfactant transport equation is not needed to close the mathematical model, and the only relevant surface stresses are the Young–Laplace pressure and the surface viscous stresses. The main conditions needed to achieve this limit are, first the existence of a region adjacent to the interface which needs to be highly populated with surfactant molecules, and that their corresponding adsorption time is much smaller than the characteristic hydrodynamic time. We will discuss in detail these conditions in chapter 4. As outlined in Powers (2010), a purely viscous interface can be found in biological membranes and vesicles, for instance in liposomes (Dimova *et al.*, 1999, 2000, 2006) or polymersomes (Dimova *et al.*, 2002). For example, diblock copolymer vesicles have associated surface viscosities which are up to 500 times higher than the typical values.

The dispersion relation of an axisymmetric thread whose interface is only subject to surface viscous forces and with a constant isotropic tensions, that is $\beta = 0$, reads

$$La\omega^2 F(k) - k^2(1-k^2) + \frac{k^4}{La}\left[4 + 6Bq + \frac{1-k^2}{\omega}Bq(1+\Theta) - 2\Theta Bq(1+2Bq)\right][F(k) - F(\tilde{k})] + \omega k^2 \left[2Bq(1-\Theta)F(k) + Bq(1+\Theta)(F(k)F(\tilde{k})+1) + 2(2F(k)-1)\right] = 0. \tag{3.15}$$

If we further take the limit of dominant surface viscous forces, $Bq \gg 1$, the above dispersion relation reduces to

$$\bar{\omega} = \frac{(1-k^2)(1+\Theta)}{4\Theta}, \tag{3.16}$$

where the factor $(1+\Theta)/(4\Theta)$ can be absorbed into the growth rate to yield a parameter-free amplification curve.

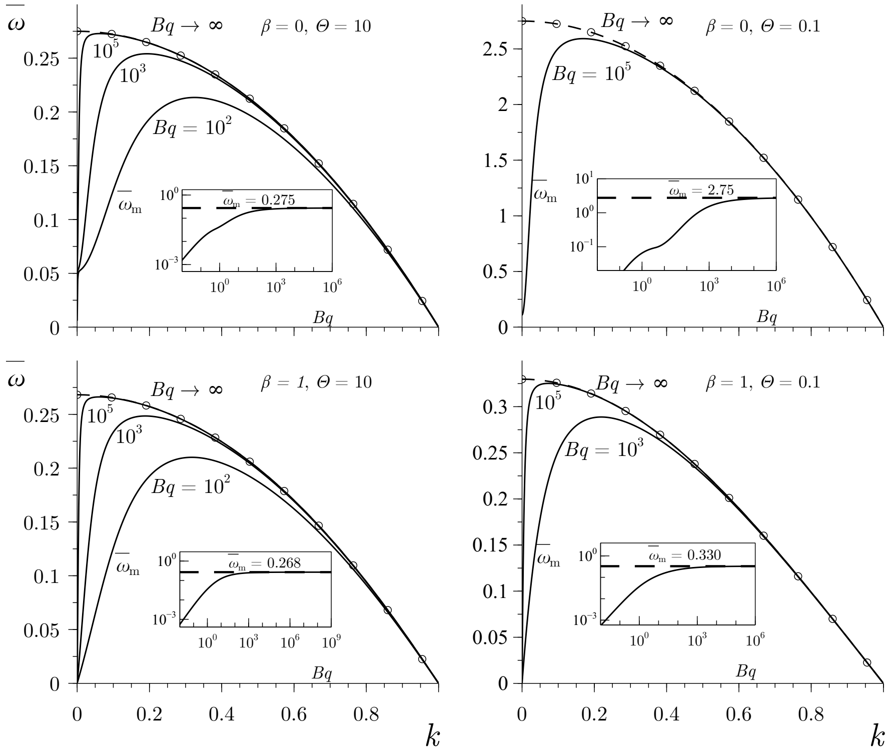

Figure 3.10: Rescaled growth rate $\bar{\omega} = \omega\, Bq$ as a function of k, computed with equation (3.11), for $\beta = 0$ (top row), $\beta = 1$ (bottom row), $\Theta = 10$ (left column) and $\Theta = 0.1$ (right column). The dashed line with open circles is the amplification curve given by equation (3.14) in the limit $Bq \gg 1$. The insets show the dependence of the rescaled maximum growth rate, $\bar{\omega}_m$, on Bq, while the dashed line is the horizontal asymptote predicted by equation (3.14) evaluated at $k = 0$.

3.5 Surface diffusion

The diffusion of surfactant molecules, macromolecules, or proteins may have an important effect on the dynamics of material cylinders, specifically when inertial effects are negligible, as discussed in section 1.4 of chapter 1. Here we investigate the effect of surface diffusion on the linear stability of liquid threads immersed in a passive ambient. Hence, we extend the results of section §3.3 first deduced by Timmermans & Lister (2002), following the same procedure as in the previous sections. As in section §3.3, it is convenient to express equation (1.18) in cylindrical coordinates, which for an axisymmetric interface reads

$$\frac{\partial \Gamma}{\partial t} + w\frac{\partial \Gamma}{\partial z} + \frac{\Gamma}{a\sqrt{1+a'^2}}\frac{\partial (a u_t)}{\partial z} + C\Gamma u_n = \frac{1}{Pe_s a\sqrt{1+a'^2}}\frac{\partial}{\partial z}\left(\frac{a}{\sqrt{1+a'^2}}\frac{\partial \Gamma}{\partial z}\right). \qquad (3.17)$$

The resulting dispersion relation that accounts for Marangoni stresses and surface diffusion reads

$$\begin{aligned}&La\,\omega^2 F(k) - k^2(1-k^2) + \frac{k^4}{La}\left[4 - \frac{\beta}{\Omega}\left(2 - \frac{1-k^2}{\omega}\right)\right][F(k) - F(\tilde{k})] + \\ &\omega k^2\left\{2[2F(k)-1] + \frac{\beta}{\Omega}[1 + F(k)(F(\tilde{k}) - 2)]\right\} = 0,\end{aligned} \tag{3.18}$$

where $\Omega = \omega + k^2 Pe_s^{-1}$. Note that the dispersion relation (3.18) is the same as the on deduced by Timmermans & Lister (2002) when $Pe_s \longrightarrow \infty$, and that of Martínez-Calvo & Sevilla (2018) in the limit of negligible surface viscous effects. Indeed, it is straightforward to obtain the above dispersion relation but also taking into account surface viscous forces, just by substituting $\beta \longrightarrow \beta/\Omega$ in the dispersion relation (3.11) of section §3.4.

Figure (a) shows that surface diffusion has a destabilizing effect in the linear regime, since ω increases as Pe_s decreases. This effect can be explained by the fact that surface diffusion tends to inhibit surface gradients of σ, which is the only stabilizing effect induced by the presence of surfactants in the linear regime. When Pe_s becomes sufficiently small, the dominant effect associated to the absorbed surfactant is the modified capillary pressure that acts in the normal direction to the interface, thus enhancing the Rayleigh–Plateau mechanism.

Figure 3.11 shows the maximum growth rate ω_m (a-c) and its associated most amplified wavenumber k_m (d-f) as functions of Pe_s and several values of β indicated in the legend, for $La = 0.01$ (a,d), $La = 1$ (b,e), and $La = 100$ (c,f). The insets display isocontours of ω_m and k_m in the (β, Pe_s) parameter plane. For $Pe_s \longrightarrow \infty$ we recover the results of Timmermans & Lister (2002). In this limit, ω reaches a finite value when $\beta \longrightarrow \infty$, and the stabilizing effect of the surface elasticity is stronger for viscous threads, i.e. $La \ll 1$, as discussed in §3.3. Furthermore, the effect of both, β and Pe_s, is weaker when inertia is dominant. Figures 3.11 (a-c) also show that ω_m increases monotonously when Pe_s decreases, reaching a plateau that is independent of β. Indeed, when $Pe_s \longrightarrow 0$ surface gradients of σ are completely inhibited and the whole amplification curve $\omega(k)$ becomes independent of β, recovering the result of a clean interface since σ is uniform in the whole thread. This fact can also be observed in figure (a), and was previously described by Hansen *et al.* (1999) for a liquid-liquid configuration. The value of Pe_s at which the plateau is reached strongly depends on β since both are always coupled in the dispersion relation (3.18). On the contrary, when $\beta \longrightarrow \infty$ the amplification curve and thus ω_m and k_m become independent of Pe_s, and we recover the result of Timmermans & Lister (2002) of a rigid interface.

We finally note that the analysis of the combined effect of Marangoni forces, surface viscous forces, and surface diffusion on the linear stability of a free liquid thread under is out of the scope of the thesis.

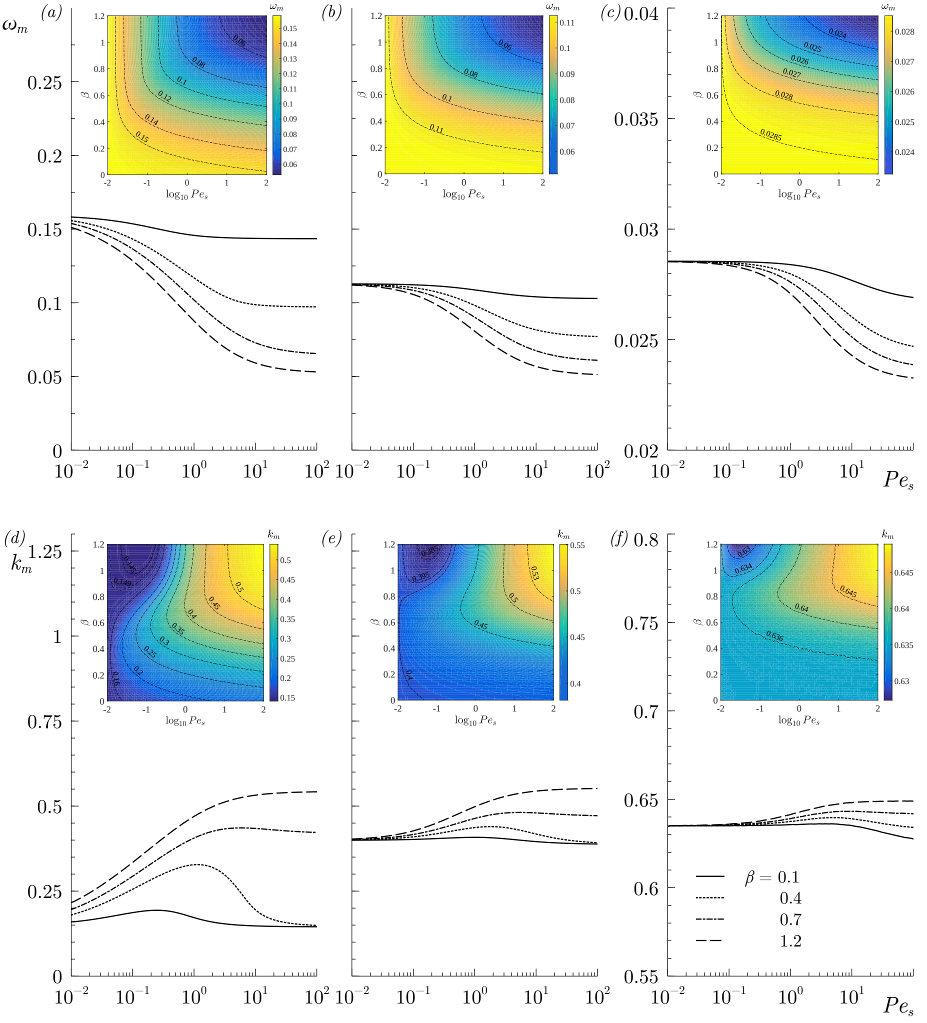

Figure 3.11: (Color online) (a)-(c) Maximum growth rate, ω_m, and (d)-(f) corresponding wavenumber, k_m, as functions of Pe_s and several values of β indicated in the legend, for (a,d) $La = 0.01$, (b,e) $La = 1$ and (c,f) $La = 100$. The insets show isocontours of ω_m (a–c) and k_m (d–f) in the (β, Pe_s) parameter plane.

3.6 Solid-like interface: Hookean and neo-Hookean interface

To close this chapter, in this section we study the linear stability of an axisymmetric solid-like interface separating two immiscible media. As in the previous sections, we consider that the filament is embedded in a passive ambient bath, thus $N_\mu \ll 1$, and following the same

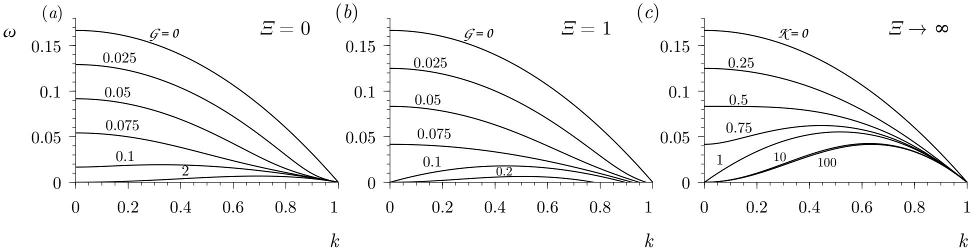

Figure 3.12: Amplification curves obtained from the dispersion relation (3.20) ($La \ll 1$) for (a) $\Xi = 0$, (b) $\Xi = 1$, and (c) $\Xi \to \infty$, and different values of $\mathcal{G}$ (or $\mathcal{K}$ when $\Xi \to \infty$) indicated in the labels.

procedure, we derive the corresponding dispersion relation. In particular, as we outlined in chapter 1, we will only consider the Hookean and neo-Hookean models, which in the linear regime yield the same dispersion relation,

$$La\,\omega^2 F(k) + \frac{k^4}{\omega La}\left[4\omega + 6\mathcal{G} + \frac{(1-k^2)\mathcal{G}(1+\Xi)}{\omega} - 2\mathcal{G}\Xi\left(1+\frac{2\mathcal{G}}{\omega}\right)\right][F(k) - F(\tilde{k})]+$$
$$k^2\left[2\mathcal{G}(1-\Xi)F(k) + \mathcal{G}(1+\Xi)(F(k)F(\tilde{k})+1) + 2\omega(2F(k)-1)\right] - k^2(1-k^2) = 0. \tag{3.19}$$

For simplicity, we only consider the limit of negligible inertia, $La \to 0$, for which equation (3.19) reduces to

$$2\omega[F(k)^2 - 1 - k^2] - (1-k^2) + \mathcal{G}[1 + 4F(k)(F(k)-1) + k^2(\Xi - 3) + \Xi] -$$
$$\frac{\mathcal{G}[k^2 - 1 + \Xi(4\mathcal{G} + k^2 - 1)][F(k)(F(k)-2) - k^2]}{2\omega} = 0. \tag{3.20}$$

As opposed to the other filaments with Marangoni and/or viscous interfacial forces, here the cut-off wavenumber k_c depends on the parameters governing the solid-like behavior of the interface,

$$k_c = \sqrt{1 - \frac{4\mathcal{G}\Xi}{1+\Xi}}. \tag{3.21}$$

Hence, there is a critical value of the elastic shear parameter, $\mathcal{G}$, or its dilatational counterpart, which we denote by $\mathcal{K} = \mathcal{G}\,\Xi$, above which the filament becomes stable. Nonetheless, equation (3.21) makes evident that both, shear and dilatational elastic parameters, must be different from zero for k_c to be different from $k_c = 1$. For instance, we can obtain the critical value of $\mathcal{G}$ which reads, $\mathcal{G}_c = (1+\Xi)/(4\Xi)$. In the limit of $\Xi \gg 1$, $\mathcal{G}_c = 1/4$, and in the opposite limit, that is when shear dominates, $\Xi \ll 1$, $\mathcal{K}_c = 1/4$.

Figure 3.12 shows the amplification curves obtained from the dispersion relation in the Stokes limit (3.20) for (a) $\Xi = 0$, (b) $\Xi = 1$, and (c) $\Xi \to \infty$, and different values of $\mathcal{G}$ (or $\mathcal{K}$ when $\Xi \to \infty$), indicated in the labels. Panel (b) shows that the cut-off wavenumber changes as dictated by equation (3.21), but remains $k_c = 1$ in the limits $\Xi = 0$ and $\Xi \to \infty$, shown in panels (a,c). In particular, the three panels show a strong stabilization due to the interfacial

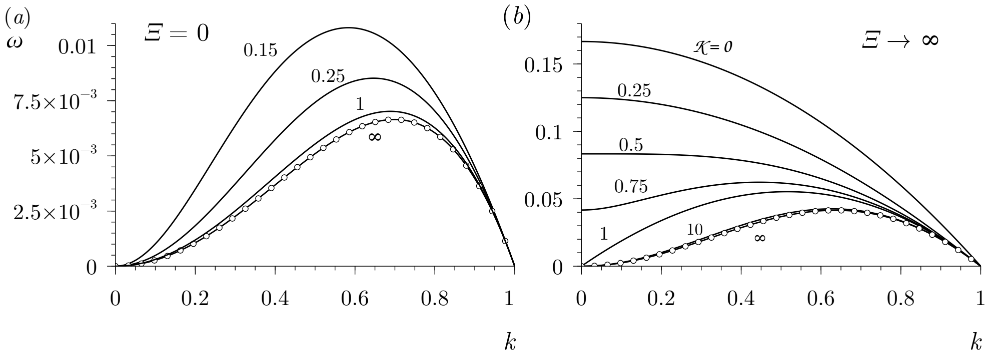

Figure 3.13: Amplification curves obtained from the dispersion relation (3.20) ($La \ll 1$) for (a) $\Xi = 0$, and (b) $\Xi \to \infty$, showing the limits of an interface purely dominated by shear elastic forces in (a), and dilatational elastic forces in (b).

elastic forces. Indeed, for $\Xi = 0$ and other finite values of Ξ, the growth rate is reduced approximately by 10 when $\mathcal{G} \simeq 0.1$. The limiting case of a purely dilatational interface, that is $\mathcal{G} = 0$ and finite $\mathcal{K}$, is less sensitive to changes in $\mathcal{K}$ as shown in panel (c). Indeed this limit coincides exactly with the Stokes dispersion relation (3.10) obtained in section §3.3, for liquid filament with Marangoni stresses acting at its interface.

The limiting form of (3.20) when interfacial elastic forces dominate only makes sense when $\Xi = 0$ or $\Xi \to \infty$, since for finite values of Ξ, $\mathcal{G} \gg 1$ or $\mathcal{K} \gg 1$ yield a stable configuration. In particular, in the limit of an interface dominated by shear elastic forces, $\mathcal{G} \gg 1$, equation (3.20) reduces to the following parameter-free expression,

$$\omega = \frac{(1-k^2)[F(k)(F(k)-2)-k^2]}{2[3k^2-1-4F(k)(F(k)-1)]}. \tag{3.22}$$

In the opposite limit where dilatational elastic forces dominate, $\mathcal{K} \gg 1$, the dispersion relation reads

$$\omega = \frac{(1-k^2)[k^2-F(k)(F(k)-2)]}{2(k^2+1)}, \tag{3.23}$$

which is exactly the same as equation (3.9) deduced in section §3.3, for an interface dominated by Marangoni stresses, $\beta \to \infty$.

References

CHANDRASEKHAR, S. 1961 *Hydrodynamic and Hydromagnetic Stability*. ed and Transl. E MacCurdy (New York: George Brazillier).

DIMOVA, R., ARANDA, S., BEZLYEPKINA, N., NIKOLOV, V., RISKE, K. A. & LIPOWSKY, R. 2006 A practical guide to giant vesicles. probing the membrane nanoregime via optical microscopy. *J. Phys.: Condens. Matter* **18** (28), S1151.

DIMOVA, R., DIETRICH, C., HADJIISKY, A., DANOV, K. & POULIGNY, B. 1999 Falling ball viscosimetry of giant vesicle membranes: finite-size effects. *Eur. Phys. J. B* **12** (4), 589–598.

DIMOVA, R., POULIGNY, B. & DIETRICH, C. 2000 Pretransitional effects in dimyristoylphosphatidylcholine vesicle membranes: optical dynamometry study. *Biophys. J.* **79** (1), 340–356.

DIMOVA, R., SEIFERT, U., POULIGNY, B., FÖRSTER, S. & DÖBEREINER, H.-G. 2002 Hyperviscous diblock copolymer vesicles. *Eur. Phys. J. E* **7** (3), 241–250.

DONNELLY, R. J. & GLABERSON, W. I. 1966 Experiments on the capillary instability of a liquid jet. *Proc. Roy. Soc.* **A290**, 547–566.

EDWARDS, D. A., BRENNER, H. & WASAN, D. T. 1991 *Interfacial transport processes and rheology*. Butterworth-Heinemann.

EGGERS, J. & DUPONT, T. F. 1994 Drop formation in a one-dimensional approximation of the Navier-Stokes equation. *J. Fluid Mech.* **262**, 205–222.

EGGERS, J. & VILLERMAUX, E. 2008 Physics of liquid jets. *Rep. Prog. Phys.* **71**, 036601.

FARUTIN, A., ÉTIENNE, J., MISBAH, C. & RECHO, P. 2019 Crawling in a fluid. *Phys. Rev. Lett.* **123** (11), 118101.

GARCÍA, F. J. & CASTELLANOS, A. 1994 One-dimensional models for slender axisymmetric viscous liquid jets. *Phys. Fluids* **6** (8), 2676–2689.

GOEDDE, E. F. & YUEN, M. C. 1970 Experiments on liquid jet instability. *J. Fluid Mech.* **40** (3), 495–511.

GONZÁLEZ, H. & GARCÍA, F. J. 2009 The measurement of growth rates in capillary jets. *J. Fluid Mech.* **619**, 179–212.

HANSEN, S., PETERS, G.W.M. & MEIJER, H.E.H. 1999 The effect of surfactant on the stability of a fluid filament embedded in a viscous fluid. *J. Fluid Mech.* **382**, 331–349.

LAPLACE, P. S. 1805 Mechanique celeste supplement au x libre .

MARTÍNEZ-CALVO, A. & SEVILLA, A. 2018 Temporal stability of free liquid threads with surface viscoelasticity. *J. Fluid Mech.* **846**, 877–901.

MIETKE, A., JEMSEENA, V., KUMAR, K. V., SBALZARINI, I. F. & JÜLICHER, F. 2019*a* Minimal model of cellular symmetry breaking. *Phys. Rev. Lett.* **123** (18), 188101.

MIETKE, A., JÜLICHER, F. & SBALZARINI, I. F. 2019*b* Self-organized shape dynamics of active surfaces. *Proc. Natl. Acad. Sci. U.S.A.* **116** (1), 29–34.

NARSIMHAN, V., SPANN, A. P. & SHAQFEH, E. S. G. 2015 Pearling, wrinkling, and buckling of vesicles in elongational flows. *J. Fluid Mech.* **777**, 1–26.

PEREIRA, A. & KALLIADASIS, S. 2008 On the transport equation for an interfacial quantity. *Eur. Phys. J. Appl. Phys.* **44** (2), 211–214.

PLATEAU, J. 1849 Statique expérimentale et théorique des liquides soumis aux seules forces moléculaires acad. *Sci. Bruxelles Mém* **23** (5).

POWERS, THOMAS R. 2010 Dynamics of filaments and membranes in a viscous fluid. *Rev. Mod. Phys.* **82**, 1607–1631.

QUÉRÉ, D. & DE RYCK, A. 1998 Le mouillage dynamique des fibres. , vol. 23, pp. 1–149. EDP Sciences.

RAYLEIGH, W. S. 1878 On the instability of jets. *Proc. R. Soc. Lond.* **10**, 4–13.

RAYLEIGH, W. S. 1892 On the instability of a cylinder of viscous liquid under capillary force. *Phil. Mag. and J. Science* **34** (207), 145–154.

SCHEID, B., DELACOTTE, J., DOLLET, B., RIO, E., RESTAGNO, F., VAN NIEROP, E. A., CANTAT, I., LANGEVIN, D. & STONE, H. A. 2010 The role of surface rheology on liquid film formation. *EPL* **90**, 24002.

SCHEID, B., DORBOLO, S., ARRIAGA, L. R. & RIO, E. 2012 Antibubble dynamics: the drainage of an air film with viscous interfaces. *Phys. Rev. Lett.* **109** (26), 264502.

STONE, H. A. & BRENNER, M. P. 1996 Note on the capillary thread instability for fluids of equal viscosities. *J. Fluid Mech.* **318**, 373–374.

TIMMERMANS, M.-L. & LISTER, J. R. 2002 The effect of surfactant on the stability of a liquid thread. *J. Fluid Mech.* **459**, 289–306.

TING, L., WASAN, D.T., MIYANO, K. & XU, S.Q. 1984 Longitudinal surface waves for the study of dynamic properties of surfactant systems. II. air-solution interface. *J. Colloid Interf. Sci.* **102** (1), 248–259.

TOMOTIKA, S. 1935 On the instability of a cylindrical thread of a viscous liquid surrounded by another viscous fluid. *Proc. Roy. Soc.* **150**, 322–337.

WHITAKER, S. 1976 Studies of the drop-weight method for surfactant solutions III. Drop stability, the effect of surfactants on the stability of a column of liquid. *J. Colloid Interf. Sci.* **54** (2), 231–248.

WONG, H., RUMSCHITZKI, D. & MALDARELLI, C. 1996 On the surfactant mass balance at a deforming fluid interface. *Phys. Fluids* **8** (11), 3203–3204.

YOUNG, T. 1805 An essay on the cohesion of fluids. *Phil. Trans. R. Soc. Lond.* **95**, 65–87.

CHAPTER 4

Nonlinear Dynamics and Breakup of Complex Liquid Filaments[†]

4.1 Introduction

The break-up of free-surface flows has been investigated for a long time. As outlined in the introductory chapter 1, the first quantitative studies on the instability responsible for the spontaneous break-up of cylindrical liquid threads date back to the 19th century. The correct physical description of the instability mechanism was due to Plateau (1873), who deduced that a small perturbation with a wavelength larger than the circumference of the unperturbed column is unstable, finally breaking up into main drops and smaller satellite droplets in between. A few years later, Rayleigh in Rayleigh (1878) and Rayleigh (1892) calculated the most unstable wavelength using a linear temporal stability analysis The subject experienced a renaissance fifty years ago that lasts to date due to its central role in industrial and medical applications such as chemical reactors, ink-jet and 3D printing, additive manufacturing, drug and protein encapsulation or cytometry, to cite a few (the reader is referred to the reviews of Bogy, 1979; Eggers, 1997; Christopher & Anna, 2007; Eggers & Villermaux, 2008; Derby, 2010; Anna, 2016).

The theoretical approach to study the dynamics of jet break-up was first based on the linear stability analysis of infinite liquid threads, which have been discussed in detail in the previous chapter. It is important to emphasize that, although linear stability theory cannot describe the final stages of the dynamics prior to pinch-off, it can be used to predict the break-up time $\bar{t}_b$ with small relative errors, provided that the initial amplitude of the disturbance, ε, accomplishes $\epsilon = \varepsilon/\bar{R} \ll 1$. In the spatial setting, this fact can be used to estimate the break-up length as $U\bar{t}_b$, in close agreement with the experiments (Kalaaji *et al.*, 2003; González & García, 2009).

However, to describe the subsequent nonlinear events, such as breakup and satellite formation process, which is the main objective of the present chapter, a nonlinear approach is needed. In particular, Goedde & Yuen (1970) first investigated such nonlinear effects in detail, comparing their experiments with the weakly nonlinear theory of Yuen (1968). The

---

[†] The present chapter includes the results obtained in Martínez-Calvo *et al.* (*J. Fluid Mech.*, vol. 883, 2020, A35), and in Martínez-Calvo & Sevilla (*Phys. Rev. Lett.*, vol. 125, 2020, 114502)

satellite drop formation process was first quantified by Rutland & Jameson (1970) and Lafrance (1975), while Chaudhary & Maxworthy (1980) studied how the satellite drop formation is affected by forcing the liquid jet with different harmonics, revealing the conditions needed to inhibit their formation. These efforts to control drop formation were mainly motivated by the practical need of increasing the performance of the inkjet printing devices under development at that time. The increase in computational power finally allowed a fully nonlinear approach by means of direct numerical simulations of the axisymmetric Navier-Stokes equations. In particular Mansour & Lundgren (1990) and Ashgriz & Mashayek (1995) computed the satellite droplet radii just prior to pinch-off, finding an excellent agreement with the experiments of Rutland & Jameson (1970) and Lafrance (1975).

Within the context of liquid threads, the effect of surfactants has been explored by means of theory (Whitaker, 1976; Timmermans & Lister, 2002; Martínez-Calvo & Sevilla, 2018) and numerical simulations (Campana & Saita, 2006; Dravid *et al.*, 2006; McGough & Basaran, 2006; Kamat *et al.*, 2018). In particular, the two latter works focused on the micro-thread cascade that appears close to break-up due to the presence of surfactants. These works also analyze the different scalings close to pinch-off and the evolution of the minimum radius of the thread and its axial position during the unfolding of the micro-cascade. Moreover, Kamat *et al.* (2018) revealed that the mechanism responsible for the dynamical surface tension effects induced by surfactants in filament break-up is the action of Marangoni stresses rather than surface tension lowering. In the case of a surfactant-free liquid thread, Ashgriz & Mashayek (1995) already reported the axial movement of the location of minimum radius for low-viscosity filaments, $La \gg 1$. More recently, Castrejón-Pita *et al.* (2015) generalized this result, showing that this translation occurs for any finite value of La, leading to the asymptotic inertial-viscous regime (Eggers, 1993). Furthermore, by means of experiments and high precision numerical simulations of the full axisymmetric Navier-Stokes equations, Castrejón-Pita *et al.* (2015) demonstrated that, depending on the value of La, the thinning of the filament experiences different transitions that delay the occurrence of the universal inertial-viscous regime.

The effect of surface viscous forces on the nonlinear dynamics of axisymmetric threads has been investigated to a lesser extent, mostly due to the computational complexity of integrating the Boussinesq–Scriven law defined in §1.7. In particular, the recent experimental and numerical work of Ponce-Torres *et al.* (2017) shows that surface viscosities dictates the amount of surfactant present at the satellite droplets after pinch-off.

In this chapter, by means of numerical simulations of the full conservation equations detailed in chapter 1, we unravel the nonlinear dynamics of filaments whose interface is endowed with surface rheology of different nature, namely Marangoni stresses, surface viscous forces, and intrinsic elastic forces. In particular, we will focus on the satellite droplet formation regimes in the natural breakup of the thread, that is when perturbations grow according to the most amplified wavenumber k_m, and the local structure of the flow close to rupture, where we will also investigate the existence of self-similarity.

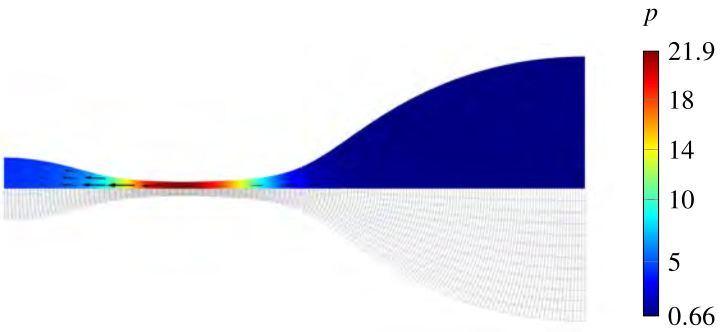

Figure 4.1: (Colour online) (*a*) Dimensional sketch of the flow configuration. (*b*) Example of a liquid thread approaching pinch-off for $La = 0.01$, $\beta = 1$, $\epsilon = 10^{-3}$ and $k = k_m = 0.516$ at time $t = 123$. The contour map represents the dimensionless pressure field p, and the arrows show the dimensionless velocity field $\boldsymbol{u}$, both at the top, while the deformed mesh is shown at the bottom.

4.2 Numerical technique

The numerical simulations reported herein are performed using an arbitrary Lagrangian-Eulerian (ALE) method, in which the domain $\boldsymbol{x}(\boldsymbol{X}, t) \in \mathcal{V}(t)$ is parametrized by the initial position $\boldsymbol{X} = \boldsymbol{x}(\boldsymbol{X}, 0) \in \mathcal{V}(0)$, defining a time-dependent displacement field, $\boldsymbol{x} - \boldsymbol{X}$ which is enforced to satisfy the Laplace equation with proper boundary conditions specified below. The local time derivatives are evaluated in the spatial reference frame as

$$\frac{\partial \boldsymbol{u}}{\partial t} = \frac{\partial \hat{\boldsymbol{u}}}{\partial t} - \frac{\partial \boldsymbol{x}}{\partial t} \cdot \boldsymbol{\nabla} \boldsymbol{u} \qquad \text{at } \mathcal{V}, \tag{4.1}$$

where $\hat{\boldsymbol{u}}(\boldsymbol{X}, t) = \boldsymbol{u}(\boldsymbol{x}, t)$ is the velocity in the material reference frame.

Moreover, here, $\boldsymbol{x}_s$, which represents any position at the surface $\boldsymbol{x}_s(\boldsymbol{X}_s, t) \in \partial\mathcal{V}(t)$, is parametrized by its initial position $\boldsymbol{X}_s = \boldsymbol{x}_s(\boldsymbol{X}_s, 0) \in \partial\mathcal{V}(0)$. The local time derivatives at the interface are evaluated in the spatial reference frame as

$$\frac{\partial \Gamma}{\partial t} = \frac{\partial \hat{\Gamma}}{\partial t} - \frac{\partial \boldsymbol{x}_s}{\partial t} \cdot \boldsymbol{\nabla}_s \Gamma \qquad \text{at } \partial\mathcal{V}, \tag{4.2}$$

where $\hat{\Gamma}(\boldsymbol{X}_s, t) = \Gamma(\boldsymbol{x}_s, t)$ is the concentration of surfactant in the material frame of reference, which is needed in order to be implemented with the ALE method that is used in the present chapter. The reader is referred to section §1.3 of the present document, and to the works of Stone (1990), Wong *et al.* (1996) and Pereira & Kalliadasis (2008) for further details on the time derivative of a surface quantity.

Moreover, in the following sections we use the nonlinear equation of state relating σ and Γ, as defined in chapter 3, section §3.3. Note that, in the limit of small surface concentration variations around the initial value, $\bar{\Gamma} = \Gamma_0 + \delta\bar{\Gamma}$, with $\delta\bar{\Gamma} \ll \Gamma_0$, one has $\Gamma = 1 + \delta\Gamma$ with

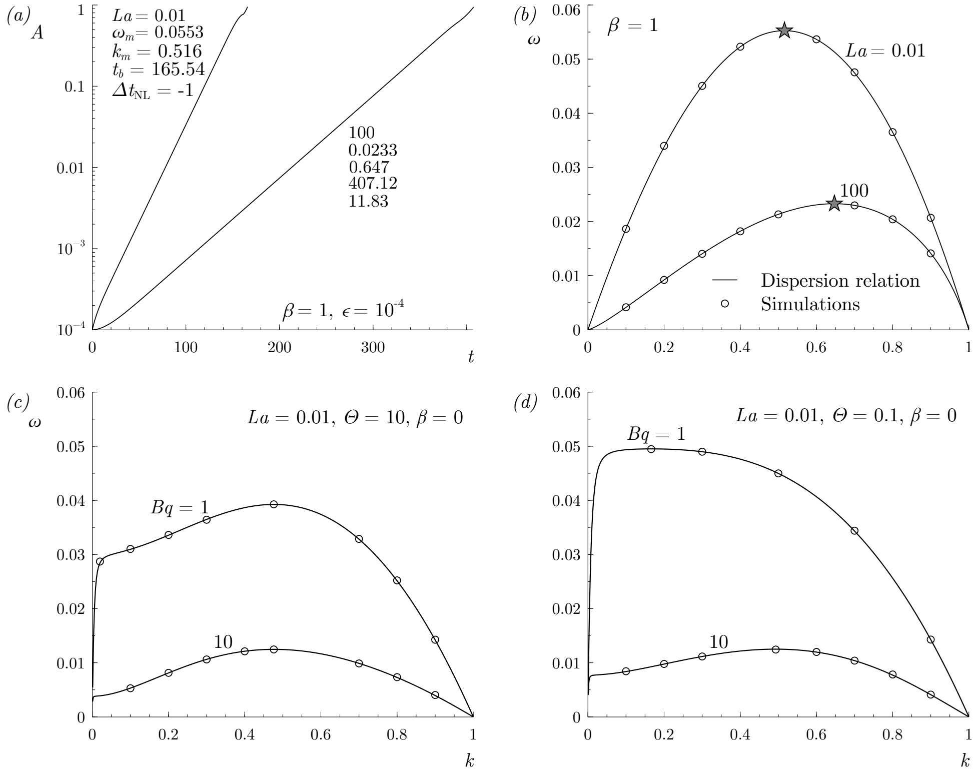

Figure 4.2: (Colour online) (*a*) Semi-logarithmic plot of the radius amplitude $A(t)$ as a function of time, extracted from two numerical simulations for $\epsilon = 10^{-4}$, $\beta = 1$ and two values of the Laplace number, namely $La = (0.01, 100)$. The corresponding optimal wavenumbers, $k_m(La, \beta)$, highlighted in (*b*) with stars, are used to build the initial conditions, and their values are indicated near each curve together with the associated linear temporal growth rates, $\omega_m(La, \beta)$ and La. (*b*) Temporal growth rate ω as a function of the axial wavenumber k, computed with the dispersion relation (3.7) (solid lines) and with the numerical simulations (circles), for $\beta = 1$ and two different values of $La = (0.01, 100)$, indicated near each curve. The maximum growth rates ω_m computed in (*a*) are marked with stars. Equivalent results are shown in (*c*,*d*), but taking into account surface viscous effects, where the value of Bq is indicated near each curve, $La = 0.01$, $\beta = 0$, and (*c*) $\Theta = 10$, and (*d*) $\Theta = 0.1$.

$\delta\Gamma \ll 1$, and the equation of state (1.37) can be linearized to yield $\sigma = 1 - \beta\delta\Gamma$, which is equivalent to the equation of state employed by Dravid *et al.* (2006). However, it is important to emphasize that the relative variations of Γ during the thread break-up process are not small, as demonstrated in §4.3. Therefore, the use of a linearized equation of state introduces considerable errors and it is not justified. At this point, the limitations of the nonlinear equation of state (1.37) should be clearly stated. Indeed, the main shortcoming of equation (1.37) is that $\sigma \longrightarrow \infty$ as $\Gamma \longrightarrow 0$, what eventually occurs as the surfactant is depleted from the pinch-off region due to the local advection out of the collapsing neck. Hence, a different equation of state is required to properly model the dynamics of the smallest scales close to breakup, that properly captures the saturation of σ to the clean interface value as $\Gamma \to 0$ (see McGough & Basaran, 2006; Kamat *et al.*, 2018, among others). Nevertheless, for the purposes of the following sections, the equation of state (1.37) is perfectly valid. In effect, at the smallest scales that need to be resolved to provide robust measures of the satellite droplet volume and mass of surfactant trapped at the droplet, the relative variations of Γ and σ are small enough as to guarantee the validity of equation (1.37) in all the results reported herein.

Concerning the computational domain and the corresponding boundary conditions, in the temporal approach adopted herein we only consider half a perturbation wavelength subjected to the following symmetry conditions,

$$w = 0, \quad \frac{\partial u}{\partial z} = 0, \quad \text{and} \quad \frac{\partial \Gamma}{\partial z} = 0 \qquad \text{at } z = 0, \pi/k. \tag{4.3}$$

where k is the dimensionless axial wavenumber, together with the axisymmetry condition,

$$\frac{\partial w}{\partial r} = 0, \quad \text{and} \quad u = 0 \qquad \text{at } r = 0. \tag{4.4}$$

Finally, regarding the initial conditions imposed at $t = 0$, we perturb the position of the liquid cylinder with a harmonic disturbance of amplitude ϵ,

$$\boldsymbol{x}_s = z\boldsymbol{e}_z + [R - \epsilon\cos(kz)]\boldsymbol{e}_r, \tag{4.5}$$

where $R = (1 - \epsilon^2/2)^{1/2}$ is a dimensionless radius defined in terms of ϵ, such that the liquid volume remains constant as ϵ varies (Ashgriz & Mashayek, 1995). We also assume that the liquid thread is initially at rest and that the surfactant concentration is uniform

$$\boldsymbol{u}(\boldsymbol{x}, 0) = \boldsymbol{0}, \quad \Gamma(\boldsymbol{x}_s, 0) = 1. \tag{4.6}$$

Note that the assumption of a uniform initial concentration of surfactant is a good approximation, since our main results have been obtained in the limit $\epsilon \ll 1$ in which the deviations from a uniform concentration can be neglected. As explained in chapter 3, our results can also be applied to describe the spatial instability and subsequent downstream break-up of liquid jets moving with uniform velocity U with respect to the injector reference frame, provided that $U \gg U_\sigma$, where U_σ is the speed of small-amplitude capillary waves. If the latter condition is satisfied, the spatial evolution of the jet is obtained by the downstream advection of the temporal results presented herein with a uniform velocity U. In particular, the jet break-up length is given by Ut_b in a first approximation.

To perform the numerical simulations, the liquid domain $0 \leq r \leq a(z, t), 0 \leq z \leq \pi/k$ is partitioned into a rectangular or triangular finite-element mesh which is dynamically deformed using the ALE method. In particular, the displacement field, $\boldsymbol{x} - \boldsymbol{X}$, is enforced to satisfy the Laplace equation, and the normal mesh velocity, $u_{n,\text{mesh}} = \boldsymbol{nn} \cdot \boldsymbol{u}$, solves the kinematic condition (1.6b). To that end, equations (1.4)–(1.6), and (1.9), together with the boundary and initial conditions (4.3)–(4.6), are written in weak form following the methodology described

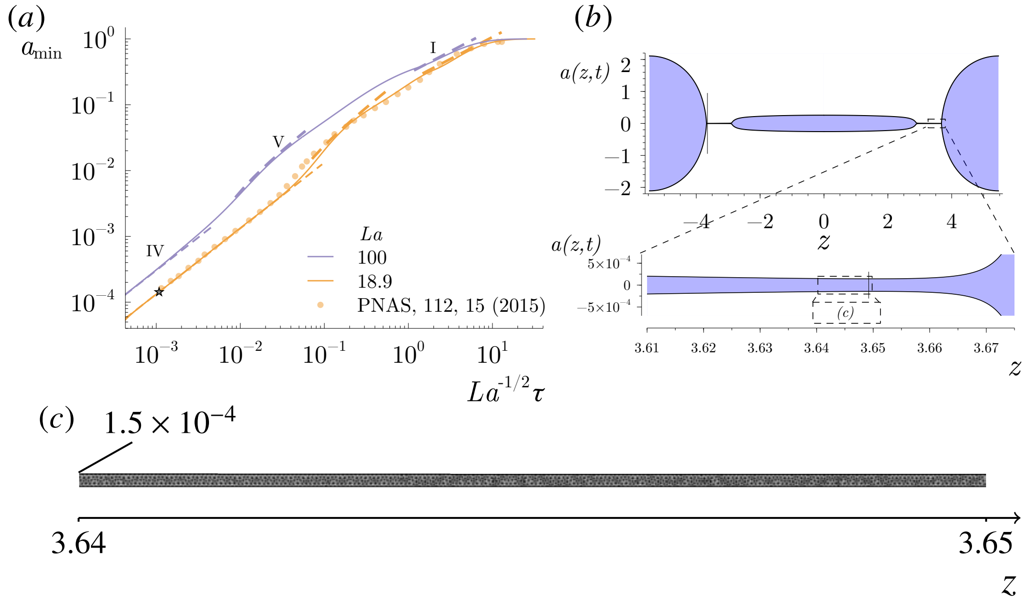

Figure 4.3: (a) Minimum thread radius $a_{\min}$ as a function of the time to break-up τ for two different values of the Laplace number, namely $La = 18.9$ and 100, and $\beta = 0$. The dashed lines indicate the scaling laws in the different regimes, and the symbols correspond to the results extracted from the numerical simulations of Castrejón-Pita *et al.* (2015). (b) Shape of the thread for the case $La = 18.9$ at $t = 138.017$, where $a_{\min} = 1.43 \times 10^{-4}$ and $z_{\min} = 3.65$, and which corresponds to the star symbol in (a) for $\tau = 1.08 \times 10^{-3}$. The zoomed region shows the micro-filament formed just prior to pinch-off. (c) Local mesh in the micro-filament region.

by Rivero-Rodríguez & Scheid (2018a,b), and the spatial discretisation is carried out using the finite-element method (FEM) provided by COMSOL, where Lagrange linear (P1) elements are used for p, and quadratic (P2) elements are used for $\boldsymbol{x}$, $\boldsymbol{u}$ and Γ. The time discretisation was performed using the first-order backward Euler method with adaptive time stepping. Figure 4.1(b) shows a representative deformed mesh for a simulation with $La = 0.01$, $\beta = 1$, $\epsilon = 10^{-3}$ and $k = k_m = 0.516$ at the time $t = 123$, together with the pressure field as a contour plot and the velocity field represented by arrows. All the results reported were carefully checked to be mesh-independent, with an integration tolerance of the order of 10^{-6}–10^{-7}. In addition, it was checked that the relative variations of liquid volume and surfactant mass where smaller than 10^{-5} during each simulation. The numerical code has been validated with the linear theory in figure 4.2, and in the nonlinear regime by comparing our results with those of Ashgriz & Mashayek (1995) and Castrejón-Pita *et al.* (2015) for a clean interface (see figure 4.3), and with those of McGough & Basaran (2006) and Kamat *et al.* (2018) for a surfactant-laden thread (not shown). In particular, this section is also devoted to show the performance of our numerical framework close to pinch-off, comparing our results with the different theoretical scalings of the minimum radius as a function of time to break-up.

As shown experimentally by Goedde & Yuen (1970), and numerically by Mansour &

Lundgren (1990) and Ashgriz & Mashayek (1995), a convenient way to compute the temporal growth rate of small disturbances is through the radius amplitude, extracted from the present simulations as $A(t) = (\max_z[a(z,t)] - \min_z[a(z,t)])/2$. Figure 4.2($a$) shows the temporal evolution of $A(t)$ in semi-logarithmic scale, extracted from two numerical simulations for an initial perturbation amplitude $\epsilon = 10^{-4}$, an elasticity parameter $\beta = 1$, and two values of the Laplace number, $La = 0.01$ and $La = 100$, close to the Stokes and Euler regimes, respectively. In each case, the most amplified wavenumber, $k_m(La, \beta)$, is used to build the initial condition. As expected due to the smallness of ϵ, figure 4.2(a) shows that during most of the time the amplitude grows exponentially, i.e. $A \propto \exp(\omega_m t)$, and thus the maximum temporal growth rate, $\omega_m(La, \beta)$, can be easily computed as the slope of the linear region in the semi-logarithmic plot, $\omega_m = \mathrm{d}\ln(A)/\mathrm{d}t$. It can also be deduced from figure 4.2(a) that there is an initial transient during which the growth of $A(t)$ is not exponential, what can be explained by the fact that the initial conditions in the numerical simulations are imposed on the shape of the interface, but disregard the associated disturbances in the velocity, pressure and surfactant concentration fields. As shown in figure 4.2(b), this procedure was used to obtain ω for different values of k (symbols), and the results are compared with the amplification curves $\omega(k)$ computed from the dispersion relation (3.7) (solid lines), obtaining an excellent agreement that validates the numerical code in the linear regime.

To demonstrate the performance of our numerical technique close to rupture, we also report numerical simulations comparing our results with the well-known scaling laws of $a_{\min}$ as a function of the time to break-up, $\tau = t_b - t$, for two different values of the Laplace number, namely $La = 18.9$ and 100, in the case of a clean interface, $\beta = 0$. Figure 4.3 shows $a_{\min}$ as a function of τ, where the dashed lines represent the different scaling laws, and symbols have been extracted from the results of Castrejón-Pita *et al.* (2015) for the particular case of $La = 18.9$. Since La is moderately high in both cases, intertial and capillary forces balance initially, providing $a_{\min} \sim \tau^{2/3}$ (Keller & Miksis, 1983; Day *et al.*, 1998; Eggers & Fontelos, 2015), a regime usually referred to as the inertial (I) regime. However, as the thread thins, viscous forces come into play, as shown numerically and experimentally by Castrejón-Pita *et al.* (2015), leading to the linear behavior $a_{\min} = 0.0709\tau$ (Papageorgiou, 1995), which is known as the viscous (V) regime. Finally, when $a_{\min}$ is sufficiently small, inertial, capillary and viscous forces balance, leading to what is usually known as the inertial-viscous (IV) regime, in which $a_{\min} = 0.0304\tau$ (Eggers, 1993). As revealed by figure 4.3(a), our numerical method is in excellent agreement with these scaling laws close to pinch-off, and with the numerical computations of Castrejón-Pita *et al.* (2015), thereby validating our numerical framework. Finally, although not shown here for conciseness, we have checked that the unphysical singularity of the equation of state (1.37) as $\Gamma \to 0$ leads to a spurious deviation from the asymptotic IV regime, which precludes its use to correctly predict the smallest scales prior to pinch-off for $\beta \neq 0$. To that end, a different equation of state that provides the clean-interface constant value of σ as $\Gamma \to 0$ must be used (McGough & Basaran, 2006; Kamat *et al.*, 2018).

4.3 Marangoni Effects

In contrast with the studies of McGough & Basaran (2006), Castrejón-Pita *et al.* (2015), and Kamat *et al.* (2018), which focused on a detailed description of the transitions between the different scaling laws prior to pinch-off, the present section aims at providing a global parametric description of the satellite formation process when the interface is coated with an insoluble surfactant monolayer.

Therefore, following the same strategy as Mansour & Lundgren (1990) and Ashgriz & Mashayek (1995) for a clean interface, and Dravid *et al.* (2006) and McGough & Basaran (2006) for a surfactant-laden interface, in the present contribution our approach is to numerically integrate the Navier-Stokes equations in a temporal setting, thereby avoiding the approximations involved in one-dimensional models. Unlike Dravid *et al.* (2006), we use a nonlinear equation of state to relate the surface tension with the surfactant concentration, derived from first principles, that leads to substantial differences calling out for a careful experimental analysis. Moreover, we perform an exhaustive parametric study, accurately quantifying the volume of the satellite droplet prior to pinch-off and the amount of surfactant trapped at its surface, as a function of the two dimensionless governing parameters, namely the elasticity parameter and the Laplace number.

The problem depends on four dimensionless parameters, namely the Laplace number, La, the elasticity parameter, β, the axial wavenumber, k, and the amplitude of the initial perturbation, ϵ. However, in the present document we are concerned with the unforced breakup of cylindrical threads due to small radius disturbances. Therefore, all the results were obtained by setting $k = k_m$, where $k_m(La, \beta)$ is the most unstable wavenumber (see chapter 3). Moreover, it will be shown that, in the small-disturbance limit, $\epsilon \ll 1$, the only result that depends on ϵ is the break-up time of the thread, $t_b(La, \beta, \epsilon)$. However, our results have revealed that the functional dependence of t_b can be split into a contribution predicted by linear theory in explicit form, $t_{b,L}(La, \beta, \epsilon)$, plus a nonlinear correction, $\Delta t_{\mathrm{NL}}(La, \beta)$, which does not depend on ϵ. Consequently, only two independent dimensionless parameters appear in our formulation, namely La and β.

Since we are interested in the spontaneous break-up of the surfactant-laden thread, all the results were computed from an initial condition where the liquid cylinder is perturbed with the wavenumber of maximum amplification, $k_m(La, \beta)$, obtained as indicated in chapter 3. Note that k_m is needed to define the initial geometry and the initial condition (4.5), while ω_m is used to compute the nonlinear correction to the linear break-up time, which is defined in §§4.3.1. Subsections §§4.3.1 and 4.3.2 are devoted to analyse the nonlinear break-up and the satellite formation dynamics, separating the weak-elasticity limit, and the surfactant-laden case. To that end, we have performed direct numerical simulations of the equations defined in chapter 1 and section §4.2 of the present chapter, until times very close to pinch-off. In particular, we report a parametric study for different values of La and β, computing the volume of the satellite droplet, the mass of surfactant trapped at its interface, the satellite shape at pinch-off, and the break-up time.

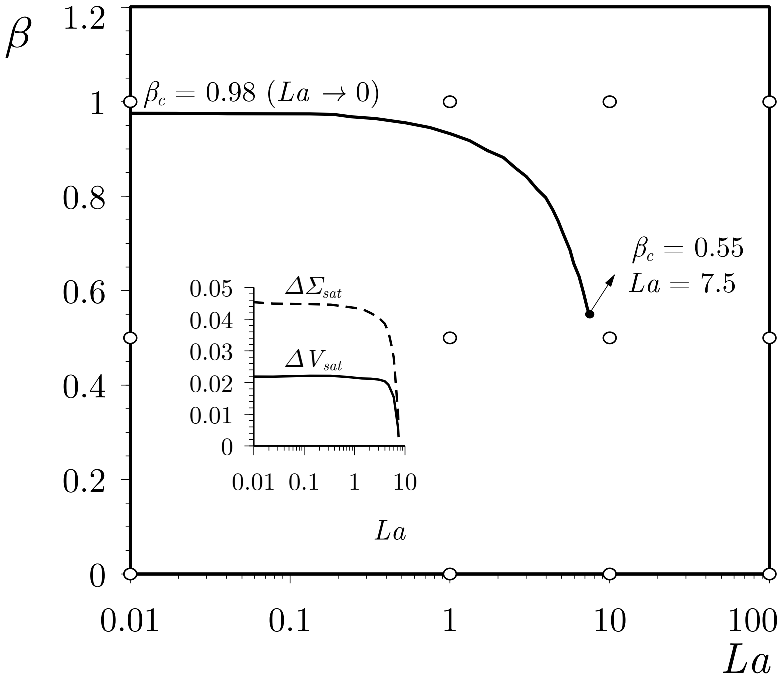

Figure 4.4: The structure of the (La, β) parameter plane. An abrupt transition takes place along the solid line, $\beta = \beta_c(La)$, across which both the satellite volume and the entrapped mass of surfactant experience a discontinuous jump, such that both magnitudes are larger above the solid line. The inset shows the jumps in the satellite volume, $\Delta V_{\mathrm{sat}}(La) = V_{\mathrm{sat}}(\beta - \beta_c \to 0^+) - V_{\mathrm{sat}}(\beta - \beta_c \to 0^-)$, and in the associated entrapped mass of surfactant, $\Delta\Sigma_{\mathrm{sat}}$. Both jumps, together with β_c, increase monotonically as La decreases, and reach respective Stokes asymptotes as $La \to 0$, namely $\Delta V_{\mathrm{sat}} \to 0.022$, $\Delta\Sigma_{\mathrm{sat}} \to 0.045$, and $\beta_c \to 0.98$. The filled circle indicates the origin of the discontinuous transition, $(La, \beta_c) = (7.5, 0.55)$, at which both jumps become zero. For $La > 7.5$, the satellite volume is a continuous function of β. The open circles correspond to the values of La and β of the shapes just before pinch-off shown in figure 4.4.

At this point, it has to be pointed out that a similar phenomenology had been previously reported by Dravid *et al.* (2006) for $La = 0.01$ and 100, although using the linearized equation of state $\sigma(\Gamma) = 1 - \beta(\Gamma - 1)$. In addition, these authors did not consider the natural break-up of the thread, since the disturbance wavenumber k was restricted to fixed values different from the most amplified one, k_m.

4.3.1 Satellite formation regimes and transitions in the (La, β) parameter plane

Let us first present the structure of the (La, β) parameter plane in terms of the satellite formation process. To that end, we conducted an exhaustive parametric study in which the Laplace and elasticity parameters were varied in small steps within wide ranges, namely

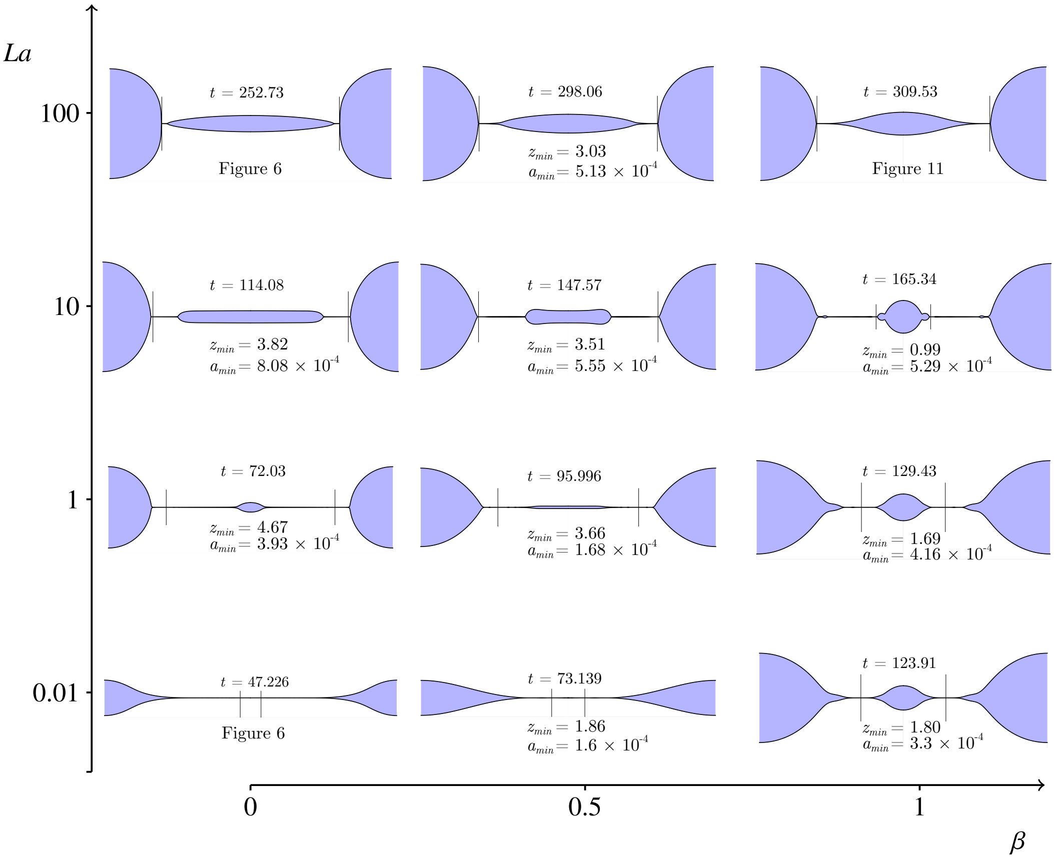

Figure 4.5: The satellite shapes just prior to pinch-off in the (La, β) parameter plane (see open circles in figure 4.4). The vertical lines indicate the axial positions, $z_{\min}$, of the minimum thread radii, $a_{\min}$.

$0.01 \leq La \leq 100$ and $0 \leq \beta \leq 1$. Thus, for each pair of values of La and β, we simulated the instability-driven time evolution of the thread from an initial condition with $\epsilon \ll 1$ until a time t_b very close to break-up. In total, around 10^4 time-dependent simulations were carried out to characterize the (La, β) parameter plane shown in figures 4.4 and 4.6.

At this point, it is important to emphasize that the fate of the main and satellite drops after pinch-off is outside the scope of the present work, and therefore we do not explore the possible successive break-up events that may take place and lead to the formation of sub-satellites. Keeping this in mind, we have extracted the satellite volume at the last numerical step, $t = t_b$. Normalizing its value with the total volume provides the definition

$$V_{\text{sat}} = \frac{\int_0^{z_{\min}} a^2 \mathrm{d}z}{\int_0^{\pi/k_m} a^2 \mathrm{d}z}, \tag{4.7}$$

where $z_{\min}$ is the axial position where the liquid column reaches its minimum radius, $a_{\min}$, at

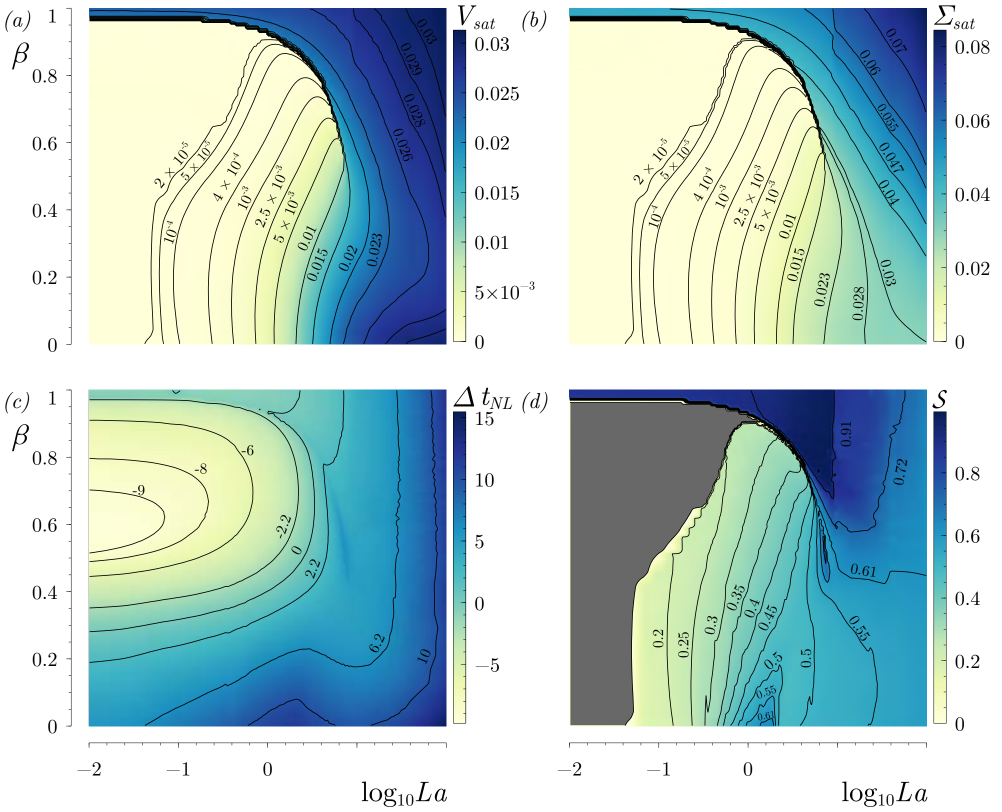

Figure 4.6: Isocontours in the (La, β) parameter plane of (a) the normalized satellite volume V_{sat}, (b) the normalized mass of surfactant trapped at its interface Σ_{sat}, (c) the nonlinear correction to the break-up time, Δt_{NL}, and (d) the sphericity of the satellite droplet, $\mathcal{S}$.

$t = t_b$. A more common measure of the satellite size is its equivalent radius, R_{sat}, which is the radius of a spherical drop of the same volume as the satellite (Rutland & Jameson, 1971; Mansour & Lundgren, 1990; Ashgriz & Mashayek, 1995; Mashayek & Ashgriz, 1995). All the results reported herein in terms of V_{sat} can be easily converted to R_{sat} through the equation $R_{\text{sat}} = [3\pi V_{\text{sat}}/(2k_m)]^{1/3}$. Following the same procedure, we have also computed the mass of surfactant trapped at the satellite surface which, normalized with the total mass of surfactant, provides the definition

$$\Sigma_{\text{sat}} = \frac{\int_0^{z_{\min}} a\Gamma\sqrt{1+\left(\frac{\partial a}{\partial z}\right)^2}\,\mathrm{d}z}{\int_0^{\pi/k_m} a\Gamma\sqrt{1+\left(\frac{\partial a}{\partial z}\right)^2}\,\mathrm{d}z}. \tag{4.8}$$

We would like to point out that, since V_{sat} and Σ_{sat} are always obtained when $a_{\min}$ is within the range $a_{\min} \sim 10^{-4} - 8\times10^{-3}$, the sensitivity of these magnitudes to the exact value of

$a_{\min}$ is negligible, such that both represent very robust measures. Similarly, the corresponding break-up time t_b is barely sensitive to the value of $a_{\min}$.

In contrast with V_{sat} and Σ_{sat}, which do not depend on the initial amplitude in the limit $\epsilon \ll 1$, the break-up time is a function of the form $t_b(La, \beta, \epsilon)$ such that $t_b \to \infty$ as $\epsilon \to 0$. Indeed, the break-up time can be easily estimated from linear theory through the equation $a_{\min}(t) \sim 1 - \epsilon \exp(\omega_m t)$, where ω_m is the growth rate associated with the most amplified wavenumber k_m, leading to the estimation $t_b \sim \ln(\epsilon^{-1})/\omega_m$. Based on the latter result, we define the nonlinear correction to the linear break-up time as

$$\Delta t_{\mathrm{NL}} = t_b - \frac{\ln(\epsilon^{-1})}{\omega_m}, \tag{4.9}$$

where t_b is obtained by extrapolating $a_{\min}$ to zero using the last few computed time steps. Unlike t_b, Δt_{NL} only depends on La and β, but not on ϵ, provided only that $\epsilon \ll 1$. The latter fact is demonstrated in §§4.3.2. Finally, we have also computed the sphericity of the satellite droplet at pinch-off as

$$\mathcal{S} = \frac{2\left(\frac{3}{4}\int_0^{z_{\min}} a^2 \mathrm{d}z\right)^{2/3}}{\int_0^{z_{\min}} a\sqrt{1 + \left(\frac{\partial a}{\partial z}\right)^2}\,\mathrm{d}z}, \tag{4.10}$$

which is the ratio between the surface of a sphere of the same volume as the satellite and its actual surface. The quantification of the satellite formation process will be based on the four functions V_{sat}, Σ_{sat}, Δt_{NL} and $\mathcal{S}$, extracted from the numerical simulations. These four functions only depend on La and β when ϵ is sufficiently small, as will be demonstrated in §§4.3.2. Thus, the main results reported herein have been computed in the limit $\epsilon \to 0$.

The structure of the (La,β) parameter plane is summarized in figures 4.4 and 4.5 in terms of the satellite formation process. In particular, figure 4.4 depicts the most salient features of the parameter plane, and figure 4.5 displays several satellite shapes at the last computed numerical step just prior to pinch-off, whose associated values of La and β are indicated with circles in figure 4.4. The most important feature of the parameter plane is the solid line shown in figure 4.4, which represents a discontinuous transition that takes place for a critical elasticity, $\beta = \beta_c(La)$ for $La < 7.5$. In particular, both the satellite volume and the associated entrapped mass of surfactant experience sudden jumps from certain values $V_{\mathrm{sat}}(\beta - \beta_c \to 0^-)$ and $\Sigma_{\mathrm{sat}}(\beta - \beta_c \to 0^-)$, to larger values $V_{\mathrm{sat}}(\beta - \beta_c \to 0^+)$ and $\Sigma_{\mathrm{sat}}(\beta - \beta_c \to 0^+)$. Indeed, the inset of figure 4.4 shows the jumps experienced by the satellite volume, $\Delta V_{\mathrm{sat}}(La) = V_{\mathrm{sat}}(\beta - \beta_c \to 0^+) - V_{\mathrm{sat}}(\beta - \beta_c \to 0^-)$, and by the associated entrapped mass of surfactant, $\Delta\Sigma_{\mathrm{sat}}$. Both jumps and β_c increase monotonically as La decreases, and reach respective Stokes asymptotes as $La \to 0$, namely $\Delta V_{\mathrm{sat}} \to 0.022$, $\Delta\Sigma_{\mathrm{sat}} \to 0.045$, and $\beta_c \to 0.98$. The filled circle in figure 4.4 indicates the origin of the discontinuous transition, $(La, \beta_c) = (7.5, 0.55)$, at which both jumps become zero. For values of $La > 7.5$, V_{sat} and Σ_{sat} are continuous functions of La and β.

As shown in figure 4.5, for values of $\beta = 0 < \beta_c$ and $\beta = 0.5 < \beta_c$ the sequence of interface shapes at pinch-off depend continuouly on La, with the trend that bigger satellites are formed as La increases, reaching the regular limit of inviscid flow as $La \to \infty$. For $\beta < \beta_c$ and small values of La, figure 4.5 reveals that the main drops are separated by very thin threads of tiny volume whose break-up behavior has been characterized in previous studies (see e.g. Kowalewski, 1996). For $\beta < \beta_c$ and intermediate values of La, the main drops are separated by a satellite centered at $z = 0$ that is connected with the main drops by very thin threads (see e.g. the case for $La = 1$ and $\beta = 0$ in figure 4.5). Finally, for $\beta < \beta_c$ and large values of La, the satellite drop is directly connected to the main drops. In contrast, when $\beta = 1 > \beta_c$, figure 4.5 shows a different picture, where large satellites are formed for all values of La. These results have also been analysed quantitatively, and will be discussed in detail below.

From figures 4.4 and 4.5 it is deduced that, although the physical mechanisms are different, both the liquid inertia and the interfacial elastic stress favour the formation of satellites. In particular, surface elasticity tends to form spherical-shaped satellites at pinch-off, whereas the increase of the liquid inertia generates oval-shaped satellites. In the set of shapes close to pinch-off shown in figure 4.5, the discontinuous transition is observed for $La = 0.01$ and 1, as β increases. However, for $La = 10 > 7.5$ a continuous transition of the thread shape is observed as β increases. Finally, for $La = 100$, the upper row evidences that the influence of the elastic stress on the shape of the thread is much weaker when the value of La is large enough. The physics underlying these transitions can be explained in terms of the coupling between the liquid inertia, the viscous stress, the surface tension, and the interfacial elastic stress. The competition between these forces will be discussed in §§4.3.2, based on the trends exhibited by the functions V_{sat}, Σ_{sat}, Δt_{NL} and $\mathcal{S}$, and also by analysing the temporal evolution of the interface shapes starting from small disturbances, depending on the values of La and β.

4.3.2 Nonlinear dynamics of a surfactant-laden interface: satellite drop formation

To unveil the effect of liquid inertia, viscous stresses and surface elasticity on the satellite droplet formation regimes, here we present and discuss the quantitative results of the detailed numerical analysis that has been carried out in the present section.

Figure 4.6 shows the isocontours of V_{sat}, Σ_{sat}, Δt_{NL} and $\mathcal{S}$ in the (La, β) parameter plane. We first observe that, at the discontinuous transition that occurs for $La < 7.5$, the value of V_{sat} increases from 10^{-3}–1.5 ‰ to 2–2.3 ‰, whereas Σ_{sat} increases from 10^{-3}–1.5 ‰ to 3.5–4.7 ‰. The exact value of both jumps as functions of La can be found in the inset of figure 4.4. In contrast, for $La > 7.5$ or $\beta > \beta_c(La)$, the values of V_{sat}, Σ_{sat}, Δt_{NL} and $\mathcal{S}$ vary continuously.

As a first general observation, it is deduced from figure 4.6 that the linear theory may either underestimate or overestimate the break-up time, in a way that does not necessarily coincide with the transitions in the satellite formation process. Indeed, t_b is underestimated for $La \gg 1$ independently of the value of β. However, for $La \ll 1$, t_b is overestimated for $0.28 \lesssim \beta \lesssim 1$, while it is underestimated outside this range. Regarding the sphericity $\mathcal{S}$, figure 4.6 confirms the trend deduced from figure 4.5: the most spherical satellite shapes,

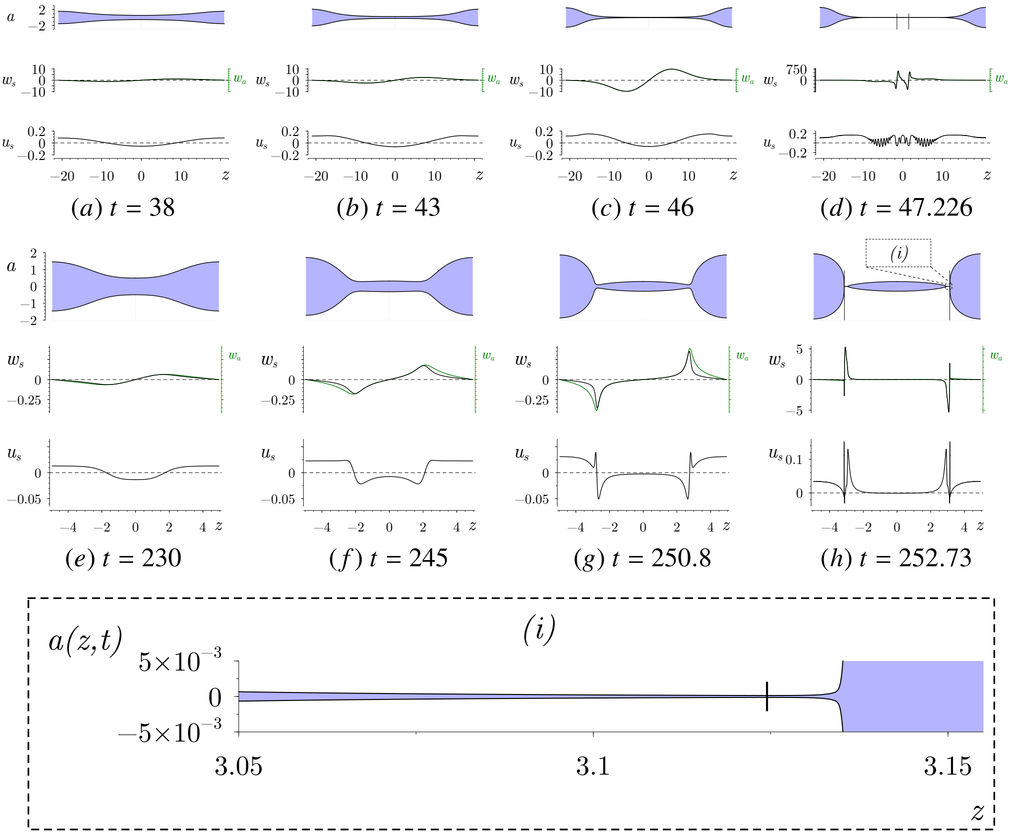

(*a*) $t = 38$ (*b*) $t = 43$ (*c*) $t = 46$ (*d*) $t = 47.226$

(*e*) $t = 230$ (*f*) $t = 245$ (*g*) $t = 250.8$ (*h*) $t = 252.73$

Figure 4.7: Temporal evolution of the liquid thread radius a (upper row), of the axial velocities at the free surface, w_s, and at the axis, w_a (middle row) and the radial surface velocity u_s (bottom row), for $\epsilon = 10^{-3}$, $\beta = 0$, (*a*–*d*) $La = 0.01$, $k = k_m = 0.150$, and (*e*–*h*) $La = 100$, $k = k_m = 0.635$. The vertical lines in each last snapshot indicate the axial position $z_{\min}$ of minimum radii $a_{\min}$, being $z_{\min} = 1.49$ and $a_{\min} = 3.63 \times 10^{-5}$ for $La = 0.01$, and $z_{\min} = 3.12$ and $a_{\min} = 1.29 \times 10^{-4}$ for $La = 100$. (*i*) Zoomed region close to the neck at the instant shown in (*h*).

with $\mathcal{S} \gtrsim 0.9$, take place for $\beta \gtrsim \beta_c$ and $La \lesssim 10$. In contrast, the shapes become most elongated, with $\mathcal{S} \lesssim 0.2$, when $\beta < \beta_c$ and $La \lesssim 0.1$ (grey area in figure 4.6*d*).

4.3.2.1 Analysis of the temporal evolution of clean interfaces

To present the dynamics of satellite droplet formation, we will take as reference cases the two canonical temporal evolutions of clean interfaces ($\beta = 0$) illustrated in figure 4.7, for $La = 0.01$ in (*a*–*d*), close to the Stokes limit, and for $La = 100$ in (*e*–*h*), an almost inviscid case close to the Euler limit (as shown in §§§4.3.2.4). Specifically, we plot snapshots at different times, indicated in the labels, of the jet radius a (upper rows), the axial surface velocity w_s (middle rows, black lines), the axial velocity at the centerline w_a (middle rows, green lines), and the radial surface velocity u_s (bottom rows). In both cases the initial disturbance amplitude is very small, $\epsilon = 10^{-3}$, and thus the initial evolution is triggered by the Plateau–Rayleigh instability mechanism, and can be described with linearized theory. This initial stage is not shown in figure 4.7 for conciseness, but it can be appreciated in figure 4.3(*a*). The initial disturbance, of most amplified wavelength k_m, creates an axial capillary pressure gradient that induces a flow from the valley to the crest of the wave. The latter mechanism finally leads to the break-up of the liquid thread and the formation of two main drops with either a liquid thread or a satellite droplet in between.

A key feature that determines the nonlinear evolution of the destabilized thread is the fact that the axial curvature makes the capillary pressure gradient to be locally larger in the regions that connect the central part of the thread with the growing crests, as evidenced by the surface and axis velocities in the snapshot (f). This enhanced pressure gradient drives liquid towards the crests faster in the nearby regions than in the central part, and explains the appearance of two local minima in the jet radius for large enough values of La, as can be clearly appreciated in snapshots (f,g) for $La = 100$. In addition, the axial position of the minimum radii $z_{\min}$ is advected with the flow along with the maximum pressure gradient, i.e. towards higher values of z as time advances (Ashgriz & Mashayek, 1995; Castrejón-Pita *et al.*, 2015). These two local minima become the two neck regions where pinch-off takes place, leading to the formation of an oval-shaped satellite droplet, as can be observed in snapshot (h). This scenario applies to cases where $La \gg 1$ (figure 4.7 *e*–*h*), for which the viscous stress is negligible, and the capillary pressure gradient is entirely transferred to liquid inertia leading to a self-accelerated process.

In contrast, when $La \ll 1$ (figure 4.7 *a*–*d*), the viscous dissipation inhibits the growth of higher harmonics, and larger pressure gradients are needed to overcome the viscous damping, as was already pointed out by Ashgriz & Mashayek (1995). Hence, the axial movement of the minimum radius is delayed by the viscous stress, since it weakens the capillary pressure and the concomitant liquid advection. Consequently, the central region shrinks almost uniformly until the last instants before break-up, giving rise to long and thin filaments without the formation of appreciable satellite droplets before detachment. Notice also that, for $La \ll 1$, the axial velocities at the centreline, w_a, and at the interface, w_s, are almost equal (green and black lines in figures 4.7 *a*–*d*, respectively), indicating that the radial profile of axial velocity inside the thread is nearly uniform at low Laplace numbers.

4.3.2.2 Analysis of the temporal evolution of surfactant-laden interfaces

To explain the different trends and transitions observed in figure 4.6, let us first focus on the effect of β for the particular cases of $La = 0.01$ and $La = 100$. Figure 4.8 shows V_{sat} (*a*,*c*), Σ_{sat} (*b*,*d*) and Δt_{NL} (insets in *b* and *d*), as functions of β for $La = 0.01$ in (*a*,*b*), and for $La = 100$ in (*c*,*d*). In addition, we have computed the results for several values of ϵ indicated in the legend of figure 4.8(*a*), with the aim at clearly establishing the limit of infinitesimal disturbances. In

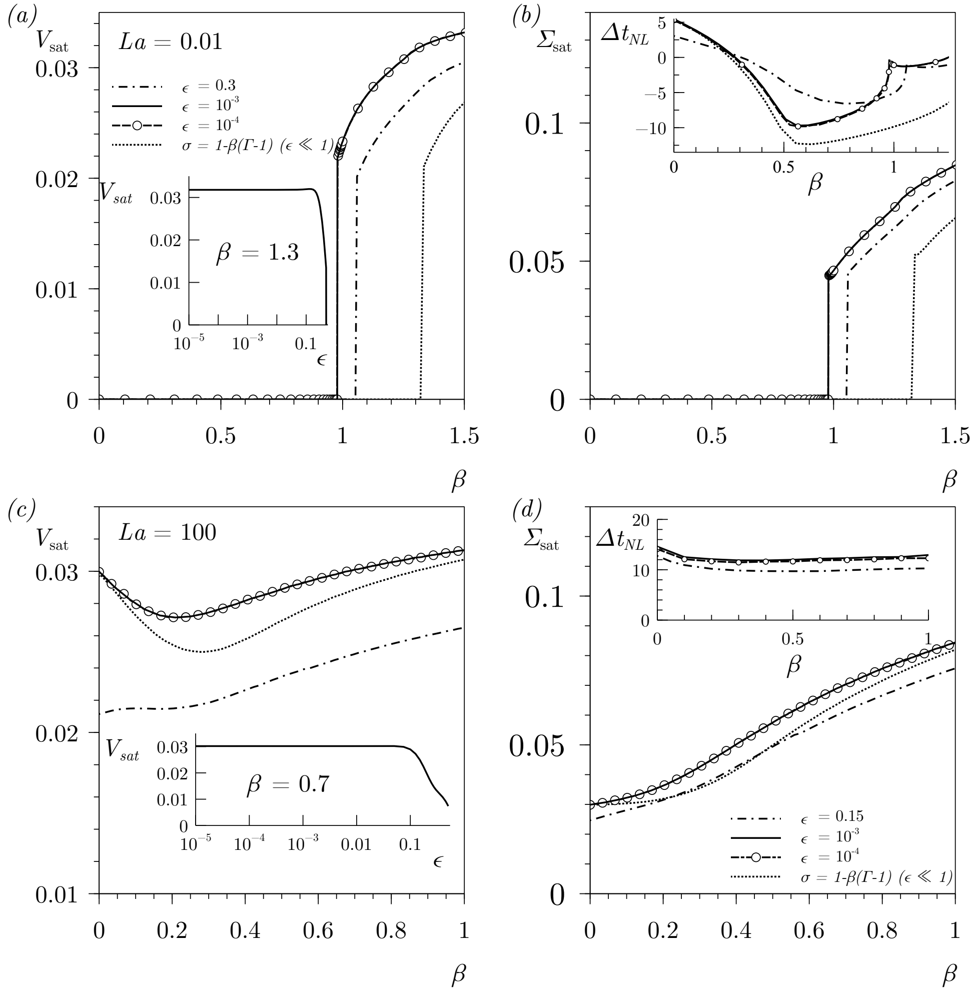

Figure 4.8: $V_{\rm sat}$ and $\Sigma_{\rm sat}$ as a function of β for (a,b) La = 0.01 and (c,d) La = 100, and for different values of the initial perturbation amplitude ϵ indicated in the legend. The dotted line represents the results of using the linear equation of state $\sigma = 1 - \beta(\Gamma - 1)$ (Dravid *et al.*, 2006). The insets show $V_{\rm sat}$ as a function of ϵ in logarithmic scale for (a) $\beta = 1.3$ and (c) $\beta = 0.7$, demonstrating that the final stage of the liquid thread just before pinch-off becomes independent of ϵ when its value is sufficiently small. The insets in (b, d) show the nonlinear correction to the break-up time $\Delta t_{\rm NL}$ as a function of β.

particular, figure 4.8 shows that $V_{\rm sat}$, $\Sigma_{\rm sat}$ and $\Delta t_{\rm NL}$ become independent of ϵ provided that ϵ is small enough, as stated before. Indeed, the insets in (a,c), which show the dependence of $V_{\rm sat}$ on ϵ, clearly demonstrate that the value of $V_{\rm sat}$ reaches the infinitesimal-disturbance plateau when $\epsilon \lesssim 0.1$. Figure 4.8 also displays the results obtained with the linear equation of state $\sigma = 1 - \beta(\Gamma - 1)$ (dotted line), instead of the nonlinear one (1.37). It is important to note that the use of the linear equation of state leads to substantial quantitative differences with respect

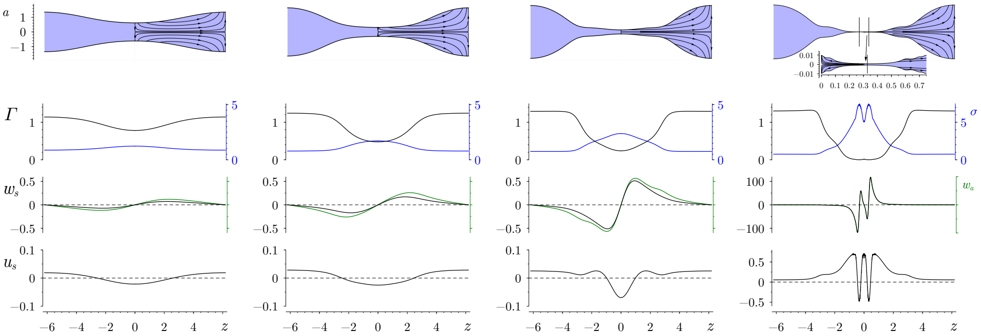

(*a*) $t = 100$ (*b*) $t = 112$ (*c*) $t = 118$ (*d*) $t = 119.03$

Figure 4.9: Temporal evolution of the liquid thread radius a (first row), surfactant concentration Γ (second row, black lines), surface tension σ (second row, blue lines), axial velocity at the interface w_s (third row, black lines) and at the centreline w_a (third row, green lines), and radial surface velocity u_s (fourth row), for $La = 0.01$, $\epsilon = 10^{-3}$ and $\beta = 0.960 < \beta_c(La = 0.01)$, with $k = k_m = 0.508$. The vertical line in the last snapshot of a indicates the position of z_{min}. Here $z_{\text{min}} = 0.33$ and $a_{\text{min}} = 7.29 \times 10^{-4}$.

to the nonlinear one (1.37). In particular, the linear equation underestimates the values of V_{sat} and Σ_{sat} considerably. We note also that we compared our numerical results using the linear equation of state with those reported by Dravid *et al.* (2006), finding very good agreement. However, their results were calculated for wavenumbers $k \neq k_m$, and the satellite droplet was measured by these authors by means of the thread radius at $z = 0$ close to pinch-off, instead of using either V_{sat} or R_{sat}.

Figures 4.8(*a*,*b*) show the discontinuous transition in V_{sat} and Σ_{sat} that occurs when β is increased above the critical value $\beta_c(La = 0.01) = 0.978 \pm 0.0003$. For $\beta > \beta_c(La = 0.01)$ a satellite drop centered at $z = 0$ is formed, trapping approximately 2.1% of the total volume of liquid and 4.5% of the total mass of surfactant.

4.3.2.3 Physical explanation of the discontinuous transition

To explain the abrupt transition induced by the presence of surfactants, figures 4.9 and 4.10 show the temporal evolution of the liquid thread for $La = 0.01$ and two different values of β, namely $\beta = 0.960 < \beta_c(La = 0.01)$, with $k = k_m = 0.508$, and $\beta = 0.979 > \beta_c(La = 0.01)$, with $k = k_m = 0.512$, respectively. In both cases, we have computed the thread radius a (first row), the surfactant concentration Γ together with the surface tension σ (second row), the axial velocity at the interface, w_s, and at the centreline, w_a (third row), and the radial surface velocity u_s (fourth row). Time is indicated in the labels.

The presence of surfactants introduces two main effects. The advection of surfactant molecules outside the central region of the thread increases the local surface tension in this region, as can be observed in the figures 4.9(*a*) and 4.10(*a*). This surfactant depletion generates two opposed effects: first, the axial capillary pressure gradient is enhanced, since the value of σ becomes larger in the central region, where Γ is smaller, while σ becomes smaller away from the center, where Γ is larger. Second, there is a stabilising effect induced by the elastic or Marangoni stress, which competes with the destabilising Plateau-Rayleigh mechanism enhanced by the first effect. Actually, the gradient of σ generates a tangential stress at the interface directed towards increasing values of σ, which opposes the drainage flow and tends to replenish the central zone with surfactant.

In the case of $\beta < \beta_c(La = 0.01)$, figure 4.9(*b*,*c*) shows that the Marangoni stress reduces the axial surface velocity, w_s, compared with the centreline velocity, w_a, the difference between both velocities being larger in the region where $\boldsymbol{\nabla}_s\sigma$ is higher. As the fluid is drained from the center for increasing times, $\boldsymbol{\nabla}_s\sigma$ becomes larger. When $\beta < \beta_c(La = 0.01)$ the capillary pressure gradient is able to remove most of the liquid from the center. Eventually, close to pinch-off, inertia becomes important and the flow is reverted close to $z = 0.33$, so that the rate of thinning increases in this region and $z_{\min}$ moves towards the latter axial position where the liquid thread finally detaches forming a tiny satellite droplet with $V_{\text{sat}} < 10^{-5}$, as evidenced by figure 4.9(*d*). Note that, during the thread evolution, two bulges connecting the central and outer regions grow due to the reduction of the surface velocity, and are finally connected by a thin liquid thread close to pinch-off.

When $\beta > \beta_c(La = 0.01)$ the foregoing explanation still holds, but the elastic stress is large enough to revert the flow near the interface at early times far from break-up, as shown in figure 4.10(*a*). The associated stagnation point diffuses radially inwards, and leads to a counterflow separating a region where liquid flows towards the center and induces the formation of a satellite, from another region where the incipient main drop is fed with liquid. Consequently, the thread detaches in between these two regions. If β increases further, the break-up time increases and the flow reversal occurs at earlier stages, so that V_{sat} and Σ_{sat} increase monotonically, as shown in figures 4.8(*a*,*b*).

When $La = 100$, figures 4.8(*c*,*d*) show that the effect of surface elasticity is much weaker in the case of dominant inertia, as was anticipated both in figure 4.6 and also by the shapes shown in the upper row of figure 4.5. The small influence of insoluble surfactants in the inviscid limit, $La \gg 1$, had been already noted in the linear stability analyses of Whitaker (1976), Hansen *et al.* (1999) and Timmermans & Lister (2002). Indeed, the effect of Marangoni stresses is confined to a thin boundary layer at the free surface, where the viscous stress rapidly restores any imbalance of σ, and which does not have any influence in the bulk liquid motion. Consequently, for $La = 100$, the satellite volume, V_{sat}, varies only slightly with respect to the value of a clean liquid thread, $V_{\text{sat}}(\beta = 0, La = 100) \simeq 0.03$, with a minimum at $\beta \simeq 0.203$, whereas Σ_{sat} increases monotonically as β increases. To explain this result, figures 4.11 and 4.12 show two sets of snapshots of a, Γ, σ, w_s, w_a and u_s for $\beta = 0.203$, at which V_{sat} is minimum, and for $\beta = 1$, respectively.

In the weak-elastic limit, $\beta \to 0$, a satellite droplet with volume $V_{\text{sat}} \simeq 3\%$ is formed at pinch-off, as already shown in figures 4.6 and 4.8(*c*). The satellite volume decreases as β increases in the range $0 < \beta \lesssim 0.203$. Indeed, when β increases, the Marangoni rigidification of the interface slows down the pinch-off process by decreasing the interfacial velocities, as

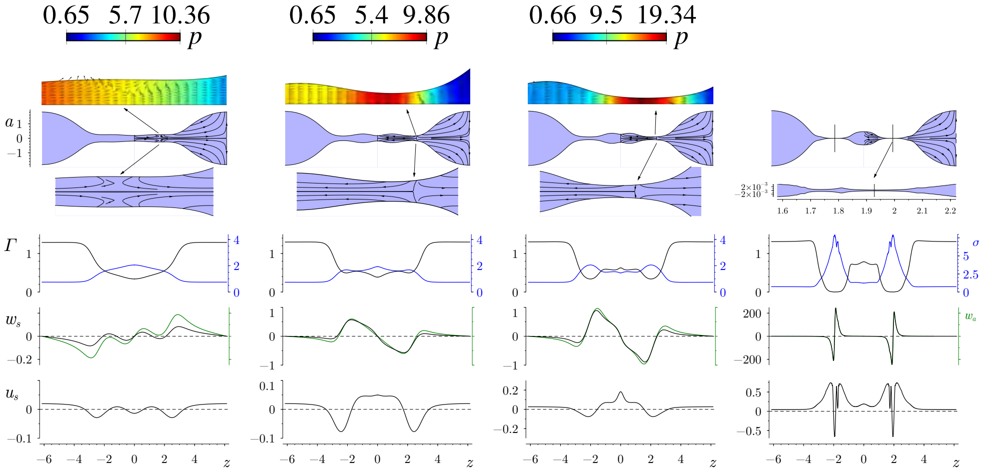

(*a*) $t = 119.8$ (*b*) $t = 122$ (*c*) $t = 122.8$ (*d*) $t = 123.7$

Figure 4.10: Same as figure 4.9 but for $\beta = 0.979 > \beta_c(La = 0.01)$, with $k = k_m = 0.512$. The insets are zooms showing the normalized velocity vector field and isocontours of the pressure field. Here $z_{\text{min}} = 1.93$ and $a_{\text{min}} = 2.5 \times 10^{-4}$.

evidenced by the time evolution of w_s, w_a and u_s in figure 4.11 with respect to figure 4.7(*e*–*h*). The latter behavior, together with the fact that the pressure gradient is locally enhanced due to the variations of σ, explain why a larger volume is drained out of the satellite droplet compared to the case of a clean interface. However, the Marangoni stress that opposes the drainage flow away from the center reduces the advection of surfactant towards the main drops, and thus the value of Σ_{sat} increases, as shown in figure 4.8(*d*). The snapshot in figure 4.11(*c*) shows that the flow is reversed near the neck region, as happens for a clean interface (see e.g. figures 4.7*h* and 4.7*i*). However, in the elastic regime the flow reversal takes place earlier than in the clean interface limit. This behavior at high values of La and low values of β was previously noticed by Kamat *et al.* (2018), who showed that the stagnation point occurs at earlier stages in surfactant-laden interfaces compared with clean interfaces, due to the strong Marangoni stress in the neck region.

A representative case of $La = 100$ and $\beta > 0.203$ is shown in the snapshots of figure 4.12 for $\beta = 1$. The main change with respect to the preceding case is the fact that for $\beta = 1$ the Marangoni stress is strong enough to revert the surface flow at earlier stages, as shown in panels (*b*) and (*d*). Therefore, the stagnation point appears earlier than in the case of figure 4.11, and diffuses almost instantaneously in the radial direction, leading to a satellite droplet with larger values of the normalized volume and of the surfactant mass. It can thus be deduced that the minimum value of V_{sat} displayed in figure 4.8(*c*) appears due to a competition between the two aforementioned opposite effects induced by the presence of surfactants.

For $La < 7.5$, the two effects described previously coexist when β is increased, as shown by the isocontours of V_{sat} in figure 4.6. For instance, when $La = 1$, V_{sat} first decreases

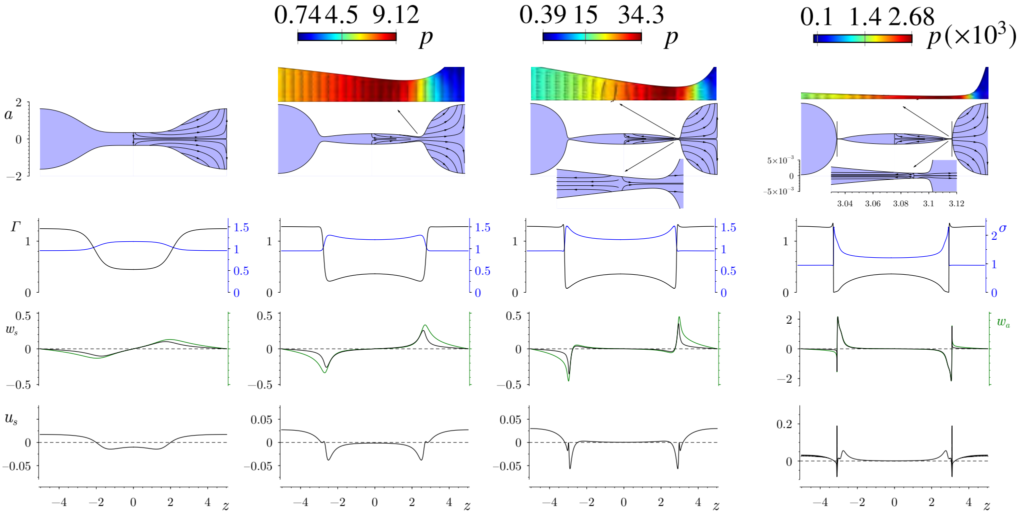

(a) $t = 268$ (b) $t = 278.5$ (c) $t = 280.5$ (d) $t = 281.06$

Figure 4.11: Same as figure 4.9 but for $La = 100$ and $\beta = 0.203$, with $k = k_m = 0.625$. Here $z_{\min} = 3.09$ and $a_{\min} = 7.89 \times 10^{-4}$.

as β increases, and when the elastic stress is strong enough, the flow is reversed and the discontinuous transition occurs. Note that, in the latter case, inertia is important since La is of order unity, and a small but finite satellite droplet exists in the clean limit, $\beta \to 0$ (see e.g. the second row of figure 4.5), where $V_{\mathrm{sat}} = 0.394$ % (a value significantly larger than in the limit $La \ll 1$, as shown in the isocontours of figure 4.6). Hence, the main difference with respect to the limit $La \gg 1$ is that in this case, since $V_{\mathrm{sat}}(\beta \to 0)$ is small, the increase of β reduces the satellite volume and may even make it negligible. For $La < 7.5$, Σ_{sat} also decreases monotonically together with V_{sat} when $\beta < \beta_c$, what can be explained by the fact that V_{sat} is already small when $\beta = 0$, so that Σ_{sat} necessarily decreases when β is increased.

Let us recall at this point that the critical elasticity, $\beta_c(La)$, decreases as La increases within the range $0 < La < 7.5$, as shown in figures 4.4 and 4.6. The reason for the latter trend is the fact that the advection of surfactant away from the central region is enhanced by the liquid inertia, so that $\boldsymbol{\nabla}_s\sigma$ also increases, and thus the value of β for which the elastic stress reverts the flow is smaller. Furthermore, the value of $V_{\mathrm{sat}}(La, \beta \to 0)$ increases as La becomes larger, and therefore the jumps experienced by V_{sat} and Σ_{sat} at the discontinuous transition, $\beta = \beta_c$, decrease, as deduced from the inset of figure 4.4. Finally, for $La > 7.5$, the discontinuous transition disappears.

4.3.2.4 Scaling laws for V_{sat} and Σ_{sat} as functions of La

Figure 4.13 shows V_{sat} and Σ_{sat} as functions of La for different values of β indicated in the legend. The circle with error bars corresponds to the experiment of Rutland & Jameson

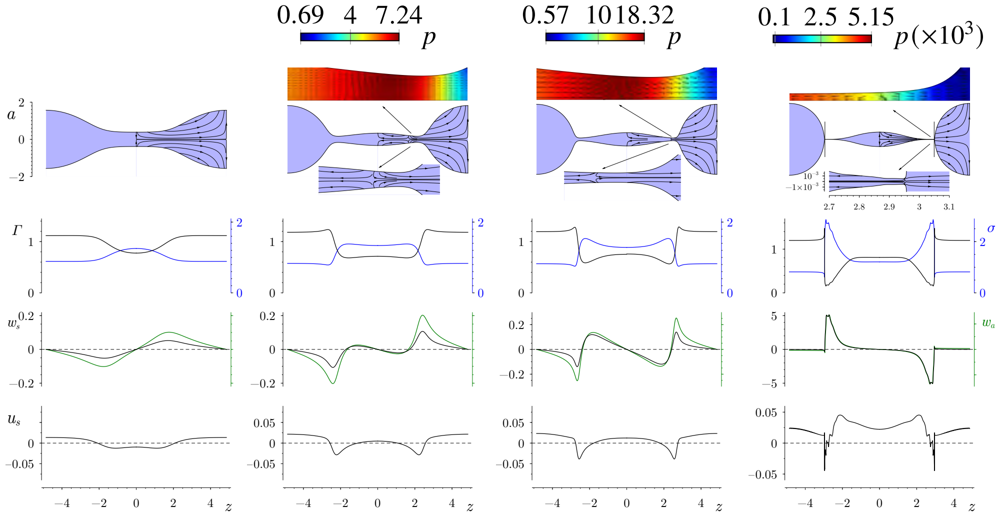

(a) $t = 290$ (b) $t = 304.5$ (c) $t = 307.5$ (d) $t = 309.53$

Figure 4.12: Same as figure 4.11 but for $\beta = 1$ with $k = k_m = 0.647$. Here $z_{\min} = 2.94$ and $a_{\min} = 5.14 \times 10^{-4}$.

(1971) on the natural break-up of a liquid jet of clean water, which is in close agreement with our numerical result for $\beta = 0$. The inset displays the most unstable wavenumber, k_m, as a function of La, showing the inviscid plateau $k_m \simeq 0.697$ for $La \gg 1$ (Rayleigh, 1878), as well as the power-law dependence for small values of La. The latter power law can be deduced from the long-wave approximation of the dispersion relation (3.4) or, equivalently, from the leading-order one-dimensional (1D) model deduced by Eggers & Dupont (1994) and García & Castellanos (1994). In the clean case, $\beta = 0$, the leading-order 1D results are $k_m \sim (2 + 3\sqrt{2}La^{-1/2})^{-1/2}$ and $\omega_m \sim (2\sqrt{2} + 6La^{-1/2})^{-1}$ (Eggers & Villermaux, 2008). The latter long-wave result provides very accurate results in the whole range of La, since $k \in (0, 1)$ accomplishes the slenderness assumption. In the inviscid limit, $La \to \infty$, both ω_m and k_m are slightly overestimated by the 1D model, namely $\omega_m \to 2^{-3/2}$ and $k_m \to 2^{-1/2}$. However, in the Stokes limit, $La \ll 1$, the values of $\omega_m \to 1/6$ and $k_m = 3^{-1/2}2^{-1/4}La^{1/4}$ are in excellent agreement with the exact linear theory. When $\beta > 1/2$, the elastic stress regularizes k_m in the limit of $La \to 0$, as analysed in detail by Timmermans & Lister (2002) (see also the amplification curves and the isocontours of k_m in figures 3.3*a* and *c*, respectively, of chapter 3 and section §3.3).

In the limit of a clean interface, $\beta = 0$, V_{sat} increases monotonically with La, as previously shown in figures 4.5 and 4.6, and explained in figure 4.7. In particular, our numerical results reveals that the satellite volume scales as $V_{\text{sat}} = 0.00421La^{1.64}$ when $La \lesssim 2$, and thus $V_{\text{sat}} \to 0$ and $\Sigma_{\text{sat}} \to 0$ as $La \to 0$. When La is finite, a satellite drop is always formed, since the liquid thread always experiences a transition to the inertial-viscous regime (Eggers, 1993; Castrejón-Pita *et al.*, 2015) and thus $z_{\min}$ moves from $z = 0$ towards higher values when t is

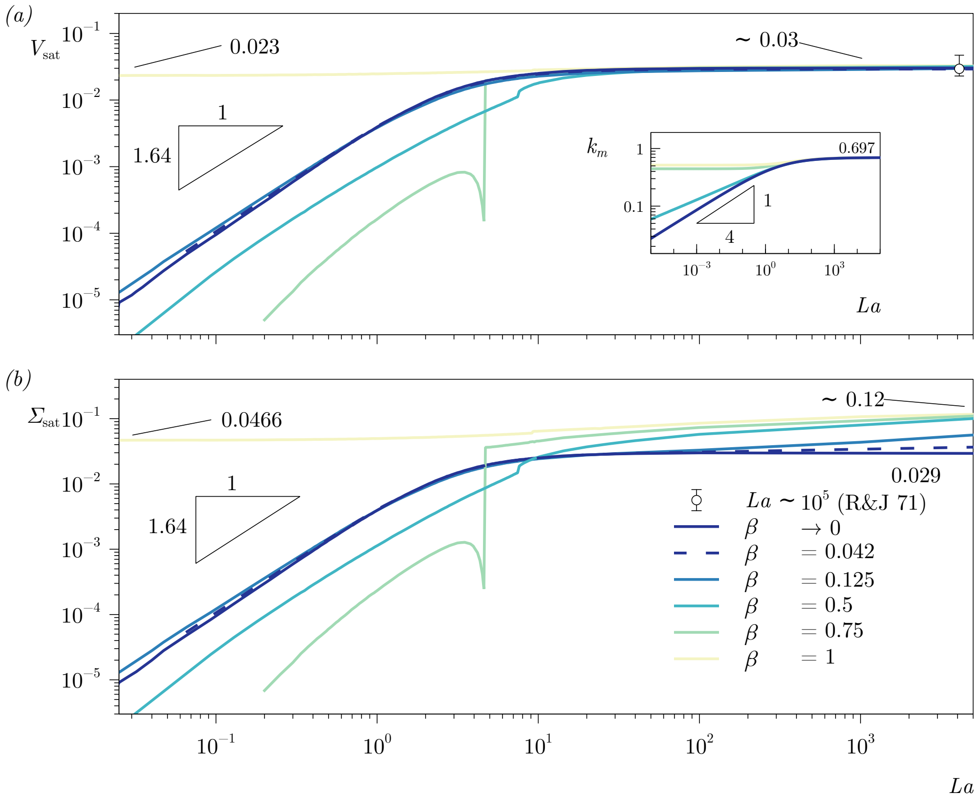

Figure 4.13: Normalized satellite's volume V_{sat}, and normalized mass of surfactant trapped at its interface Σ_{sat}, as a function of the Laplace number *La* in log-log for different values of β indicated in the legend. The inset shows the dependence of the maximum amplification wavenumber k_m with respect to *La* in log-log. The circle with error bars corresponds to the experiments of the natural break-up of a liquid jet of water performed by Rutland & Jameson (1970).

close enough to t_b. The elongated satellite droplet formed when $La \ll 1$ can break-up into more droplets after pinch-off as it relaxes, depending on the value of *La* (Notz & Basaran, 2004; Castrejon-Pita *et al.*, 2012; Wang *et al.*, 2019; Anthony *et al.*, 2019), unless $La \to 0$ (Eggers & Fontelos, 2005). Alternatively, using the expression for the equivalent radius R_{sat} developed in §§4.3.1, which depends on k_m, and since $k_m = 3^{-1/2}2^{-1/4}La^{1/4}$ within the range of *La* for which V_{sat} exhibits power-law scaling, it is deduced that $R_{\text{sat}} = 0.34La^{0.463}$.

When $La \gtrsim 10$, the value of V_{sat} reaches a plateau of about 3%, as already discussed in the context of figures 4.6 and 4.8(*c*). Equivalently, since $k_m \simeq 0.697$ when $La \gg 1$, $R_{\text{sat}} \simeq 0.588$ in the inviscid limit, in excellent agreement with the experiments of Rutland & Jameson (1971) (circle with error bars in figure 4.13*a*), and also with the numerical simulations of Ashgriz & Mashayek (1995). In the weak-elasticity limit, $\beta < 0.05$, the behavior of Σ_{sat} is identical to that of V_{sat}, displaying the same scaling law within the same range in *La*, and also reaching an inviscid plateau of about 2.9% when $La \gtrsim 10$. This scaling law for V_{sat} and Σ_{sat} prevails when $\beta < \beta_c$ and $La < La_c$, although the prefactor changes with β as shown in figure 4.13. In particular, when β increases the prefactor is smaller and thus V_{sat} and Σ_{sat} reach smaller values as $La \to 0$. This can be explained by the translation of z_{min}, which is inhibited as β becomes higher and thus the surface stress exerted at the interface increases.

Figure 4.13 also shows that, when $La \gg 1$, the 3% plateau reached by V_{sat} is barely affected by β since, as explained previously, inertia dominates and the elastic stress cannot induce any substantial change in the bulk motion (Whitaker, 1976; Hansen *et al.*, 1999; Timmermans & Lister, 2002). As inertia increases, the influence of β on V_{sat} becomes even weaker than in the case of $La = 100$ displayed in figure 4.8(*c*). Although the satellite shape at pinch-off is the same because viscosity cannot balance the elastic stress and transmit it to the bulk, Σ_{sat} reaches different inviscid limits as β increases. In particular, the 2.9% inviscid plateau reached by Σ_{sat} in the weak-elasticity limit increases with β, the reason being the same as in the case of figure 4.8(*d*).

When $\beta = 1 > \beta_c(La)$ for arbitrary values of La, a satellite is always formed with $V_{\mathrm{sat}} \gtrsim 2\%$ and $\Sigma_{\mathrm{sat}} \gtrsim 4\%$, and both increase smoothly with La as inertia becomes more important. In fact, V_{sat} and Σ_{sat} reach respective plateaus both in the Stokes and Euler limits. For $La \to 0$, the values of V_{sat} and Σ_{sat} are about 2.30% and 4.67%, respectively, whereas in the limit $La \to \infty$, their values are 3% and 12%, approximately. This trend prevails provided that $\beta > \beta_c(La \to 0) = 0.978$, as shown in the isocontours of V_{sat} and Σ_{sat} in figure 4.6. Hence, in the elasticity-dominated regime where $\beta > \beta_c$, the effect of inertia on V_{sat} and Σ_{sat} is weaker, although the column for $\beta = 1$ in figure 4.5 reveals that the shape of the thread at pinch-off changes substantially. As already mentioned, inertia tends to form oval-shaped satellites, which are more likely to break-up in the relaxation process after pinch-off, whereas the surface elasticity tends to form spherical satellites which will not experience secondary break-up events.

4.3.3 Conclusions

In this section we have reported an exhaustive numerical study of the unforced break-up of free axisymmetric threads of Newtonian liquid whose interface is coated with insoluble surfactants. Our main objective was to describe and explain how the presence of these molecules affects the nonlinear dynamics of the liquid thread and the satellite drop formation regimes when the dynamics is triggered by the most dangerous initial disturbance. Under these conditions we have shown that, when the initial perturbation amplitude is sufficiently small, the flow depends on two dimensionless parameters, namely the Laplace number La and the elasticity parameter β. Our numerical simulations have allowed us to characterize the influence of these two parameters on the satellite volume V_{sat}, the mass of surfactant trapped at its interface Σ_{sat}, the nonlinear correction to the linear break-up time Δt_{NL}, and the satellite sphericity $\mathcal{S}$, all of them computed at times very close to break-up. It is important to emphasize that our numerical simulations do not contemplate the post break-up behavior of the threads and satellites, including their relaxation or eventual secondary break-up events. Indeed, an accurate analysis of the dynamics beyond break-up is an important though technically challenging task, that is out of the scope of the present study. Clearly, a future task to be pursued is to extend the present results by performing numerical simulations that are able to compute the post pinch-off dynamics to unveil the ultimate state of the unstable liquid thread.

We have found a discontinuous transition at a critical elasticity number $\beta = \beta_c(La)$ within the range $0 < La < 7.5$, at which V_{sat} and Σ_{sat} change abruptly. We have explained this behavior in terms of a competition between the Plateau-Rayleigh instability mechanism and the elastic or Marangoni stresses that arise due to interfacial surface tension gradients. When β is high enough, the elastic stress that opposes the flow induced by the capillary pressure gradient is able to revert it at the interface. Afterwards, the surface stagnation point diffuses radially inwards, and finally a net flux of liquid swells the central region forming a satellite droplet prior to pinch-off.

When $La < 7.5$, V_{sat} and Σ_{sat} increase from a non-zero satellite droplet for $\beta < \beta_c$, to a larger value when $\beta > \beta_c$. When $La \lesssim 0.2$, the critical elasticity number reaches a plateau, $\beta_c = 0.978$. Finally when $La > 7.5$ the abrupt transition disappears. In between, β_c decreases monotonically with La, since inertia enhances the gradients of surface tension.

For a clean liquid thread, $\beta \to 0$, we have provided a new scaling law for the normalized satellite volume, namely $V_{\text{sat}} = 0.00421 La^{1.64}$, which is valid for $La \lesssim 1$. We have shown the existence of a regular weak-elasticity limit, $\beta < 0.05$, for which the latter scaling law holds, and for which the normalized mass of surfactant carried by the satellite, Σ_{sat}, exhibits the same scaling law as V_{sat}. In this limit, when inertia is sufficiently dominant, namely $La \gtrsim 10$, both V_{sat} and Σ_{sat} reach respective limits of about 3% and 2.9%, the value of 3% being in close agreement with previous experiments (Rutland & Jameson, 1971) and numerical simulations (Ashgriz & Mashayek, 1995).

When $La = 100$ the 3% inviscid plateau in V_{sat} varies slightly with β, and displays a minimum within the range $0.2 \lesssim \beta \lesssim 0.4$, whereas the 2.9% inviscid plateau of Σ_{sat} increases monotonically. The existence of this minimum has been explained by the competition between two opposed effects induced by the presence of surfactants: (I) the reduction of the surface tension σ when Γ increases, which enhances the capillary pressure gradient, and (II) the Marangoni stress exerted at the interface due to the gradients of σ. The initial decrease of V_{sat} when β grows is due to (I), whereas the increase above the minimum value is due to (II), which is able to revert the flow at earlier stages of the thread evolution when β is sufficiently high. The decrease of V_{sat} with β also coexists with the discontinuous transition for $La < 7.5$. Additionally, the increase of Σ_{sat} when $La > 7.5$ is explained by the reduction of the interfacial velocity due to (II), what tends to accumulate surfactant molecules at the satellite.

When $La \gg 1$, the effect of surface elasticity is very weak and the 3 % plateau of V_{sat} does not vary with β, since its effect is confined to a thin Marangoni boundary layer at the interface, where viscous dissipation tends to restore a modified but constant value of σ. The most important effect of β in the inviscid limit is the fact that Σ_{sat} increases with β due to the reason explained in the previous paragraph.

Here, we have considered a nonlinear equation of state for $\sigma(\Gamma)$ that is deduced from the equilibrium thermodynamics of the interface together with the conservation of molecules in the insoluble limit. We have shown that using this nonlinear equation leads to substantial quantitative differences with respect to the use of its linearized version (Dravid *et al.*, 2006). These differences call out for a careful experimental study of the present jet flow configuration or a similar one, e.g. a cylindrical liquid bridge between two static disks whose length is above the critical one for spontaneous break-up. The latter configuration has been recently studied experimentally by Kovalchuk *et al.* (2018) for concentrations above the CMC. An experimental campaign would also be needed to probe the validity of the insoluble approximation. In fact, it would be interesting to extend the present numerical study to the soluble case, contemplating both bulk diffusion and sorption kinetics. To that end, the bulk diffusion equation together with appropriate adsorption and desorption kinetic equations should be coupled to the equations integrated in this section (Karapetsas & Bontozoglou, 2013). We believe that the numerical techniques employed herein should be able to properly tackle the soluble problem with minor modifications.

A natural and important extension of this section is tackling the forced jet problem, in which the wavenumber k is not restricted to the most unstable one, and the amplitude ϵ is not necessarily small. Another feature that deserves future work is the effect of surface diffusion on the satellite drop formation regimes described herein, especially in cases where $La \lesssim O(1)$, for which the surface diffusion time could be of the order of the thread break-up time. Similarly, for small-scale threads, the surface shear and dilational viscosities could also play an important role (Boussinesq, 1913; Scriven, 1960; Martínez-Calvo & Sevilla, 2018). The present numerical analysis should also be extended together with the experiments, to unveil the conditions under which diffusive and surface viscous effects become relevant, and how they affect the transitions described in the present work.

4.4 The limit of a saturated interface

We have seen throughout the document that the adsorption of surfactants at fluid interfaces induces substantial modifications of their mechanical properties that lead to a number of effects of relevance in many physiological and technological contexts (Van Golde *et al.*, 1988; Tweedy & Ethier, 2011; Rodríguez-Rodríguez *et al.*, 2015; Hermans *et al.*, 2015; Anna, 2016). The variety and complexity of the interactions between the bulk fluids and the surface layer at the microscopic level complicates the development of rigorous mean-field models, that are necessary to describe interfacial dynamics using continuum theories (Fuller & Vermant, 2012; Jaensson & Vermant, 2018). As we have seen in chapter 1, the simplest constitutive equation relating the surface stress with the surface rate of strain is the Boussinesq–Scriven (BS) law (Boussinesq, 1913; Scriven, 1960), which may be seen as the surface analog of the Navier–Poisson law. Indeed, the BS law assumes that the surface state of stress is isotropic, instantaneous and linear in the surface rate of strain, and disregards complex surface rheology (Edwards *et al.*, 1991; Fuller & Vermant, 2012; Langevin, 2014; Jaensson

& Vermant, 2018), leading to the concept of a *Newtonian surface* (Scriven, 1960). The BS law introduces three material parameters, namely the surface tension coefficient, $\sigma(\Gamma, T)$, and the surface shear and dilatational viscosity coefficients (Rayleigh, 1890), $\mu_s(\Gamma, T)$ and $\kappa_s(\Gamma, T)$, respectively, which depend on the surface concentration of surfactant, Γ, and on the temperature T. An important difficulty in the practical use of the BS law concerns the fact that most surfactants are soluble in the bulk fluids, which implies the need to account for bulk diffusion and adsorption-desorption kinetics in the description. In fact, since Γ is extremely difficult to measure directly, the bulk concentration of surfactants, $\bar{C}$, is normally used instead as the experimental control parameter. However, the relationship between Γ and $\bar{C}$ is not universal, but depends on the particular system under study in a nontrivial way that is usually rationalized in terms of appropriate adsorption isotherms (Prosser & Franses, 2001). The latter difficulty can be avoided by using high bulk concentrations, typically several times the critical micelle concentration (CMC), in which case the interface is highly packed and is said to be saturated, $\Gamma = \Gamma_\infty$, where the values of the surface tension and surface viscosity coefficients reach corresponding asymptotes $\sigma^{\text{sat}} = \sigma(\Gamma_\infty, T)$, $\mu_s^{\text{sat}} = \mu_s(\Gamma_\infty, T)$ and $\kappa_s^{\text{sat}} = \kappa_s(\Gamma_\infty, T)$ (Edwards *et al.*, 1991; Quéré & de Ryck, 1998; Scheid *et al.*, 2010, 2012). Moreover, as indicated in chapters 1 and 3, sections §3.4.3 and §3.4.4, not only surfactants can confer surface viscous resistance to fluid interfaces. Surface viscous forces also arise, for instance in vesicles, biological membranes, or active interfaces, where they coexist with the intrinsic elastic forces, and they may have a dominant role in their dynamics as detailed in Powers (2010); Narsimhan *et al.* (2015); Mietke *et al.* (2019*b*,*a*); Farutin *et al.* (2019) and references therein, polymersomes being the prominent example.

For isothermal saturated interfaces, the Marangoni stress is negligible, and the only relevant surface stresses are the Young–Laplace pressure and the surface viscous stresses (Quéré & de Ryck, 1998; Scheid *et al.*, 2010, 2012). Since the surface viscosity coefficients are very difficult to measure under the presence of significant Marangoni stresses and sorption kinetics in that all these effects are intrinsically entangled (Prosser & Franses, 2001; Elfring *et al.*, 2016), working at saturated conditions opens promising avenues to develop novel measurement techniques. Another difficulty that must be circumvented is the fact that the known values of the surface viscosity coefficients are very small, and thus the corresponding stresses tend to be hindered by bulk stresses. At small Reynolds numbers, the relative importance of the surface-to-bulk viscous stresses is given by the Boussinesq numbers $Bq = \mu_s/(\mu\ell)$ and ΘBq, where $\Theta = \kappa_s/\mu_s$ is the dilatational-to-shear surface viscosity ratio, μ is the viscosity of the bulk fluid, and ℓ is the characteristic length scale. Consequently, for the surface viscous stresses to be larger than the bulk viscous stresses it is necessary that $Bq > 1 \Rightarrow \ell < \mu_s/\mu$, where the length scale μ_s/μ plays here a similar role as the *Saffman-Delbrück length* in membrane biophysics (Saffman & Delbrück, 1975; Saffman, 1976; Stone, 1995; Powers, 2010). As outlined by Powers (2010), this length can be $\ell \approx 1\mu$m for liposomes (Dimova *et al.*, 1999, 2000, 2006), and $\ell \approx 1$ mm for polymersomes (Dimova *et al.*, 2002), where surface viscous forces dominate. For example, diblock copolymer vesicles have associated surface viscosities which are up to 500 times higher than the typical values. These small scales can be reached by means of several thinning mechanisms, e.g. the drainage

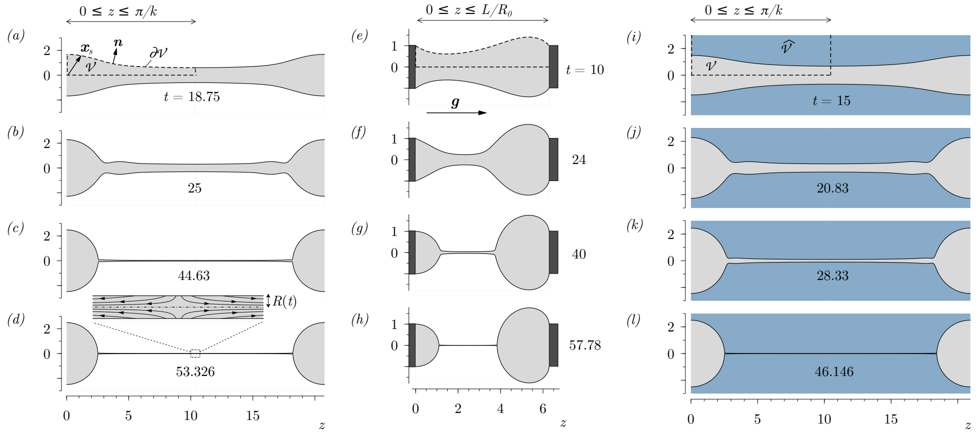

Figure 4.14: Snapshots of the liquid thread extracted from the numerical simulations. (*a–d*) Case I with $Bq = 3.4$, $\Theta = 1$ and $k = 0.3$. (*e–h*) Case II with $Bq = 0.1$, $\Theta = 2$, $L/R_0 = 2\pi$ and $Bo = 0.3$. (*i–l*) Case III with $Bq = 2$, $\Theta = 3$, $N_\mu = 10^{-3}$ and $k = 0.3$.

of foams and emulsions (Joye *et al.*, 1994; Hermans *et al.*, 2015), the formation and drainage of thin films (Scheid *et al.*, 2010; Champougny *et al.*, 2015; Bhamla *et al.*, 2017; Seiwert *et al.*, 2014; Ozan & Jakobsen, 2019), the lifetimes of antibubbles or bubbles bursting at a free surface (Dorbolo *et al.*, 2005; Scheid *et al.*, 2012; Vitry *et al.*, 2019), or the dynamical necking processes leading to the pinch-off of liquid bridges (Liao *et al.*, 2006; Ponce-Torres *et al.*, 2016; Kovalchuk *et al.*, 2018), dripping faucets (Ponce-Torres *et al.*, 2017), or vesicles and biological membranes (Bar-Ziv & Moses, 1994; Powers, 2010; Narsimhan *et al.*, 2015; Ruiz-Herrero *et al.*, 2019; Tozzi *et al.*, 2019; Mietke *et al.*, 2019*b*,*a*; Farutin *et al.*, 2019).

Here we report theoretical and numerical evidence pointing to a new asymptotic regime where surface tension balances surface viscous stresses. To that end, we consider the small scales generated by the thinning of axisymmetric liquid filaments due to capillary drainage, whereby the dominant force balance is $\sigma/R^2 \sim \mu_s\dot{R}/R^3$, where $R(t)$ is the filament radius and $\dot{R} = \mathrm{d}R/\mathrm{d}t$ its associated radial velocity. The latter balance assumes that $R \ll \mu_s/\mu$, i.e. that the local Boussinesq number $Bq_\ell = \mu_s/(\mu R) \gg 1$, and anticipates the existence of the exponential thinning regime $R(t) \propto \exp(-t/t_c)$, where $t_c \sim \mu_s/\sigma$ is a characteristic time that depends only on material parameters (Martínez-Calvo & Sevilla, 2018). Note that t_c may be called the surface-viscocapillary time in analogy with the classical viscocapillary time, $\mu\ell/\sigma$, given by the balance of surface tension and bulk viscous forces, that, in contrast with its surface analogue, depends on the length scale ℓ. In the absence of surfactants, the local balance of surface tension and bulk viscous forces, $\sigma/R^2 \sim \mu\dot{R}/R^2$, provides $\dot{R} \sim \sigma/\mu$, i.e., a thinning at the viscocapillary velocity σ/μ (Rayleigh, 1892; Papageorgiou, 1995).

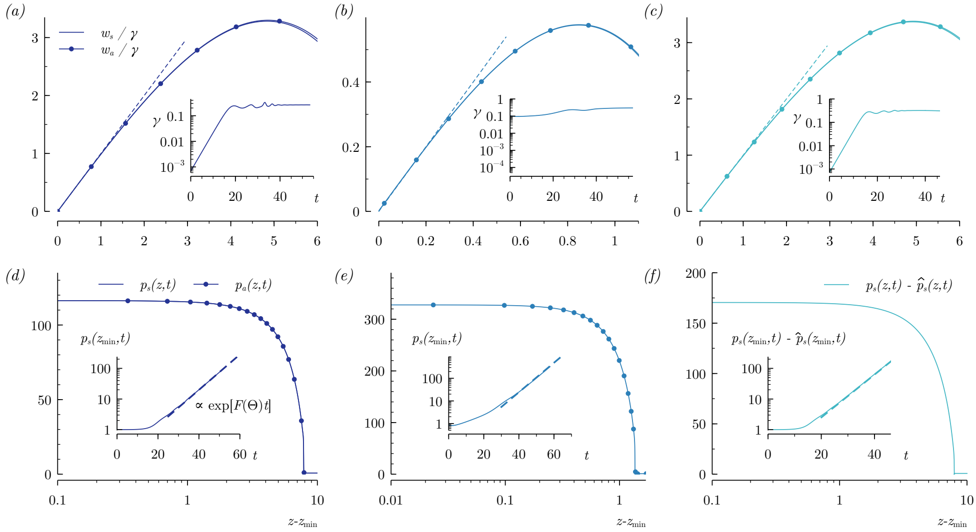

Figure 4.15: (a–c) (a-c) Axial velocity normalized with the local strain rate evaluated at the axis, w_a/γ, and at the interface, w_s/γ, as functions of z for (a) case I at $t = 53.326$, (b) case II at $t = 57.780$, and (c) case III at $t = 46.146$ [snapshots (d), (h) and (l) in figure 4.14]. The insets display the local strain rates, $\gamma(t)$. (d,e) Axial profiles of the pressure at the axis, $p_a(z,t)$, and at the interface, $p_s(z,t)$, for cases I and II. (f) Axial profile of the pressure jump at the interface, $p_s(z,t) - \hat{p}_s(z,t)$, for case III. The insets in (d–f) show $p_s(z = z_{\min}, t)$ (d,e), and $p_s(z_{\min}, t) - \hat{p}_s(z_{\min}, t)$ (f), where $z_{\min}$ is the axial position of minimum radius, with $z_{\min} = \pi/k$ in cases I and III.

4.4.1 Numerical simulations

We performed numerical simulations of the Stokes equations for three different axisymmetric flow configurations (see figure 4.14). In case I, we studied the spatially periodic dynamics of a long viscous liquid thread inside an unbounded passive ambient in the absence of gravity. The liquid filament was destabilized by a small-amplitude harmonic disturbance of the cylindrical shape with a wavenumber k below the Plateau–Rayleigh cut-off (Ashgriz & Mashayek, 1995; Kamat *et al.*, 2018; Martínez-Calvo & Sevilla, 2018; Martínez-Calvo *et al.*, 2020). In case II, we considered the unstable dynamics of a liquid bridge between two solid cylinders surrounded by a passive ambient, with gravity pointing in the axial direction and an associated Bond number $Bo = \rho g R_0^2/\sigma$, where ρ is the liquid density. The bridge length is fixed above the critical length for spontaneous breakup due to the Plateau–Rayleigh instability (Liao *et al.*, 2006; Ponce-Torres *et al.*, 2016; Kovalchuk *et al.*, 2018). Finally, case III was the same as case I, but with the liquid filament surrounded by an immiscible ambient liquid (Tomotika, 1935; Hajiloo *et al.*, 1987; Stone & Leal, 1990; Tjahjadi *et al.*, 1992; Milliken *et al.*, 1993; Stone & Brenner, 1996; Gaudet *et al.*, 1996; Hansen *et al.*, 1999).

Here we change the scales with respect to the ones indicated in the introductory chapter, thus taking characteristic scales associated with viscous interfacial properties, namely the initial thread radius as the length scale, the surface-viscocapillary time and velocity as the time and velocity scales, and the capillary pressure as the pressure scale, which read respectively

$$\ell_c = R_o, \quad v_c = \frac{\sigma_o R_o}{3\mu_s + \kappa_s}, \quad t_c = \frac{3\mu_s + \kappa_s}{\sigma_o}, \quad p_c = \frac{\sigma_o}{R_o}. \tag{4.11}$$

Hence, the dimensionless Stokes equations read:

$$\nabla \cdot \boldsymbol{u} = 0, \quad \text{and} \quad \boldsymbol{0} = \nabla \cdot \boldsymbol{T} \quad \text{in} \quad \mathcal{V}, \tag{4.12a}$$

$$\nabla \cdot \hat{\boldsymbol{u}} = 0, \quad \text{and} \quad \boldsymbol{0} = \nabla \cdot \hat{\boldsymbol{T}} \quad \text{in} \quad \hat{\mathcal{V}}, \tag{4.12b}$$

and the bulk stress tensors are:

$$\boldsymbol{T} = -p\boldsymbol{I} + \frac{1}{Bq(\Theta+3)}\left[\nabla\boldsymbol{u} + (\nabla\boldsymbol{u})^{\mathrm{T}}\right], \tag{4.13a}$$

$$\hat{\boldsymbol{T}} = -\hat{p}\boldsymbol{I} + \frac{N_\mu}{Bq(\Theta+3)}\left[\nabla\hat{\boldsymbol{u}} + (\nabla\hat{\boldsymbol{u}})^{\mathrm{T}}\right]. \tag{4.13b}$$

Note that the relative importance of liquid inertia compared with the viscous forces is measured by a local Reynolds number $Re_\ell = LaR|\dot{R}|$, where $La = \rho\sigma R_0/\mu^2$ is the Laplace number. Anticipating that $R \sim \exp(-t)$ for $t \gg 1$, it is deduced that $Re_\ell \sim La \exp(-2t)$, indicating that inertia becomes negligible at large times. The interfacial stress balance reads:

$$(\hat{\boldsymbol{T}} - \boldsymbol{T}) \cdot \boldsymbol{n} + \nabla_s \cdot \boldsymbol{T}_s = \boldsymbol{0} \quad \text{at} \quad \partial\mathcal{V}, \tag{4.14}$$

where $\boldsymbol{T}_s$ is modeled using the BS law (Boussinesq, 1913; Scriven, 1960), which, in this scales, read

$$\boldsymbol{T}_s = \left[1 + \frac{\Theta-1}{\Theta+3}(\nabla_s \cdot \boldsymbol{u}_s)\right]\boldsymbol{I}_s + \frac{1}{\Theta+3}\left[(\nabla_s\boldsymbol{u}_s)\cdot\boldsymbol{I}_s + \boldsymbol{I}_s\cdot(\nabla_s\boldsymbol{u}_s)^{\mathrm{T}}\right]. \tag{4.15}$$

As explained throughout the document, μ_s and κ_s generally depend on the surface concentration of surfactant (Edwards *et al.*, 1991), unless the region adjacent to the interface is highly populated with surfactant molecules, and their adsorption time is much smaller than the characteristic hydrodynamic time. In the latter saturated limit, the effect of the Marangoni stress $\nabla_s\sigma$ becomes negligible (Quéré & de Ryck, 1998; Scheid *et al.*, 2010, 2012), and thus a surfactant transport equation is not needed to close the mathematical model. The BS law has also been used in the context of passive and active vesicles and membranes (Powers, 2010; Narsimhan *et al.*, 2015; Farutin *et al.*, 2019; Mietke *et al.*, 2019*b*,*a*), in the latter case coupled with continuum theories borrowed from nematic and active-gel theories (Marchetti *et al.*, 2013; Prost *et al.*, 2015; Hakim & Silberzan, 2017; Jülicher *et al.*, 2018; Farutin *et al.*, 2019; Mietke *et al.*, 2019*b*,*a*). Additionally, at the interface $\partial\mathcal{V}$ we impose the continuity of velocities, $\hat{\boldsymbol{u}} = \boldsymbol{u}$, and the kinematic condition, $\boldsymbol{u}_s \cdot \boldsymbol{n} = \dot{\boldsymbol{x}}_s \cdot \boldsymbol{n}$, as indicated in chapter 3. The boundary conditions in the z direction are $\partial_z u = w = 0$ at $z = 0, \pi/k$ for cases I and III, while

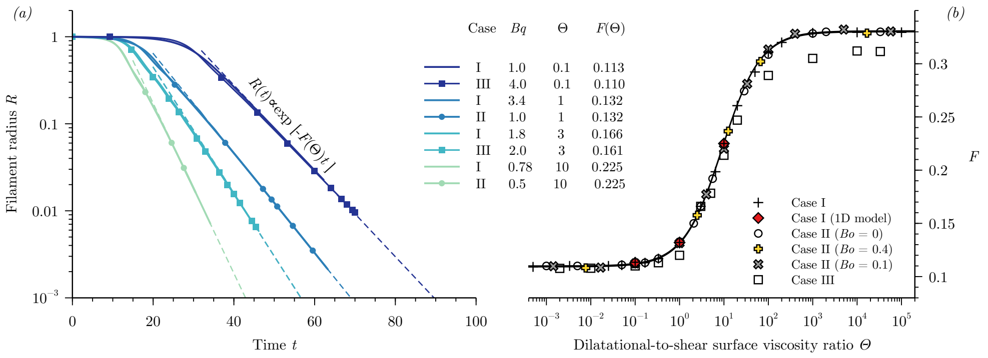

Figure 4.16: (a) The minimum thread radius $R(t)$ for different conditions specified in the legend. (b) The universal function $F(\Theta)$. The solid line corresponds with the approximation $F(\Theta) \approx (3+\Theta)/(28+3.02\Theta)$.

in case II we impose $u = w = 0$ at $z = 0, L/R_0$, where L is the length of the liquid bridge. In the three cases, the axisymmetry condition $\partial_r w = u = 0$ holds at the axis, $r = 0$.

As for the initial conditions, we assume that the fluids are initially at rest, $\boldsymbol{u} = \boldsymbol{0}$, and impose shape disturbances of the form $\boldsymbol{x}_s = [1 + \epsilon \cos(kz)]\boldsymbol{e}_r + z\,\boldsymbol{e}_z$ in cases I and III, and $\boldsymbol{x}_s = \{1 + \epsilon\,[\cos\,(2\pi z/(L/R_0)) - 1]\}\,\boldsymbol{e}_r + z\boldsymbol{e}_z$ in case II, where $\epsilon \ll 1$ is a small disturbance amplitude.

We now have a closed system to determine $\boldsymbol{u}$, p and $\boldsymbol{x}_s$ in cases I and II, and additionally $\hat{p}$ and $\hat{\boldsymbol{u}}$ in case III. The numerical integration employs the same methodology explained in previous studies (Rivero-Rodríguez & Scheid, 2018*a*; Martínez-Calvo *et al.*, 2020) and in §4.2, where a detailed description can be found.

Figure 4.14 shows representative interface evolutions for the three cases under study. The computational domains are indicated in the snapshots (a),(e),(i) with dashed lines, and the inset in (d) shows the local flow near the symmetry plane of the elongated thin thread connecting the two main drops. As anticipated before, the surface viscous stresses avoid the occurrence of the finite-time singularity that would lead to pinch-off if only bulk viscous stresses balanced interfacial tension (Papageorgiou, 1995). Instead, the radius of the cylindrical filament is observed to relax exponentially at large times, as evidenced in figure 4.16(a), which also shows that the thread relaxation rate increases monotonically with Θ. It is noteworthy that these exponentially decaying filamentary structures resemble the celebrated beads-on-a-string structure in viscoelastic liquid threads (Goldin *et al.*, 1969; Bazilevskii *et al.*, 1981; Entov & Hinch, 1997; Clasen *et al.*, 2006). Nevertheless, the physical mechanisms underlying both phenomena are completely different, as demonstrated below.

4.4.2 Local analysis of the large-time behavior

To develop a simple theory that accounts for the exponential relaxation of the liquid thread, we examined the numerical evidence carefully. In particular, motivated by the shape evolution shown in figure 4.14, we approximate the thinning ligament by a cylinder of radius $R(t)$, and we assume that the axial velocity inside the ligament is uniform in the radial direction, $w = w(z,t)$, as evidenced by the profiles of axial velocity extracted at the axis, $w_a(z,t)$, and at the interface, $w_s(z,t) \approx w_a(z,t)$, represented in figures 4.15(*a*–*c*). For simplicity, we decided to develop the local model disregarding the bulk viscous stresses of the outer flow, so that $\hat{\boldsymbol{T}} \approx -\hat{p}\boldsymbol{I}$. Indeed, although a cylindrical interface cannot be an exact solution of (4.12) when $N_\mu \neq 0$, we will show below that the exponential thinning regime occurs when the inner and outer bulk stresses are both negligible compared to the surface stresses. The continuity equation in (4.12a) implies that the radial velocity $u(r,z,t) = -\gamma r/2$, where $\gamma = \partial_z w$ is the axial strain rate. Moreover, the kinematic condition applied at $r = R(t)$ implies that $\gamma(t) = -2\dot{R}(t)/R(t)$ is only a function of time, and thus $w(z,t) = \gamma(t)z$, as observed in figures 4.15(*a*–*c*) in the region $0 \leq z - z_{\min} \lesssim 2$. It is thereby deduced that the local elongational flow field $\boldsymbol{u}(r,z,t) = -2z\dot{R}/R\,\boldsymbol{e}_z + r\dot{R}/R\,\boldsymbol{e}_r$ provides a good description of the local dynamics inside the filament. According to the Stokes equation for the inner stream (4.12a), the latter velocity field is an exact solution provided that the pressure field depends only on time, $p = p(t)$, in agreement with the results of figures 4.15(*d*–*f*), which show that the pressure field inside the thread is approximately uniform in the region where $w = \gamma(t)z$. The dynamics of the thread is then given by the function $R(t)$, which is determined from the interfacial stress balance (4.14). In particular, the surface stress tensor (4.15) simplifies to

$$\mathsf{T}_s^{zz} = 1 - \frac{\dot{R}}{R}, \quad \text{and} \quad \mathsf{T}_s^{\theta\theta} = 1 + \frac{3-\Theta}{3+\Theta}\frac{\dot{R}}{R}, \tag{4.16a,b}$$

the remaining entries being null, whereby the surface stress and the bulk stress jump at the interface read, respectively,

$$\boldsymbol{\nabla}_s \cdot \boldsymbol{T}_s = -\left(\frac{1}{R} + \frac{3-\Theta}{3+\Theta}\frac{\dot{R}}{R^2}\right)\boldsymbol{e}_r + \partial_z\left(1 - \frac{\dot{R}}{R}\right)\boldsymbol{e}_z, \tag{4.17a}$$

$$\left(\hat{\boldsymbol{T}} - \boldsymbol{T}\right)\cdot\boldsymbol{n} = \left(p_s - \hat{p}_s - \frac{2}{Bq(3+\Theta)}\frac{\dot{R}}{R}\right)\boldsymbol{e}_r + \frac{\partial_z\dot{R}}{Bq(3+\Theta)}\boldsymbol{e}_z, \tag{4.17b}$$

Using equations (4.14) and (4.17) we obtain the normal and tangential interfacial stress balances. For $\Theta \neq 3$ and $t \gg 1$, the normal component reduces to $\dot{R} = -F(\Theta)\,R$, where we have defined the positive-definite function $F(\Theta) = [(3+\Theta)/(3-\Theta)]\,[1 - \lim_{t\to\infty}(p_s - \hat{p}_s)R]$, represented for the three cases in figure 4.16(*b*) together with the approximation $F(\Theta) \approx (3+\Theta)/(28+3.02\Theta)$, which provides a good fit to the numerical results. Note that the value $F(\Theta = 3) \simeq 0.166$ is obtained using the tangential stress balance. Finally, the thread radius obeys $R(t) \propto \exp\left[-F(\Theta)\,t\right]$, in close agreement with all the numerical results represented in figure 4.16(*a*).

Finally, it is interesting to note that the results obtained herein using a fully two-dimensional Stokes and Boussinesq-Scriven description cannot be deduced from the one-dimensional lubrication approximation derived in Martínez-Calvo & Sevilla (2018) which, assuming that the curvature is h^{-1} in the surface viscous terms, the axial momentum equation has the following conservation form, together with continuity equation,

$$0 = \partial_z \left[h^2 \mathcal{K} + \frac{3\, h^2 \partial_z u}{Bq(\Theta + 3)} + \frac{h \partial_z u(\Theta + 9)}{2(\Theta + 3)} \right], \quad \partial_t h^2 + \partial_z (h^2 u) = 0 \tag{4.18}$$

where $\mathcal{K} = h^{-1}(1 + h'^2)^{-1/2} + h''(1 + h'^2)^{-3/2}$ (Entov & Yarin, 1984; Clasen *et al.*, 2006) and primes indicate derivatives with respect to z. Integrating equation (4.18) yields a function of time $f(t)$ that can be seen as the total force acting on the filament (Li & Fontelos, 2003; Fontelos & Li, 2004), with $f(t) \sim R(t)$ to balance the capillary pressure term, so that $f(t)/R(t) \to \Lambda$ for $t \gg 1$, where Λ is a function of Θ only. Although purely cylindrical solutions of equation (4.18) obey an equation similar to that deduced above from the Stokes equations, the parameter Λ can only be related with the liquid pressure if the full equations (4.12)–(4.15) are considered, providing $\lim_{t\to\infty}(p_s - \hat{p}_s)R = 1 - (3-\Theta)(\Lambda-1)/(9+\Theta)$, as deduced also with the second-order parabolic model (Martínez-Calvo & Sevilla, 2018).

4.4.3 Satellite droplet formation in a liquid thread with saturated interface

In the previous subsection, we reported numerical results of the thinning of a saturated interface with surface viscous resistance that does no form satellite drops. Indeed, as shown in the snapshots of figure 4.14, the two main drops are always connected by an almost straight cylinder that remains stable while it thins. This subsection is devoted to explore the satellite-drop formation regimes in the limit of a saturated interface. To this end, we conduct a numerical study equivalent to that of section §4.3, characterizing the morphology of the thread just prior to breakup. As in the previous subsection, we consider inertial effects to be negligible, $La \to 0$, and a passive ambient bath, $N_\mu \ll 1$. Additionally, as we did in section §4.3, we focus on the natural breakup of the thread, and thus all the numerical simulations are conducted imposing as initial condition the most amplified wavenumber, $k = k_m$, obtained from the dispersion relation (3.11) of chapter 3, section §3.4. Therefore, the only governing dimensionless parameters are Bq and Θ.

Figure 4.17 displays a panoramic view of the thread shapes very close to breakup, for three different values of Θ, namely $\Theta = 0$ in (*a*–*c*), $\Theta = 1$ in (*d*–*f*), and $\Theta \to \infty$ in (*g*–*i*), and also several values of Bq, indicated in the labels. In particular, in the limit $\Theta \to \infty$, where surface viscous dilatational forces dominate over surface viscous shear forces, that is $\kappa_s \gg \mu_s$, the appropriate Boussinesq number must be defined in terms of κ_s, which we denote here as $Bq_\kappa = \kappa_s/(\mu R_o) = \Theta\, Bq$, to avoid ambiguity.

As outlined in section §4.3, a clean cylindrical thread in the Stokes limit, $La \to 0$, forms an elongated filament as it thins, which eventually breaks up at different axial positions due

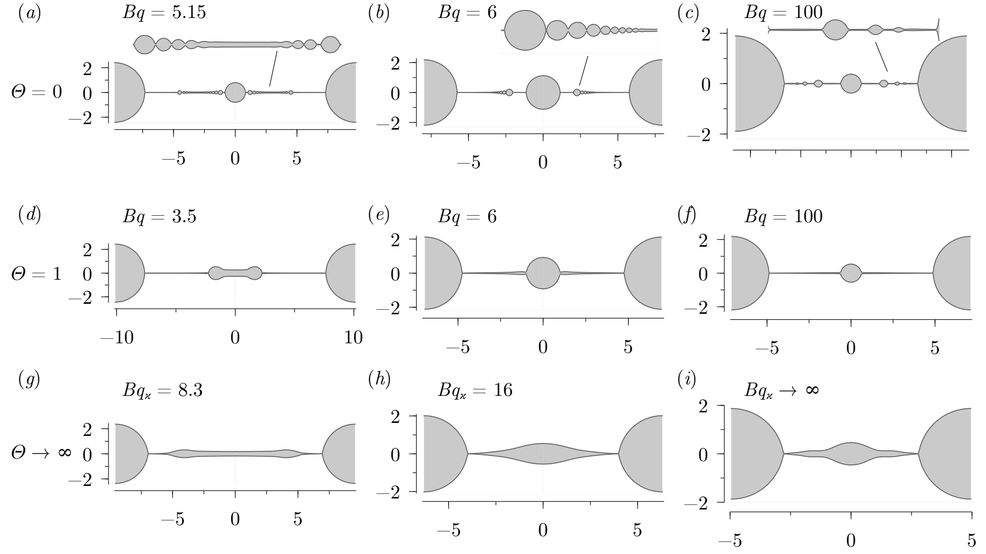

Figure 4.17: Snapshots of the liquid thread extracted from the numerical simulations, for (*a*–*c*) $\Theta = 0$, (*d*–*f*) $\Theta = 1$, and (*g*–*i*) $\Theta \longrightarrow \infty$, and different labels of the Boussinesq numbers indicated in the labels.

to external ambient noise or thermal noise, forming a myriad of tiny droplets (Kowalewski, 1996). However, significantly large satellite droplets are not formed during the thinning process. Just like the critical elasticity parameter in low-viscosity threads characterized in section §4.3, here we reveal that there is a critical value of Bq (or Bq_κ) in the limit of a saturated interface, for which $\beta \longrightarrow 0$, above which a structure of satellite drops and sub-satellite droplets is formed between the two main drops, whose morphology strongly depends on the values of Bq and Θ. In particular, the shapes close to breakup shown in figure 4.17 are computed for values of Bq and Θ lying above this critical curve. Before characterizing such curve, let us discuss the formation of satellite droplets and their morphology depending on the values of Bq and Θ by analyzing the shapes close to pinch-off.

Figures 4.17(*g*–*i*) show different thread shapes close to breakup in the limit $Bq \ll 1$, or equivalently $\Theta \gg 1$, for three values of Bq_κ, namely (*g*) $Bq_\kappa = 8.3$, (*h*) $Bq_\kappa = 16$, and (*i*) $Bq_\kappa = 1000$. When surface viscous dilatational forces dominate over their shear counterpart, the surface stress tensor reduces to the isotropic tensor $\boldsymbol{T}_s = [1 + Bq_\kappa(\boldsymbol{\nabla}_s \cdot \boldsymbol{u}_s)]\boldsymbol{I}_s$, which results in a viscous resistance to area dilatation in the normal and tangential directions. As Bq_κ increases, the satellite droplet becomes less slender and the thin filament connecting the satellite droplet with the mother drops disappears. In particular, when $Bq_\kappa \gtrsim 100$, the shape becomes universal and, interestingly, it resembles the shapes obtained experimentally and numerically by Tjahjadi *et al.* (1992) for a liquid thread with a clean interface embedded in a viscous bath of similar viscosity, $N_\mu \sim 1$.

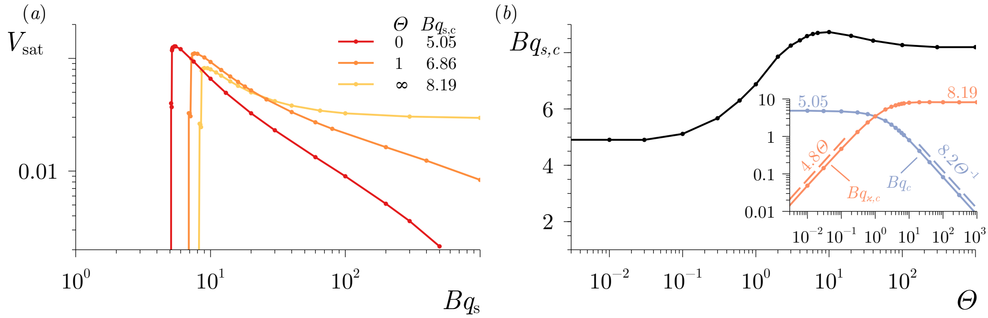

Figure 4.18: (*a*) Satellite volume V_{sat} as a function of the sum of the Boussinesq numbers $Bq_s = Bq(1+\Theta) = Bq + Bq_\kappa$ for three different values of Θ indicated in the legend.

In the opposite limit, $\Theta = 0$, which corresponds to an interface that only presents surface viscous resistance to shear, the surface stress tensor reduces to trace-free tensor $\boldsymbol{T}_s = [1 - Bq(\boldsymbol{\nabla}_s \cdot \boldsymbol{u}_s)]\boldsymbol{I}_s + Bq[(\boldsymbol{\nabla}\boldsymbol{u}_s)\cdot\boldsymbol{I}_s + \boldsymbol{I}_s\cdot(\boldsymbol{\nabla}\boldsymbol{u}_s)^{\mathrm{T}}]$. In this limit, figures 4.17(*a*–*c*) show, for the first time, that surface shear viscous forces can form a structure of satellite and sub-satellite droplets interconnected between the main drops, resembling the two celebrated phenomena of *beads-on-a-string* formation in threads with bulk viscoelasticity (Goldin *et al.*, 1969; Bazilevskii *et al.*, 1981; Entov & Hinch, 1997; Clasen *et al.*, 2006), and the *pearling structure* observed in lipidic membranes (Bar-Ziv & Moses, 1994; Seifert, 1997; Kantsler *et al.*, 2008; Powers, 2010; Narsimhan *et al.*, 2015). Here, surface shear viscous forces are able to trigger the formation of an almost spherical satellite droplet between the two main drops, where the thin filaments connecting them eventually becomes unstable producing a necklace of smaller spherical sub-satellite drops. As Bq increases, the short necks connecting the tiny drops forming a pearled structure, as in (*a*) for $Bq = 5.15$, disappear and the characteristic wavelength separating the sub-satellite drop becomes larger, as evidenced in (*c*) for $Bq = 100$, where the droplets are connected by almost perfectly cylindrical filaments. This change in the satellite-droplet structure can be explained qualitatively in terms of the local Boussinesq number and invoking the linear stability results obtained in chapter 3, where we showed that the most amplified wavenumber k_m first increases as Bq increases, and eventually decreases towards $k_m \to 0$ as $Bq \gg 1$. The thinning of the filament connecting the mother drops with the first satellite droplet increases the associated local Bq. When the value of the initial Bq is 100 as in (*c*), the local Bq associated with the filament lies within the region where the most amplified wavenumber is decreasing, which renders into a larger wavelength connecting the drops. For intermediate Bq, as in (*a*,*b*), the local Bq is not too high and the wavenumber is still large, thus the characteristic wavelength between sub-satellite droplets is small.

Although the outcome is similar, the underlying physical mechanism responsible of forming these pearled and beads-on-a-string structures is completely different to that of vesicles composed of lipidic bilayers and bulk viscoelastic threads. Indeed, in the former case, the interfacial area is typically constrained to remain constant, a condition usually referred to as the *surface incompressibility condition* (Powers, 2010; Narsimhan *et al.*, 2015), and the pearled structure is formed due to a buckling instability. In the latter case, the cascade of sub-satellite droplets in a beads-on-a-string fashion results from a combination between bulk viscoelasticity and inertia, which is a necessary condition for the formation of sub-satellite droplets, as shown by Li & Fontelos (2003) and Bhat *et al.* (2010), whereas in our scenario, surface shear viscous forces suffice to produce a cascade of tiny satellite droplets interconnected by straight thin filaments in the absence of liquid inertia.

When $\Theta = 1$, as in figures 4.17(*d*–*f*), a portion of liquid is formed between the main drops, which eventually retracts to form only one spherical satellite droplet connected by thin filaments. Here, we do not observe a destabilization of this thinning filament. In particular, the associated surface stress tensor reads $\boldsymbol{T}_s = \boldsymbol{I}_s + Bq[(\nabla \boldsymbol{u}_s) \cdot \boldsymbol{I}_s + \boldsymbol{I}_s \cdot (\nabla \boldsymbol{u}_s)^{\mathrm{T}}]$. We thus deduce that only pure surface viscous shear is able to form a cascade of sub-satellite droplets.

Finally, in figure 4.18 we characterize the critical Boussinesq number above which satellite droplets are formed. To account for both limits, namely $\Theta \ll 1$ and $\Theta \gg 1$, we introduce the sum of the Boussinesq numbers, $Bq_s = Bq + Bq_\kappa = Bq(1+\Theta)$. In particular, panel (*a*) shows the normalized satellite volume V_{sat} defined as in equation (4.7), as a function of Bq_s for the values of Θ considered in figure 4.17, that is $\Theta = 0$, $\Theta = 1$, and $\Theta = \infty$. As it occurred in section §4.3 with the surface elasticity, V_{sat} experiences a sharp transition at a critical Boussinesq number $Bq_{s,c}$ of order unity, from which V_{sat} increases abruptly to a value of order $V_{\mathrm{sat}} \sim 0.1$, and where the thread prior to breakup transitions from the shapes displayed in figure 4.14, to the ones shown in figure 4.17. In the limit $\Theta \gg 1$, when the value of Bq_s increases, V_{sat} decreases but eventually reaches a plateau where $V_{\mathrm{sat}} \simeq 2.965\%$, associated with the shape shown in figure 4.17(*i*). For other values of Θ, the value of V_{sat} decreases monotonously as Bq_s increases, and eventually $V_{\mathrm{sat}} \longrightarrow 0$ when $Bq_s \gg 1$, as evidenced by figures 4.17(*c*,*f*), with a larger negative slope as Θ becomes smaller.

Panel (*b*) shows the critical Boussinesq number, $Bq_{s,c}$, as a function of Θ, which reaches its maximum value when $\Theta \simeq 10$, and two plateaus already shown in (*a*), namely $Bq_{s,c} = Bq_c = 5.05$ when $\Theta = 0$, and $Bq_{s,c} = Bq_{\kappa,c} = 8.19$ when $\Theta \longrightarrow \infty$. The inset displays the corresponding critical shear and dilational Boussinesq numbers, Bq_c and $Bq_{\kappa,c}$, respectively, and their corresponding power laws as functions of Θ. In particular, $Bq_{\kappa,c} = 4.8\Theta$ for $\Theta \lesssim 1$, and $Bq_c = 8.2/\Theta$ for $\Theta \gtrsim 10$.

4.4.4 Discussion and applicability conditions

The assumptions of constant surface viscosities and negligible Marangoni stress clearly need some justification. As discussed by Quéré & de Ryck (1998) and by Scheid *et al.* (2010) in the context of axisymmetric and planar coating flows, respectively, two conditions must be fulfilled to ensure the validity of these hypotheses. First, as the thread shrinks, there must be enough available surfactant at the sublayer adjacent to the interface. This condition is satisfied when $\bar{C} \gg \Gamma_\infty R_0^{-1}$, and can be easily guaranteed in experiments by means of a liquid bath with a high concentration of surfactant surrounding the inner thread [*], as in the simulations of case III considered herein. Moreover, it could be advantageous to use outer liquids of small viscosity, $N_\mu \ll 1$, to replenish the interface with surfactants, in that the ambient fluid acts passively, as in cases I and II of the present investigation. Second, the adsorption velocity must be larger than the characteristic interfacial velocity, what implies that the flux from the bulk, $k_a\,\bar{C}$, where k_a is the adsorption velocity, is much larger than the surface flux $\Gamma_\infty\,\sigma^{\mathrm{sat}}(3\mu_s^{\mathrm{sat}}+\kappa_s^{\mathrm{sat}})^{-1}\,\dot{R}R^{-1}$, requiring that $\bar{C} \gg \Gamma_\infty\,k_a^{-1}\,\sigma^{\mathrm{sat}}(3\mu_s^{\mathrm{sat}}+\kappa_s^{\mathrm{sat}})^{-1}\,F(\Theta)$, a condition that, again, can be accomplished using an outer bath highly concentrated with surfactant molecules.

4.4.5 Conclusions

We have shown that a fluid interface saturated with surfactant molecules displays an exponential capillary thinning regime where surface viscous stresses balance surface tension. This new dynamical regime had not been reported in previous numerical (Ponce-Torres *et al.*, 2016, 2017) and experimental (Liao *et al.*, 2006; Ponce-Torres *et al.*, 2017; Kamat *et al.*, 2018; Kovalchuk *et al.*, 2018) investigations within the context of surfactant-laden threads, probably because, in all these studies, the depletion of surfactant due to interfacial advection was not compensated by an outer reservoir able to replenish the interface. Additionally, we have shown that, in the limit of a saturated interface, there is a critical value of the surface viscosities above which satellite droplets are formed between the main drops. The morphology and number of such small droplets strongly depend on the ratio Θ. Our findings could well open promising avenues in developing novel techniques for the high-precision measurement of the surface viscosity coefficients (Fuller & Vermant, 2012; Langevin, 2014; Jaensson & Vermant, 2018).

4.5 Effect of surface diffusion on satellite drop formation

In this section we conduct a study equivalent to those of sections §4.3 and §§4.4.3, but focusing on the effect of surface diffusion on the satellite-drop formation regimes. As outlined in the introductory chapter (section §1.4), surface diffusion of surfactants may only have an effect in sufficiently viscous threads, that is when $La \lesssim O(1)$. Hence, in this section we restrict to order-unity and small values of La. Additionally, to isolate the effects of surface diffusion, we consider a passive ambient fluid, $N_\mu \ll 1$, and we also neglect surface viscous forces, $Bq = Bq_\kappa = 0$.

To characterize the satellite-drop formation regimes, as we did in previous sections, we compute V_{sat} and Σ_{sat}. In particular, figure 4.19 shows these quantities as a function of β for $La = 0.01$ in (*a*,*b*), and $La = 1$ in (*c*,*d*), and several values of Pe_s indicated in the legend. In section 4.3, we showed that in the limit of negligible surface diffusion, $Pe_s \to \infty$, a sharp jump in V_{sat} and Σ_{sat} occurs when $La \lesssim 7.5$ at a certain critical value of the elasticity parameter,

---

[*] B. Scheid (private communication)

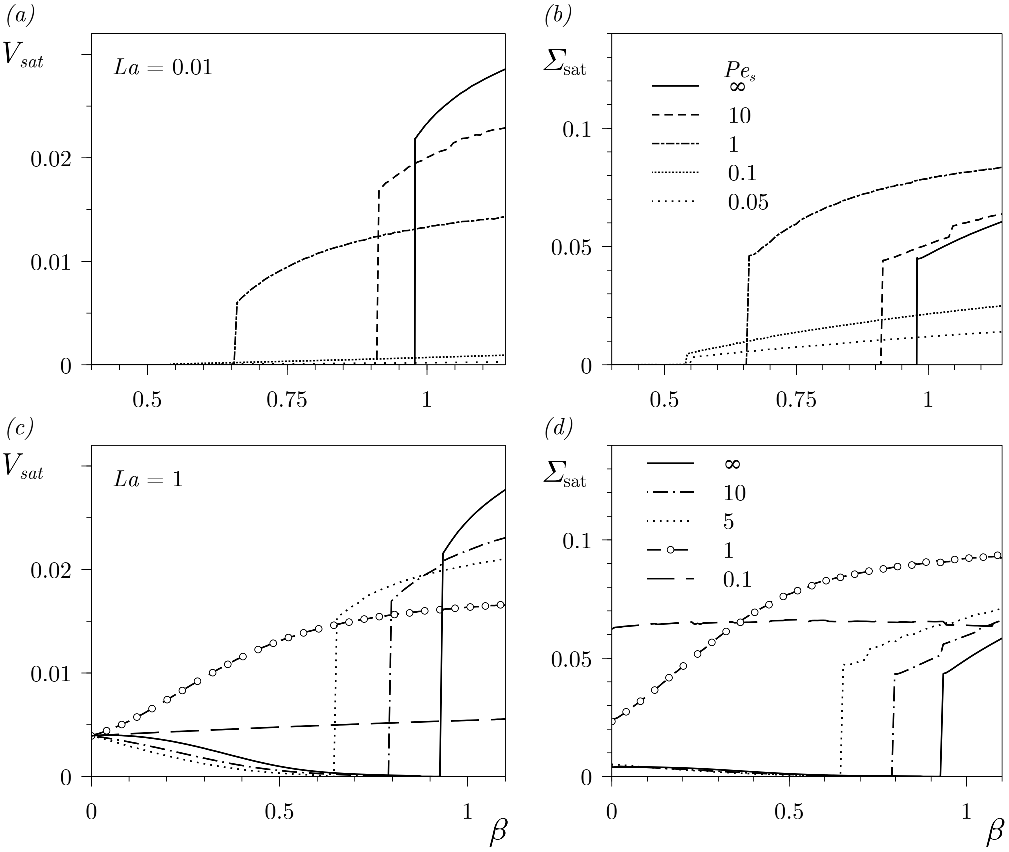

Figure 4.19: Volume of the satellite droplet $V_{\rm sat}$, and mass of surfactant at its interface $\Sigma_{\rm sat}$ as a function of β for (*a*-*b*) *La* = 0.01 and (*c*-*d*) *La* = 1, and different values of the surface Péclet number Pe_s indicated at each legend.

$\beta_c(La)$, which is of order unity. Here we show that this phenomenon, which results from a competition between the Rayleigh–Plateau instability mechanism and the elastic interfacial stress, is strongly affected by surface diffusion.

Figures 4.18(a,b) prove that the critical elasticity parameter, β_c, and the height of the discontinuous jumps found in §4.3, are substantially altered by the effect of surface diffusion. The main reason is that, when the value of Pe_s decreases, surface diffusion is capable of retaining a larger concentration of surfactant in the central region than in the non-diffusive limit. This leads to a weaker enhancement of the capillary pressure gradient, which is responsible of draining the fluid from the centre of the thread, since the difference in the surface tension coefficient between the crest and the valley is smaller. Hence, a lower value of β_c is needed for the the tangential elastic stress to overcome the Rayleigh–Plateau mechanism modified by the local renormalization of σ, and thus to trigger the discontinuous transition.

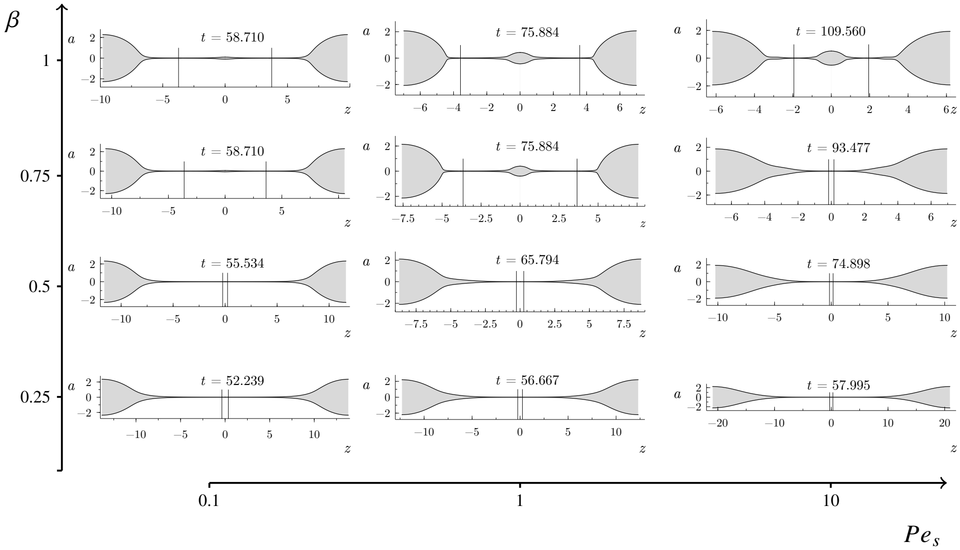

Figure 4.20: Satellite shapes close to pinch-off in the (Pe_s, β) parameter plane for $La = 0.01$. The vertical lines indicate the position of the minimum thread radii.

Additionally, since $\nabla_s \sigma$ is weaker, the stagnation point due to the interfacial elastic stress described in §4.3, arises closer to breakup, and thus less volume of liquid is re-filled in the central region, resulting in a smaller satellite droplet, as revealed by figures 4.19(*a*,*c*). On the contrary, the mass of surfactant at the satellite droplets' interface, Σ_{sat}, increases when Pe_s is diminished and $\beta > \beta_c$, as shown in figures 4.19(*b*,*d*). This is also a direct consequence of surface diffusion, which retains a larger surfactant concentration in the central region. This effect is most clearly illustrated in the weak-elasticity limit, $\beta \ll 1$, shown in figure 4.19(*d*) when $La = 1$. Here the Marangoni stress is almost negligible and has a very weak effect on the shape of the thread, and thus in V_{sat}, while Σ_{sat} experiences a large increase as the value of Pe_s decreases.

When the transport of surfactant is dominated by diffusion, $Pe_s \ll 1$, the interfacial gradients of Γ and σ become negligible, which results in a negligible tangential Marangoni stress at the interface. In this limit, the surfactant at the interface plays a passive role, as it is evident from figures 4.19 when $Pe_s \lesssim 0.1$, and from the corresponding shapes displayed in figures 4.20. In particular, V_{sat} and Σ_{sat} are nearly constant for any value of β, and the critical transition disappear as $Pe_s \to 0$, as shown in figure 4.21, which displays the critical elasticity parameter β_c as a function of Pe_s for the two values of La considered in this section. In particular, figure 4.21 shows that the value of Pe_s at which $\beta_c \to 0$ strongly depends on La.

References

ANNA, S.L. 2016 Droplets and bubbles in microfluidic devices. *Annu. Rev. Fluid Mech.* **48**,

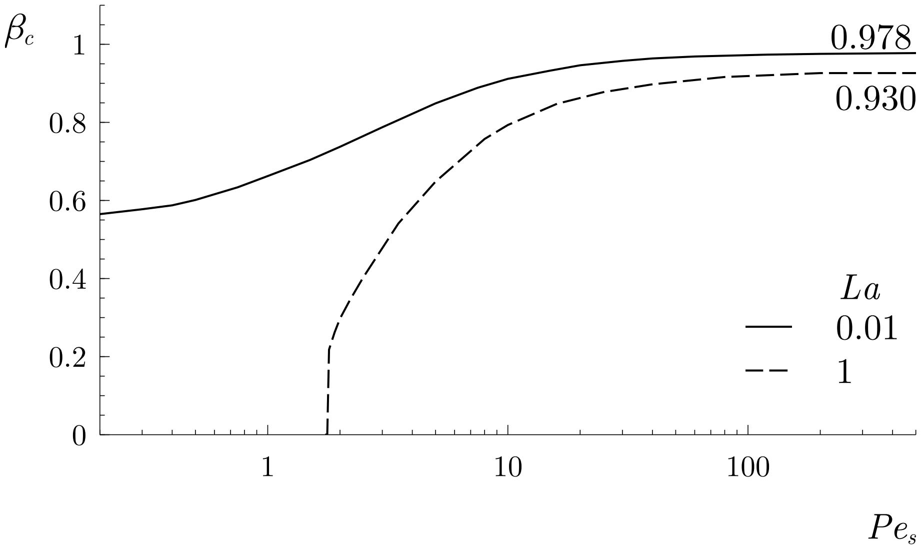

Figure 4.21: Critical elastic number, β_c, as a function of the surface Péclet number, Pe_s, for $La = 0.01$ (solid line) and $La = 1$ (dashed line).

285–309.

Anthony, C.R., Kamat, P.M., Harris, M.T. & Basaran, O.A. 2019 Dynamics of contracting filaments. *Phys. Rev. Fluids* **4** (9), 093601.

Ashgriz, N. & Mashayek, F. 1995 Temporal analysis of capillary jet breakup. *J. Fluid Mech.* **291**, 163–190.

Bar-Ziv, R. & Moses, E. 1994 Instability and "pearling" states produced in tubular membranes by competition of curvature and tension. *Phys. Rev. Lett.* **73** (10), 1392.

Bazilevskii, A. V., Voronkov, S. I., Entov, V. M. & Rozhkov, A. N. 1981 Orientational effects in the decomposition of streams and strands of diluted polymer solutions. , vol. 26, pp. 333–335.

Bhamla, M. S., Chai, C., Alvarez-Valenzuela, M. A., Tajuelo, J. & Fuller, G. G. 2017 Interfacial mechanisms for stability of surfactant-laden films. *PloS one* **12** (5), e0175753.

Bhat, P. P., Appathurai, S., Harris, M. T., Pasquali, M., McKinley, G. H. & Basaran, O. A. 2010 Formation of beads-on-a-string structures during break-up of viscoelastic filaments. *Nat. Phys.* **6** (8), 625–631.

Bogy, D.B. 1979 Drop formation in a circular liquid jet. *Annu. Rev. Fluid Mech.* **11**, 207–228.

Boussinesq, J. V. 1913 *J. Ann. Chim. Phys.* **29**, 349.

CAMPANA, D. M. & SAITA, F. A. 2006 Numerical analysis of the rayleigh instability in capillary tubes: The influence of surfactant solubility. *Phys. Fluids* **18**, 022104.

CASTREJON-PITA, A. A., CASTREJON-PITA, J. R. & HUTCHINGS, I. M. 2012 Breakup of liquid filaments. *Phys. Rev. Lett.* **108** (7), 074506.

CASTREJÓN-PITA, J. R., CASTREJÓN-PITA, A. A., THETE, S. S., SAMBATH, K., HUTCHINGS, I. M., HINCH, J., LISTER, J. R. & BASARAN, O. A. 2015 Plethora of transitions during breakup of liquid filaments. *Proc. Natl. Acad. Sci. U.S.A.* **112** (15), 4582–4587.

CHAMPOUGNY, L., SCHEID, B., RESTAGNO, F., VERMANT, J. & RIO, E. 2015 Surfactant-induced rigidity of interfaces: a unified approach to free and dip-coated films. *Soft Matter* **11** (14), 2758–2770.

CHAUDHARY, K.C. & MAXWORTHY, T. 1980 The nonlinear capillary instability of a liquid jet. part 3. experiments on satellite drop formation and control. *J. Fluid. Mech.* **96** (2), 287–297.

CHRISTOPHER, G.F. & ANNA, S.L. 2007 Microfluidic methods for generating continuous droplet streams. *J. Phys. D: Appl. Phys.* **40**, R319–R336.

CLASEN, C., EGGERS, J., FONTELOS, M. A., LI, J. & MCKINLEY, G. H. 2006 The beads-on-string structure of viscoelastic threads. *J. Fluid Mech.* **556**, 283–308.

DAY, R. F., HINCH, E. J. & LISTER, J. R. 1998 Self-similar capillary pinchoff of an inviscid fluid. *Phys. Rev. Lett.* **80** (4), 704.

DERBY, B. 2010 Inkjet printing of functional and structural materials: Fluid property requirements, feature stability, and resolution. *Annu. Rev. Mater. Res.* **40**, 395–414.

DIMOVA, R., ARANDA, S., BEZLYEPKINA, N., NIKOLOV, V., RISKE, K. A. & LIPOWSKY, R. 2006 A practical guide to giant vesicles. probing the membrane nanoregime via optical microscopy. *J. Phys.: Condens. Matter* **18** (28), S1151.

DIMOVA, R., DIETRICH, C., HADJIISKY, A., DANOV, K. & POULIGNY, B. 1999 Falling ball viscosimetry of giant vesicle membranes: finite-size effects. *Eur. Phys. J. B* **12** (4), 589–598.

DIMOVA, R., POULIGNY, B. & DIETRICH, C. 2000 Pretransitional effects in dimyristoylphosphatidylcholine vesicle membranes: optical dynamometry study. *Biophys. J.* **79** (1), 340–356.

DIMOVA, R., SEIFERT, U., POULIGNY, B., FÖRSTER, S. & DÖBEREINER, H.-G. 2002 Hyperviscous diblock copolymer vesicles. *Eur. Phys. J. E* **7** (3), 241–250.

DORBOLO, S., REYSSAT, E., VANDEWALLE, N. & QUÉRÉ, D. 2005 Aging of an antibubble. *EPL* **69** (6), 966–970.

DRAVID, V., SONGSERMPONG, S., XUE, Z., CORVALAN, C. M. & SOJKA, P. E. 2006 Two-dimensional modeling of the effects of insoluble surfactant on the breakup of a liquid filament. *Chem. Eng. Sci.* **61**, 3577–3585.

EDWARDS, D. A., BRENNER, H. & WASAN, D. T. 1991 *Interfacial transport processes and rheology*. Butterworth-Heinemann.

EGGERS, J. 1993 Universal pinching of 3d axisymmetric free-surface flow. *Phys. Rev. Lett.* **71**, 3458.

EGGERS, J 1997 Nonlinear dynamics and breakup of free surface flows. *Rev. Mod. Phys.* **69**, 865–929.

EGGERS, J. & DUPONT, T. F. 1994 Drop formation in a one-dimensional approximation of the Navier-Stokes equation. *J. Fluid Mech.* **262**, 205–222.

EGGERS, J. & FONTELOS, M. A. 2005 Isolated inertialess drops cannot break up. *J. Fluid Mech.* **530**, 177–180.

EGGERS, J. & FONTELOS, M. A. 2015 *Singularities: formation, structure, and propagation*, , vol. 53. Cambridge University Press.

EGGERS, J. & VILLERMAUX, E. 2008 Physics of liquid jets. *Rep. Prog. Phys.* **71**, 036601.

ELFRING, G. J., LEAL, L. G. & SQUIRES, T. M. 2016 Surface viscosity and marangoni stresses at surfactant laden interfaces. *J. Fluid Mech.* **792**, 712–739.

ENTOV, V. M. & HINCH, E. J. 1997 Effect of a spectrum of relaxation times on the capillary thinning of a filament of elastic liquid. *J. Non-Newton. Fluid Mech.* **72** (1), 31–53.

ENTOV, V. M. & YARIN, A. L. 1984 Influence of elastic stresses on the capillary breakup of jets of dilute polymer solutions. *Fluid Dyn.* **19** (1), 21–29.

FARUTIN, A., ÉTIENNE, J., MISBAH, C. & RECHO, P. 2019 Crawling in a fluid. *Phys. Rev. Lett.* **123** (11), 118101.

FONTELOS, M. A. & LI, J. 2004 On the evolution and rupture of filaments in giesekus and fene models. *J. Non-Newton. Fluid Mech.* **118** (1), 1–16.

FULLER, G.G. & VERMANT, J. 2012 Complex fluid-fluid interfaces: rheology and structure. *Annu. Rev. Chem. Biomol. Eng.* **3**, 519–543.

GARCÍA, F. J. & CASTELLANOS, A. 1994 One-dimensional models for slender axisymmetric viscous liquid jets. *Phys. Fluids* **6** (8), 2676–2689.

GAUDET, S., MCKINLEY, G. H. & STONE, H. A. 1996 Extensional deformation of newtonian liquid bridges. *Phys. Fluids* **8** (10), 2568–2579.

GOEDDE, E. F. & YUEN, M. C. 1970 Experiments on liquid jet instability. *J. Fluid Mech.* **40** (3), 495–511.

GOLDIN, M., YERUSHALMI, J., PFEFFER, R. & SHINNAR, R. 1969 Breakup of a laminar capillary jet of a viscoelastic fluid. *J. Fluid Mech.* **38** (4), 689–711.

GONZÁLEZ, H. & GARCÍA, F. J. 2009 The measurement of growth rates in capillary jets. *J. Fluid Mech.* **619**, 179–212.

HAJILOO, A., RAMAMOHAN, T.R. & SLATTERY, J.C. 1987 Effect of interfacial viscosities on the stability of a liquid thread. *J. Colloid Interf. Sci.* **117** (2), 384–393.

HAKIM, V. & SILBERZAN, P. 2017 Collective cell migration: a physics perspective. *Rep. Prog. Phys.* **80** (7), 076601.

HANSEN, S., PETERS, G.W.M. & MEIJER, H.E.H. 1999 The effect of surfactant on the stability of a fluid filament embedded in a viscous fluid. *J. Fluid Mech.* **382**, 331–349.

HERMANS, E., BHAMLA, M. S., KAO, P., FULLER, G. G. & VERMANT, J. 2015 Lung surfactants and different contributions to thin film stability. *Soft Matter* **11** (41), 8048–8057.

JAENSSON, N. & VERMANT, J. 2018 Tensiometry and rheology of complex interfaces. *Curr. Opin. Colloid Interface Sci* **37**, 136–150.

JOYE, J.-L., HIRASAKI, G. J. & MILLER, C. A. 1994 Asymmetric drainage in foam films. *Langmuir* **10**, 3174–3179.

JÜLICHER, F., GRILL, S. W & SALBREUX, G. 2018 Hydrodynamic theory of active matter. *Rep. Prog. Phys.* **81** (7), 076601.

KALAAJI, A., LOPEZ, B., ATTANE, P. & SOUCEMARIANADIN, A. 2003 Breakup length of forced liquid jets. *Phys. Fluids* **15**, 2469–2479.

KAMAT, P. M., WAGONER, B. W., THETE, S. S. & BASARAN, O. A. 2018 Role of marangoni stress during breakup of surfactant-covered liquid threads: Reduced rates of thinning and microthread cascades. *Phys. Rev. Fluids* **3** (4), 043602.

KANTSLER, V., SEGRE, E. & STEINBERG, V. 2008 Critical dynamics of vesicle stretching transition in elongational flow. *Phys. Rev. Lett.* **101** (4), 048101.

KARAPETSAS, GEORGE & BONTOZOGLOU, VASILIS 2013 The primary instability of falling films in the presence of soluble surfactants. *J. Fluid Mech.* **729**, 123–150.

KELLER, J. B. & MIKSIS, M. J. 1983 Surface tension driven flows. *SIAM J. App. Math.* **43** (2), 268–277.

KOVALCHUK, N. M., JENKINSON, H., MILLER, R. & SIMMONS, M. J. H. 2018 Effect of soluble surfactants on pinch-off of moderately viscous drops and satellite size. *J. Colloid Interf. Sci.* **516**, 182–191.

KOWALEWSKI, T. A 1996 On the separation of droplets from a liquid jet. *Fluid Dyn. Res.* **17**, 121–145.

LAFRANCE, P. 1975 Nonlinear breakup of a laminar liquid jet. *Phys. Fluids* **18** (4), 428–432.

LANGEVIN, D. 2014 Rheology of adsorbed surfactant monolayers at fluid surfaces. *Annu. Rev. Fluid Mech.* **46**, 47–65.

LI, J. & FONTELOS, M. A. 2003 Drop dynamics on the beads-on-string structure for viscoelastic jets: A numerical study. *Phys. Fluids* **15** (4), 922–937.

LIAO, Y. C., FRANSES, E. I. & BASARAN, O. A. 2006 Deformation and breakup of a stretching liquid bridge covered with an insoluble surfactant monolayer. *Phys. Fluids* **18** (2), 022101.

MANSOUR, NAGI N & LUNDGREN, THOMAS S 1990 Satellite formation in capillary jet breakup. *Phys. Fluids A: Fluid Dyn.* **2** (7), 1141–1144.

MARCHETTI, M. C., JOANNY, J.-F., RAMASWAMY, S., LIVERPOOL, T. B., PROST, J., RAO, M. & SIMHA, R. A. 2013 Hydrodynamics of soft active matter. *Rev. Mod. Phys.* **85** (3), 1143.

MARTÍNEZ-CALVO, A., RIVERO-RODRÍGUEZ, J., SCHEID, B. & SEVILLA, A. 2020 Natural break-up and satellite formation regimes of surfactant-laden liquid threads. *J. Fluid Mech.* **883**, A35.

MARTÍNEZ-CALVO, A. & SEVILLA, A. 2018 Temporal stability of free liquid threads with surface viscoelasticity. *J. Fluid Mech.* **846**, 877–901.

MASHAYEK, F. & ASHGRIZ, N. 1995 Nonlinear instability of liquid jets with thermocapillarity. *J. Fluid Mech.* **283**, 97–123.

MCGOUGH, P. T. & BASARAN, O. A. 2006 Repeated formation of fluid threads in breakup of a surfactant-covered jet. *Phys. Rev. Lett.* **96** (5), 054502.

MIETKE, A., JEMSEENA, V., KUMAR, K. V., SBALZARINI, I. F. & JÜLICHER, F. 2019*a* Minimal model of cellular symmetry breaking. *Phys. Rev. Lett.* **123** (18), 188101.

MIETKE, A., JÜLICHER, F. & SBALZARINI, I. F. 2019*b* Self-organized shape dynamics of active surfaces. *Proc. Natl. Acad. Sci. U.S.A.* **116** (1), 29–34.

MILLIKEN, W. J., STONE, H. A. & LEAL, L. G. 1993 The effect of surfactant on the transient motion of Newtonian drops. *Phys. Fluids A: Fluid Dynamics* **5** (1), 69–79.

NARSIMHAN, V., SPANN, A. P. & SHAQFEH, E. S. G. 2015 Pearling, wrinkling, and buckling of vesicles in elongational flows. *J. Fluid Mech.* **777**, 1–26.

NOTZ, P. K. & BASARAN, O. A. 2004 Dynamics and breakup of a contracting liquid filament. *J. Fluid Mech.* **512**, 223–256.

OZAN, S. C. & JAKOBSEN, H. A. 2019 On the role of the surface rheology in film drainage between fluid particles. *Int. J. Multiphase Flow* **120**, 103103.

PAPAGEORGIOU, D.T. 1995 On the breakup of viscous liquid threads. *Phys. Fluids* **7** (7), 1529–1544.

PEREIRA, A. & KALLIADASIS, S. 2008 On the transport equation for an interfacial quantity. *Eur. Phys. J. Appl. Phys.* **44** (2), 211–214.

PLATEAU, J. 1873 *Statique expérimentale et théorique des liquides*. Gauthier-Villars et C^{ie}, Paris.

PONCE-TORRES, A., HERRADA, M. A., MONTANERO, J. M. & VEGA, J. M. 2016 Linear and nonlinear dynamics of an insoluble surfactant-laden liquid bridge. *Phys. Fluids* **28**, 112103.

PONCE-TORRES, A., MONTANERO, J. M., HERRADA, M. A., VEGA, E. J. & VEGA, J. M. 2017 Influence of the surface viscosity on the breakup of a surfactant-laden drop. *Phys. Rev. Lett.* **118**, 024501.

POWERS, THOMAS R. 2010 Dynamics of filaments and membranes in a viscous fluid. *Rev. Mod. Phys.* **82**, 1607–1631.

PROSSER, A. J. & FRANSES, E. I. 2001 Adsorption and surface tension of ionic surfactants at the air-water interface: Review and evaluation of equilibrium models. *Colloid Surface A* **178** (1-3), 1–40.

PROST, J., JÜLICHER, F. & JOANNY, J.-F. 2015 Active gel physics. *Nat. Phys.* **11** (2), 111–117.

QUÉRÉ, D. & DE RYCK, A. 1998 Le mouillage dynamique des fibres., vol. 23, pp. 1–149. EDP Sciences.

RAYLEIGH, W. S. 1878 On the instability of jets. *Proc. R. Soc. Lond.* **10**, 4–13.

RAYLEIGH, W. S. 1890 On the superficial viscosity of water. *Proc. R. Soc. Lond.* **48**, 127–140.

RAYLEIGH, W. S. 1892 On the instability of a cylinder of viscous liquid under capillary force. *Phil. Mag. and J. Science* **34** (207), 145–154.

RIVERO-RODRÍGUEZ, J. & SCHEID, B. 2018*a* Bubble dynamics in microchannels: inertial and capillary migration forces. *J. Fluid Mech.* **842**, 215–247.

RIVERO-RODRÍGUEZ, J. & SCHEID, B. 2018*b* Bubble dynamics in microchannels: inertial and capillary migration forces – CORRIGENDUM. *J. Fluid Mech.* **855**, 1242–1245.

RODRÍGUEZ-RODRÍGUEZ, J., SEVILLA, A., MARTÍNEZ-BAZÁN, C. & GORDILLO, J. M. 2015 Generation of microbubbles with applications to industry and medicine. *Annu. Rev. Fluid Mech.* **47**, 405–429.

RUIZ-HERRERO, T., FAI, T. G. & MAHADEVAN, L. 2019 Dynamics of growth and form in prebiotic vesicles. *Phys. Rev. Lett.* **123** (3), 038102.

RUTLAND, D.F. & JAMESON, G.J. 1970 Theoretical prediction of the sizes of drops formed in the breakup of capillary jets. *Chem. Eng. Sci.* **25** (11), 1689–1698.

RUTLAND, D.F. & JAMESON, G.J. 1971 A non-linear effect in the capillary instability of liquid jets. *J. Fluid Mech.* **46** (2), 267–271.

SAFFMAN, P. G. 1976 Brownian motion in thin sheets of viscous fluid. *J. Fluid Mech.* **73** (4), 593–602.

SAFFMAN, P G & DELBRÜCK, M 1975 Brownian motion in biological membranes. *Proc. Natl. Acad. Sci. USA* **72** (8), 3111–3113.

SCHEID, B., DELACOTTE, J., DOLLET, B., RIO, E., RESTAGNO, F., VAN NIEROP, E. A., CANTAT, I., LANGEVIN, D. & STONE, H. A. 2010 The role of surface rheology on liquid film formation. *EPL* **90**, 24002.

SCHEID, B., DORBOLO, S., ARRIAGA, L. R. & RIO, E. 2012 Antibubble dynamics: the drainage of an air film with viscous interfaces. *Phys. Rev. Lett.* **109** (26), 264502.

SCRIVEN, L. E. 1960 Dynamics of a fluid interface. Equation of motion for Newtonian surface fluids. *Chem. Eng. Sci.* **12** (2), 98–108.

SEIFERT, U. 1997 Configurations of fluid membranes and vesicles. *Adv. Phys.* **46** (1), 13–137.

SEIWERT, J., DOLLET, B. & CANTAT, I. 2014 Theoretical study of the generation of soap films: Role of interfacial visco-elasticity. *J. Fluid Mech.* **739**, 124–142.

STONE, H. A. 1990 A simple derivation of the time-dependent convective-diffusion equation for surfactant transport along a deforming interface. *Phys. Fluids A* **2** (1), 111–112.

STONE, H. A. 1995 Fluid motion of monomolecular films in a channel flow geometry. *Phys. Fluids* **7** (12), 2931–2937.

STONE, H. A. & BRENNER, M. P. 1996 Note on the capillary thread instability for fluids of equal viscosities. *J. Fluid Mech.* **318**, 373–374.

STONE, H. A. & LEAL, L. G. 1990 The effects of surfactants on drop deformation and breakup. *J. Fluid Mech.* **220**, 161–186.

TIMMERMANS, M.-L. & LISTER, J. R. 2002 The effect of surfactant on the stability of a liquid thread. *J. Fluid Mech.* **459**, 289–306.

TJAHJADI, M., STONE, H. A. & OTTINO, J. M. 1992 Satellite and subsatellite formation in capillary breakup. *J. Fluid Mech.* **243**, 297–317.

TOMOTIKA, S. 1935 On the instability of a cylindrical thread of a viscous liquid surrounded by another viscous fluid. *Proc. Roy. Soc.* **150**, 322–337.

TOZZI, C., WALANI, N. & ARROYO, M. 2019 Out-of-equilibrium mechanochemistry and self-organization of fluid membranes interacting with curved proteins. *New J. Phys.* **21** (9), 093004.

TWEEDY, J. & ETHIER, C. 2011 Fluid mechanics of the eye. *Annu. Rev. Fluid Mech.* **44**, 347–372.

VAN GOLDE, L. M., BATENBURG, J. J. & ROBERTSON, B. 1988 The pulmonary surfactant system: biochemical aspects and functional significance. *Physiological Reviews* **68** (2), 374–455.

VITRY, Y., DORBOLO, S., VERMANT, J. & SCHEID, B. 2019 Controlling the lifetime of antibubbles. *Adv. Colloid Interface Sci.* .

WANG, F., CONTÒ, F.P., NAZ, N., CASTREJÓN-PITA, J.R., CASTREJÓN-PITA, A.A., BAILEY, C.G., WANG, W., FENG, J.J. & SUI, Y. 2019 A fate-alternating transitional regime in contracting liquid filaments. *J. Fluid Mech.* **860**, 640–653.

WHITAKER, S. 1976 Studies of the drop-weight method for surfactant solutions III. Drop stability, the effect of surfactants on the stability of a column of liquid. *J. Colloid Interf. Sci.* **54** (2), 231–248.

WONG, H., RUMSCHITZKI, D. & MALDARELLI, C. 1996 On the surfactant mass balance at a deforming fluid interface. *Phys. Fluids* **8** (11), 3203–3204.

YUEN, M.-C. 1968 Non-linear capillary instability of a liquid jet. *J. Fluid Mech.* **33** (1), 151–163.

CHAPTER 5

Linear and Nonlinear Dynamics of Confined Capillary Jets†

5.1 Introduction

The great research effort devoted in the past to understand and control the dynamics of liquid jets is justified by their rich phenomenology and the large number of technological applications where they play a central role, such as fuel atomization, chemical reactors, ink-jet and 3D printing, additive manufacturing, microfluidic platforms, drug encapsulation, mass spectrometry or cytometry, to name a few (see e.g. the reviews by Bogy, 1979; Eggers, 1997; Lin & Reitz, 1998; Basaran, 2002; Barrero & Loscertales, 2007; Christopher & Anna, 2007; Eggers & Villermaux, 2008; Derby, 2010; Anna, 2016). These applications often require the generation of micrometre-sized jets and drops, in which case it proves convenient to downscale the disperse phase from a typically millimetre-sized injector to the desired micrometer scales to avoid clogging issues. This stretching effect can be achieved through different techniques like fibre spinning (Matovich & Pearson, 1969; Pearson & Matovich, 1969), electrospinning (Doshi & Reneker, 1995), flow focusing (Gañán-Calvo, 1998), viscous co-flows (Suryo & Basaran, 2006; Marín *et al.*, 2009; Evangelio *et al.*, 2016) and gravitational stretching (Sauter & Buggisch, 2005; Rubio-Rubio *et al.*, 2013). The latter configuration is particularly simple to implement, and the present work naturally extends the investigation of Rubio-Rubio *et al.* (2013) to assess the influence of a finite jet length and nonlinearity on the dynamics of the liquid thread.

In the absence of axial confinement, previous studies of the downwards injection of a constant flow rate of liquid into a passive gaseous atmosphere have demonstrated the existence of two different flow states, namely dripping and jetting, respectively prevailing for small and large enough values of the flow rate (Clanet & Lasheras, 1999; Ambravaneswaran *et al.*, 2004). The jetting regime is characterized by the formation of a liquid column which breaks-up into drops at a certain distance from the injector due to the downstream growth of axisymmetric capillary instability waves (see e.g. Plateau, 1873; Rayleigh, 1878; Donnelly & Glaberson, 1966; Kalaaji *et al.*, 2003; González & García, 2009). In contrast, the dripping regime features the emission of comparatively larger drops near the injector (Wilkes *et al.*,

---

[†] Published as Martínez-Calvo, Rubio-Rubio & Sevilla (*J. Fluid Mech.*, vol. 834, 2018, pp. 335–358)

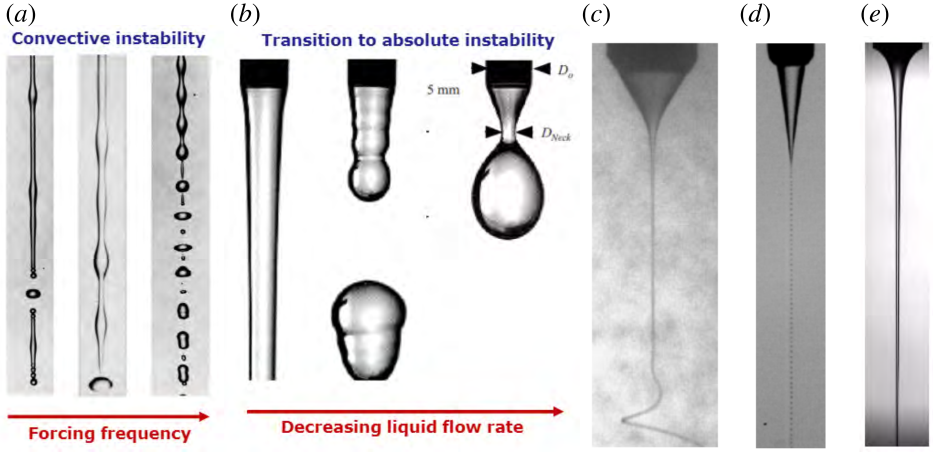

Figure 5.1: (*a*) Convectively unstable capillary jet forced at three different frequencies. Adapted from Rutland & Jameson (1971) (*b*) The jetting-dripping transition that takes place as the flow rate decreases. Adapted from Clanet & Lasheras (1999). Three different techniques for stretched liquid interfaces: (*c*) electrospinning (Doshi & Reneker, 1995), (*d*) viscous coflow (Suryo & Basaran, 2006; Marín *et al.*, 2009), (*e*) gravitational stretching (Sauter & Buggisch, 2005; Rubio-Rubio *et al.*, 2013)

1999; Coullet *et al.*, 2005; Subramani *et al.*, 2006). From the point of view of local stability theory, the jetting regime is a convectively unstable flow, in which the downstream advection of growing disturbances by the underlying base flow allows the formation of a long liquid column. Moreover, several works have successfully described the transition from jetting to dripping as a global instability that, in the case of quasi-parallel jets, is linked with the onset of local absolute instability (Leib & Goldstein, 1986*a*,*b*; Le Dizès, 1997; Vihinen *et al.*, 1997; O'Donnell *et al.*, 2001; Söderberg, 2003; Sevilla, 2011; Guerrero *et al.*, 2016).

The concepts of convective and absolute instability rely on the assumption of quasi-parallel flow, and do not apply to cases where the wavelength of disturbances is of the order of the development length of the base flow, as happens in highly stretched jets like those studied in the present work. In these cases a global stability analysis must be performed, in which the spatial structure of the eigenfunctions is obtained as part of the solution (Theofilis, 2011). The global stability analysis is greatly simplified by the use of one-dimensional approximations to the full conservation equations, since the eigenvalue problem involves only the axial coordinate as an eigendirection (see e.g. Pearson & Matovich, 1969; Sauter & Buggisch, 2005; Rubio-Rubio *et al.*, 2013; Gordillo *et al.*, 2014). In particular, a global stability analysis of the leading-order one-dimensional model for viscous liquid columns (García & Castellanos, 1994; Eggers & Dupont, 1994) derived in chapter 2, was first applied to gravitationally stretched viscous jets by Sauter & Buggisch (2005), and refined later on by Rubio-Rubio *et al.* (2013). The latter works revealed that the axisymmetric self-excited oscillations observed in long viscous jets below a certain critical flow rate are explained by the destabilisation of a linear global mode.

Despite the usefulness of linearized theory to predict many features of liquid jets, there are relevant aspects of their dynamics that can only be described using a nonlinear approach, prominent examples being the pinch-off singularity (Eggers, 1993) and the formation of satellite droplets (Yuen, 1968; Nayfeh, 1970; Rutland & Jameson, 1971; Ashgriz & Mashayek, 1995; Martínez-Calvo *et al.*, 2020). In the present work we introduce a new configuration where nonlinearity provides the selection mechanism between two different regimes after the jet becomes globally unstable: either a limit-cycle state without breakup described here for the first time, or a fully developed dripping state.

Liquid threads of finite length, either by their impingement onto a bath of the same liquid, or by their impact on a solid plate, have also been considered in previous works. Thus, the shape and stability of quasi-static axisymmetric liquid bridges formed between a solid rod and an infinite bath were studied by Kovitz (1975), and more recently by Benilov & Oron (2010) and Benilov & Cummins (2013). Christodoulides & Dias (2010) studied the steady structure of planar vertical inviscid jets impinging onto a horizontal solid plate. However, most of the literature deals with the phenomenon of coiling, the fascinating buckling instability associated with the impact of a jet or film of viscous liquid on a solid substrate (see Ribe *et al.*, 2012, and references therein). Another beautiful and surprisingly rich phenomenon that has been studied is the deposition of viscous threads on moving solid substrates (Chiu-Webster & Lister, 2006; Blount & Lister, 2011). These coiling states and deposition patterns break the axial symmetry, and their mathematical description is complicated by the fact that the thread centreline must be obtained as part of the solution (Entov & Yarin, 1984; Guerrero *et al.*, 2014; Rivero-Rodriguez & Pérez-Saborid, 2015). Although in the experiments reported herein we have observed coiling under certain conditions, our focus is on the global self-excited oscillations caused by the destabilisation of the axisymmetric breathing mode studied by Sauter & Buggisch (2005) and Rubio-Rubio *et al.* (2013). It should be pointed out that the breathing mode and the coiling phenomenon coexist in a wide region of parameter space. Nevertheless, in all the cases considered herein the coupling between both modes is weak enough for a purely axisymmetric model to provide a reasonably good leading-order description, not only of the neutral conditions for the onset of the breathing mode, but also of the long-time regime of the jet.

In the present chapter we report experiments performed to characterize the linear and nonlinear stability properties of jets of Newtonian liquid, injected at a constant flow rate through a circular tube, that impinge on the free surface of a reservoir of the same liquid placed at a controlled distance from the injector. The experiments are complemented with a global stability analysis and numerical simulations, both based on the leading-order one-dimensional mass and momentum equations retaining the full expression of the interfacial curvature (Eggers & Dupont, 1994; Rubio-Rubio *et al.*, 2013). This slender approximation has been derived in detail in chapter 2. We also study the selection of nonlinear regimes under globally unstable conditions. The experimental setup and the mathematical model are described in §5.2, and the results are presented in §5.3, finally leading to the conclusions drawn in §5.4.

5.2 Experimental setup and mathematical model

In this section we detail the experimental setup where the experiments are carried out, and the mathematical modeling used throughout the chapter.

5.2.1 Flow configuration and experimental setup

Figure 5.2(a) sketches the configuration under study, where a liquid of density ρ, kinematic viscosity ν, and surface tension coefficient σ is injected at a constant flow rate Q through a circular tube of radius R whose length is sufficiently large to guarantee a fully-developed velocity profile at its outlet. The resulting free liquid jet is confined in the axial direction through its impact with the free surface of a reservoir of the same liquid placed at a distance L from the injector outlet. To ensure that the results are independent of the downstream boundary condition, we have also performed several experiments where the jet impacts a solid horizontal plate, obtaining nearly identical results. The surrounding gaseous atmosphere, at pressure p_a, has a negligible dynamic effect on the jet due to the smallness of the typical liquid velocities.

The experiments were performed in the same setup used by Rubio-Rubio *et al.* (2013), with the only addition of a vertical positioning stage located below the injection tube and mounting a platform onto which a reservoir filled with the working liquid was placed. The free surface of the reservoir, located at a distance L from the injector outlet, was impinged by the liquid jet as shown in figure 5.2. The liquid was supplied with a Harvard Apparatus PhD Ultra syringe pump, and the free jet was recorded using a Red Lake Motion Pro X high speed camera. To minimize the effect of ambient noise, both the injector and the camera were installed inside a transparent isolation chamber, and the entire system except the syringe pump was placed on an optical table with a passive vibration damping system. Two stainless steel capillary tubes acquired from Tubca were used as injectors, of inner radii $R = 1.5$ mm and $R = 1.75$ mm, that were carefully machined at their tip to ensure that the contact line remained pinned at their inner radii. Two different Newtonian liquids were used in the experiments, both of them PDMS silicon oils from Sigma-Aldrich, whose properties at 25 °C are $\rho = 970$ kg m^{-3}, $\sigma = 21.1$ mN m^{-1}, and kinematic viscosities $\nu = 500$ and $\nu = 1000$ mm^2 s^{-1}, with corresponding values of the Kapitza number, $Ka = 3\nu[(\rho^3 g)/\sigma^3]^{1/4}$, of $Ka = 8.33$ and $Ka = 16.67$, respectively. In each experimental run, first an injection tube and a silicone oil were selected, and the vertical stage was positioned to provide the desired value of L. The syringe pump was programmed to inject an initial liquid flow rate large enough to provide a jetting regime, and to smoothly decrease until the desired target value of Q was achieved.

5.2.2 Basic experimental evidence

From the results of the experiments it is deduced that, leaving the presence of coiling apart, there are three possible regimes whose occurrence depends on the values of the control

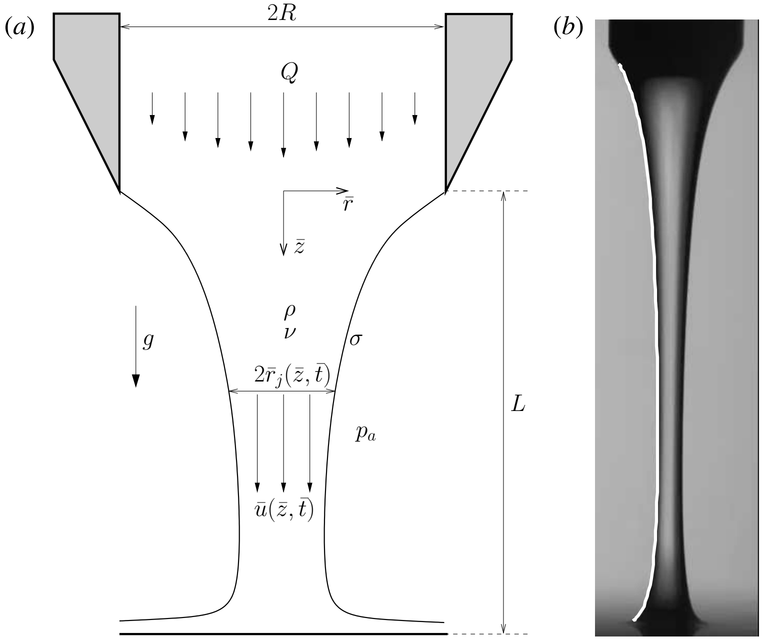

Figure 5.2: (*a*) Sketch of the flow configuration. (*b*) Photograph of a steady jet for ν = 500 cSt (Ka = 8.33), R = 1.75 mm (Bo = 1.38), Q = 3.5 ml/min ($We = 3.05 \times 10^{-3}$) and L = 16.6 mm (L/R = 9.47). The white line shows the steady solution of equations (5.1)–(5.3).

parameters. Let us begin by classifying these regimes following the order in which they are observed when Q decreases smoothly and the rest of the control parameters are fixed:

1. **Steady jetting:** This regime is illustrated in figure 5.2(*b*), which shows a photograph of a steady jet of silicone oil with ν = 500 cSt injected through a tube of radius R = 1.75 mm at a constant flow rate Q = 3.5 ml/min that impinges on the free surface of an oil reservoir placed at a distance L = 16.6 mm of the injector. The steady jetting regime is stable if Q is larger than a certain critical value, Q_c.

When $Q < Q_c$ the jet is unstable due to an oscillatory axisymmetric global mode, leading to self-sustained oscillations of shape and velocity whose amplitude increases with time (Sauter & Buggisch, 2005; Rubio-Rubio *et al.*, 2013). This linear global mode is also referred to as the *breathing mode* throughout the chapter. Our experiments reveal that two different nonlinear states may take place if $Q < Q_c$:

2. **Oscillatory jetting:** When $Q_b < Q < Q_c$ a limit-cycle state without breakup is achieved, whereby the oscillation amplitude saturates to a certain function of the downstream position (see figure 5.9). This regime can be observed in figures 5.7–5.11. Note that the oscillatory jetting regime is a nonlinear saturated state of limit-cycle kind achieved by the liquid thread, and it should not be confused with the linear breathing mode, which

is linearly globally unstable under the conditions where both the oscillatory jetting and dripping regimes take place.

3. **Dripping:** When $Q < Q_b$, the amplitude of the oscillations grows until the breakup of the jet takes place, finally leading to a jetting-dripping transition, as illustrated in figure 5.12.

This evidence calls out for an experimental and numerical characterisation of the functions $Q_c\,(\nu, R, L)$ and $Q_b\,(\nu, R, L)$, that were thus obtained in a wide region of parameter space, as reported in §5.3.

5.2.3 One-dimensional model

To model the liquid jet we use the dimensionless leading-order one-dimensional mass and momentum equations (Eggers & Dupont, 1994; García & Castellanos, 1994) derived previously in chapter 2, section §2.2, and which in the limit of negligible surface elasticity and viscosities reads

$$\frac{\partial a^2}{\partial t} + \frac{\partial (w a^2)}{\partial z} = 0, \tag{5.1}$$

$$\frac{\partial w}{\partial t} + w\frac{\partial w}{\partial z} = 1 - \frac{\partial C}{\partial z} + \frac{Ka}{a^2}\frac{\partial}{\partial z}\left(a^2\frac{\partial w}{\partial z}\right), \tag{5.2}$$

$$C = a^{-1}\left[1 + \left(\frac{\partial a}{\partial z}\right)^2\right]^{-1/2} - \frac{\partial^2 a}{\partial z^2}\left[1 + \left(\frac{\partial a}{\partial z}\right)^2\right]^{-3/2}, \tag{5.3}$$

where the dependent variables w and a are the liquid velocity and jet radius respectively, z is the axial coordinate, t is the time and C is the interfacial curvature. It is worth pointing out that the full expression for the curvature needs to be retained for the model to provide good quantitative predictions of the stability in the case of large injector diameters, for which the jet experiences a strong gravitational stretching close to the neutral conditions and, correspondingly, the stabilizing effect of the axial curvature must be taken into account (Rubio-Rubio *et al.*, 2013). The variables in equations (5.1)-(5.3) have been made dimensionless using different characteristic scales than those used in chapter 1, namely the liquid density ρ, the capillary length $l_\sigma = (\sigma/\rho\, g)^{1/2}$, and the associated characteristic velocity $\sqrt{g\, l_\sigma}$ (Senchenko & Bohr, 2005). Thus, the system (5.1)-(5.3) only depends on Ka, which is constant for a given liquid and a fixed value of g. The solution depends on the constant flow rate, Q, and on the injector radius, R, through the dimensionless versions of the boundary conditions at $z = 0:\ a = R/l_\sigma = Bo^{1/2}$ and $w = U/\sqrt{g\, l_\sigma} = We^{1/2}Bo^{-1/4}$, where $Bo = \rho g R^2/\sigma$ is the Bond number, $We = \rho U^2 R/\sigma$ is the Weber number and $U = Q/(\pi R^2)$ the mean velocity at the nozzle exit. In addition, a Dirichlet boundary condition is imposed for the velocity at the downstream end of the domain, $z = L/l_\sigma$: $w = w_{\text{out}}$, as a crude but simple way to represent the impingement of the jet on the reservoir. Specifically, the value of w_{out} is

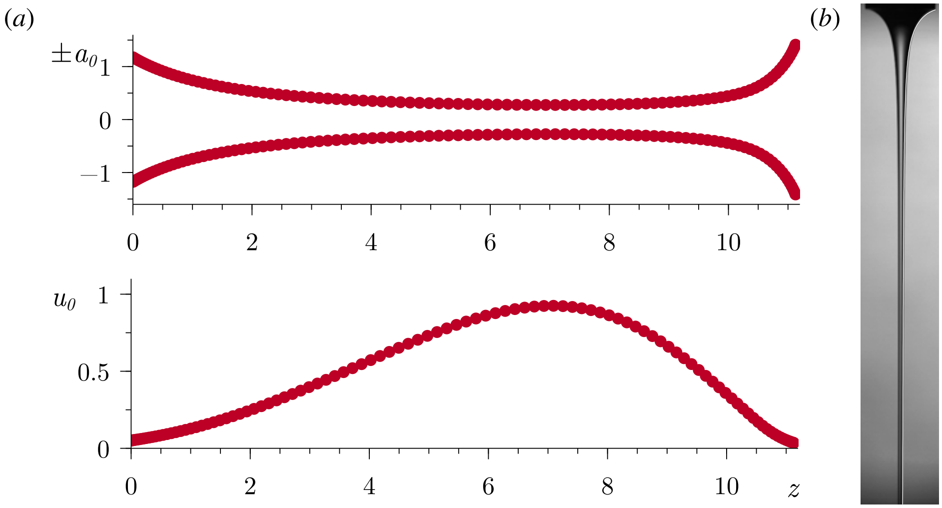

Figure 5.3: (a) Base flow radius $a_0(z)$ and velocity $w_0(z)$ for Ka = 3.33, Bo = 5.53, We = 1.85×10^{-3} and $L/R \gg 1$. The discrete points, N = 90, are plotted with symbols and the parameter which controls the coordinate transformation has a value of b = 10. (b) Photograph of a steady non-confined thread for the same configuration as in (a), which in dimensonal terms is, ν = 200 cSt, R = 3.5 mm, L > 48.68 mm and Q = 5.75 ml/min. The white line shows the steady solution of the equations (5.1)-(5.3)

small enough to properly describe the impact region, since the liquid bath is at rest far from the jet. This simple method provides fairly good results, as illustrated in figure 5.2(b) for the particular case of a steady jet. In addition, we have carefully checked that the results barely depend on the value chosen for the outflow velocity, provided that $w_{\text{out}} \lesssim 0.1$. In the case of relatively long jets with $L/R \gtrsim 20$, the value of w_{out} does not affect the results at all. Indeed, in this limit the impact region is very small compared to the length of the jet, and the outflow boundary condition affects neither the base flow nor its linear and nonlinear stability. In particular, these cases can be easily modeled either by imposing a Neumann outlet boundary condition, or even without imposing any outlet boundary condition at all (Rubio-Rubio *et al.*, 2013). The mathematical model is governed by four control parameters, namely Ka, Bo and We and the dimensionless length of the jet, $L/R = L/l_\sigma Bo^{-1/2}$, hereafter scaled with the injector radius for convenience.

5.3 Experimental and theoretical results

In this section we present the results of the experiments, as well as the linear stability analysis and the numerical simulations based on the one-dimensional model (5.1)-(5.3).

5.3.1 Linear stability analysis: the role of axial confinement

Let us begin by extending the linear stability results of Rubio-Rubio *et al.* (2013) to account for the effect of L/R on the critical Weber number, We_c, below which the jet becomes globally unstable. Since the methodology is identical to that presented in Rubio-Rubio *et al.* (2013), except for the treatment of the downstream boundary condition, the details of the formulation are provided in appendix 5.A. The procedure consists of linearizing equations (5.1)-(5.3) around a given steady basic state according to the following decomposition in temporal normal modes,

$$a(z,t) = a_0(z) + \epsilon a_1(z) e^{\omega t}, \tag{5.4}$$

$$w(z,t) = w_0(z) + \epsilon w_1(z) e^{\omega t}, \tag{5.5}$$

where $\epsilon \ll 1$ accounts for the smallness of the perturbation around the base flow $[a_0(z), w_0(z)]$, ω is the complex eigenfrequency, and $a_1(z)$ and $w_1(z)$ are the corresponding eigenfunctions. The values of $\omega_r = \Re(\omega)$ and $\omega_i = \Im(\omega)$ represent the growth rate and the angular frequency of a normal mode, respectively. Accordingly, the basic steady jet will be stable if $\max(\omega_r) < 0$, and unstable if $\max(\omega_r) > 0$. In the latter case, it is important to emphasize that the linearized description given by (5.4)-(5.5) is only valid during the initial stages of growth of small disturbances, so that the nonlinear terms are negligible in equations (5.1)-(5.3). It is also worth pointing out that the decomposition (5.4)-(5.5) does not rely on a local stability analysis, which would involve the usual expansion in normal modes of wavepacket form $\exp(\omega t + ikz)$. Thus, instead of searching for a dispersion relation $D(\omega, k) = 0$, here no a priori assumption is made about the shape of the eigenfunctions, whose spatial structure is obtained as part of the solution.

The basic flow, which satisfies the steady version of equations (5.1)-(5.3), was calculated using the procedure detailed in appendix 5.A.1. The discretized solution of equations (5.8)-(5.9) can be seen in Figures 5.3 and 5.4. In particular Figure 5.3 shows the radius and velocity of an unconfined steady jet, that is in the limit $L/R \gg 1$, for $Ka = 3.33$, $Bo = 5.53$, $We = 1.85 \times 10^{-3}$. In this limit, the impact region is not modeled since it does not affect the reliability of the results. On the contrary, Figure 5.4, shows the discretized solution for a steady finite-length jet which impacts onto a bath of the same liquid, for $Ka = 8.33$, $Bo = 1.38$, $We = 3.04 \times 10^{-3}$ and $L/R = 9.47$. In both cases, if an appropriate initial seed is chosen, the system converges to the steady solution, thus being no need to impose additional boundary conditions.

Once the base flow has been found, the critical conditions for the transition from a globally stable to a globally unstable jet are easily determined as a function of the governing parameters, $(Ka, Bo, We, L/R)$, by solving the linear stability problem as explained in appendix 5.A.2.

If the flow is stable, $\max(\omega_r) < 0$, small disturbances are damped and thus a steady flow is expected, like that shown in figure 5.2(*b*). In contrast, if $\max(\omega_r) > 0$ the jet is globally unstable and the development of spontaneous oscillations of increasing amplitude is predicted.

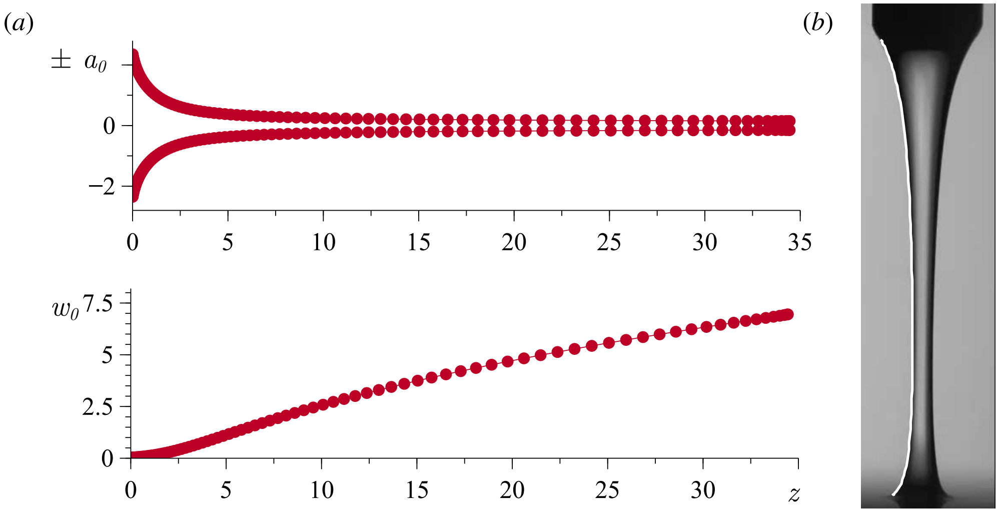

Figure 5.4: (*a*) Base flow radius $a_0(z)$ and velocity $w_0(z)$ for a generic setting of the flow, $Ka = 8.33$, $Bo = 1.38$, $We = 3.04 \times 10^{-3}$ and $L/R = 9.47$. The discrete points, $N = 108$, are plotted with symbols and the parameter which controls the coordinate change has a value of $b = 84$. (*b*) Photograph of a steady non-confined thread for the same configuration as in (a), which in dimensonal terms is, $\nu = 500$ cSt, $R = 1.75$ mm, $L = 16.58$ mm and $Q = 3.5$ ml/min. The white line shows the steady solution of the equations (5.1)-(5.3).

In particular, figure 5.5 shows the eigenvalue spectrum of an unstable configuration in (*a*), the baseflow in (*b*) and the real (solid lines) and imaginary (dashed lines) parts of the shape and velocity eigenfunctions in (*c*,*d*), respectively. In this case, two different scenarios emerge according to the experimental evidence described in §5.2.2: either the oscillations saturate to a limit cycle without breakup (see figures 5.7-5.11), or their growth leads to the pinch-off of the liquid column, eventually leading to a dripping regime (see figure 5.12). Since the oscillation amplitude increases in the downstream direction (see figure 5.9) it can be anticipated that the confinement parameter, L/R, will have a strong influence not only on the neutral stability curves, but also on the selection of the final nonlinear regime (see §5.3.2).

Both the experiments and the stability analysis reveal that the eigenvalue spectrum is strongly affected by the axial confinement for sufficiently small values of L/R. Consequently, We_c and $\omega_{c,i}$ are certain functions of L/R which can be easily computed with the methodology described in appendices 5.A.2 and 5.B.1. The main result is summarized in figure 5.6, which shows the good agreement of the experiments (symbols) with the prediction of the linear stability analysis (lines), especially for values of $L/R \lesssim 10$. Figure 5.6 reveals that both We_c and $\omega_{c,i}$ decrease as L/R decreases, indicating that axial confinement stabilizes the jet and reduces the critical frequency of the self-sustained oscillations. The symbols $\vartriangle$, $\triangledown$ in figure 5.6(*a*) define the experimentally determined range of neutral stability, due to the fact that the flow rate decreased in smooth ramps programmed with the syringe pump as described in §5.2.1. For sufficiently long jets, $L/R \gg 1$, the stability properties become independent of

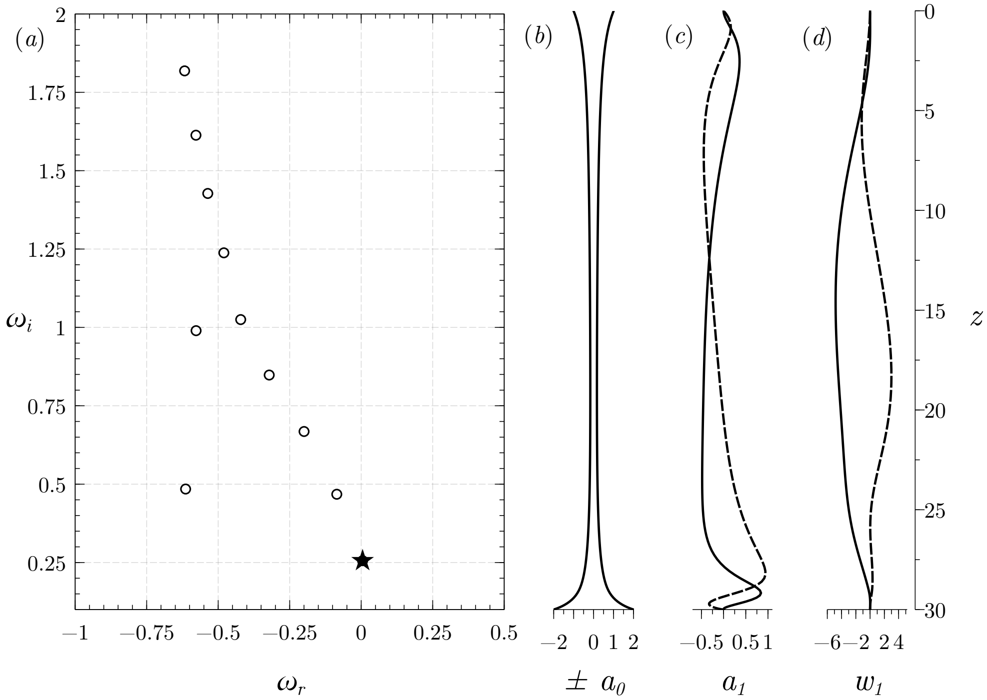

Figure 5.5: (*a*) Spectrum of eigenvalues ω, (*b*) base flow $a_0(z)$, and (*c*) and (*d*) the real (solid lines) and imaginary (dashed lines) parts of the leading eigenfunctions, a_1 and w_1, for $Ka = 16.67$, $Bo = 1$, $We = 6.5 \times 10^{-3}$ and $L/R = 30$, predicting an unstable capillary jet.

L/R, reaching the limit already studied by Sauter & Buggisch (2005) and Rubio-Rubio *et al.* (2013). In the opposite limit of strongly confined jets, figure 5.6(*a*) suggests the existence of a vertical asymptote, $We_c \longrightarrow 0$, and a corresponding critical value of the jet length, L_c/R. Indeed, the vertical lines plotted in figure 5.6(*a*) are the maximum lengths for which a static axisymmetric liquid bridge between a solid rod and an infinite pool is stable (Kovitz, 1975; Benilov & Cummins, 2013), namely $(Bo, L_c/R) \simeq (1, 1.31)$ and $(1.38, 1.19)$. Note from figure 5.6 that these values of L_c/R are consistent with our results in the hydrostatic limit, $We_c \longrightarrow 0$. It is therefore concluded that axial confinement stabilizes the liquid thread, and that the jet length below which such effect is noticeable depends on Ka and Bo, having values $L/R \lesssim 15$ for $(Ka, Bo) = (8.33, 1.38)$ and $L/R \lesssim 23$ for $(Ka, Bo) = (16.67, 1.00)$, as can be deduced from figure 5.6. In contrast, the hydrostatic limit reached as L/R decreases is independent of the parameter Ka, which incorporates the liquid viscosity, and is only a function of Bo. Figure 5.6 also reveals that the quantitative agreement between experiments and theory deteriorates for $L/R \gtrsim 10$, probably due to the limitations of the one-dimensional model. In particular, as emphasized by Rubio-Rubio *et al.* (2013), the model does not contemplate the viscous relaxation from the parabolic velocity profile at the injector outlet to the uniform

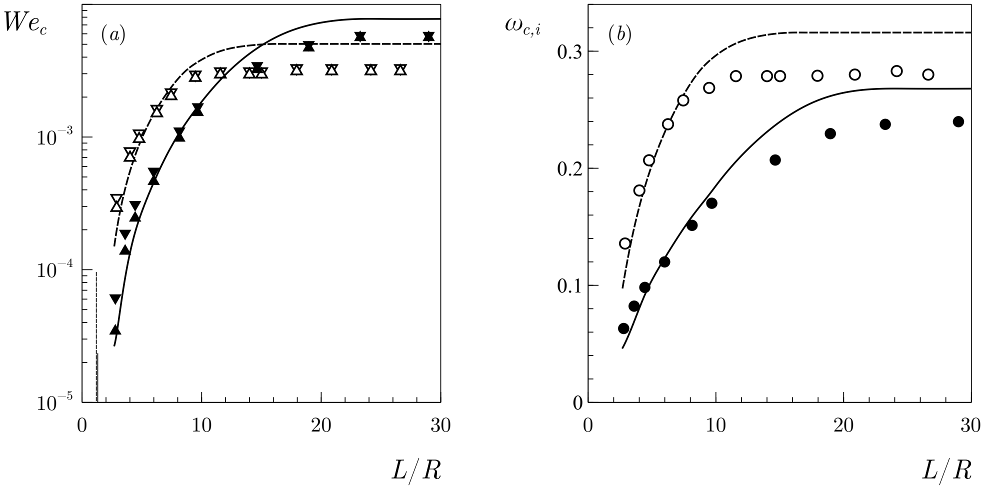

Figure 5.6: (*a*) Critical Weber number, We_c, and (*b*) corresponding angular frequency, $\omega_{c,i}$, as functions of L/R, for $(Ka, Bo) = (16.67, 1.00)$ (solid lines and filled symbols) and $(Ka, Bo) = (8.33, 1.38)$ (dashed lines and open symbols). The lines are the neutral curves obtained with the linear stability analysis. The symbols represent the experimental results for the maximum (▽) and minimum (△) values of We_c, and for the critical frequency (○). The vertical thin lines in panel (a) are the critical lengths given by the hydrostatic limit, $We_c \to 0$ (Kovitz, 1975; Benilov & Cummins, 2013).

velocity profile achieved downstream. In contrast, the good quantitative agreement found for $L/R \lesssim 10$ may well be due to the fact that the hydrostatic limit, $We_c \to 0$, is described exactly by the theoretical model thanks to the use of the full expression for the interfacial curvature in equation (5.3).

5.3.2 Nonlinear stability

The present section is devoted to address the influence of the control parameters on the selection of the final jet state under globally unstable conditions, $Q < Q_c$. Although the linear stability analysis presented in §5.3.1 provides values of Q_c in fairly good agreement with experiments, it cannot predict the final state of the jet at large times, which is determined by nonlinear effects. Therefore, in addition to the experiments, we have conducted numerical simulations of equations (5.1)-(5.3), which were integrated by means of the simple and efficient method explained in appendix 5.B.2. In particular, this approach allows to numerically compute the nonlinear saturation process that takes place in the oscillatory jetting regime, and to determine the breakup flow rate, Q_b, as a function of the governing parameters ν, R and L.

Let us first describe the main characteristics of the oscillatory jetting regime, which takes place for $Q_b < Q < Q_c$ or, in dimensionless terms, for $We_b < We < We_c$. For clarity, hereinafter the values of the variables provided by experiments, linear stability analysis and numerical simulations will be denoted using the superscripts $()^{\mathrm{exp}}$, $()^{\mathrm{lsa}}$ and $()^{\mathrm{num}}$, respectively.

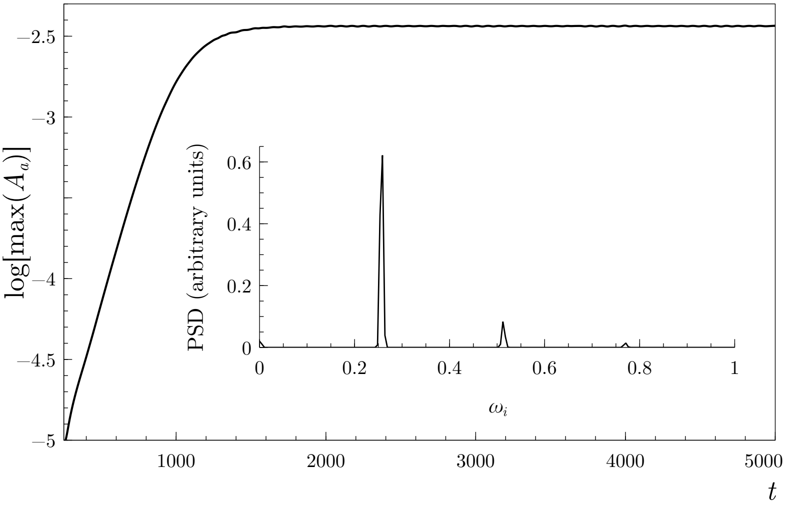

Figure 5.7: Logarithm of the radius oscillation amplitude at $z = z^* = 0.73L$ as a function of time extracted from a numerical simulation of equations (5.1)-(5.3) starting from a very small disturbance superimposed on a slightly unstable steady solution, namely $Ka = 16.67$, $Bo = 1$, $L/R = 23.26$ and $We^{\mathrm{num}} = 6.8 \times 10^{-3} < We_c^{\mathrm{num}}$. After an initial stage of exponential growth during the linear regime, $t \lesssim 800$, the amplitude saturates to a constant value for $t \gtrsim 2000$ due to nonlinear effects. The inset shows the power spectral density of the saturated oscillations, where the most energetic frequency and its two leading harmonics can be appreciated.

Figure 5.7 shows a numerical example of the oscillation amplitude growth induced by a very small initial disturbance superimposed on the steady state solution under globally unstable conditions, namely $Ka = 16.67$, $Bo = 1$, $L/R = 23.26$ and $We^{\mathrm{num}} = 6.8 \times 10^{-3} < We_c^{\mathrm{num}} = We_c^{\mathrm{lsa}} = 7.88 \times 10^{-3}$. In figure 5.7 the logarithm of the maxima of a pointwise measure of the radius oscillation, $A_a = a(z^*, t) - a_0(z^*)$, where $z^* = 0.73L$, is plotted as a function of time. The choice of the value $z^* = 0.73L$ to measure the jet oscillations was motivated by the fact that their amplitude is sufficiently large at this distance from the injector to allow a precise measurement. In addition, in cases where coiling takes place, like that shown in figure 5.9(*b*), the coiling amplitude at this point is small enough for its influence on the results to be negligible. Three different stages can be clearly identified in figure 5.7. First, an initial linear growth regime for $t \lesssim 800$, where the small disturbance increases exponentially with time with a growth rate given by $\omega_r^{\mathrm{num}} = 3.28 \times 10^{-3}$ and $\omega_r^{\mathrm{lsa}} = 3.23 \times 10^{-3}$ according to the numerical simulation and the linear stability analysis presented in §5.3.1, respectively. During the second stage, $800 \lesssim t \lesssim 2000$, a transition regime takes place where nonlinear effects become important and moderate the exponential growth. Third, for $t \gtrsim 2000$, the oscillation amplitude saturates to a certain constant. The inset of figure 5.7 represents the power spectral density (PSD) of the saturated signal, clearly showing the dominant angular frequency and its two leading harmonics. The value of the dominant frequency extracted from the numerical PSD is $\omega_i^{\mathrm{num}} = 0.259$, to be compared with the corresponding value of the leading eigenmode computed with the linear stability analysis of §5.3.1, $\omega_i^{\mathrm{lsa}} = 0.259$.

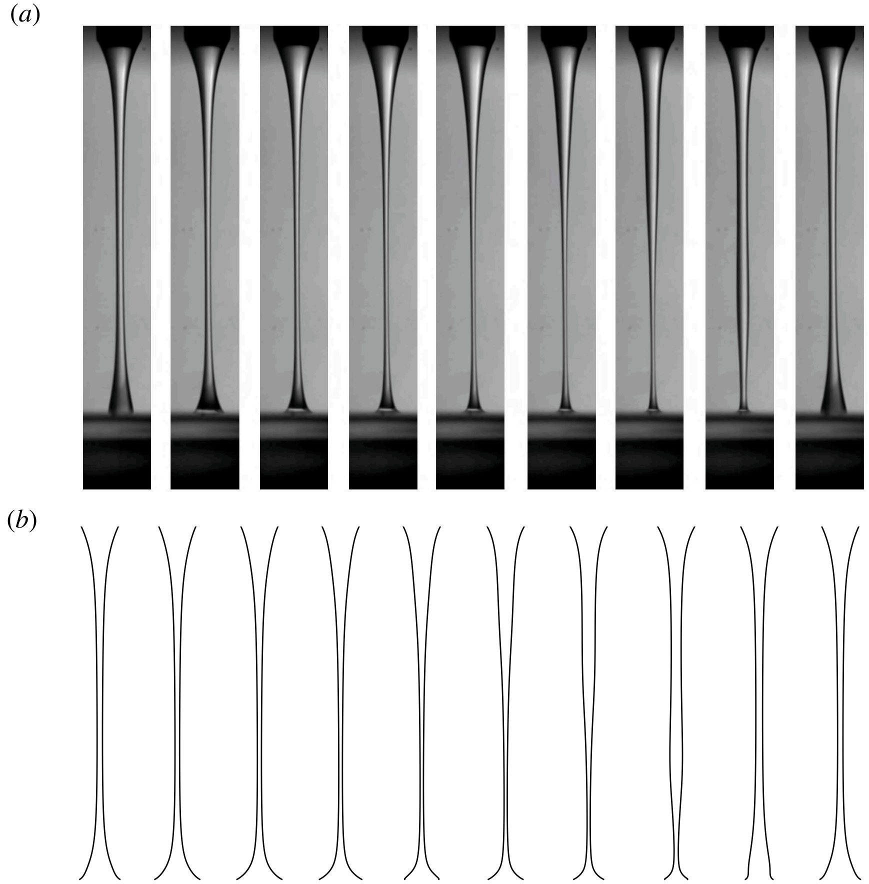

Figure 5.8: (*a*) Photographs of the liquid jet during a period of self-sustained oscillations for $\nu = 500$ cSt ($Ka = 8.33$), $R = 1.75$ mm ($Bo = 1.38$), $L = 28$ mm ($L/R = 16$), and $Q^{\mathrm{exp}} = 3.5$ ml/min ($We^{\mathrm{exp}} = 2.96 \times 10^{-3}$), smaller than the experimental critical flow rate, $Q_c^{\mathrm{exp}} = 3.8$ ml/min ($We_c^{\mathrm{exp}} = 3.49 \times 10^{-3}$). The time interval between photographs is 38 ms, and the oscillation frequency is 3.33 Hz ($\omega_i^{\mathrm{exp}} = 0.258$). (*b*) Numerically computed period of self-sustained oscillations for $Ka = 8.33$, $Bo = 1.38$, $L/R = 16$ and $We^{\mathrm{num}} = 4.43 \times 10^{-3}$, smaller than the critical flow rate provided by the one-dimensional model, $We_c^{\mathrm{lsa}} = We_c^{\mathrm{num}} = 5.03 \times 10^{-3}$. The time interval is 37 ms and the oscillation frequency is 3.83 Hz ($\omega_i^{\mathrm{num}} = 0.297$). Note that similar distances to the critical point have been chosen in the experiment and in the numerical simulation, namely $We_c^{\mathrm{exp}} - We^{\mathrm{exp}} \simeq 5.3 \times 10^{-4}$ and $We_c^{\mathrm{num}} - We^{\mathrm{num}} \simeq 6 \times 10^{-4}$ in panels (a) and (b), respectively.

The typical limit cycle behavior observed at large times in the oscillatory jetting regime is illustrated in figure 5.8. Specifically, figure 5.8(*a*) shows a sequence of photographs captured during one period of self-sustained oscillations, and figure 5.8(*b*) displays the corresponding numerically computed interface profiles under similar conditions. The values of all the dimensionless parameters except *We* are the same in figures 5.8(*a*) and 5.8(*b*), namely $Ka = 8.33$, $Bo = 1.38$, $L/R = 16$, for which the critical Weber numbers for the onset of global

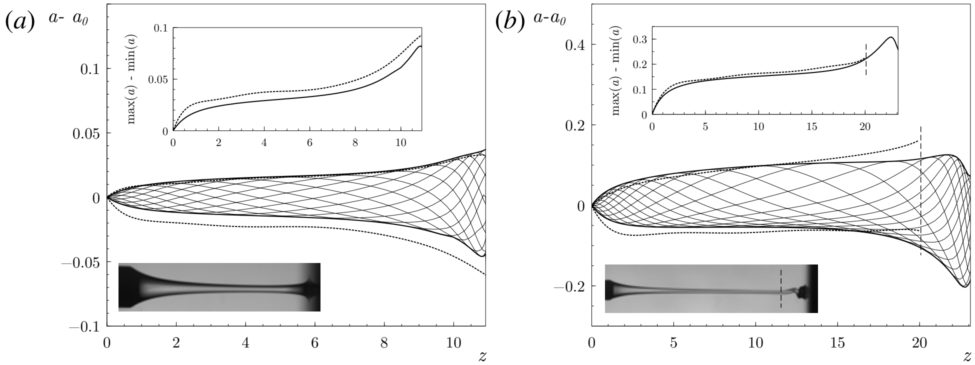

Figure 5.9: Upper and lower envelopes of the oscillations around the basic steady state, $a - a_0$, after the saturation to a limit cycle, obtained from experiments (dotted lines) and numerical simulations of equations (5.1)-(5.3) (solid lines). Numerical jet shapes at several instants during one oscillation period are also plotted as thin solid lines bounded by their corresponding envelope. The inset plots show the difference between the maxima and minima of a as a function of z. (a) Configuration without coiling, illustrated by the inset photograph: $Ka = 8.33$, $Bo = 1.38$, $L/R = 9.36$ and values of $We < We_c$ close to the experimental and numerical neutral conditions, namely $We^{\text{exp}} = 2.96{\times}10^{-3}$, for which $\omega_i^{\text{exp}} = 0.269$, and $We^{\text{num}} = 3.75 \times 10^{-3}$, for which $\omega_i^{\text{num}} = 0.296$. ($b$) Configuration with coiling, illustrated by the inset photograph: $Ka = 16.67$, $Bo = 1$, $L/R = 23.26$ and values of $We^{\text{exp}} = 3.93 \times 10^{-3}$, for which $\omega_i^{\text{exp}} = 0.215$, and $We^{\text{num}} = 6.418 \times 10^{-3}$, for which $\omega_i^{\text{num}} = 0.256$. The vertical dashed line marks the upper limit imposed on the value of z in the post-processing of the experiment.

instability are $We_c^{\text{exp}} = 3.49 \times 10^{-3}$ and $We_c^{\text{lsa}} = We_c^{\text{num}} = 5.03 \times 10^{-3}$ according to the experiments and to the prediction given by the linear stability analysis and the numerical integration of equations (5.1)-(5.3), respectively. Due to the difference in the experimental and numerical values of We_c, which can also be observed in figure 5.6(a), we decided to choose values of We^{exp} and We^{num} in figure 5.8 such that the distance to the corresponding critical Weber numbers was similar, namely $We_c^{\text{exp}} - We^{\text{exp}} \simeq 5.3 \times 10^{-4}$ in the experiment of figure 5.8(a) and $We_c^{\text{num}} - We^{\text{num}} \simeq 6 \times 10^{-4}$ in the numerical simulation of figure 5.8(b). In view of the results shown in figure 5.8 it is clear that the simple one-dimensional model used in the present work is able to qualitatively reproduce the main features of the oscillatory jetting regime including not only its frequency, but also the spatial structure of the limit cycle.

A quantitative comparison between the typical experimental and numerical behavior in the oscillatory jetting regime is provided in figures 5.9–5.11. In particular, figure 5.9 shows the numerically computed saturated oscillations of the jet radius around the basic steady state, $a\,(z,t) - a_0(z)$ as $t \rightarrow \infty$ (thin solid lines). The thick solid and dashed lines are, respectively, the upper and lower envelopes of the numerical and experimental oscillations, obtained as the maximum and minimum values of $a - a_0$ over time at each value of z. The insets display the amplitude of the oscillations as the difference between the upper and the lower envelopes, $\max(a) - \min(a)$. The oscillation amplitude is seen to increase monotonically downstream until the impact region is reached, explaining why the liquid jets studied herein always break-up close to the free surface of the reservoir, as observed in figure 5.12. A

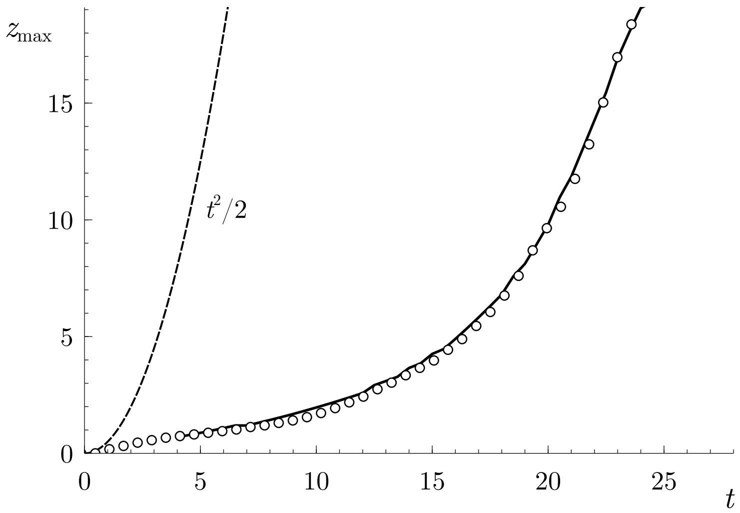

Figure 5.10: Axial coordinate of the point of maximum radius of the liquid bulge, $z_{\max}$, as a function of time during one cycle of the self-sustained oscillatory jetting state of figure 5.9(*b*), obtained from experiments (symbols) and numerical simulations (solid line). The dashed line shows the free-fall law $t^2/2$.

particularly interesting aspect of the flow is illustrated in figure 5.9(*b*), which shows that the self-sustained oscillations may coexist with the phenomenon of coiling (Ribe *et al.*, 2012). Indeed, our experiments have revealed new regimes of steady and oscillatory coiling as a function of the parameters of the problem, respectively associated with the steady jetting and with the oscillatory jetting regimes. In the latter case, the coiling is unsteady and its frequency varies enslaved to that of the axisymmetric breathing mode. Another scenario that we have observed is the disappearance of coiling due to the increase of the oscillation amplitude as the value of *We* decreases or the value of L/R increases (see figures 5.13*a* and 5.13*c*). Although these features cannot be predicted using an axisymmetric model, their effect on the saturation amplitude upstream of the impact region is relatively small, as deduced from the results of figure 5.9(*b*). In fact, it is deduced from figure 5.9 that the quantitative agreement between the experiments and the numerical integration of the one-dimensional model equations (5.1)-(5.3) is fairly good, provided that the values of *We* are chosen such that $We_c - We$ have similar values in the experiments and numerical simulations.

Another interesting aspect of the oscillatory jetting regime is the periodic formation of a liquid bulge which falls downstream during each oscillation period, as deduced from figures 5.8 and 5.9. Figure 5.10 shows the axial position of the point of maximum radius inside the liquid bulge, $z_{\max}$, as a function of time, under the conditions of figure 5.9(*b*). The symbols and the solid line represent the experimental and numerical results, respectively, while the dashed line is a plot of the free-fall law which, in dimensionless terms, is the function $t^2/2$. The results of figure 5.10 reveal that the vertical velocity of the bulge is smaller than that associated with free fall during most of its time evolution. Only during the last stages, when

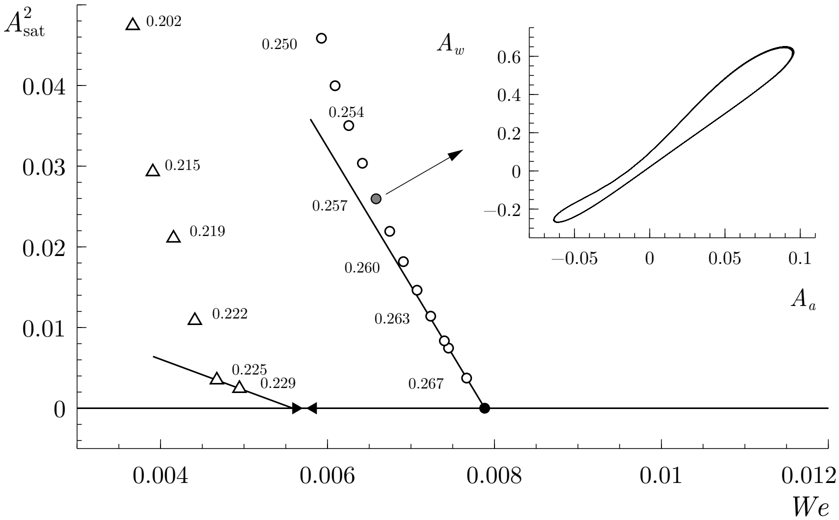

Figure 5.11: Bifurcation diagram for $Ka = 16.67$, $Bo = 1$ and $L/R = 23.26$, where the square of the saturated amplitude of the radius oscillations, A^2_{sat} (defined in the main text), is represented as a function of We. Results from experiments (△) and numerical integrations of equations (5.1)-(5.3) (○) are shown. The experimental critical Weber number lies in the range $5.62 \times 10^{-3} < We_c^{\mathrm{exp}} < 5.83 \times 10^{-3}$, represented by the symbols ► and ◄. The numerical simulations provide the value $We_c^{\mathrm{num}} = 7.88 \times 10^{-3}$ (●), in agreement with the result of the linear stability analysis, We_c^{lsa}. The solid lines are linear fits close to the experimental and numerical neutral points, according to the supercritical Stuart-Landau model. The saturated oscillation frequencies, ω_i, are indicated close to several data points. The inset shows the structure of the numerical limit cycle in the (A_w, A_a) plane associated with the gray-filled circle. The offset between the values of We_c^{exp} and We_c^{num} can also be seen in figures 5.6 and 5.13(*d*).

the volume accumulated inside the fluid bulge becomes larger than the volume of the liquid filaments connecting the bulge with the injector upstream and with the reservoir downstream, the free-fall law is approached. This fact suggests that the liquid bulge behaves like a freely falling liquid drop when its volume becomes large enough.

The bifurcation diagram represented in Figure 5.11 shows the squared amplitude of the saturated radius oscillations, A^2_{sat}, as a function of We, obtained from the experiments (△) and numerical simulations (○). Here the saturated amplitude is defined as $A_{\mathrm{sat}} = \max(A_a) - \min(A_a)$ with $t > t_{\mathrm{sat}}$, t_{sat} being a value of time large enough for the asymptotic limit cycle behavior illustrated by the inset of figure 5.11 to be reached. Moreover, the amplitude is defined by the same pointwise measure used in figure 5.7, namely $A_a = a(z^*, t) - a_0(z^*)$ and, similarly, $A_w = w(z^*, t) - w_0(z^*)$. The results shown in figure 5.11 prove that the axially-confined jets under study behave as hydrodynamic oscillators governed by a supercritical Hopf bifurcation. Indeed, in the case of the numerical simulations, as the value of We^{num} decreases and the critical value We_c^{lsa} given by the linear analysis of figure 5.6 is crossed (●), a branch of finite-amplitude, orbitally stable periodic solutions emerges for $We^{\mathrm{num}} < We_c^{\mathrm{lsa}}$ (○). A similar scenario holds also for the experiments, but at smaller values of We^{exp}, since $We_c^{\mathrm{exp}} < We_c^{\mathrm{lsa}}$ as deduced from figure 5.6. In addition, figure 5.11 shows that close to the critical point the amplitude grows as $A_{\text{sat}}^2 \propto (We_c - We)$, as expected from the Stuart-Landau equation (Stuart, 1958; Landau, 1944). Note also that the frequency decreases as the value of We decreases, whilst the growth rate increases leading to shorter saturation times.

Since, as revealed by figure 5.9, the saturated oscillation amplitude increases with z, it can be anticipated that the breakup of the liquid thread will occur as the value of L/R increases, leading to a jetting-dripping transition. Moreover, since the minimum jet radius is always located slightly upstream of the impact region, pinch-off should take place near the reservoir. Indeed, this fact is shown experimentally in the photograph of figure 5.12(*a*), and numerically in figure 5.12(*b*). Note that the one-dimensional model correctly captures the shape of the interface close to breakup except for the impact region downstream of the minimum radius, probably due to the crude model adopted herein of the outlet boundary condition.

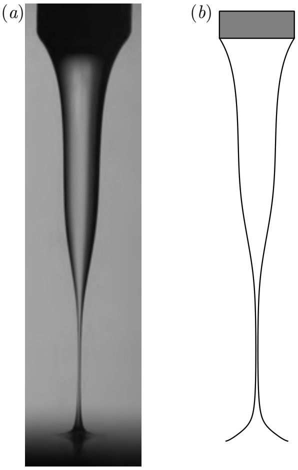

Figure 5.12: (*a*) Photograph illustrating the incipient breakup of a jet with $\nu = 500$ cSt, $R = 1.75$ mm, $L = 16.6$ mm, injected at a flow rate, $Q = 3.3$ ml/min. These conditions are represented in the phase diagrams of figures 5.13(*a*) and 5.13(*c*) with the symbol ▲, which lies within the dripping region. Since $Q < Q_b$, the oscillation amplitude increases and finally leads to dripping through the breakup of a thin thread that connects the meniscus attached to the injector with the liquid reservoir. (*b*) Instantaneous jet shape at incipient breakup obtained by numerically integrating equations (5.1)-(5.3) for the equivalent dimensionless configuration, namely $Ka = 8.33$, $Bo = 1.38$, $We = 2.63 \times 10^{-3}$, $L/R = 9.49$.

The preceding discussion naturally leads to the following question: For a constant value of We, how much can L/R increase while avoiding the breakup of the liquid filament? Or, alternatively, how much can We decrease for a constant value of L/R to avoid pinch-off? To address these questions we will make use of the breakup flow rate Q_b or, in dimensionless terms, the breakup Weber number, We_b. The experimental and numerical phase diagrams represented in figure 5.13 show the long time regimes reached by the liquid jet in the (Q, L) dimensional parameter plane in panels (*a*,*b*), and in the equivalent dimensionless parameter plane $(We, L/R)$ in panels (*c*,*d*). Two different combinations of liquid and injector radius are reported in figure 5.13, namely $\nu = 500$ cSt ($Ka = 8.33$) and $R = 1.75$ mm ($Bo = 1.38$) in panels (*a*,*c*), while $\nu = 1000$ cSt ($Ka = 16.67$) and $R = 1.5$ mm ($Bo = 1$) in panels (*b*,*d*). The dark and light gray regions correspond to the steady jetting and oscillatory jetting states according to the experiments, while the dripping regime falls within the unshaded regions. The solid curve is the critical flow rate Q_c^{lsa} (We_c^{lsa}) given by the linear stability analysis of §5.3.1, and the dashed line is the breakup flow rate Q_b^{num} (We_b^{num}) according to the numerical simulations of equations (5.1)-(5.3), obtained by extrapolating the minimum saturated jet radius for several values of We slightly larger than We_b^{num}. The agreement between We_b^{exp} and We_b^{num} is fairly good for the case with $Ka = 16.67$ ($\nu = 1000$ cSt), but quite poor for the case with $Ka = 8.33$ ($\nu = 500$ cSt) and values of $L/R \gtrsim 10$. This discrepancy between theory and experiment for values of $L/R \gtrsim 10$ may be due to the limitations of the one-dimensional model that have already been pointed out in the discussion of figure 5.6. Indeed, the model does not account for the downstream viscous relaxation of the parabolic velocity profile at the injector outlet. More importantly, our crude modeling of the non-slender impact region where, as shown in figure 5.12, the break-up of the thread takes place, may also contribute to the difference between the values of We_b^{exp} and We_b^{num} observed in figure 5.13.

A salient feature of the phase maps is the existence of a critical length, $L^*(\nu, R)$ for which $Q_c = Q_b = Q^*$. For values of $L < L^*$ a direct transition between steady jetting and dripping takes place, without the existence of an intermediate oscillating jet state. The corresponding transition points are shown as gray-filled circles in figure 5.13, displaying a very good agreement with the value of Q_c^{lsa}. It is important to emphasize that this phenomenon was observed both in the experiments and in the numerical simulations. Let us also point out that, in the cases where a direct transition from steady jetting to dripping takes place, there is no qualitative change in the linear stability mode, which is still the same breathing mode that is destabilized for $Q < Q_c$. Moreover, the nature of the bifurcation that takes place in these cases is also the same Hopf bifurcation shown in figure 5.11, with the only difference that the amplitude of the oscillations grows with time without saturation, until break-up takes place, for very small values of $Q_c - Q$. Ideally there should always exist a value of $Q_c - Q$ small enough for the oscillatory jetting regime to be achieved, since the amplitude of the oscillations increases as $(Q_c - Q)^{1/2}$ for sufficiently small values of $Q_c - Q$. In practice, however, the value of $Q_c - Q_b$ is so small in these cases that it cannot be extracted from our experiments or numerical simulations.

Figure 5.13 also reveals that the region of oscillatory jetting decreases as the value of L/R increases, since the amplitude of the oscillations grows with z, and thus Q_b increases with L, while the value of Q_c reaches an asymptote as $L \to \infty$ (see also figure 5.6). Therefore, for values of L larger than those considered herein, it is expected that the values of Q_c and Q_b will intersect, providing a bounded region of oscillatory jetting. Finally, figure 5.13 shows the important influence of ν, which increases the size of oscillatory jetting region due to its stabilizing role. Similarly, the region of oscillatory jetting becomes smaller as R increases due to the stabilizing effect of axial stretching.

5.4 Conclusions

The linear and nonlinear dynamics of jets of viscous liquid falling under gravity and confined in the axial direction has been studied by means of experiments and the leading-order one-dimensional model explained in §2, originally deduced by Eggers & Dupont (1994) and García & Castellanos (1994), which is extremely efficient from a computational point of view.

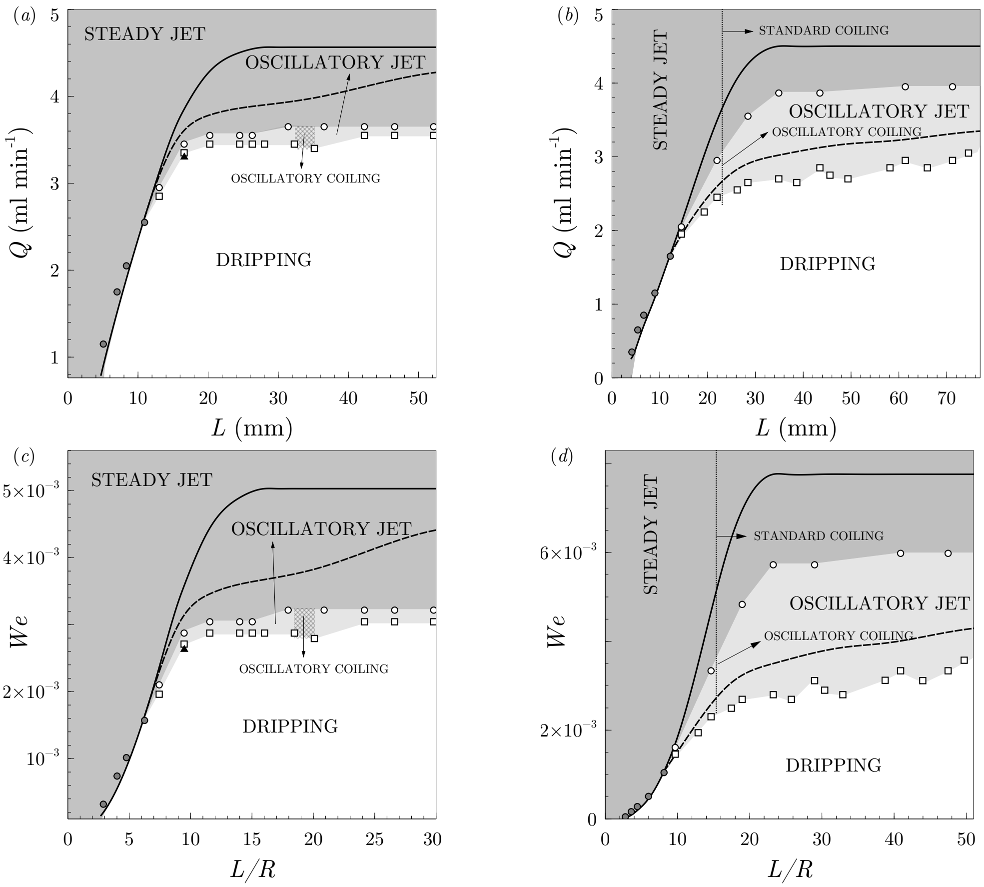

Figure 5.13: Phase diagrams represented in the dimensional parameter plane (Q, L) (a,b), and in the equivalent dimensionless parameter plane $(We, L/R)$ (c,d), showing the different regimes identified for an axially-confined viscous liquid jet falling under gravity. The dark gray, light gray and unshaded regions correspond with the steady jetting, oscillatory jetting and dripping regimes, respectively. Results are shown for two different combinations of liquid and injector radius, namely (a,c) $\nu = 500$ cSt $(Ka = 8.33)$ and $R = 1.75$ mm $(Bo = 1.38)$, and (b,d) $\nu = 1000$ cSt $(Ka = 16.67)$, $R = 1.5$ mm $(Bo = 1)$. The mean between the upper and lower limits of the experimental critical flow rate, Q_c^{exp} (We_c^{exp}), and breakup flow rate, Q_b^{exp} (We_b^{exp}), are plotted with the symbols ○ and □, respectively. The solid line is the critical flow rate for the onset of the breathing mode given by the linear stability analysis, Q_c^{lsa} (We_c^{lsa}), and the dashed line represents the function Q_b^{num} (We_b^{num}) obtained from the numerical integration of equations (5.1)-(5.3). The gray-filled circles correspond with direct transitions between steady jetting and dripping, while the symbols ▲ represents the conditions of figure 5.12. The different coiling states identified in the experiments are indicated.

The global linear stability analysis reported by Sauter & Buggisch (2005) and Rubio-Rubio *et al.* (2013) has been extended in the present work to contemplate the effect of the axial confinement length, L. We have shown both experimentally and theoretically that the critical flow rate Q_c for the onset of the axisymmetric breathing mode decreases as L decreases, thus stabilizing the liquid thread. For small enough values of L, a limit is reached whereby $We_c \longrightarrow 0$ and the marginal stability point is given by hydrostatics, in agreement with previous works on static liquid bridges (Kovitz, 1975; Benilov & Oron, 2010; Benilov & Cummins, 2013).

The nonlinear dynamics has been characterized both experimentally and with numerical integrations of the one-dimensional model. Our results have revealed the existence of a new regime featuring the appearance limit-cycle oscillations of the thread without breakup. The latter oscillatory jetting regime has been thoroughly studied for several combinations of the governing parameters, finally leading to the phase maps presented in figure 5.13, that summarizes the main conclusions of the present chapter. In particular, the central role of L has been clearly unveiled. In contrast with the linear theory, which only distinguishes between stable and unstable configurations, three distinct long-time nonlinear regimes can be observed in figure 5.13: steady jetting, oscillatory jetting and dripping. Although different coiling regimes have also been identified in the experiments, namely a standard and an oscillatory coiling, a detailed study of these coiling regimes is left for a future study.

The experiments and numerical simulations have revealed that there is a critical value of the confinement length, L, below which the oscillatory jetting is no longer observed. This is due to the fact that, as L decreases, Q_c decreases with a larger slope than the critical flow rate associated to the breakup of the jet, Q_b. Hence, the size of the oscillatory jetting region decreases as the jet becomes shorter, due to the stabilizing effect of confinement. Consequently, there is a value of $L = L^*$ where $Q_c = Q_b = Q^*$, and for values of $L < L^*$ the transition occurs directly between steady jetting and dripping as Q decreases. The experiments and numerical simulations are in very good agreement in their prediction of the value of L^* and the corresponding Q^*.

Future work should contemplate wider ranges of the control parameters, allowing to obtain experimental and numerical phase maps for values of Ka and Bo different from those reported herein. Additionally, in view of the new coiling regimes found in our experiments, it could be worthwhile to describe them in detail. Another important extension is the characterization of the physical effects present in typical technological applications, such as the use of liquids with complex rheology or the presence of surfactants. Their inclusion in the analysis is crucial for applications such as 3D printing or additive manufacturing, in which our findings may be of relevance.

Appendix 5.A Linear stability analysis

The detailed mathematical formulation to obtain the base flow and of the linear stability problem is provided in the present appendix.

5.A.1 Base flow

The base flow $[a_0(z), w_0(z)]$ satisfies the steady versions of the system of equations (5.1)-(5.3). In particular, the continuity equation (5.1) allows to substitute the steady state velocity, $w_0(z)$, by the base flow jet radius, $a_0(z)$,

$$w_0 = \frac{q}{a_0^2}, \tag{5.6}$$

where $q = We^{1/2}Bo^{3/4}$, is the dimensionless liquid flow rate. In addition, the steady version of the momentum equation (5.2) reduces to

$$w_0 w_0{}' = 1 - C_0{}' + Ka\, a_0{}^{-2}(a_0{}^2 w_0{}')', \tag{5.7}$$

where primes indicate derivatives with respect to z and C_0 is the mean curvature associated with the steady jet shape, $a_0(z)$, which satisfies equation (5.3). Substituting (5.6) into (5.7), the function $a_0(z)$ satisfies

$$-a_0^2 C_0{}' + 2qKa\left[a_0^{-2}\left(a_0'\right)^2 - a_0^{-1}a_0''\right] + 2q^2 a_0^{-3} a_0' + a_0^2 = 0, \tag{5.8}$$

where

$$-a_{a0}^2 C_0{}' = \frac{a_0'}{\left[1+\left(a_0'\right)^2\right]^{1/2}} + \frac{a_0 a_0' a_0'' + a_0^2 a_0'''}{\left[1+\left(a_0'\right)^2\right]^{3/2}} - \frac{3a_0^2 a_0'\left(a_0''\right)^2}{\left[1+\left(a_0'\right)^2\right]^{5/2}}, \tag{5.9}$$

to be solved with the boundary conditions

$$z = 0 \quad : \quad a_0 = Bo^{1/2}, \tag{5.10}$$

$$z = 0 \quad : \quad w_0 = We^{1/2}Bo^{-1/4}, \tag{5.11}$$

$$z = \frac{L}{l_\sigma} \quad : \quad w_0 = w_{\text{out}}, \tag{5.12}$$

as discussed in §5.2.3. Note that equations (5.8)-(5.9) are the same as those solved in Rubio-Rubio *et al.* (2013) (hereinafter R13), the only difference being the outlet boundary condition (5.12), which in the present work is imposed as a Dirichlet condition, while a free boundary condition was considered in R13. The numerical method used herein to solve equations (5.8)-(5.9) is also the same as that used by R13, and is explained in appendix 5.B.1.

5.A.2 Linear stability problem

Substituting (5.4)-(5.5) into (5.1)-(5.3), the $O(\epsilon)$ eigenvalue problem can be written in the following compact form,

$$\begin{bmatrix} \mathcal{M}_a^c & \mathcal{M}_w^c \\ \mathcal{M}_a^m & \mathcal{M}_w^m \end{bmatrix} \begin{bmatrix} a_1 \\ w_1 \end{bmatrix} = \omega \begin{bmatrix} a_1 \\ w_1 \end{bmatrix}, \tag{5.13}$$

with $\mathcal{M}_i^j$ denoting the following differential operators,

$$\mathcal{M}_a^c = -\frac{q}{a_0^2}\,\mathrm{D} + \frac{q\,a_0'}{a_0^3}\,\mathrm{I}\,, \tag{5.14}$$

$$\mathcal{M}_w^c = -\frac{a_0}{2}\,\mathrm{D} - a_0'\,\mathrm{I}\,, \tag{5.15}$$

$$\mathcal{M}_a^m = -4Ka\,q\left(\frac{a_0'}{a_0^4}\,\mathrm{D} - \frac{\left(a_0'\right)^2}{a_0^5}\,\mathrm{I}\right) + \sum_{k=1}^{4} \mathcal{S}^{2k-1}\,\mathcal{H}_k\,, \tag{5.16}$$

$$\mathcal{M}_w^m = Ka\left(\mathrm{D}^2 + \frac{2a_0'}{a_0}\,\mathrm{D}\right) - \frac{q}{a_0^2}\,\mathrm{D} + \frac{2q\,a_0'}{a_0^3}\,\mathrm{I}\,. \tag{5.17}$$

In (5.14)-(5.17), I is the identity, $\mathrm{D}^n \equiv \mathrm{d}^n/\mathrm{d}z^n$, $\mathcal{S}(z) = [1 + (a_0')^2]^{-1/2}$ and

$$\mathcal{H}_1 = \frac{1}{a_0^2}\,\mathrm{D} - \frac{2a_0'}{a_0^3}\,\mathrm{I}, \tag{5.18}$$

$$\mathcal{H}_2 = \mathrm{D}^3 + \frac{a_0'}{a_0}\,\mathrm{D}^2 - \left[\frac{\left(a_0'\right)^2}{a_0^2} - \frac{a_0''}{a_0}\right]\mathrm{D} - \frac{a_0'\,a_0''}{a_0^2}\,\mathrm{I}, \tag{5.19}$$

$$\mathcal{H}_3 = -6\,a_0'\,a_0''\,\mathrm{D}^2 - 3\left[\frac{\left(a_0'\right)^2 a_0''}{a_0} + \left(a_0''\right)^2 + a_0'\,a_0'''\right]\mathrm{D}, \tag{5.20}$$

$$\mathcal{H}_4 = 15\left(a_0''\right)^2\left(a_0'\right)^2\,\mathrm{D}. \tag{5.21}$$

Note that equation (5.13) is a linear eigenvalue problem, complemented with the boundary conditions

$$z = 0 \quad : \quad w_1 = 0, \tag{5.22}$$

$$z = 0 \quad : \quad a_1 = 0, \tag{5.23}$$

$$z = \frac{L}{l_\sigma} \quad : \quad w_1 = 0. \tag{5.24}$$

Equations (5.22) and (5.23) represent the pinned contact line and constant flow rate conditions, respectively. However, equation (5.24) just represents in a crude way the fact that the disturbed jet velocity is small in the impact region onto the bath at rest. If a small enough value of w_{out} is assumed for the base flow, the results of the stability analysis do not vary significantly, thereby justifying the use of equation (5.24). Moreover, for values of the jet length $L/R \gtrsim 20$ the results are independent of the value of w_{out}, and in fact we have checked that both the base flow and its linear stability are virtually the same whether imposing a Neumann condition at $z = L/l_\sigma$, or even not imposing any condition at all, in agreement with the results of R13.

Appendix 5.B Numerical methods

In the present Appendix we describe the numerical methods used for the computation of the steady jet and its linear stability, as well as the integration of equations (5.1)-(5.3).

5.B.1 Base flow and linear stability analysis

To solve both equation (5.8) for a_0, and the system (5.13) for the eigenvalues ω and the corresponding eigenfunctions, we discretized the differential operators using a Chebyshev collocation method (Canuto *et al.*, 2006). To that end, the physical domain, $0 \leq z \leq L/l_\sigma$ is mapped into the interval $-1 \leq y \leq 1$ by means of the transformation

$$z = \frac{bL/l_\sigma(1+y)}{2b + L/l_\sigma(1-y)}, \tag{5.25}$$

where b is a parameter that controls the clustering of nodes at $z = 0$ and $z = L/l_\sigma$. Derivatives with respect to z are calculated using the standard Chebyshev differentiation matrices and the chain rule. The nonlinear differential equation (5.8) with boundary conditions (5.10)-(5.12) is solved first using an iterative Newton-Raphson method. Once a_0 is known at the N Chebyshev collocation points, the discretized version of (5.13), which results in a linear algebraic eigenvalue problem to determine the $2N$ eigenvalues ω^k, $k = 1 \ldots 2N$, and their corresponding eigenfunctions (a_1^k, w_1^k) at the N collocation points, is solved using standard Matlab routines. Notice that the eigenfunctions must satisfy the boundary conditions (5.22)-(5.24). Although all the results reported in the present paper were computed with values of N and b within the ranges $30 \leq N \leq 200$ and $5 \leq b \leq 80$, we have carefully checked that the leading eigenvalues and eigenfunctions are insensitive to the values of these parameters.

5.B.2 Direct numerical simulation

The system of equations (5.1)-(5.3), supplemented with the boundary conditions discussed above were solved with a very simple and efficient method of lines in which the spatial derivatives were approximated using the Chebyshev collocation method described in §5.B.1. The resulting system of $2N$ nonlinear ordinary differential equations were integrated in time with an initial condition taken as the base flow $[a_0(z), w_0(z)]$, slightly perturbed by a Gaussian function of very small amplitude. The ODE23T routine from the Matlab ODE suite was chosen, since Dirichlet or Neumann boundary conditions can be easily imposed through a mass matrix, and also allows to implement the Jacobian matrix of the nonlinear system to improve the speed and accuracy of the computations. The solver ODE23T uses the Bogacki–Shampine algorithm, which is a method based on two single-step formulas, of second and third order respectively, and computes three stages for each time step. Briefly stated, to calculate the temporal evolution of the a and w, the semi-discretized equations were written in the matrix form

$$\frac{\mathrm{d}\boldsymbol{y}}{\mathrm{d}t} = \boldsymbol{B}(\boldsymbol{y},t), \tag{5.26}$$

where the column vector $\boldsymbol{y} = [\boldsymbol{a}(z,t), \boldsymbol{w}(z,t)]^{\mathrm{T}}$ contains the values of the jet radius and axial velocity computed at the N Chebyshev collocation points, z, and the matrix $\boldsymbol{B}$ is

$$\boldsymbol{B}(\boldsymbol{y},t) = \begin{bmatrix} \boldsymbol{B}_a^c & \boldsymbol{B}_w^c \\ \boldsymbol{B}_a^m & \boldsymbol{B}_w^m \end{bmatrix}_{2N\times 2N} \cdot \begin{bmatrix} \boldsymbol{a}(z=0,t) \\ \vdots \\ \boldsymbol{a}(z=L/l_\sigma,t) \\ \boldsymbol{w}(z=0,t) \\ \vdots \\ \boldsymbol{u}(z=L/l_\sigma,t) \end{bmatrix}_{2N\times 1} + \begin{bmatrix} 0 \\ \vdots \\ 0 \\ 1 \\ \vdots \\ 1 \end{bmatrix}_{2N\times 1} . \tag{5.27}$$

The $N \times N$ submatrices $\boldsymbol{B}_i^j$ appearing in equation (5.27) are

$$\boldsymbol{B}_a^c = -\mathrm{diag}\,(\boldsymbol{w}) \cdot \boldsymbol{D}, \tag{5.28}$$

$$\boldsymbol{B}_w^c = -\frac{1}{2}\,\mathrm{diag}\,(\boldsymbol{a}) \cdot \boldsymbol{D}, \tag{5.29}$$

$$\boldsymbol{B}_a^m = \sum_{n=1}^{3} \boldsymbol{C}_n \cdot \boldsymbol{D}^n, \tag{5.30}$$

$$\boldsymbol{B}_w^m = -\mathrm{diag}\,(\boldsymbol{w}) \cdot \boldsymbol{D} + Ka\left[\boldsymbol{D}^2 + 2\,\mathrm{diag}\,(\boldsymbol{a})^{-1} \cdot \mathrm{diag}\,(\boldsymbol{D}\cdot\boldsymbol{a}) \cdot \boldsymbol{D}\right], \tag{5.31}$$

where $\boldsymbol{D}^n$ is the $N \times N$ n-th order Chebyshev differentiation matrix, diag $(\cdot)$ maps an N-tuple to the corresponding diagonal matrix, and the curvature gradient diagonal matrices, $\boldsymbol{C}_n$, are

$$\boldsymbol{C}_1 = \mathrm{diag}\,(\boldsymbol{a})^{-2} \cdot \left[\boldsymbol{I} + \mathrm{diag}\,(\boldsymbol{D}\cdot\boldsymbol{a})^2\right]^{-1/2} - 3\,\mathrm{diag}\left(\boldsymbol{D}^2\cdot\boldsymbol{a}\right)^2 \cdot \left[\boldsymbol{I} + \mathrm{diag}\,(\boldsymbol{D}\cdot\boldsymbol{a})^2\right]^{-5/2}, \tag{5.32}$$

$$\boldsymbol{C}_2 = \mathrm{diag}\,(\boldsymbol{D}\cdot\boldsymbol{a}) \cdot \mathrm{diag}\,(\boldsymbol{a})^{-1} \cdot \left[\boldsymbol{I} + \mathrm{diag}\,(\boldsymbol{D}\cdot\boldsymbol{a})^2\right]^{-3/2}, \tag{5.33}$$

$$\boldsymbol{C}_3 = \left[\boldsymbol{I} + \mathrm{diag}\,(\boldsymbol{D}\cdot\boldsymbol{a})^2\right]^{-3/2}, \tag{5.34}$$

where $\boldsymbol{I}$ is the $N \times N$ identity matrix. Note that, for clarity, in equations (5.28)-(5.34) the functional dependence of $\boldsymbol{a}$ and $\boldsymbol{w}$ on (z,t) has been omitted.

The boundary conditions (5.10)–(5.12) described in §5.2.3 can be readily implemented by imposing

$$\frac{\mathrm{d}\boldsymbol{a}}{\mathrm{d}t}(z=0,t) = \frac{\mathrm{d}\boldsymbol{w}}{\mathrm{d}t}(z=0,t) = \frac{\mathrm{d}\boldsymbol{w}}{\mathrm{d}t}(z=L/l_\sigma,t) = 0. \tag{5.35}$$

References

AMBRAVANESWARAN, B., SUBRAMANI, H.J., PHILLIPS, S.D. & BASARAN, O.A. 2004 Dripping-jetting transitions in a dripping faucet. *Phys. Rev. Lett.* **93**, 034501.

ANNA, S.L. 2016 Droplets and bubbles in microfluidic devices. *Annu. Rev. Fluid Mech.* **48**, 285–309.

ASHGRIZ, N. & MASHAYEK, F. 1995 Temporal analysis of capillary jet breakup. *J. Fluid Mech.* **291**, 163–190.

BARRERO, A. & LOSCERTALES, I. G. 2007 Micro- and nanoparticles via capillary flows. *Annu. Rev. Fluid Mech.* **39**, 89–106.

BASARAN, O. A. 2002 Small-scale free surface flows with breakup: drop formation and emerging applications. *AIChE J.* **48**, 1842–1848.

BENILOV, E.S. & CUMMINS, C.P. 2013 The stability of a static liquid column pulled out of an infinite pool. *Phys. Fluids* **25**, 112105.

BENILOV, E.S. & ORON, A. 2010 The height of a static liquid column pulled out of an infinite pool. *Phys. Fluids* **22**, 102101.

BLOUNT, M. J. & LISTER, J. R. 2011 The asymptotic structure of a slender dragged viscous thread. *J. Fluid Mech.* **674**, 489–521.

BOGY, D.B. 1979 Drop formation in a circular liquid jet. *Annu. Rev. Fluid Mech.* **11**, 207–228.

CANUTO, C., HUSSAINI, M.Y., QUARTERONI, A. & ZANG, T.A. 2006 *Spectral methods. Fundamentals in single domains*. Springer-Verlag, Berlin.

CHIU-WEBSTER, S. & LISTER, J. R. 2006 The fall of a viscous thread onto a moving surface: a fluid-mechanical sewing machine. *J. Fluid Mech.* **569**, 89–111.

CHRISTODOULIDES, P. & DIAS, F. 2010 Impact of a falling jet. *J. Fluid Mech.* **657**, 22–35.

CHRISTOPHER, G.F. & ANNA, S.L. 2007 Microfluidic methods for generating continuous droplet streams. *J. Phys. D: Appl. Phys.* **40**, R319–R336.

CLANET, C. & LASHERAS, J. C. 1999 Transition from dripping to jetting. *J. Fluid Mech.* **383**, 307–326.

COULLET, P., MAHADEVAN, L. & RIERA, C.S. 2005 Hydrodynamical models for the chaotic dripping faucet. *J. Fluid Mech.* **526**, 1–17.

DERBY, B. 2010 Inkjet printing of functional and structural materials: Fluid property requirements, feature stability, and resolution. *Annu. Rev. Mater. Res.* **40**, 395–414.

DONNELLY, R. J. & GLABERSON, W. I. 1966 Experiments on the capillary instability of a liquid jet. *Proc. Roy. Soc.* **A290**, 547–566.

DOSHI, J. & RENEKER, D.H. 1995 Electrospinning process and applications of electrospun fibers. *J. Electrostat.* **35** (2), 151–160.

EGGERS, J. 1993 Universal pinching of 3d axisymmetric free-surface flow. *Phys. Rev. Lett.* **71**, 3458.

EGGERS, J 1997 Nonlinear dynamics and breakup of free surface flows. *Rev. Mod. Phys.* **69**, 865–929.

EGGERS, J. & DUPONT, T. F. 1994 Drop formation in a one-dimensional approximation of the Navier-Stokes equation. *J. Fluid Mech.* **262**, 205–222.

EGGERS, J. & VILLERMAUX, E. 2008 Physics of liquid jets. *Rep. Prog. Phys.* **71**, 036601.

ENTOV, V. M. & YARIN, A. L. 1984 The dynamics of thin liquid jets in air. *J. Fluid Mech.* **140**, 91–111.

EVANGELIO, A., CAMPO-CORTÉS, F. & GORDILLO, J.M. 2016 Simple and double microemulsions via the capillary breakup of highly stretched liquid jets. *J. Fluid Mech.* **804**, 550–577.

GAÑÁN-CALVO, A.M. 1998 Generation of steady liquid microthreads and micron-sized monodisperse sprays in gas streams. *Phys. Rev. Lett.* **80** (2), 285–288.

GARCÍA, F. J. & CASTELLANOS, A. 1994 One-dimensional models for slender axisymmetric viscous liquid jets. *Phys. Fluids* **6** (8), 2676–2689.

GONZÁLEZ, H. & GARCÍA, F. J. 2009 The measurement of growth rates in capillary jets. *J. Fluid Mech.* **619**, 179–212.

GORDILLO, J.M., SEVILLA, A. & CAMPO-CORTÉS, F. 2014 Global stability of stretched jets: conditions for the generation of monodisperse micro-emulsions using coflows. *J. Fluid Mech.* **738**, 335–357.

GUERRERO, J., GONZÁLEZ, H. & GARCÍA, F.J. 2016 Spatial modes in one-dimensional models for capillary jets. *Phys. Rev. E* **93**, 033102.

GUERRERO, J., RIVERO, J., GUNDABALA, V. R., PEREZ-SABORID, M. & FERNANDEZ-NIEVES, A. 2014 Whipping of electrified liquid jets. *Proc. Natl. Acad. Sci. U.S.A.* **111** (38), 13763–13767.

KALAAJI, A., LOPEZ, B., ATTANE, P. & SOUCEMARIANADIN, A. 2003 Breakup length of forced liquid jets. *Phys. Fluids* **15**, 2469–2479.

KOVITZ, A. A. 1975 Static fluid interfaces external to a right circular cylinder. experiment and theory. *J. Colloid Interf. Sci.* **50**.

LANDAU, L.D. 1944 On the problem of turbulence. *C.R. Acad. Sci. URSS* **44**, 311–314.

LE DIZÈS, S. 1997 Global modes in falling capillary jets. *Eur. J. Mech. B/Fluids* **16**, 761–778.

LEIB, S. J. & GOLDSTEIN, M. E. 1986*a* Convective and absolute instability of a viscous liquid jet. *Phys. Fluids* **29** (4), 952–954.

LEIB, S. J. & GOLDSTEIN, M. E. 1986*b* The generation of capillary instabilities on a liquid jet. *J. Fluid Mech.* **168**, 479–500.

LIN, S.P. & REITZ, R.D. 1998 Drop and spray formation from a liquid jet. *Annu. Rev. Fluid Mech.* **30**, 85–105.

MARÍN, A.G., CAMPO-CORTÉS, F. & GORDILLO, J.M. 2009 Generation of micron-sized drops and bubbles through viscous coflows. *Colloid Surface A* **344**, 2–7.

MARTÍNEZ-CALVO, A., RIVERO-RODRÍGUEZ, J., SCHEID, B. & SEVILLA, A. 2020 Natural break-up and satellite formation regimes of surfactant-laden liquid threads. *J. Fluid Mech.* **883**, A35.

MATOVICH, M. A. & PEARSON, J. R. A. 1969 Spinning a molten threadline. Steady-state isothermal viscous flow. *Ind. Eng. Chem. Fundamen.* **8** (3), 512–520.

NAYFEH, A.H. 1970 Nonlinear stability of a liquid jet. *Phys. Fluids* **13** (4), 841–847.

O'DONNELL, B., CHEN, J. N. & LIN, S. P. 2001 Transition from convective to absolute instability in a liquid jet. *Phys. Fluids* **13** (9), 2732–2734.

PEARSON, J. R. A. & MATOVICH, M. A. 1969 Spinning a molten threadline. Stability. *Ind. Eng. Chem. Fundamen.* **8** (4), 605–609.

PLATEAU, J. 1873 *Statique expérimentale et théorique des liquides*. Gauthier-Villars et C^{ie}, Paris.

RAYLEIGH, W. S. 1878 On the instability of jets. *Proc. R. Soc. Lond.* **10**, 4–13.

RIBE, N.M., HABIBI, M. & BONN, D. 2012 Liquid rope coiling. *Annu. Rev. Fluid Mech.* **44**, 249–266.

RIVERO-RODRIGUEZ, J. & PÉREZ-SABORID, M. 2015 Numerical investigation of the influence of gravity on flutter of cantilevered pipes conveying fluid. *J. Fluids Struct.* **55**, 106–121.

RUBIO-RUBIO, M., SEVILLA, A. & GORDILLO, J. M. 2013 On the thinnest steady threads obtained by gravitational stretching of capillary jets. *J. Fluid Mech.* **729**, 471–483.

RUTLAND, D.F. & JAMESON, G.J. 1971 A non-linear effect in the capillary instability of liquid jets. *J. Fluid Mech.* **46** (2), 267–271.

SAUTER, U. S. & BUGGISCH, H. W. 2005 Stability of initially slow viscous jets driven by gravity. *J. Fluid Mech.* **533**, 237–257.

SENCHENKO, S. & BOHR, T. 2005 Shape and stability of a viscous thread. *Phys. Rev. E* **71**, 056301.

SEVILLA, A 2011 The effect of viscous relaxation on the spatiotemporal stability of capillary jets. *J. Fluid Mech.* **684**, 204–226.

SÖDERBERG, L. D. 2003 Absolute and convective instability of a relaxational plane liquid jet. *J. Fluid Mech.* **493**, 89–119.

STUART, J. T. 1958 On the non-linear mechanics of hydrodynamic stability. *J. Fluid Mech.* **4**, 1–21.

SUBRAMANI, H.J., YEOH, H.K., SURYO, R., XU, Q., AMBRAVANESWARAN, B. & BASARAN, O.A. 2006 Simplicity and complexity in a dripping faucet. *Phys. Fluids* **18** (3), 032106.

SURYO, R. & BASARAN, O.A. 2006 Tip streaming from a liquid drop forming from a tube in a co-flowing outer fluid. *Phys. Fluids* **18**, 082102.

THEOFILIS, V. 2011 Global linear instability. *Annu. Rev. Fluid Mech.* **43**, 319–352.

VIHINEN, I., HONOHAN, A. M. & LIN, S. P. 1997 Image of absolute instability in a liquid jet. *Phys. Fluids* **9** (11), 3117–3119.

WILKES, E.D., PHILLIPS, S.D. & BASARAN, O.A. 1999 Computational and experimental analysis of dynamics of drop formation. *Phys. Fluids* **11** (12), 3577–3598.

YUEN, M.-C. 1968 Non-linear capillary instability of a liquid jet. *J. Fluid Mech.* **33** (1), 151–163.

Conclusions and Future Work

This thesis reports novel fundamental studies concerning the linear and nonlinear dynamics of cylindrical filaments whose interface is endowed with interfacial rheology, which arises due to the presence of surface-active molecules, proteins, lipids, or particles. The complex microstructure that they form at the interface and their coupling with hydrodynamic forces, manifest macroscopically in linear and nonlinear rheological properties and complex constitutive equations relating the surface stress with the deformation of the material surface. Despite this complexity, these liquid filaments share the same instability mechanism, usually referred to as the Rayleigh–Plateau instability, where disturbances of sufficiently long wavelength trigger the instability by decreasing the surface energy at constant volume.

After appropriately deducing the components of the surface stress balance modified by interfacial elastic and viscous forces, in chapter 2 we have derived a leading-order and a second-order one-dimensional models that account for such interfacial viscoelasticity. The performance of these slender approximations has been evaluated in the linear regime by comparing their predictions for the growth rate of small perturbations with those obtained from the complete equations of motion. In particular, we have concluded that the leading-order slender model cannot accurately predict the linear stability properties when surface viscous forces become important, as already deduced by Timmermans & Lister (*J. Fluid Mech.*, vol. 459, 2002, pp. 289–306) for the case of surfactant-induced elasticity. Indeed, the leading-order model does not appropriately accommodate strong interfacial stress. Hence, a second-order lubrication model is needed, which has been shown to yield excellent results for any value of the Boussinesq numbers, which measure the relative importance of surface and bulk viscous stresses.

In chapter 3 we have extended Rayleigh's temporal stability analysis of the complete equations of motion to study the effect of interfacial viscoelasticity on the linear dynamics of an axisymmetric liquid filament. After briefly revisiting the results obtained by Timmermans & Lister (2002) on the effect of surface elasticity when an insoluble monolayer populates the interface, we have unraveled the effect of surface viscous forces on the linear regime. The surface viscous forces have been modelled using the Boussinesq–Scriven constitutive equation, leading to the conclusion that they have a strong stabilizing effect. We have also studied the distinguished limits of a saturated interface, where Marangoni stresses are negligible, and that of dominant surface viscous forces introducing, for the first time, the idea of a surface visco-capillary time scale, of central importance when studying the thinning and nonlinear dynamics of a saturated interface with surface viscous resistance in chapter 4. Additionally, we have shown that surface diffusion of surfactant molecules produces a destabilizing effect in the linear regime, since it opposes the creation of gradients of surfactant concentration that act against the Rayleigh–Plateau mechanism. Finally, we also deduce the dispersion relation corresponding to a solid-like interface modeled by the Hookean and neo-Hookean constitutive laws, showing that shear and elastic forces strongly stabilize the filament, and that the limit of purely dilatational elastic forces coincides with that of a surfactant-induced elasticity.

In chapter 4 we have extended the results of the previous chapter to the nonlinear regime by performing numerical simulations of the full conservation equations accounting for interfacial viscoelasticity in the limit of insoluble surfactants. We have first explored the nonlinear dynamics when only the effect of surface elasticity acts on the interface. In particular, we have performed an extensive parametric study using a nonlinear temporal approach, quantifying the influence of La and β on four key magnitudes: the normalized satellite droplet volume just prior to pinch-off, V_{sat}, the normalized mass of surfactant trapped at the surface of the satellite, Σ_{sat}, the breakup time, and the shape of the satellite drop at pinch-off. We have shown that, in the weak-elasticity limit, $\beta \lesssim 0.05$, the satellite volume and the associated mass of surfactant obey the scaling law $V_{\text{sat}} = \Sigma_{\text{sat}} = 0.0042 La^{1.64}$ for $La \lesssim 2$. For $La \gtrsim 10$, V_{sat} and Σ_{sat} reach a plateau of about 3% and 2.9%, respectively, where V_{sat} is in excellent agreement with previous experiments of low-viscosity threads with clean interfaces. For $La < 7.5$, we have revealed the existence of a discontinuous transition in V_{sat} and Σ_{sat} at a critical elasticity, $\beta_c(La)$, with $\beta_c \to 0.98$ for $La \lesssim 0.2$, such that V_{sat} and Σ_{sat} abruptly increase at $\beta = \beta_c$ for increasing β. The jumps experienced by both quantities reach a plateau when $La \lesssim 0.2$, while they decrease monotonically as La increases up to $La = 7.5$, where both become zero. We have then extended these results to account for surface diffusion, showing that, in the limit of weak inertial effects, the value of β_c is strongly reduced as surface diffusion becomes important, that is when the surface Péclet number Pe_s decreases significantly, evidencing that surface diffusion favours the formation of satellite droplets.

Regarding the effect of surface viscous forces on the nonlinear regime of unstable liquid filaments, in chapter 4 we have focused on the saturated regime, in which Marangoni stresses are negligible, and the surface tension and surface viscosity coefficients reach constant values. The saturated regime arises at high superficial concentration of surfactants with fast sorption kinetics, or in certain lipidic vesicles. In particular, by means of theory and numerical simulations, we have discovered a new universal asymptotic thinning regime where surface tension balances surface viscous stresses, leading to an exponential thinning of the thread with an e-fold time that only depends on the surface shear and dilational viscosity coefficients and on the surface tension coefficient. We have discussed the use of this phenomenon as the potential basis of a new non-intrusive method of measurement of the surface viscosity coefficients. Then, we have performed an extensive parametric study of the satellite-formation regimes in the limit of a saturated interface, demonstrating that there is also a critical value of the surface viscosities above which satellite droplets are spontaneously formed. In particular, the case where the surface viscous shear dominates over the dilational surface viscous force leads to the formation of more than one satellite droplet. Indeed, in the limit of negligible surface viscous dilatational stresses, a structure of satellite and sub-satellite droplets interconnected by thin filaments is formed, where the characteristic distance between droplets depends on the shear Boussinesq number.

Finally, in chapter 5 we have shown, both theoretically and experimentally, that a liquid jet injected at a constant velocity parallel to the direction of gravity and impacting in a bath of the same liquid, undergoes a Hopf bifurcation at a certain critical injection flow rate, below which the capillary jet sustains spontaneous oscillations of velocity and shape. In particular, the jet exhibits three different states depending on the injection flow rate, liquid viscosity, nozzle radius, and jet length, which are: steady jet, self-oscillating jet, and breakup. By means of experiments, a global linear stability analysis, and numerical simulations of the leading-order one-dimensional model, we have characterized the different regions as a function of the relevant governing parameters. The region where the self-sustain oscillations occur increases with viscosity and decreases as the distance between the nozzle and the bath increases, whereas the steady-jet region increases when the jet length decreases. Additionally, we have shown that below a certain critical jet length, self-oscillations do not arise, and the jet experiences a direct transition from steady jetting to breakup as the injection flow rate is decreased.

Future research avenues

The results obtained in chapters 3 and 4 need an experimental verification, for instance the stabilizing effect of interfacial viscoelasticity in the linear regime, the discontinuous transitions observed in the numerical simulation of the formation of satellite droplets above a certain critical interfacial elasticity and viscosity, and the exponential thinning of a saturated interface when surface viscous forces dominate over volumetric ones. Hence, the most pressing future research direction within the context of this thesis is to carry out appropriately designed experimental campaigns aimed at testing these theoretical and numerical results. Indeed, throughout this thesis all the results have been obtained either in the limit of insoluble surfactants, or in the limit of saturated interfaces. Nonetheless, in most real processes where surface-active molecules are involved, their solubility in the bulk and the sorption/desorption kinetics with the interface are usually important. Hence, a highly relevant direction that clearly deserves to be explored, is to extend the linear and nonlinear analyses reported in the thesis to account for surfactant solubility, and to compare with experiments using soluble surfactants.

Additionally, many applications involve configurations where the interface separates two fluids with similar viscosities. In most of this dissertation, the effect of an outer viscous bath has been neglected by taking the limit $N_\mu \to 0$. It is thus of great importance to extend the seminal work of Tomotika (*Proc. R. Soc. Lond. A*, vol. 150, no. 870, 1935, pp. 322-337) to unravel the effect of interfacial viscoelasticity on the linear regime of a thread immersed in a viscous bath, and also to explore the nonlinear dynamics and satellite-drop formation regimes when $N_\mu \gtrsim 1$.

In this thesis we have also studied the linear stability of an interface with elastic shear resistance to deformation modeled by means of the Hookean and neo-Hookean surface constitutive equations. However, the nonlinear dynamics of a solid-like interface, and the derivation of leading-order and second-order one-dimensional models, is a research direction that clearly deserves further study.

Active and living matter

A relevant extension of this thesis is to study small-scale interfacial flows within the context of active and living systems. Such systems, usually termed as *active matter*, are far-from-equilibrium systems whose constituents constantly convert local energy into mechanical work. The dynamics of active and living matter have raised fascination among scientists, not only for their beauty from the fundamental point of view, but for their crucial relevance and profound implications in many phenomena, namely bacterial growth, morphogenesis, or the cytokinesis of cells, to cite a few. In particular, there is a growing research interest in taming the novel physics that epitomize the behavior of active and living systems, the main efforts being directed towards developing living or synthetic active materials which are able, for instance, to move autonomously or to self-heal.

Thus, it would be interesting to extend the results of this thesis accounting for effects that usually arise in living systems and biological environments, namely tension anisotropy, active stresses, and chemical reactions, as a result of the presence of active units like bacteria, active filaments, or colloids. Indeed, such effects are present within and beneath the cortex of many biological membranes and cells, usually coupled with elastic and viscous interfacial forces, and bulk rheology. Additionally, these systems are usually riddled with suspensions of polymers, organelles, bacteria, or cytoskeletal filaments, whereby their theoretical study can lead to the fascinating research area of elastic and nematic turbulence at low Reynolds numbers.